2. SITE 504[1]

Shipboard Scientific Party[2]

HOLE 504B

Date occupied: 28 January 1993

Date departed: 6 March 1993

Time on hole: 24 days, 2 hr

Position: 1°13.611'N, 83°43.818'E

Bottom felt (drill-pipe measurement from rig floor, m): 3474.0

Distance between rig floor and sea level (m): 11.23

Water depth (drill-pipe measurement from sea level, m): 3462.8

Water depth (sea level, corrected m, echo sounding): 3460

Total depth (from rig floor, m): 5585.0

Penetration (m): 2111.0

Number of cores (including cores with no recovery): 18

Total length of cored section (m): 110.6

Total core recovered (m): 9.58

Core recovery (%): 8.66

Hard rock:

Depth (mbsf): 2111.0
Nature: Moderately phyric plagioclase-olivine-clinopyroxene diabase
Measured velocity(km/s): 5.4 to 6.0

Principal results: The primary objective of Leg 148 was to revisit Hole 504B in the eastern equatorial Pacific in order to deepen the hole into oceanic Layer 3 and to determine the nature of the transition from Layer 2 to Layer 3. Site 504 is located on 5.9-m.y.-old crust 201 km south of the Costa Rica Rift, the easternmost segment of the Galapagos Spreading Center (at 1°13.611'N, 83°43.818'W, at a water depth of 3460 m). Prior to Leg 148, Hole 504B was the deepest scientific drill hole in the oceans, extending 2000.4 meters below seafloor (mbsf; 1725.9 m sub-basement). It is the only hole to penetrate through the volcanic section into the underlying sheeted dike complex, and the site has become an important in-situ reference section for the physical and chemical structure of the upper oceanic crust. Results from recent drilling in Hole 504B during Leg 140 in late 1991, as well as seismic evidence, suggested that the bottom of the hole lay within the lower portion of the sheeted dike complex, close to the seismic Layer 2/Layer 3 boundary. Many scientists believe that the Layer 2/Layer 3 transition coincides with the change downward from sheeted dikes to underlying gabbros as is observed in ophiolites, but the seismic boundary may be a metamorphic transition within gabbros or within the lower sheeted dikes. Although the transition from sheeted dikes to gabbros has been observed by submersible (Auzende et al., 1989; Francheteau et al., 1992) in tectonic exposures of both Atlantic and Pacific ocean crust, this transition has never been observed in situ in undisturbed ocean crust, and its relation to the Layer 2/Layer 3 boundary remains unproven.

Upon re-entering Hole 504B on 28 January, 1993, temperatures were logged from seafloor to just above the total depth of the hole (2000.4 mbsf) with somewhat ambiguous results caused by a calibration error or instrumentation problem. The measured gradient through the cased section was close to the background value in the sediments, indicating that presently there is no downhole flow like that observed in the past. A slight dip in temperatures immediately below the bottom of the casing is similar to that recorded during Leg 140, indicating some hydrologic activity in the uppermost basement. Deep in the hole the gradient is generally linear and consistent with logs taken during Legs 137 and 140, indicating a maximum recorded temperature of about 180°C at the bottom of the hole.

Following temperature measurements, borehole waters were sampled on 28–29 January. Water was collected in 6 of 8 runs, at 560, 796, 1031, 1266, 1501, and 1970 mbsf. One sample (1501 mbsf) clearly displays chemical characteristics of seawater that has reacted with basalt at elevated temperatures, whereas the compositions of other samples are close to seawater. Following drilling operations, the hole was spiked with a NaBr tracer, so future water sampling can detect fluid movement from basement and overlying seawater into or out of the borehole.

Fifteen cores (148-504B-239R through -253R) were drilled from 30 January to 9 February, penetrating from 2000.4 to 2111.0 mbsf (110.6 m), for an average recovery of 10.4%. Twenty-five lithologic units were identified on Leg 148, for a total of 294 units in Hole 504B. The recovered rocks are massive diabases and are a continuation of the sheeted dike complex drilled on previous legs. Five chilled dike contacts were found; other units were identified by differences in mineralogy, grain size, and texture. All rocks are fine-grained with average grain size ranging from 0.4 to 1.0 mm. Fourteen units are sparsely to moderately phyric plagioclase-olivine-pyroxene diabase; four units are sparsely to moderately phyric olivine-plagioclase + pyroxene diabase; three units are aphyric; and four units are sparsely phyric plagioclase-olivine diabase. A trace of chrome spinel is also present in about half the units. Intergranular material is primarily plagioclase and pyroxene, with opaque oxide minerals and olivine in small amounts. Titanomagnetite ranges from 0.02 mm to 0.45 mm in size, and the larger grains contain exsolution lamellae of ilmenite.

Plagioclase phenocrysts occur in every unit and are usually the most abundant phenocryst followed by olivine, then clinopyroxene. Plagioclase phenocrysts are generally 1.0–1.5 mm in diameter, but range up to 5 mm. Pyroxene phenocrysts are similar in size to plagioclase, and olivine phenocrysts are generally 1 mm. Coarse-grained glomerocrysts of plagioclase ± clinopyroxene, olivine, magnetite, or spinel occur in many units, and some of these glomerocrysts have gabbroic textures.

Alteration of the rocks is heterogeneous. The diabases are affected by a pervasive, slight to moderate background alteration (10%–40% recrystallized), with locally more intensively altered zones (40%–100% recrystallized) in centimeter- to decimeter-sized patches and in centimeter-sized alteration halos around veins. Patches and halos make up a few percent of the recovered core. Actinolite (± magnetite) replaces interstitial material, and olivine is totally replaced by talc + magnetite, chlorite + quartz, and actinolite. Clinopyroxene is partially to totally replaced by actinolitic amphiboles, whereas plagioclase is the least altered phase, and is partly replaced by secondary anorthite, chlorite, albite, actinolite, and rare epidote. Titanite(?) partly replaces igneous magnetite, but the ilmenite exsolution lamellae generally appear to remain unaltered. Cr-spinel is partially altered to magnetite around the margins and along internal cracks. Other secondary minerals include traces of pyrite and chalcopyrite, and single occurrences of secondary clinopyroxene, Fe-pumpellyite, and laumontite.

Actinolite (± titanite) veins are the most common veins, and they range in width from 0.05 to 3.0 mm. Dips of actinolite veins are variable, but

[1] Alt, J.C., Kinoshita, H., Stokking, L.B., et al., 1993. *Proc. ODP, Init. Repts.,* 148: College Station, TX (Ocean Drilling Program).

[2] Shipboard Scientific Party is as given in the list of participants preceding the contents.

maxima occur at 20°–25° and 85°–90°. Chlorite ± actinolite forms thin (< 0.5 mm wide), mainly steeply dipping (75°–90°) veins. Single occurrences of chlorite + quartz + titanite, chlorite + quartz + pyrite, chlorite + laumontite, and epidote veins were also observed. There is an average of 21 veins per meter of recovered rock, and veins account for about 1.2 vol% of the total recovered material. The abundance of alteration minerals continues depth trends noted during previous legs involving Site 504, consistent with generally higher alteration temperatures in the lowermost 400 m of sheeted dikes.

Three oriented dike margins were recovered during Leg 148; they dip from 76° to 88°, similar to shallower dikes cored on previous legs. All diabase samples show well-preserved primary (igneous) characteristics and no shape fabric or preferred orientation of grains related to crystal-plastic deformation have been found. Observed structures include veins, microfaults, fractures, chilled margins and rare <1-mm-wide cataclastic zones. Open fractures are common and tend to have gentle or steep dips; they probably were formed by decompression during drilling. Vein orientations are very similar to those recovered from shallower dikes, and they are predominantly dike-parallel and dike-normal; the latter possibly are shrinkage cracks that formed during cooling of the dikes. The morphology and the internal fabric of the veins suggest they formed as extension fractures, possibly by the crack-seal mechanism. Subsequent compression of some veins is indicated by kinked fibers. Shearing, possibly associated with formation of very fine-grained amphibole, appears to have affected some of the veins.

Microfaults are common in Leg 148 cores, leading to an abundance of flat, platy-shaped fragments in the recovered cores. The microfaults are lineated and have steps, but are discontinuous and show no resolvable displacement in thin section. The microfaults are steeply dipping, and slickenlines suggest both dip-slip and strike-slip movement. Microfaults are most abundant from 2026–2052 mbsf, where recovery was relatively low. Large-scale faulting is likely from 2026–2052 mbsf, and at the bottom of Hole 504B (2103–2111 mbsf), where microfaults are abundant, the drilling rate was rapid, and the drill string became stuck.

Magnetic measurements were made on 11 oriented minicores and were supplemented by measurements of natural remanent magnetization (NRM) and bulk susceptibility on 11 small unoriented samples. Magnetic susceptibilities average 0.018 ± 0.013 SI units, similar to values for shallower dikes. The Leg 148 cores lack the steeply inclined drilling-induced remanence observed in shallower dikes. Instead, a relatively weak viscous component is observed, which is generally removed by AF demagnetization at 20 mT. As a result, natural remanent intensities (mean = 0.48 ± 0.39 A/m) and Koenigsberger ratios (mean = 2.2) are lower and mean destructive fields are higher than those for shallower dikes. Measurements of anisotropy of magnetic susceptibility are consistent, despite low degrees of anisotropy. The observed fabric has a minimum axis that is horizontal and north, and a maximum axis that is horizontal and east (corrected using the stable remanence direction). This may be interpreted as horizontal dike-parallel flow at the dike margins and crystal settling at the dike center.

The wet-bulk densities range narrowly from 2.88–3.05 g/cm^3, with most >2.90, and compressional-wave velocities range from 5.4–6.0 km/s in response to slight variations in olivine abundance and alteration over the cored interval, consistent with values obtained for the immediately overlying dikes. The velocities are too low for rocks of this density, suggesting the opening of microcracks during decompression as the rocks were brought to the surface. Resistivities range from 80 to 250 Ωm in response to changes in porosity (1%–5%) and alteration. The thermal conductivity values range from 2.0–2.2 W/(m · K), within the limits observed throughout the overlying sheeted dikes.

The penetration rate for the last core (148-504B-253R) was very fast (7 m/hr), and after picking up the bit off the bottom to retrieve the core the drill string became stuck near the bottom of the hole on February 9. The high penetration rate for this core and the recovery of tabular rock pieces with microfaults and slickenlines in this core and most of the preceding cores suggest that drilling penetrated a fault.

Approximately 30 hr were spent in efforts to free the string. When it became clear that we were making no progress, and in order to avoid damaging the drill string, it was backed off near the top of the bottom hole assembly (BHA). Operations at Site 504 were discontinued to await arrival of fishing tools (fishing jars, mill bits), which took 9 days. Hole 504B was not logged at this time in order to avoid jeopardizing fishing operations by knocking wallrocks onto the junk in the hole or leaving additional junk from logging tools in the hole. Because the most interesting part of the hole was the newly drilled section, and the BHA left in the hole extended through the Leg 148 section and up to 100 m into the overlying Leg 140 section (to 1900 mbsf), the scientific benefit of logging at this time was minimized. After setting a reentry cone and coring at nearby Site 896, the fishing tools arrived on 20 February and operations were continued in Hole 504B. The drill string was freed using the fishing jars, and all of the drill string was recovered on deck except for the drill bit, which had broken off and remained at the bottom of the hole. Mill bits were then run to grind up the drill bit and clean the hole. The first mill run was successful, but the second mill run encountered rubble that filled the hole to 19 m above the lost drill bit; on deck it was discovered that the fishing jars had broken, leaving the mill bit, various subs, and a drill collar stuck in the hole. The junk was ultimately fished out using an overshot and the fishing jars. The seals on the jars were damaged and leaking oil, however, rendering the jars unusable after this operation. Because of the scientific value of the hole, the high probability of getting stuck again, and the lack of any usable fishing or drilling jars, it was decided to log Hole 504B at this time rather than attempt cleaning the rubble and milling the lost drill bit without the means to free a stuck drill string. Such hole cleaning and milling operations were left to a future leg equipped with the proper tools, and any time remaining after logging Hole 504B would be devoted to the contingency Hole 896A.

Four days were spent logging Hole 504B. The geophysical, FMS, and magnetometer logs were run over the entire length of basement, and two unsuccessful attempts at the VSP were made 25–27 February. The VSP was finally run successfully 4 March.

The various logs give a consistent and clear picture of the 504B basement section. Sonic velocities from the log generally fall between 4.5 and 5.5 km/s in the volcanic section and transition zone above 1100 mbsf, but are greater (6.0–6.5 km/s) in the dikes from 1200 to 1800 mbsf. Below this depth velocities drop slightly and then increase steadily to a value of 6.8 km/s at the lowermost depths measured (2060 mbsf). The velocities of the sheeted dikes fall in the upper range for seismic Layer 2, but the maximum velocity recorded (6.8 km/s) near the bottom of the hole is typical of Layer 3. Rocks recovered from this interval are fine-grained diabase dikes, suggesting the possibility that the transition to seismic Layer 3 may begin within sheeted dikes and may not necessarily correspond directly with the appearance of gabbros.

A VSP experiment was run using the Schlumberger WST vertical-component seismic tool from 1516 to 2076 mbsf. Combined with the data from the VSP run on Leg 111, this provides complete coverage of the entire basement section. Preliminary interval velocities below 1550 mbsf range from 5.5 to 7 km/s with an average of 6.58 km/s, in agreement with data from the sonic log and for high-pressure measurements on recovered samples. No reflector that could be attributed to the fault at the bottom of the hole was observed.

The resistivities are generally low in the volcanic section and increase downward into the dikes. Spikes of low resistivity at 1925 and 1935 mbsf suggest the presence of locally intense horizontal fracturing. The generally high resistivities in the dikes decrease below 2040 mbsf where microfaults are common in the recovered core, consistent with increased fracturing leading up to a larger fault at the base of the hole.

The uncorrected profile from the magnetometer log can be divided into three zones: the volcanic section from 275 to 850 mbsf, with total field amplitudes of up to 4000 nanoteslas (nT); the transition zone from 850 to 1050 mbsf, with anomalies less than 100 nT; and the sheeted dikes from 1050 to 2079 mbsf, with anomalies of up to 1000 nT. The extrusive zone produces predominantly negative horizontal and positive vertical field anomalies, indicating reverse remanent magnetization of the basalts consistent with location of the site within a reversed magnetic anomaly. The anomalies in the sheeted dikes appear to be mostly negative in the horizontal component, but detailed analysis must await final corrections of the raw data.

The FMS recorded full images in the lowermost 20 m and lower quality images in the rest of the hole because of the failure of one of the pads. The tool provided a caliper log of the borehole, showing increased diameter above 1000 mbsf, local enlargements in the dikes, and relatively uniform hole size of less than 12 in. in the lowermost 500 m. The tool also showed a change in orientation of breakouts in the hole, from predominantly 122°N in the upper portion of the hole to 015°N below 1500 mbsf, perhaps indicating a change in stress or in the response to stress in the lower part of the hole.

Results from Leg 148 suggest that Hole 504B now extends into the transition to Layer 3, but unequivocal penetration into Layer 3 stopped when drilling encountered a fault. Intriguing questions regarding what kind of material makes up the fault zone and, more particularly, what lies on the other side of the fault remain unanswered. A partly milled drill bit and some rubble lie at the bottom of the hole, but the hole can be cleaned on a future leg, given the proper equipment to stabilize the bottom of the hole and to mill the remaining small amount of junk.

BACKGROUND AND OBJECTIVES

Hole 504B is the deepest scientific drill hole in the oceans, penetrating to 2000.4 mbsf (1725.9 m sub-basement) over the course of six previous Ocean Drilling Program (ODP) and Deep Sea Drilling Project (DSDP) legs. It is the only hole to penetrate through the volcanic section into the underlying sheeted dike complex, and the site has become a reference section for the petrology, geochemistry, hydrothermal alteration, and magnetic and physical properties of the upper oceanic crust (Anderson et al., 1982; Becker, Sakai, Adamson, et al., 1989). Recent drilling results from the site (Dick, Erzinger, Stokking, et al., 1992) and seismic evidence (Becker, Sakai, et al., 1988; Collins et al., 1989; Mutter, 1992) suggest that the bottom of the hole lies within the lower portion of the sheeted dike complex, close to the seismic Layer 2/Layer 3 boundary. Many scientists believe that the Layer 2/Layer 3 transition coincides with the change downward from sheeted dikes to underlying gabbros as is observed in ophiolites, but it has also been suggested that the seismic boundary may be a metamorphic boundary within gabbros, or that it may lie within the lower sheeted dikes (e.g., Fox et al., 1973; Christensen and Salisbury, 1975). The transition from sheeted dikes to gabbros has been observed by submersible in tectonic exposures of both Atlantic and Pacific ocean crust (Auzende et al., 1990; Francheteau et al., 1990), but this transition has never been observed in situ in undisturbed ocean crust, and its relation to the Layer 2/Layer 3 boundary remains unproven. ODP Leg 148 returned to Hole 504B in the eastern Pacific in order to deepen the hole with the main goals of penetrating into oceanic Layer 3 and determining the nature of the transition from Layer 2 to Layer 3.

Geologic Setting of Site 504

Site 504 is located in 5.9-m.y.-old crust, 200 km south of the Costa Rica Rift in the eastern Pacific (Fig. 1). Dick, Erzinger, Stokking, et al. (1992) have recently provided a thorough review of the geologic and tectonic setting of Site 504, which is briefly summarized here. Site 504 is located in the center of the 171-km-long east-west segment, which is bounded by the Panama Fracture Zone on the east and by the Ecuador Fracture Zone to the west. The Costa Rica Rift is the easternmost of three rift segments along the Galapagos or Cocos-Nazca spreading center, which separates the Cocos and Nazca plates. Farther to the west lie the Ecuador and Galapagos rifts. The Costa Rica Rift spreads asymmetrically at an intermediate rate (i.e., a half-rate of 3.6 cm/yr to the south and 3.0 cm/yr to the north; Hey et al., 1977). The basement relief south of the Costa Rica Rift results from the presence of east-west normal faults parallel to the rift axis, which produce south-tilted grabens separated by ridges 1 to 2 km wide (Langseth et al., 1983; Hobart et al., 1985). The location of Site 504 at the center of a spreading segment is significant, as this influences magmatic and tectonic processes, which in turn affect physical properties and hydrothermal alteration of the crust.

Hole 504B was originally drilled as part of a comparison of sealed crust to that still open to convective cooling by seawater (Cann et al., 1983; CRRUST, 1982). Site 505 is located in 3.9-m.y.-old crust about 100 km north of Hole 504B (Fig. 2) and is characterized by rough basement topography (up to 300 m relief), relatively thin sediment cover, and low heat flow, indicating strong convective cooling of the basement. In contrast, Site 504 is located in an area where the measured heat flow falls close to the theoretical conductive cooling curve for ocean crust (Langseth et al., 1983). The high sedimentation rate (50 m/m.y.) has resulted in a thick sediment cover that effectively seals the relatively smooth basement surface (about 100–200 m relief) from open communication with seawater. Such sealing of the crust occurs throughout the oceans, but generally at much greater crustal ages (up to 20–80 m.y.; Anderson and Skilbeck, 1981). Thus, Site 504 has been sealed off from free access by seawater relatively early, which may have led to a somewhat greater geothermal gradient at the site than elsewhere in the crust. Detailed heat-flow measurements around Site 504, however, indicate continuing subdued convection around Site 504 (Langseth et al., 1988), and chemical gradients in sediment pore waters reveal that fluids advect through the sediment (Langseth et al., 1988). Modeling of the heat-flow data, however, suggests that convection is mainly restricted to the upper few hundred meters of basement, whose topography controls the geometry of circulation (Fisher et al., 1990). Klitgord et al. (1975) found that the spreading rate of the Costa Rica Rift changed from 2.6 cm/yr to 3.8 cm/yr at about 4.1 m.y., which may account for the differences in basement topography between Sites 504 and 505. Although increasing spreading rate is generally associated with smoother topography, crust generated at intermediate-spreading ridges may be either rough or smooth.

Lithostratigraphy of Hole 504B and Previous Drilling History

Six DSDP and ODP legs prior to Leg 148 contributed to the 2000.4 mbsf penetration of Hole 504B, beginning in 1979 with the first drilling (Fig. 3; Cann et al., 1983; Anderson, Honnorez, Becker, et al., 1985; Becker, Sakai, et al., 1988, 1989; Becker, Sakai, Adamson, et al., 1989; Dick, Erzinger, Stokking, et al., 1992; Becker, Foss, et al., 1992). The hole was also visited during Leg 92 in 1983 for downhole logging and borehole fluid sampling (Leinen, Rea, et al., 1986). Drilling penetrated 274.5 m of sediments (siliceous oozes, chert, limestone, and chalk); a 571.5-m volcanic section consisting of pillow and massive flows, breccias, and possible local dikes or sills in the lower half of the section; a 209-m transition zone of pillow basalts and dikes; and, prior to Leg 148, 945.4 m of dikes and massive units, interpreted to be a sheeted dike complex. Core recovery averaged 29.8% in the volcanic section, 25.3% in the transition zone, and 14.3% in the sheeted dikes at the end of Leg 140.

Drilling near Site 504 actually began at Site 501 on Leg 68 in 1979. Coring penetrated the sediments and 73 m into basement, but was terminated because of thruster problems on the *Glomar Challenger.* Hole 504B was started in the last days of Leg 69, following drilling of the pilot hole and reentry into Hole 504A, which was terminated because of the loss of two roller cones and their supports from the drill bit used to install the casing. Leg 69 spent 4.8 days coring, penetrating the sediments and 214.5 m into basement (489 mbsf) in Hole 504B. To further the scientific goals of Leg 69 and because of the relatively easy drilling in Hole 504B, Leg 70 subsequently returned to the site and the crew spent 8.9 days coring, penetrating 347 m to 836 mbsf. Leg 83 was the first leg devoted solely to Hole 504B; it spent 21.3 days at the end of 1981 to drill 514 m to 1350 mbsf. The top of the transition zone was placed at 846 mbsf where three dikes occurred close together; greenschist-grade hydrothermal alteration was encountered at 898 mbsf; a stockwork-like sulfide mineralization was cored between 910 and 928.5 mbsf; and 100% sheeted dikes

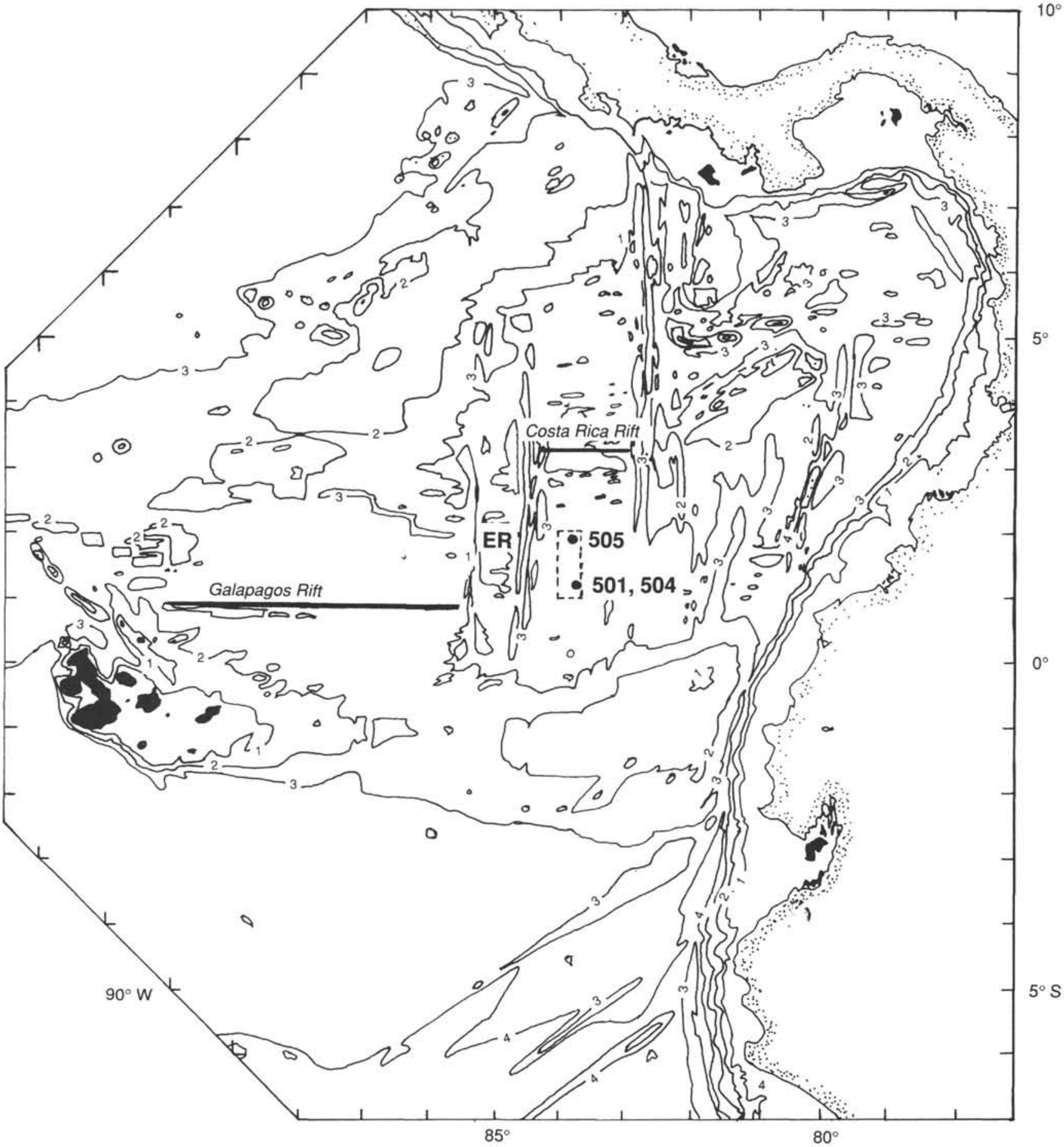

Figure 1. Location of DSDP/ODP Sites 501, 504, and 505 south of the Costa Rica Rift in the eastern equatorial Pacific (from Hobart et al., 1985). Bathymetric contours in kilometers.

began at 1055 mbsf. Leg 83 was a tremendous success, confirming the ophiolite model for the upper ocean crust and providing the first in-situ samples of hydrothermally altered rocks and sheeted dikes. Basement penetration more than doubled, to greater than 1 km into basement, despite twice breaking off more than 100 m of the drill string plus the bottom hole assembly. The site was revisited during Leg 92, which spent 9.2 days sampling borehole fluid and logging. Leg 111 returned to Hole 504B in 1986 and spent 17 days coring to 1562.3 mbsf in the dikes. Penetration was slowed by the loss of roller cones from two drill bits, whose rescue required fishing and milling operations; coring was finally halted by the loss of a diamond drill bit at the bottom of the hole.

One of the important experiments run on Leg 111 was the vertical seismic profile (VSP), which identified several reflectors beneath the bottom of the hole. A reflector at approximately 1700 mbsf was suggested to be the Layer 2/Layer 3 boundary, and a deeper reflector at approximately 2400 mbsf was thought to be a dipping reflector within Layer 3 (Becker, Sakai, et al., 1988). Given the significance

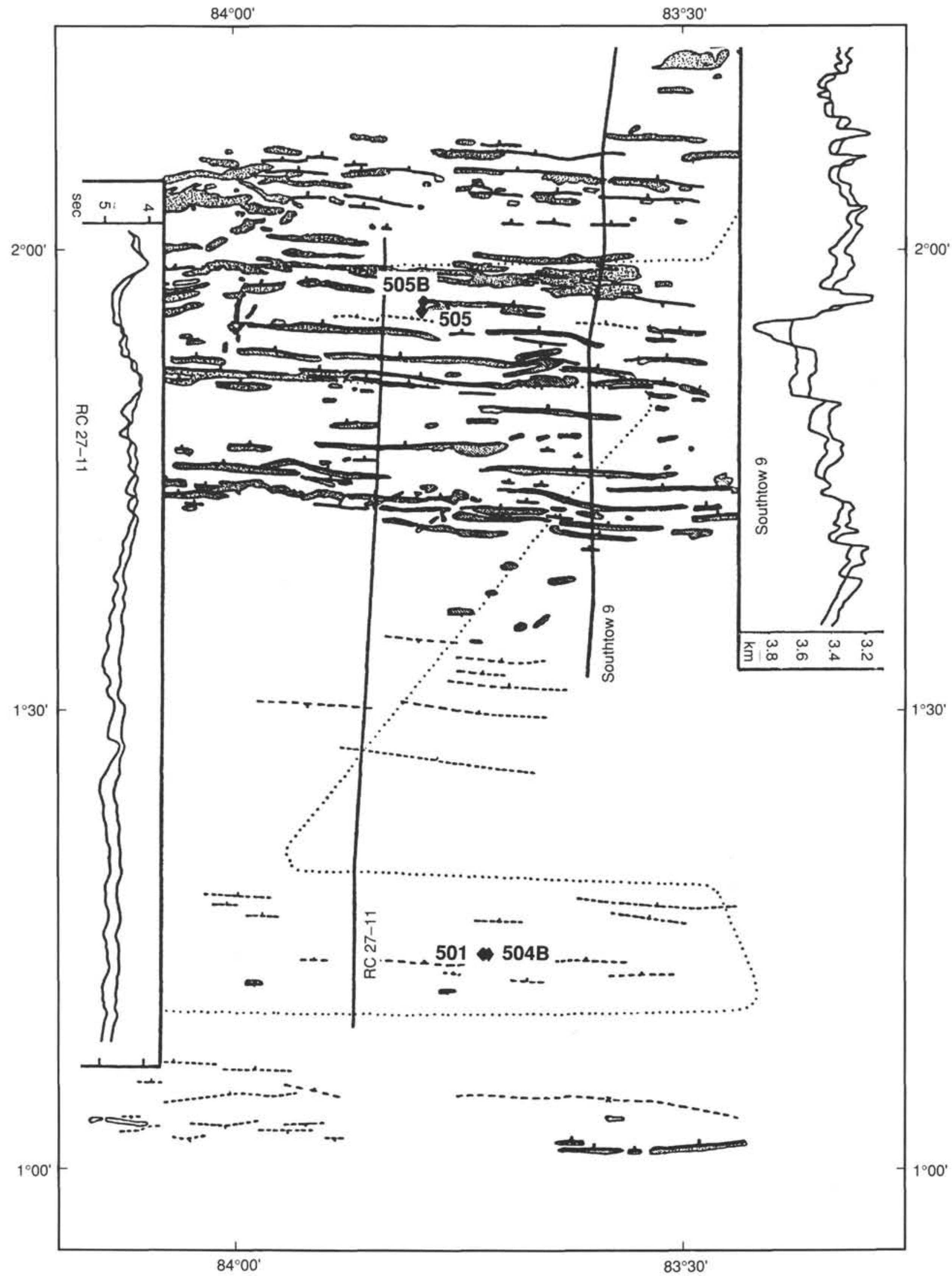

Figure 2. Regional geology south of the Costa Rica Rift based on GLORIA and seismic surveys (from Searle, 1983). Illustrated are northward-facing fault scarps and basement highs around DSDP Sites 501, 504, and 505. Shaded areas = basement outcrops, heavy lines = fault scarps, and broken lines = steep, sediment-covered slopes (possibly buried fault scarps).

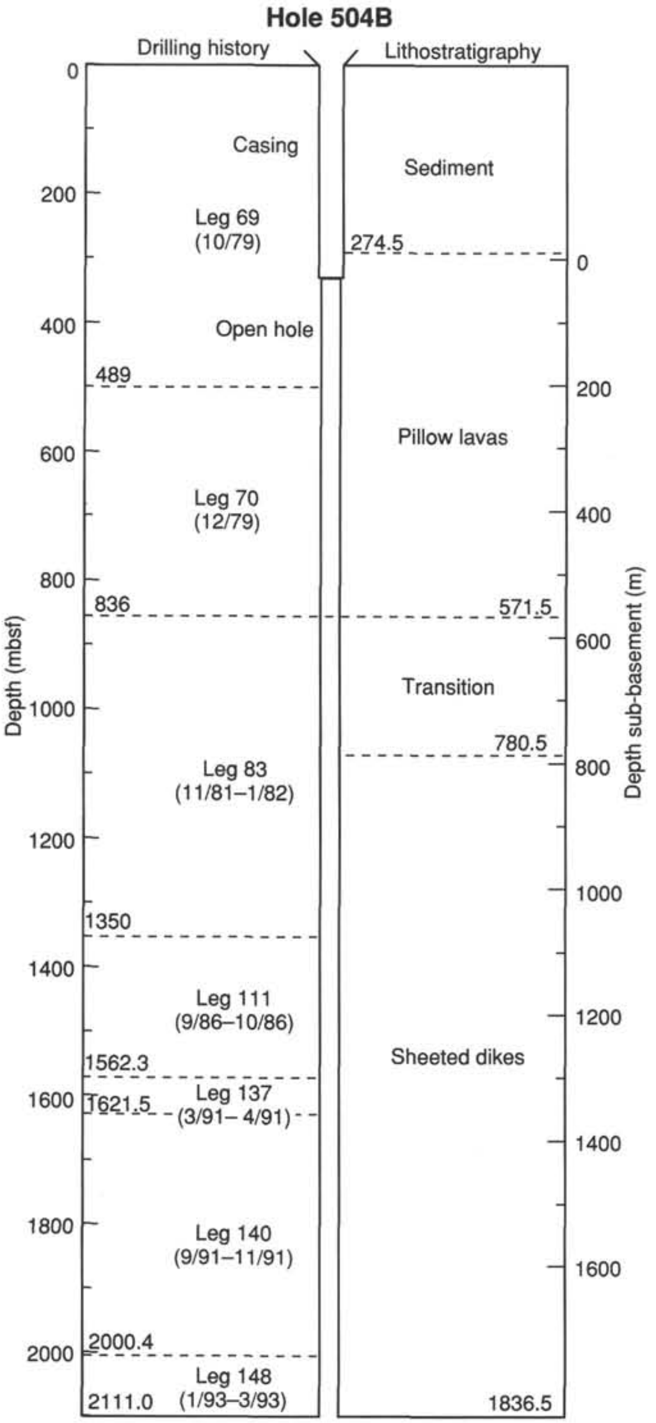

Figure 3. Generalized drilling history and lithostratigraphy of Hole 504B.

of Hole 504B as a reference section for the upper oceanic crust and the potential for continuing the hole into the lower crust, Leg 137 returned to Hole 504B in 1991 as an engineering leg, with the objective of cleaning the junk out of the hole. After only 7 days of fishing and milling the hole was cleared, and it was then drilled (10.6 m) and cored (48.6 m) to 1621.5 mbsf. Unfortunately, this success was marred by the loss of an 18-m outer core barrel with diamond drill bit in the hole near the end of the leg. Because of the lack of time and proper equipment, the junk was left in the hole. Leg 140 returned near the end of 1991, and in 10.5 days of fishing and milling managed to clean the junk out of the hole; an additional 378.9 m were then cored to reach 2000.4 mbsf in 26 days. The hole penetrated the 1700 mbsf depth that was thought to be the top of Layer 3, but there was no significant change in lithology. Coring proceeded steadily at 1–2 m/hr without the equipment problems that occurred on previous legs. This leg proved that deep drilling in oceanic basement was feasible with current technology and left open the possibility of returning to Hole 504B in order to penetrate the base of Layer 2 into Layer 3.

Petrology of Basement Rocks

The rocks recovered from Hole 504B during Leg 148 are aphyric to highly phyric tholeiitic basalts. They are divided into four major types: aphyric basalts are the most abundant, followed by olivine-plagioclase-clinopyroxene phyric basalts, olivine-plagioclase phyric rocks, and olivine-plagioclase-clinopyroxene-spinel-bearing basalts. Olivine-plagioclase and plagioclase-clinopyroxene basalts occur deeper in the hole, and aphyric rocks become more abundant with depth in the dike section. A remarkable feature of the basalts is that there are generally only slight variations in their composition throughout the entire volcanic and dike sections. Basalt compositions are similar to moderately evolved mid-ocean ridge basalt (MORB), with Mg numbers mostly in the range 0.63–0.74. The rocks are unusually depleted in incompatible elements (TiO_2 = 0.67%–1.1%, Nb < 0.3–0.7 ppm, Zr = 35–38 ppm), but have incompatible element ratios comparable to normal MORB as defined by Bryan et al. (1976). The refractory nature of the basalts is also illustrated by their high CaO/Na_2O ratios (5–8), which are in equilibrium with exceptionally calcic plagioclase at liquidus temperatures. The basalts have been interpreted as being very primitive (Emmermann, 1985; Natland et al., 1983), or the result of multi-stage melting of a normal MORB mantle source followed by moderate extents of crystal fractionation (Autio and Rhodes, 1983; Autio et al., 1989; Kempton et al., 1985). The exceptional overall uniformity in composition of the basalts has been interpreted to indicate the presence of a steady-state magma chamber beneath the rift axis (Natland et al., 1983). Three units (two volcanic and one dike) that comprise less than 2% of the core are enriched- or transitional-type MORB (Autio and Rhodes, 1983; Emmermann, 1985). A separate mantle source has been suggested for these rocks (Emmermann, 1985), but their origin remains problematic.

Alteration of basement from Hole 504B has been documented in detail (Alt et al., 1986; Alt, Muehlenbachs, and Honnorez, 1986; Alt, Anderson, and Bonnell, 1989; Alt et al., 1989; Shipboard Scientific Party, 1992a, 1992b). The core can be divided into three zones (Fig. 4): the upper 320 m of the volcanic section was affected by oxidizing "seafloor weathering" at low temperatures (0°–100°C) and high water/rock ratios (~100); the lower portion of the volcanic section was affected by low temperature (<150°C), reducing alteration at lower water/rock ratios (~10); and the transition zone and dikes were hydrothermally altered under greenschist and superimposed zeolite conditions. The sequence of hydrothermal alteration in the transition zone and dikes can be summarized in three basic stages (Alt et al., 1986; Alt, Muehlenbachs, and Honnorez, 1986). First, chlorite and amphibole formed in veins and greenschist minerals formed in the rocks during axial hydrothermal alteration at temperatures of 250°–380°C. Later, as the crust moved off-axis into a recharge zone, penetration of seawater into still-warm rocks resulted in precipitation of anhydrite in cracks and local replacement of plagioclase by anhydrite. Finally, zeolites formed in fractures and rocks during later off-axis alteration at lower temperatures (less than 150°–200°C).

Some important variations in proportions of secondary minerals occur with depth in the dikes. The abundance of amphibole replacing clinopyroxene generally increases with depth in the dikes, whereas calcic plagioclase is less extensively altered to albite, and secondary anorthite appears, as depth increases. Preliminary data for Leg 140 indicate the presence of hornblende and anorthitic secondary plagioclase in the rocks and a progressive decrease in Zn content from 1600 to 2000.4 mbsf. These mineralogical and chemical changes are inter-

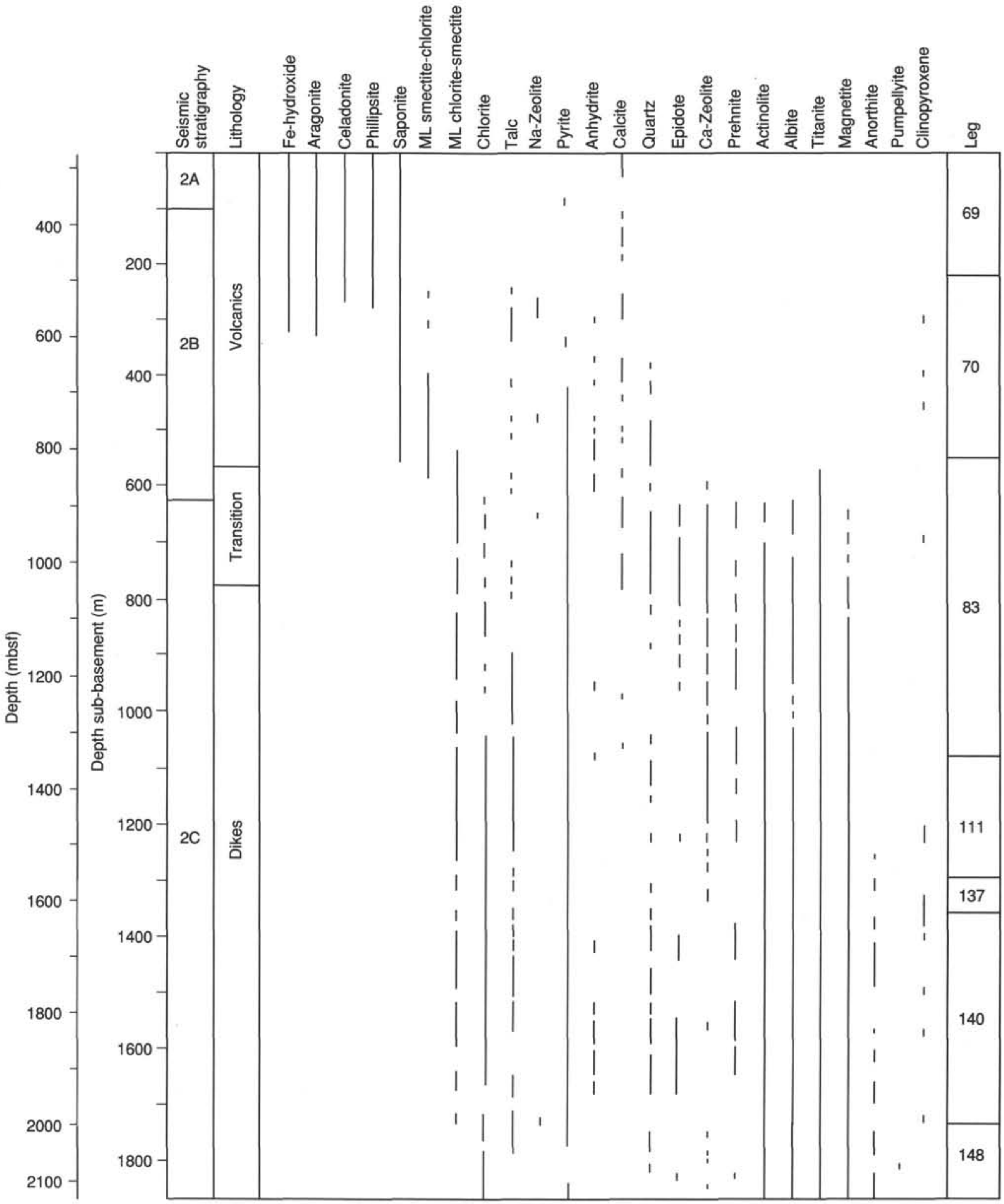

Figure 4. Seismic stratigraphy, lithology, and secondary mineralogy with depth in Hole 504B. ML = mixed-layer. After Alt et al. (1986) and Shipboard Scientific Party (1988, 1992a, 1992b).

preted to reflect higher temperatures at depth, with conditions approaching the amphibolite facies.

Physical Properties and Downhole Measurements

Hole 504B has been logged with an extensive suite of downhole tools during several legs (69, 70, 83, 92, 111, 137, and 140), providing important information about the physical properties of the crust. The sonic data indicate a thin Layer 2A (Fig. 4), consisting of highly porous and permeable volcanic rocks in the upper 100 m (Newmark et al., 1985; Newmark, Zoback, and Anderson, 1985). Layer 2B comprises the lower 500 m of volcanic rocks, where the original porosity has been mostly sealed by secondary minerals. The physical properties of the crust measured in situ change significantly across the transition from volcanic rocks to sheeted dikes: the sonic and seismic velocities increase sharply, whereas bulk permeability and porosity drop by orders of magnitude (Fig. 5; Anderson, Honnorez, et al., 1982). The sonic and seismic data are generally consistent with a sharp boundary between Layers 2A and 2B at the top of the sheeted dikes (Salisbury et al., 1985), whereas the petrological boundary is transitional. Porosities decrease and thermal conductivities increase with depth in the dikes, but sonic velocities measured at 1 atm show no increase because microcracks, which are likely sealed at in-situ pressures, may reduce the sonic velocities (Fig. 6; Dick, Erzinger, Stokking, et al., 1992).

Measurement of dip angles and magnetic reorientation of chilled dike margins suggest that the dikes strike roughly east-west and dip about 80° northward toward the rift axis (Becker, Sakai, et al., 1988; Dick, Erzinger, Stokking, et al., 1992). A change in magnetic inclination at about 800 mbsf in the lower volcanic section suggests that a fault may be present (Kinoshita et al., 1989). Clay-cemented breccias are common from the lower volcanic section (Cann et al., 1983), and the resistivity log shows a minimum at about 800 mbsf (Fig. 6), indicating increased fracturing at this depth. Evidence for small-scale offsets has also been documented from detailed study of slightly deeper rocks (840–958 mbsf; Agar, 1991).

The VSP experiment run on Leg 111 identified several reflectors beneath the bottom of the hole (Becker, Sakai, et al., 1988). A reflector at approximately 1700 mbsf was suggested to be the Layer 2/Layer 3 boundary, but penetration of this depth on Leg 140 showed no significant change in lithology. A deeper reflector at approximately 2400 mbsf was thought to be a dipping reflector within Layer 3.

Temperature measurements prior to drilling were made on several legs (Fig. 7), indicating variable flow rates of bottom seawater down the hole and out into an aquifer within Layer 2A in the upper 100 m of basement. Water within the borehole was sampled prior to drilling on Legs 70, 83, 92, 111, and 137, in attempts to sample basement formation waters. These efforts met with variable success, partly because of sampling problems. The borehole waters exhibit significant differences in composition from seawater and are attributed to reaction with basaltic basement (Mottl and Gieskes, 1990). Whether these chemical differences result from the presence of basement formation fluids or to reaction of seawater with basalt within the borehole (Becker, Foss, et al., 1992) remains enigmatic.

Objectives of Leg 148

The main objectives of Leg 148 were to deepen Hole 504B into oceanic Layer 3 and to determine the nature of the transition from Layer 2 to Layer 3. This transition is generally expected to coincide with the change downward from sheeted dikes to underlying gabbros. Of the 43 day duration of Leg 148, 32 days were to be devoted to coring Hole 504B. Prior to drilling, a maximum of two days were allotted to measurement of temperatures in the hole to examine the status of water flow into the hole and to ascertain temperatures and heat flow at depth, and to sampling of borehole waters in order to constrain seawater-rock reactions and geochemical fluxes in off-axis hydrothermal systems. Following drilling, up to 3 days were to be devoted to geophysical measurements, including the quad combo, Formation MicroScanner, geochemistry, borehole televiewer, and magnetometer. One day was allotted for a VSP experiment in the hole in order to obtain in-situ seismic data to define the transition from Layer 2 to Layer 3. Up to one day was reserved for a packer/flowmeter experiment to identify zones of fluid flow in the hole and to measure the permeability of the newly drilled section.

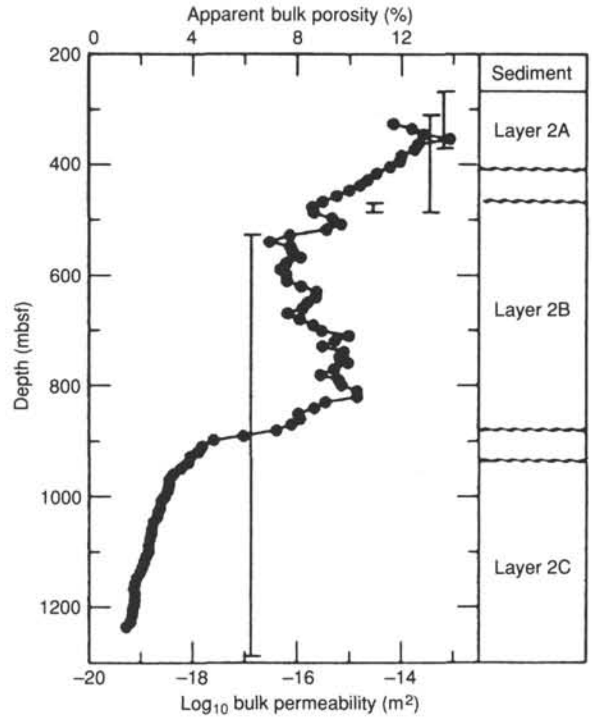

Figure 5. Variation of apparent bulk porosity of basement with depth in Hole 504B determined by applying Archie's Law to large-scale electrical resistivity logs and bulk permeabilities measured over the intervals spanned by the vertical bars. Approximate boundaries of seismic layers are shown at right (from Becker, Sakai, et al., 1988).

OPERATIONS

Leg 148 began with the first mooring line in Balboa Harbor, Panama, at 1645 UTC on 21 January, 1993. The *JOIDES Resolution* left Panama after completion of port-call activities on 25 January and approached Site 504 at 0345 UTC on 28 January. Ship control was shifted to dynamic positioning (DP) and the first beacon was dropped at 0450 UTC.

Logging: Phase 1

The initial pipe trip was begun as soon as the beacon was dropped on 28 January. Prior to reentering Hole 504B the drill pipe was circulated to clean it of any rust or pipe dope that could contaminate water samples. The drill string was slowly run into the hole to 148.14 mbsf in order to minimize disturbance of the water column. The Gable high-temperature tool was run to obtain a static borehole temperature profile (see "Downhole Measurements" section, this chapter). The tool failed shortly after its deployment and was pulled from the hole. One water sample was collected while the flooded tool was being repaired, and the temperature tool was then rerun. Water sampling resumed and 7 additional water samples were collected (see "Borehole Fluid Geochemistry" section, this chapter).

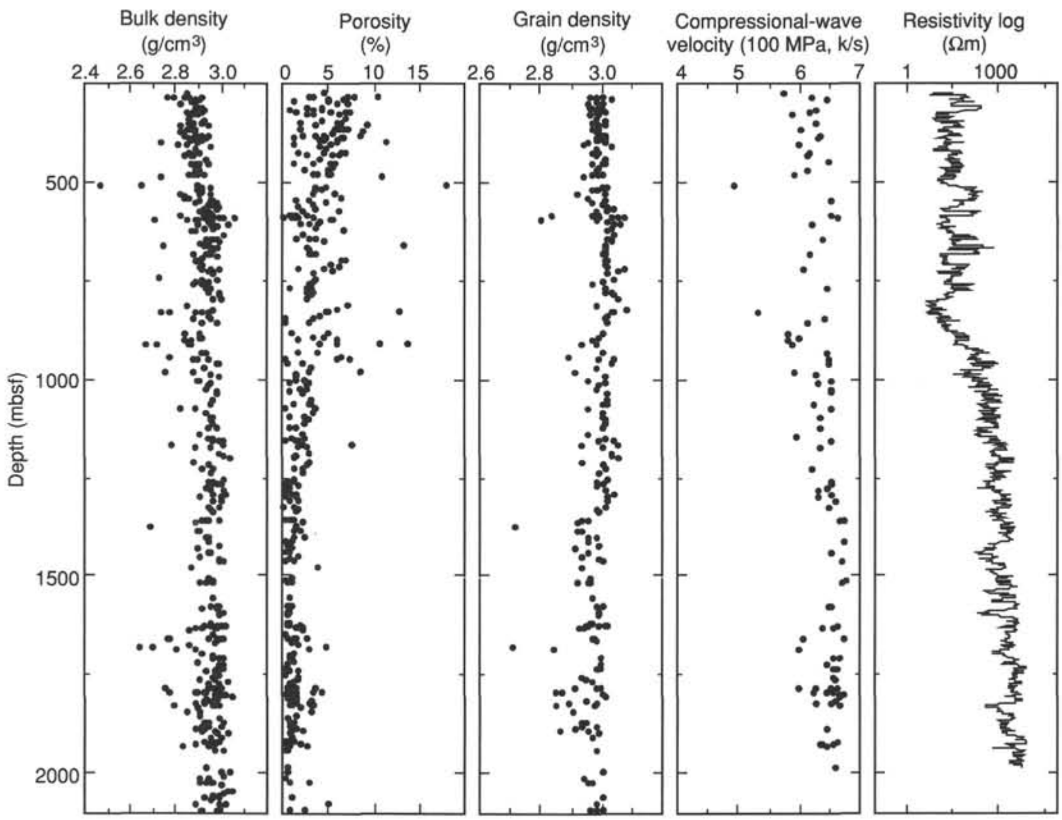

Figure 6. Variations in physical properties with depth in Hole 504B (Shipboard Scientific Party 1985, 1988, 1992a, 1992b).

Coring Operations

Bits and Bottom-hole Assembly (BHA)

In order to extend bit life and improve core recovery, strengthened tungsten-carbide-insert bits were manufactured by Rock Bits Industries (RBI) for coring at Hess Deep (Leg 147) and at Hole 504B. Two versions of the bits were available on Leg 148: C-7 bits, with longer tungsten-carbide inserts, designed to drill softer material, and C-9 bits, with shorter inserts for drilling harder rocks. The BHA used during Leg 148 consisted of a 9-7/8-in. four-cone rotary coring bit and core barrel, eleven 8-1/4-in. drill collars, McCullough jars (Coring Run 1 and Milling Run 1), two control-length drill collars, one 7-1/4-in. drill collar, two stands of 5-1/2-in. drill pipe, 150 stands of 5-in. drill pipe, and 41 stands of 5-1/2- in. drill pipe at the top of the string. The BHA was designed to provide a weight on bit of 40,000 to 45,000 lbs. Because of the high temperatures expected in the hole, butyrate liners were not used; instead, the core was received directly into either the steel or chrome barrel.

Coring Run 1

A Security 9-7/8-in. rotary coring bit (the type used during Leg 140) was run from 2000.4 to 2038.17 mbsf, coring 36.77 m in 20.5 rotating hr for an average rate of penetration of 1.79 m/hr. The bit was run with 30,000 lb weight on bit at 50 rpm. High torque was measured while drilling Cores 148-504B-239R and -243R. Penetration rate decreased while cutting Core 148-504B-243R, and the bit was pulled after having been run for over 20 hr. Two intervals of constricted hole were experienced while pulling out of the hole: one at 2028–2031 mbsf and the other at 2010–2013 mbsf. Examination of the bit revealed that one of the four cones had been lost and the others had dropped roller bearings into the hole, requiring a mill run to clean the hole.

Milling Run 1

The milling assembly included a 9-9/16-in. concave mill with two junk baskets. The trip to the bottom was interrupted periodically by stopping to cool the hole for 15-min intervals. When the milling assembly arrived at the bottom, the hole was washed and reamed from 1955.93 to 2036.66 mbsf, then milled at 95 rpm with 8000 to 10,000 lb of weight on bit. The hole was constricted and the mill became stuck at the bottom, requiring 115,000 lb overpull before it was freed. Drag of 25,000 to 30,000 lb was experienced on the trip out of the hole. The junk baskets contained large pieces of bit-cone material, 33 bearings, 16 bit inserts, klusterite from the mill, and 173.3 g of miscellaneous junk. Cracks in the McCullough jars were observed while inspecting the BHA, and the jars were removed.

Coring Run 2

Because the Security bit was destroyed in only 20.5 rotating hr, an RBI C-9 bit and a junk basket were used for the second coring run. (In this and all subsequent bit runs, the trip was interrupted to cool the hole and the lower portion of the hole was reamed.) Core 148-504B-244R was drilled at a penetration rate of 1.41 m/hr. Torque increased while cutting the next core, so the weight on bit was increased from 30,000 to 35,000 lb and the torque stabilized. Although Core 148-504B-245R recovered 0.63 m of material, it showed no evidence of having cored anything (see Table 1 and "Igneous Petrology" section, this chapter). The average rate of penetration for the first two cores cut by the second bit was 2.0 m/hr. While cutting Core 148-504B-246R, the rate of penetration varied and eventually decreased to about 1.0 m/hr. The bit was pulled after only 11.08 rotating hr. The spiral stabilizers on the bit showed evidence of having drilled junk and the teeth in middle rows of all cones were broken. The junk basket contained 660.7 g of metal, including 3 large pieces from the cone noses and 11 bit inserts.

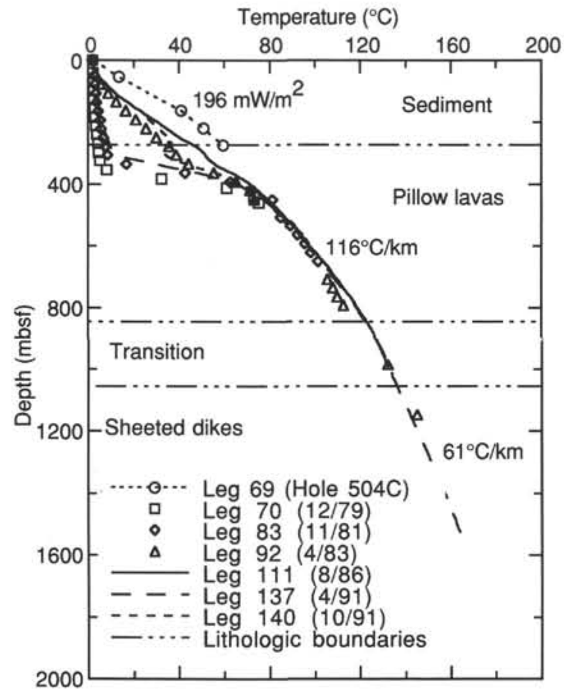

Figure 7. Temperatures measured in Hole 504B. The depressed temperatures in the upper 400 m reflect the downhole flow of cold ocean bottom water through the casing into the upper 100–150 m of basement.

Table 1. Coring summary, Hole 504B.

Core	Date (1993)	Time (UTC)	Sub-bottom top (m)	Sub-bottom bottom (m)	Meters cored	Meters recovered	Percent recovered
Coring							
239R	31 Jan.	325	2000.4	2006.9	6.5	0.52	8.00
240R	31 Jan.	1130	2006.9	2016.5	9.6	0.72	7.50
241R	31 Jan.	1830	2016.5	2025.9	9.4	1.33	14.10
242R	1 Feb.	10	2025.9	2035.3	9.4	0.39	4.20
243R	1 Feb.	1635	2035.3	2038.2	2.9	0.00	0.00
244R	4 Feb.	2320	2038.2	2042.8	4.6	0.14	3.00
245R	4 Feb.	505	2042.8	2052.2	9.4	0.63	6.70
246R	4 Feb.	2035	2052.2	2056.7	4.5	1.00	22.00
247R	5 Feb.	1740	2056.7	2061.8	5.1	0.82	16.10
248R	6 Feb.	25	2061.8	2071.2	9.4	0.61	6.50
249R	6 Feb.	720	2071.2	2080.4	9.2	1.24	13.50
250R	7 Feb.	315	2080.4	2089.9	9.5	0.95	10.00
251R	8 Feb.	25	2089.9	2099.4	9.5	0.86	9.10
252R	8 Feb.	1620	2099.4	2103.5	4.1	0.33	8.10
253R	9 Feb.	1415	2103.5	2111.0	7.5	0.04	0.50
Total					110.6	9.58	8.66%
Milling							
254M	21 Feb.	2230	0.0	1966.1		0.14	0
255M	22 Feb.	140	0.0	2111		0.10	0
256M	23 Feb.	1745	0.0	2111		0.20	0

Coring Run 3

An RBI C-9 bit and junk basket were used for the third coring run. Drilling parameters for Cores 148-504B-247R and -248R were 30,000 to 35,000 lb weight on bit at 50 rpm. Torque increased while cutting the next core, and the bit was pulled. An overpull of 30,000 lb was required to pull the string through a constriction at 1047 mbsf. Rate of penetration using the third coring bit averaged 1.62 m/hr for a recovery of 10.9%. Teeth were cracked in the middle rows of two cones, and some small bit inserts had been lost. The junk basket contained 94.2 g of metal.

Coring Run 4

The fourth coring run used an RBI C-7 bit with 25,000 lb weight on bit at 50 rpm. Torque increased after cutting only two cores and the bit was unable to support 10,000 lb without further torquing, so the bit was pulled. The rate of penetration averaged 2.09 m/hr for a recovery of 8.75%. Teeth on the heel rows of 3 of the cones were chipped and some small bit inserts were missing. The junk basket contained 86.2 g of metal, including nose and gauge inserts. The bit may have been loaded too heavily for the rock that was drilled.

Coring Run 5

The fifth bit was also an RBI C-9 bit. During the trip into the hole, the pipe became stuck at 2006.5 mbsf. It was freed using 190,000 lb overpull, and the hole was reamed.

While attempting to pull the drill string off bottom to retrieve Core 148-504B-253R, the pipe again became stuck. An overpull of 100,000 lb raised the string 3.5 m, but did not free it. The pipe was worked with overpulls of up to 260,000 lb for 2.5 hr with no further movement or rotation. The core barrel was retrieved, but it contained only 0.04 m of rock. Because the rate of penetration while cutting Core 148-504B-253R was faster than that of the preceding cores (7m/hr vs. 1–2 m/hr, respectively), shipboard scientists suspected that the bit had penetrated a highly fractured interval, perhaps a fault. The drill pipe was worked with overpulls of 290,000 lb. High torque was applied for 10-min intervals while holding 245,000 lb of tension in the drill string.

In an attempt to free the pipe, a small Schlumberger severing charge was shot 2 m below the bit. After detonating the charge, 17 wraps of torque were applied to the top drive, and the drill string was worked up and down in an attempt to free the pipe. A core-barrel fishing run was made to catch the piece of the Schlumberger severing pressure case left in the hole when the charge detonated. The teeth of the double core catchers returned to the rig floor with no evidence of having engaged the pressure case: the pressure case had fallen through the end of the bit and the flapper from the float assembly had been blown off when the charge fired. The pipe was pulled again using 235,000 to 240,000 lb of tension, but it did not move.

A second severing charge was run in the hole; however, the location of the charge in the hole could not be determined. The charge was returned to rig floor, and a damaged cable was repaired. The charge was sent down the pipe again, but it would not pass through the bit. It was brought up again and discarded over the side of the ship.

A string shot was run to the top of the first 7-1/4-in. drill collar in an attempt to back the pipe off as low as possible in the BHA. Prior to detonating the shot, 19 turns of left-hand torque were applied to the pipe and worked to the bottom. When the string shot was fired, the drill string jumped 3 feet, indicating that the drill string had backed off. The Schlumberger logging line was retrieved, but the 7-ft string-shot rod had been left in the hole. The drill string was pulled out of the hole and had been severed at the top of the 7-1/4 in. drill collar.

Operations at Site 504 were discontinued until the arrival of a fishing consultant, a shipment of fishing tools and Bowen jars, which would take about 8-9 days. Hole 504B was not logged at the time to avoid jeopardizing fishing operations by knocking wall rocks onto the fish in the hole or leaving junk from logging tools in the hole. Because the most interesting part of the hole was the newly drilled section, and the BHA left in the hole extended up to 100 m into the Leg 140 section (to 1900 mbsf), the scientific benefit of logging at this time was minimized. After considering alternatives for drilling near Site 504 the shipboard party decided to drill a new hole at nearby Site 678, which is located on a small basement topographic high about 1 km southeast of Hole 504B. On 11 February the *JOIDES Resolution* moved to drill at the newly named Site 896 while awaiting the arrival of a fishing consultant, fishing tools, and Bowen fishing jars (see "Background and Objectives", Site 896 chapter).

Fishing Run 1

After setting a reentry cone and coring at nearby Site 896, *JOIDES Resolution* returned to Site 504 on 20 February to meet the boat bringing the fishing consultant and equipment. The fishing BHA was prepared with the Bowen Super Jars that had been sent to the ship from Panama, and the drill string was run in the hole. Several stops to circulate and cool the hole were made on the trip down. The top drive was picked up about two stands above the estimated top of the fish. The drill string was rotated slowly and the fish was engaged within 15 min. Right-hand torque was applied to tighten the connection prior to jarring the fish loose. The first hits with the jars were made using 125,000 lb; the next two sets used 150,000 lb and freed the fish. The fish and BHA were pulled out of the hole. The bit, float valve, and lower support bearing had been left in the hole (which still contained two pieces of Schlumberger explosive rod). Another milling run was required because the material in the hole could not be fished.

Milling Run 2

On 22 February a 9-3/8-in. Petco concave mill that had been sent from Panama along with fishing equipment was run in the hole with two baskets and a Bowen Super Jar. Several cooling stops were made during the pipe trip. Obstructions encountered at 2047 to 2072 mbsf were reamed at 2102 mbsf. Milling parameters were 10,000-12,000 lb weight on bit at 90–100 rpm during the early part of the run, and 12,000–14,000 lbs at 110 rpm immediately before the mill was pulled off the bottom (2107.2 mbsf) and the drill string was tripped out of the hole. The interval from 2107 to 2026 mbsf was constricted and produced a drag of 25,000-30,000 lb. The bottom of the mill was completely worn and the junk baskets contained over 1.7 kg of metal.

Milling Run 3

The next milling assembly employed the same type of mill and BHA as the previous run and also included two junk baskets and the Bowen Super Jar. The mill was tripped into the hole, and the section from 2026 to 2107 mbsf was reamed. The interval from 2087.5 to 2091.25 mbsf was milled and washed using various reaming parameters. While the string and mill were being pulled out of the hole, drag increased in two intervals: 2091–2041 mbsf (up to 20,000 lb) and 2041–2008.2 mbsf (45,000 lb briefly, then 10,000–15,000 lb). The milling BHA returned to the rig floor without the lower section of the Bowen Super Jar, which had failed 15 in. above its pin end. A Petco mill, two junk baskets, a bit sub, three 8-1/4-in. drill collars, and 0.38 m of Bowen Super Jar now joined the collection of junk in the hole. The fish was now 31.9 m long and weighed about 12,000 lb.

Fishing Run 2

An overshot was prepared to engage the 7-3/4-in. body of the failed jar. The second fishing BHA included a 9-1/2-in. Bowen overshot with a 7-3/4-in. basket grapple and mill control, and Bowen Super Jars. The BHA was 176.4-m long. The drill string was run down the hole and engaged the fish within 10 min. The fish was jarred for about 1.5 hr with a maximum jarring overpull of 160,000 lb and a maximum static overpull of 260,000 lb. The jars were then allowed to cool for about an hour, and the fish was jarred again without success. An attempt to pull out of the hole failed when the overshot would not release the fish. Right-hand torque was applied to the overshot. This did not free the overshot, but it did succeed in rotating the fish. The drill string, overshot, and fish were pulled out of the hole on 24 February. The hole now contained part of a coring bit, a float valve, and a lower support bearing. The second mill showed no evidence of having milled anything. The borehole had collapsed, depositing 19 m of rubble on top of the fish. The seals on the remaining jars were leaking oil and could no longer be used.

No functional fishing jars remained on the ship; any further milling operations would risk the hole unnecessarily. With the proper equipment, milling operations on a return trip to Hole 504B would be simple and straightforward.

Final Logging

Logging: Phase 2

A logging BHA was run to the bottom of the hole for several reasons: (1) to determine the depth to which the logs could be run; (2) to circulate and cool the hole for logging; and (3) to displace the drilling mud and leave a NaBr tracer solution in the hole for future geochemical studies (see "Borehole Fluid Geochemistry" section, this chapter). During the pipe trip into the hole, the string took a weight of 15,000 to 20,000 lb at 2083.4 mbsf. Because the logging bit was not designed for reaming or drilling, the obstruction was not cleared. The bit was pulled up 2 m so the hole fluids could circulate prior to injecting the NaBr tracer. Two hole volumes of seawater were circulated at 100 strokes per minute and 740 psi (equivalent to 500 gal per min) to clear the hole of drilling mud. The NaBr tracer solution was then pumped into the hole and the pipe was pulled to logging depth (134.18 mbsf).

The first logging suite (dual laterolog, caliper log, and sonic log) started down the pipe at 0130 UTC, 27 February, and logged from 134.18 to 2075 mbsf (see "Downhole Measurements" section, this chapter). The next suite consisted of the Formation MicrosScanner (FMS) and the gamma-ray tool, which reached a depth of 2081 mbsf. The magnetometer was scheduled next, but was not run because of malfunction. Instead, the Woods Hole vertical seismic profile (VSP) was attempted, but it also failed. The repaired magnetometer was then run successfully both on the trip into and out of the hole. The borehole televiewer was attempted next without success. The VSP was tried again, though it malfunctioned. The ship departed for additional coring at Site 896 on 1 March.

Logging: Phase 3

On 4 March *JOIDES Resolution* returned to Site 504 to continue downhole measurements. A WSTP sample was collected at 468 mbsf (below the casing) as a reference for the NaBr tracer (see "Borehole Fluid Geochemistry" section, this volume). Several attempts were made to conduct the Woods Hole VSP experiment, but all failed. On 6 March a VSP experiment using the Schlumberger vertical-component seismic tool was performed successfully from 1516 to 2076 mbsf (see "Downhole Measurements" section, this chapter). The drill string was tripped out of the hole, and *JOIDES Resolution* departed for additional logging at Site 896.

IGNEOUS PETROLOGY

Lithologic Units

The rocks recovered from Hole 504B on Leg 148 are massive, have few intrusive contacts, and have the texture of diabase, and therefore appear to be a continuation of the sheeted dikes that were drilled on DSDP Leg 83 and ODP Legs 111, 137, and 140 (Anderson, Honnorez, Becker, et al., 1985; Becker, Foss, et al., 1992; Becker, Sakai, et al., 1988; Dick, Erzinger, Stokking, et al., 1992). In deepening Hole 504B from 2000.4 to 2111.0 mbsf (Cores 148-504B-239R through 148-504B-253R) rocks were recovered in every core except for Core 148-504B-243R. In all, 267 pieces of rock were recovered with a total length of 11.54 m (Fig. 8). The rock appears to have been fractured prior to drilling and further broken during drilling; thus, in the 11.54 m of rock, all but 20 of the pieces are too short to be oriented. The longest piece is 15 cm.

The rocks were described according to the procedure given in the "Explanatory Notes." Twenty-five lithologic units, starting with Unit 270, have been identified (Fig. 8). Five boundaries between units were

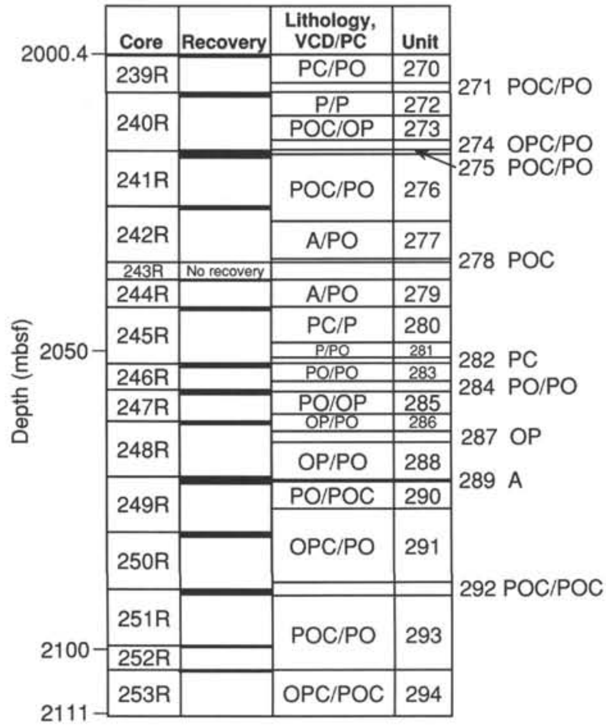

Figure 8. Drilling and recovery at Hole 504B, Leg 148. Black bars show recovery relative to core length. In the lithology column P, C, and O indicate the presence of plagioclase, clinopyroxene, and olivine phenocrysts, respectively. Letters are arranged in order of decreasing abundancies. The lithology as determined in thin section is also given. VCD = visual core description lithology; PC = lithology determined by point counting thin sections.

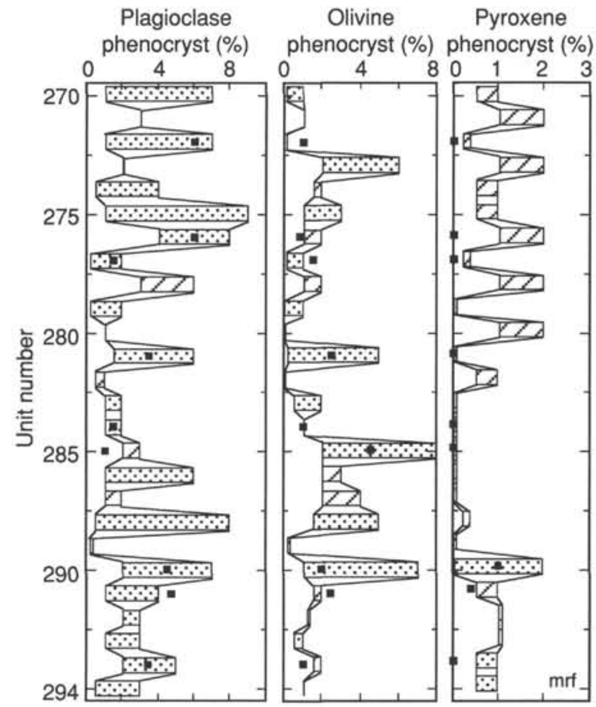

Figure 9. Comparison of estimates of phenocryst abundances. Bars show the difference between the hand specimen mineral abundance and the thin section mineral abundance. Squares are the average of two or more point counts of thin sections from the same unit. Stippled pattern indicates that the hand specimen abundance estimate is less than the thin section abundance. Ruled pattern indicates that the hand specimen abundance estimate is larger than the point count estimate.

identified by the presence of chilled contacts, and other units were identified by differences in mineralogy and grain size. All contacts, whether identified by chilled margins or by changes in lithology, are listed in the Igneous Contacts Log (Appendix A). In this log the last piece in each unit is identified by core, section, bottom of the piece (cm), and by piece number. The lithology (rock name) of the unit above the contact is given as well as the nature of the contact. The dips of only two contacts could be determined, and these were 76° and 84°, similar to those determined on Legs 83, 111, and 140 (see "Structure and Deformation" section of this chapter). Additional notes about the nature of the differences between the rocks above and below the contact are also given.

With 10% recovery, the samples may not be representative of the drilled material. In ophiolites, dikes average about 1 m wide, and this width is similar to estimates for the dikes encountered at Hole 504B (Becker, Sakai, et al., 1988). If the dikes average 1 m wide and dip at 80°, vertical drilling through 111 m would encounter 20 dikes. This is similar to the number of units (25) recognized in the core even though these units are not defined solely on the basis of contacts (see Explanatory Notes). This suggests that the core could have sampled a large proportion of the dikes in the drilled section. It is possible that recovery of some dikes was extensive and these were divided into several units, whereas other dikes may not have been sampled at all. The similarity of the estimated number of dikes encountered and the number of units described, however, suggests that the recovered samples are representative of the rocks encountered.

Mineralogy and grain size of the phenocrysts and intergranular material were recorded in the Mineralogy Log (Appendix B). Additional lithologic information about the units is given in Appendix C. The abundance of the phenocrysts are shown in Figure 9. We classified diabase with less than 1% phenocrysts as aphyric, with 1% to 2% phenocrysts as sparsely phyric, and with more than 2% and less than 10% phenocrysts as moderately phyric. Based on the hand specimen descriptions (Appendix C) 3 units are aphyric, 7 units are slightly phyric, and 15 units are moderately phyric. Of the 22 phaneritic units, 15 had plagioclase as the most abundant phenocryst, and 7 units had olivine as the most abundant phase. Olivine was more abundant than pyroxene in all units where both were present. In terms of percent recovery, plagioclase is the most abundant phenocryst in 80% of the rocks recovered. The classification of the rocks based on abundance of minerals determined by point counting thin sections often differs from the classification based on hand specimen; these differences are discussed below.

All rocks are fine-grained with the average intergranular grain size ranging from 0.3 to 1.0 mm, the latter bordering on medium-grained. The intergranular material consists primarily of plagioclase and pyroxene, but opaque oxide minerals and olivine are also present in small amounts. A trace of chrome spinel is also present. Many units contain coarse-grained glomerocrysts of plagioclase, or plagioclase plus clinopyroxene, olivine, magnetite, or spinel, and some of these glomerocrysts have gabbroic texture.

Phenocryst Phases

Plagioclase

Plagioclase occurs as megacrysts, phenocrysts, glomerocrysts, and intergranular material in the diabase and basalt. Plagioclase phenocrysts are typically 1 to 1.5 mm long, but they can be as large as 5 mm. The phenocrysts and megacrysts show complex zoning with considerable variety, which can be correlated with occurrence of the plagioclase. In phenocrysts and megacrysts the zoning can be divided into 3 parts: core, mantle, and rim (Fig. 10).

Plagioclase grains at the center of glomerocrysts are not conspicuously zoned, but plagioclase in contact with intergranular material

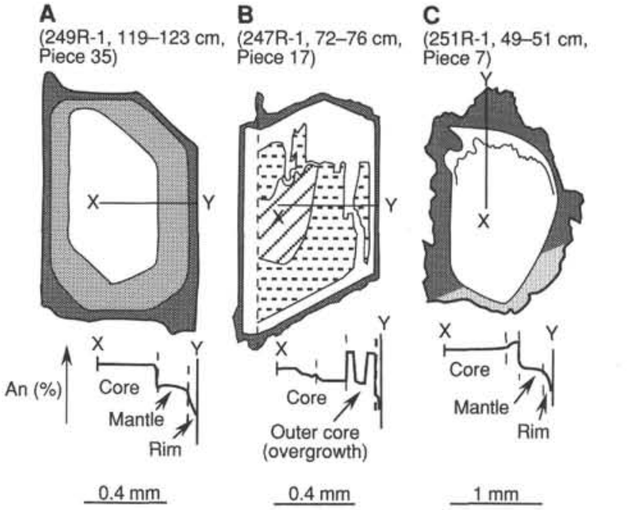

Figure 10. Three examples of zoning in plagioclase, Hole 504B. **A.** Phenocryst with normal zoning. Euhedral core is separated from the mantle by a sharp decrease in An content of the plagioclase. Outside the mantle is a rim of lower An content. **B.** Plagioclase phenocryst with a resorbed inner core (diagonal rule). Stippled area contains glass inclusions. There is an euhedral outer core (white) with high An content and a narrow mantle and rim (gray). An contents are highest in the euhedral overgrowth of the rim. **C.** Megacryst with a rounded resorbed core (white) that is reversely zoned at its outer edge. A normally zoned mantle and rim (gray) surround the core. Relative changes in An content are shown along the transects *X–Y* for each crystal. Changes in An content were estimated by the changes in the extinction angle in different regions of the crystal.

exhibits zoning similar to that of the phenocrysts. Intergranular plagioclase often has a sharp, continuous decrease in anorthite (An) content from the core to rim. These grains presumably grew in situ during rapid cooling.

Representative examples of zoned plagioclase phenocrysts are shown in Figures 10A and 11. The core is euhedral, and the boundary between the core and mantle is sharp with rapid outward decreases in anorthite contents. This abrupt contact between the core and mantle is common and suggests that the core grew slowly at a nearly constant temperature followed by an abrupt change in conditions and subsequent growth of the mantle. The anorthite content decreases from mantle to rim, the anorthite content decreases gradually, and the definition between mantle and rim is sometimes ambiguous. The absence of a mantle zone in plagioclase from the center of glomerocrysts suggests these grew under conditions similar to the phenocryst cores, but were isolated from the abrupt change in conditions that resulted in the core-mantle transition in the phenocrysts.

If the mantles and rims of phenocrysts represent the same phase of crystallization as the intergranular material, then the width of mantle and rim should be positively correlated with the intergranular grain size. The width of mantle plus rim of plagioclase phenocrysts was measured along the long axis of crystals in 20 thin sections. Measurements were made on all phenocrysts in which the boundary between the core and mantle was visible. If the width of mantle and rim was not constant, maximum and minimum values were measured and averaged. Figure 12 shows that the mean grain size of intergranular plagioclase (abcissa) and the thickness of mantle plus rim of plagioclase phenocrysts are strongly correlated. This supports the assumption that the mantle and rim of phenocrysts correspond to the same stage of crystal growth as the intergranular plagioclase.

The cores of phenocrysts may exhibit a wide variety of zoning including slight normal, fine oscillatory, undulatory, patchy, or none (Fig. 10). The cores may also have inclusions of glass, smaller plagioclase laths, and spinel. One characteristic pattern is a resorbed core containing glass inclusions (Fig. 10). Some cores include irregular-

Figure 11. Plagioclase phenocryst from Sample 148-504B-239R-1, 26–30 cm, Piece 9. There is a sharp boundary between core and mantle at the upper right end of large, twinned phenocryst at center. Resorbed inner core contains glass inclusions (zone of black dots). Length of photograph is 1.5 mm. Photograph was taken with crossed polars.

shaped patches low in An content, which is ascribed to the resorption of the plagioclase. Figure 11 shows a representative example where glass inclusions are aligned within the core. Thus, at least four stages of crystal growth can be determined for such plagioclase: (1) crystallization of primary low-An plagioclase; (2) resorption followed by euhedral overgrowth on the resorbed core; (3) abrupt decrease in An contents due to the overgrowth of mantle; and (4) final crystallization to produce the rim. Glass inclusions may be produced during the resorption and overgrowth stages.

Cores free from oscillatory zoning probably grew at nearly constant or slightly decreasing temperature, while fine-scale oscillations in composition are explained by crystal growth under rapidly changing conditions of temperature, pressure, or magma composition. Sharp and repeated occurrence of the oscillatory zoning may be due to abrupt fluctuations of volatile content, recharge of the magma chamber with hot magma, or convective overturn that repeatedly carries crystals between hotter and cooler regions of the magma chamber.

The variety of zoning patterns observed in the cores of plagioclase phenocrysts suggests that the cores underwent complex growth processes prior to, and during, emplacement of magma in the dike complex.

Olivine

Olivine is the next most abundant phenocryst after plagioclase, and on the basis of thin section observations it makes up from 0% to 8% of the diabase. It is commonly altered, although fresh, euhedral, equant

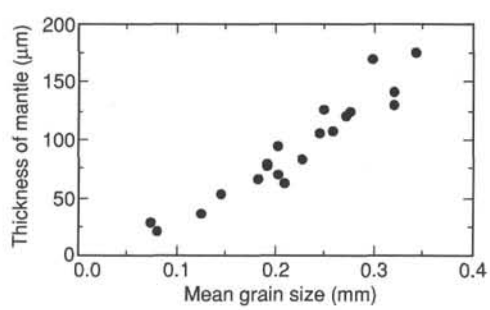

Figure 12. Thickness of mantle on plagioclase phenocrysts and mean grain size of intergranular plagioclase. Mantle thickness is the average of 10 to 20 grains from a single thin section. Mean intergranular size is based on the lengths of approximately 100 grains from Hole 504B samples.

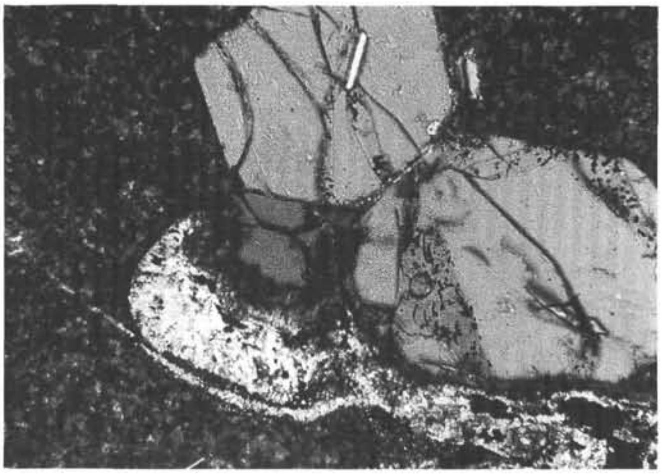

Figure 13. Olivine phenocrysts in chilled margin of Sample 148-504B-249R-1, 92–98 cm, Piece 27. The two euhedral crystals in the upper left are fresh. A third grain is partially altered where it is intersected by a crack. One grain contains an euhedral plagioclase lath. Olivines are surrounded by dark gray fine-grained groundmass. Olivine grains are approximately 1 mm diameter. Photograph was taken using a ×10 objective and plane-polarized light.

Figure 14. Clinopyroxene in Sample 148-504B-253R-1, 0–4 cm, Piece 1. The maximum dimension of the pyroxene is 3 mm. The largest plagioclase inclusion is 1 mm. The pyroxene shows twinning that is typical of phenocrysts in these samples. Photographed with a ×2.5 objective with crossed polars.

grains are preserved in some samples (Fig. 13). Olivine phenocrysts from chilled margins may host inclusions of plagioclase and altered glass. Olivine phenocrysts are approximately 1 mm in diameter and are particularly prominent in hand specimen because they were altered to chlorite, which appears black. Alteration is sometimes so severe, however, that olivine relicts are not apparent and in these samples the amount of olivine in hand specimen is underestimated.

Clinopyroxene

Clinopyroxene occurs as a phenocryst phase in 18 of the 25 units described, with modal abundances ranging from 0.2% to 2% and grain sizes ranging from 0.2 to 4 mm (measured on the long axis). In hand specimen pyroxene appears as euhedral to subhedral translucent green crystals, similar to the Cr-augite variety described on Leg 140. In thin section three distinct phenocryst morphologies are obvious: (1) embayed euhedral to subhedral crystals (amoeboidal texture described on Leg 111; Becker, Sakai, et al., 1988); (2) subhedral to anhedral grains in glomerocrysts with plagioclase; and (3) most commonly, subhedral to anhedral phenocrysts, often with subophitic margins enclosing plagioclase (Fig. 14). Simple twinning is common in all pyroxene phenocryst types. Both continuous and discontinuous zoning occur but are rare and are restricted to the oikocrystic pyroxene phenocrysts, while concentric rings of inclusions in some phenocrysts may correspond to zones of inclusions in plagioclase phenocrysts in the same samples. Intergranular pyroxene oikocrysts may be as large as the largest phenocrysts.

A representative example of the former type is shown in Figure 14. The oikocryst clinopyroxene are as much as 3 mm in grain-size and contain fine-grained plagioclase laths. As shown in Figure 14, the oikocrysts are usually attached with larger plagioclase laths up to 1 mm, and they are overgrown by the intergranular clinopyroxene. Some oikocrysts have zoning at the margin with a sharp boundary that may correspond to the same event with the boundary between the core and mantle in phenocryst plagioclases. The attached and included plagioclases exhibit no conspicuous zoning; therefore, this glomerocryst is considered a heteradcumulate.

It has previously been suggested that the subhedral to anhedral and embayed shape of some clinopyroxene phenocrysts in the lavas of Hole 504B indicates that pyroxene is partially resorbed by the magma (Natland et al., 1983). Pyroxene phenocrysts within the dikes also

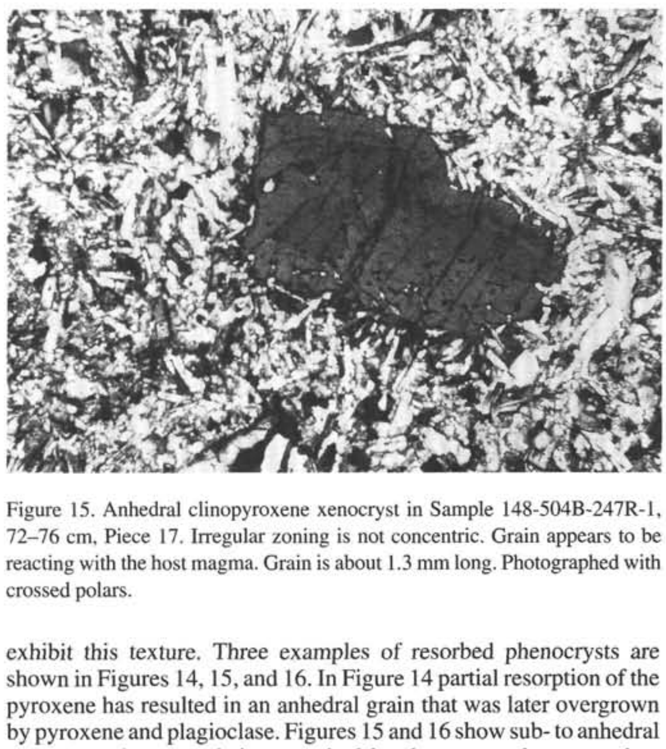

Figure 15. Anhedral clinopyroxene xenocryst in Sample 148-504B-247R-1, 72–76 cm, Piece 17. Irregular zoning is not concentric. Grain appears to be reacting with the host magma. Grain is about 1.3 mm long. Photographed with crossed polars.

exhibit this texture. Three examples of resorbed phenocrysts are shown in Figures 14, 15, and 16. In Figure 14 partial resorption of the pyroxene has resulted in an anhedral grain that was later overgrown by pyroxene and plagioclase. Figures 15 and 16 show sub- to anhedral pyroxenes that were being resorbed by the magma but were then quenched, resulting in no overgrowth.

Plagioclase inclusions may occur in the core of all three types of pyroxene phenocrysts, suggesting that pyroxene follows plagioclase in the crystallization sequence. Plagioclase inclusions in the rims of pyroxene phenocrysts distinguish them from intergranular oikocrysts, which enclose plagioclase throughout. Pyroxene phenocrysts usually do not exhibit strong chemical zonation, but some phenocrysts have a concentric ring of inclusions that may correspond to zones of inclusions in plagioclase phenocrysts in the same sample.

Spinel

Spinel is a trace mineral that occurs in about half of the lithologic units. The term spinel is used here for all oxide minerals that appear

Figure 16. Chilled margin in Sample 148-504B-249R-1, 92–98 cm, Piece 28. Largest grain and two rounded grains touching it are partially resorbed pyroxene in dark groundmass. Smaller blades and needles of plagioclase are also present. Large grain is 0.5 mm long. Photographed with crossed polarizers with a ×10 objective lens.

to be either chromian spinels and magnesiochromites. The color of the spinels ranges from light yellowish green and yellowish brown to dark reddish brown, brown, and black. The lighter-colored spinels are probably chromian spinels with low iron, and the reddish spinels are magnesiochromites. Darker spinels are likely to have more iron than the light spinels. The characteristics of spinels found in thin sections are given in Appendix D.

Spinels are present as equant grains that range in size from 10 µm to 200 µm and are included in phenocrysts of plagioclase. They are less commonly found in olivine phenocrysts and intergranular material, and they are rarely found in glomerocrystic pyroxene, in contrast to the spinels in the extrusive section of Hole 504B (Natland et al., 1983) and Site 505 (Furuta and Tokuyama, 1983) where they are found equally in plagioclase, olivine, and in the groundmass. The low abundance of spinels in the intergranular material of the diabase relative to their abundance in the groundmass of the extrusive rocks may have several alternative explanations: (1) spinel was preserved when trapped in phenocrysts or when an extrusive was rapidly quenched but spinel reacted with the mesostasis in the slowly cooled dikes; (2) in the dikes the intergranular spinel has been altered to magnetite and is indistinguishable from the magnetite that crystallized as the diabase cooled; and (3) the magmas of the extrusive section of Hole 504B may have slightly higher Cr content than the feeder dikes. Resorbed clinopyroxenes with Cr abundance of 0.5 to 1.0 wt% occur in the extrusive sequence (Natland et al., 1983) and in the dikes of Hole 504B, and the melting of these pyroxenes due to decompression could result in the high Cr abundance in the magma and the crystallization of spinel.

Intergranular spinel and spinel inclusions in olivine pseudomorphs have been extensively replaced by magnetite. This has not been previously reported in the diabase or extrusive rocks from Hole 504B. This style of alteration is distinctly different from the alteration of magnetite to ilmenite and titanite that is common in the intergranular material (Figs. 17 and 18). Spinel inclusions in plagioclase range from pristine to moderately altered. Often a thin rim of magnetite surrounds the grain, leaving a fresh core. Spinels also exhibit skeletal (Furuta and Tokuyama, 1983) or symplectic (Fisk and Bence, 1980) textures that were probably derived from reaction of the spinel with the host magma.

Spinels are most abundant in Unit 273 where 18 grains ranging in size from 30 to 130 µm were observed in a single thin section. At this level of abundance the spinels (which are typically 25% to 40% Cr_2O_3; Natland et al., 1983) would contribute 150 to 250 ppm of Cr to the bulk rocks, which range from about 100 to 400 ppm (Becker, Sakai, et al., 1988).

Figure 17. Two spinel grains included in plagioclase. Spinels (brightest minerals) are euhedral and about 130 µm across. Their cores are preserved but the rims have been altered to magnetite. Sample 148-504B-241R-1, 78–81 cm, spinels 4 and 5 in Appendix D. The mineral surrounding the spinels is plagioclase and the darkest regions are altered intergranular material. Width of photograph is 400 µm. Photographed with a ×40 objective in reflected light.

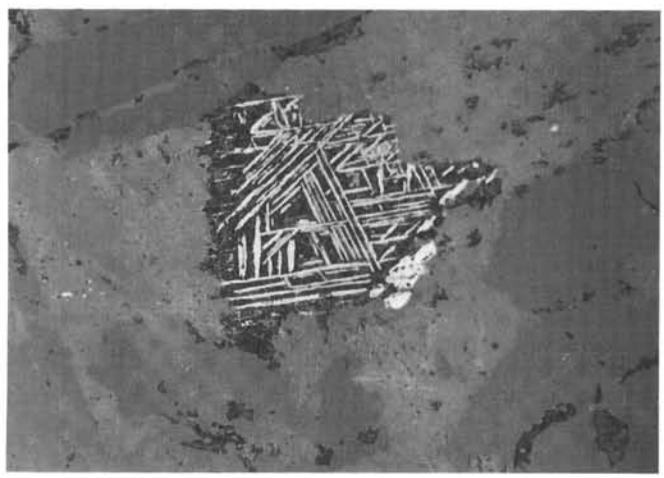

Figure 18. Altered intergranular magnetite of Sample 148-504B-241R-1, 78–81 cm. Grain shows the typical preservation of exsolved ilmenite and complete alteration of the magnetite. This style of alteration is quite different from the alteration of the spinel seen in Figure 17. Width of field of view 500 µm. Width of field of view 500 µm. Photographed in reflected light.

Intergranular Material

Plagioclase

Plagioclase is the dominant intergranular mineral (Appendix B) and usually comprises about 50% of the rock and has an average grain size of approximately 0.5 mm. The grain size, however, is variable and is probably dependent on cooling rate. Texture ranges from intergranular to ophitic (Figs. 19 and 20).

Pyroxene

Intergranular clinopyroxene is commonly up to ophitic, forming crystals that enclose large numbers of smaller plagioclase grains. The

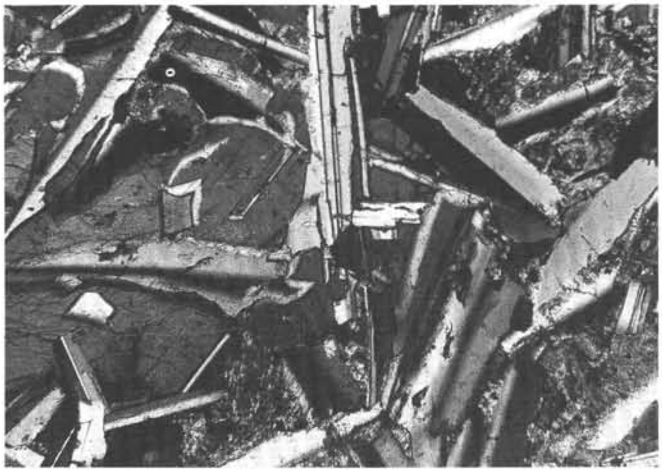

Figure 19. Typical subophitic texture with laths of plagioclase (white to light gray) partly or entirely enclosed in clinopyroxene (dark gray). Sample 148-504B-239R-1, 26–30 cm, Piece 9. Length of photograph is 2 mm. Photographed with ×10 objective lens and crossed polars.

Figure 20. Typical intergranular texture of diabase dikes. Plagioclase laths are surrounded by several pyroxene grains. Sample 148-504B-247R-1, 72–76 cm, Piece 17. Length of photograph is 2 mm. Photographed with ×10 objective with crossed polars.

oikocrysts are commonly up to 2 mm in diameter, but range up to 4 mm, larger than the pyroxene phenocrysts. The oikocrysts are easily distinguished from pyroxene in glomerophyric clots, which do not contain plagioclase chadacrysts. Also, the oikocrysts do not appear to be zoned or twinned, whereas phenocrysts and pyroxene in glomerocrysts are commonly both twinned and are sometimes zoned.

Magnetite

Titanomagnetite is usually present as an intergranular mineral (indicating late-stage crystallization) with grain size from 0.02 mm to 0.45 mm and grain shapes that are either equant euhedral to subhedral or elongated subhedral to anhedral. Magnetite also appears in extensively altered areas such as alteration patches and vein halos. In these regions, titanomagnetite is replaced by ilmenite and a fine-grained dark matrix (see the "Alteration and Metamorphism" section, this chapter, for further discussion). Ilmenite lamellae in magnetite hosts are common in larger grains, and this texture is attributed to subsolidus exsolution of ilmenite during cooling. The abundance of titanomagnetite varies between 1% and 5%, with a mode at about 3%. Rare magnetite inclusions are found in plagioclase phenocrysts and may be altered spinel.

Comparison of Mineral Abundance in Hand Specimen and Thin Section

The percentage of plagioclase, olivine, and clinopyroxene phenocrysts was estimated in a number of pieces from each unit using both the unaided eye and binocular microscope. Plagioclase abundance varies between 0% and 4%, but mostly clusters around 1%. Olivine and clinopyroxene phenocryst abundances are estimated to be from 0% to 2%, and 0% to 1%, respectively. Thin sections were made from all but four of the units and the results of the point counts of a single thin section from each unit are compared to the hand specimen estimates (Fig. 9). Where more than one thin section was made per unit, the average of the point counts is also shown as a solid square.

With few exceptions the estimated plagioclase phenocrysts content from the point counting were higher, and in some cases much higher, than that from the visual estimates. For olivine phenocrysts there is better agreement between the results of the visual estimates and those of the point counting, but in a few units the visually estimated olivine content is much lower than that determined from the thin sections. Unlike the estimates of plagioclase and olivine abundance, the amount of clinopyroxene phenocrysts are generally overestimated in hand specimen compared to the point-counting results (Fig. 9).

There are several reasons for the differences that appear in Figure 9. In hand specimen, grain size was the primary characteristic used to distinguish phenocrysts because all the units are fine-grained (average grain size <1 mm) and mineral morphology was not easily determined. This problem was compounded in some cases by the nearly continuous range of mineral sizes (i.e., seriate texture). In thin section, however, grain size and grain morphology and the existence of complex zoning in plagioclase were used to separate phenocrysts from intergranular material. Hence, in the point counts many more crystals were included in the estimate of phenocryst abundance than in the visual core description. Further, estimating the abundance of light-colored plagioclase against the dark intercrystalline material usually results in underestimation of the light minerals. This is evident in a chilled margin from Unit 291 where there is a clear distinction between phenocrysts and groundmass in hand specimen. The plagioclase abundance by point counting was 9%, while the visual estimate was about 5%.

The better agreement between the olivine visual and point counting results may stem from the alteration of olivine to dark-colored minerals (chlorite, magnetite, and actinolite) so olivine appears as distinct dark spots. The visual overestimate of clinopyroxene phenocrysts relative to thin section studies is certainly due to the fact that clinopyroxenes often appear as large (2 mm) oikocrysts that are easily seen under the binocular microscope but clearly are not phenocrysts. Other reasons for the documented discrepancy in the phenocryst contents include these factors: (1) the thin section is not entirely representative of the rock; (2) the 500 counted points are not sufficient; (3) the phenocrysts are unevenly distributed in the rock. The point-count of the thin sections is probably the more reliable estimate of phenocryst abundance because the microscope permits the use of mineral morphology and zoning to distinguish phenocrysts from interstitial minerals.

Chilled Margins

Several samples recovered during Leg 148 are clearly chilled contacts between diabase dikes. These contacts are generally planar to curvilinear and have steep dips (see "Structure and Deformation" section, this chapter), the exception being a microdike, Sample 148-504B-241R-1, 78–81 cm, which has a steep dip but also a complex

3-dimensional form. On a microscopic scale the contacts may be more irregular with apophyses into host rock and inclusions of wall rock, adjacent to the margin (e.g., Sample 148-504B-249R-1, 92–98 cm). The microdike differs from those recovered on Leg 140 in that it partly terminates in a cataclastic zone, rather than a vein.

All the chilled material is porphyritic, ranging from aphyric to moderately phyric (i.e., approximately 0.5% to 9% phenocrysts). Three phenocryst assemblages were recorded: plagioclase-olivine-clinopyroxene, plagioclase-olivine, and plagioclase. The chilled margins with only plagioclase phenocrysts appear to be much less common than in the Leg 140 section (Dick, Erzinger, Stokking, et al., 1992).

Plagioclase occurs as euhedral to subhedral phenocrysts that range in size from 0.1 to 1.2 mm. Phenocrysts occur singly or in glomerocrysts with plagioclase and/or clinopyroxene and rarely have cryptocrystalline inclusions or skeletal form. Microphenocrysts are rare whereas quench overgrowths were not recorded. Olivine phenocrysts in Sample 148-504B-249R-1, 92–98 cm, forms euhedral, slightly rounded, or anhedral fragmental grains from 0.15 to 0.8 mm diameter. Olivine is largely fresh and only completely replaced when cut by or adjacent to fine actinolite veins. Both plagioclase and rounded cryptocrystalline material, 0.05–0.08 mm diameter, occur as inclusions in olivine phenocrysts. Clinopyroxene phenocrysts in the same sample are up to 2.2 mm long and are slightly rounded and embayed euhedral to subhedral grains with inclusions of cryptocrystalline material. Clinopyroxene phenocrysts also commonly include, or are intergrown with, plagioclase. In hand specimen the large clinopyroxene phenocrysts are green, similar to the Cr-rich variety reported on Leg 140. No olivine or clinopyroxene microphenocrysts or spinel were recorded.

No glass was found in the groundmass of the 3 margins examined microscopically. Textures immediately adjacent to the contact with host rock are similar, in reflected light, to Zones 2a and b of Kempton (1985). Grain sizes range from <0.002 mm to approximately 0.01 mm. Further from the margin, textures similar to Kempton's Zone 6 are developed, although spherulitic and plumose quench intergrowths are rare, with a grain size of 0.01 to 0.03 mm.

Grain-size Distributions

Because grain-size distributions in basaltic rocks are affected by cooling rates, groundmass and intergranular-mineral grain sizes contribute to our understanding of the cooling history of lavas. In rapidly cooled lavas, the crystal nucleation rate is high and the growth rate is low; thus in quenched rocks, tiny crystals are the most abundant. At lower cooling rates the nucleation rate is lower and the growth rate becomes higher and results in fewer but larger intergranular crystals.

In dikes the central portion cools more slowly than the margin; therefore dike interiors are characterized by larger average grain sizes than are found in chilled margins. In Hole 504B the dikes are commonly 0.5 to 1 m thick (Becker, Sakai, et al., 1988), which is sufficient to allow measurable differences in grain size between their margins and centers. In addition, grain-size variations studied during Leg 140 (Dick, Erzinger, Stokking, et al., 1992) delineate a crude saw-tooth distribution with depth. This pattern is characterized by a steady downhole decrease in grain size within a group of lithologic units and ends in an abrupt increase. Single dikes should have symmetric grain-size variations across the dike. Therefore, the saw-tooth pattern is thought to represent distinct cooling units, each composed of several dikes intruding during short episodes of extension (Dick, Erzinger, Stokking, et al., 1992).

The variation of intergranular plagioclase and magnetite grain-sizes with depth has also been examined in the rocks recovered on Leg 148. The grain size was determined by the following method: the length (long axis) and width (short axis) of 100 plagioclase and magnetite grains were measured along randomly oriented traverses in each thin section. Both the intergranular and phenocrysts areas were determined in order to study the bulk rock distribution of plagioclase and magnetite. The length and width were multiplied to give an area of each grain, which is reported as the diameter of a circle with the equivalent area (Eqd).

In a similar study during Leg 140, grain sizes in the chilled margins were not measured. In the Leg 148 study the chilled margins were included, but only the plagioclase microphenocrysts were measured because the groundmass either contained plagioclase as fine-grained needles (<0.01 mm) or was cryptocrystalline. Grain-size measurements from the present study are listed in Appendix E.

Grain-size distribution of plagioclase from two thin sections are shown in Figure 21. Three grain types were identified: (1) Type I phenocrysts or megacrysts: large (1–6 mm) strongly zoned phenocrysts; (2) Type II phenocrysts: weakly zoned phenocrysts (0.6–2.0 mm); and (3) euhedral to subhedral intergranular laths (0.02–1 mm). The Type I phenocrysts are rare and often form glomerophyric or gabbroic clots that are separate from the main grain-size distribution of the host rock (Fig. 21A). In contrast in most samples the Type II phenocrysts and the intergranular plagioclase form a nearly continuous range (i.e., seriate texture; Fig. 21B). The overall distribution of the phenocrysts suggests that the Type II grains grew as the result of rapid cooling during transport and emplacement of the dikes, and the Type I grains grew slowly at a low rate of cooling in the magma chamber.

The grain-size distribution of magnetite is similar to that of the plagioclase except that there are no magnetite phenocrysts or megacrysts (Fig. 22) because the magmas intruded at temperatures well above the crystallization point of magnetite. In samples with relatively large average-intergranular mineral size (Fig. 22A) the frequency distributions of magnetite grain sizes nearly fit a normal distribution. In finer-grained samples, however, frequency distributions tend toward log-normal so the skewness of the distribution of magnetite grain sizes correlates with the average grain sizes (Fig. 23). The log-normal distribution of the fine-grained samples probably reflects the rapid cooling of those samples such that a limited range of grain sizes were produced. In contrast, in the coarser-grained samples the slower cooling results in a spectrum of grain sizes with a normal distribution.

The intergranular plagioclase and magnetite Eqd values have a marked positive correlation (Fig. 24) that converges at the origin. Overall, the plagioclase grains are 2.6 times larger than the magnetite grains, which probably indicates the earlier appearance of plagioclase as a liquidus phase.

Contacts between dikes were observed at four locations between 2040 and 2090 mbsf (Fig. 25), and Eqd values of both plagioclase and magnetite in thin sections from two of these contacts are significantly lower than in adjacent samples. One additional boundary at 2058 mbsf

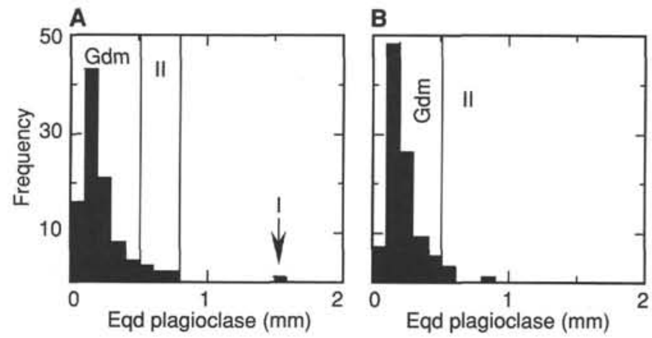

Figure 21. Plagioclase Eqd distributions. **A.** Thin-section Sample 148-504B-248R-1,43–48 cm, from Unit 288 contains Type I and II phenocrysts and intergranular material. **B.** Thin-section Sample 148-504B-240R-1, 33–38 cm, from Unit 272 has only Type II phenocrysts and intergranular material. Eqd is calculated for each grain and is the diameter of a circle with an area equal to the product of the length and width the grain. Gdm = intergranular material, I = type I phenocrysts, II = type II phenocrysts.

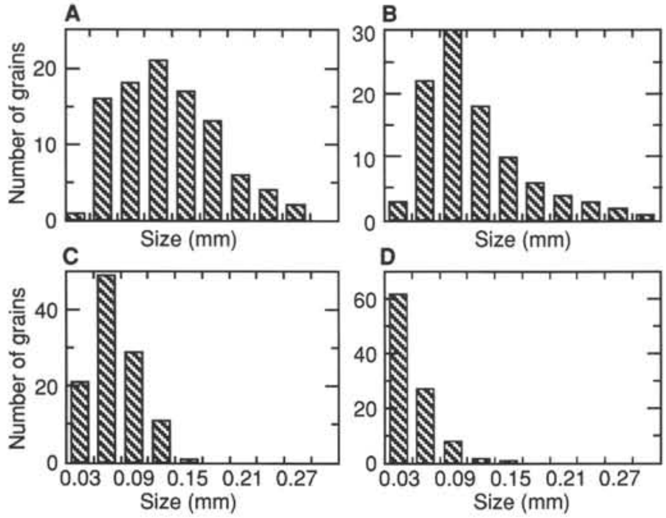

Figure 22. Grain-size distribution of magnetite in four thin sections, arranged in order of decreasing median grain size. **A.** Sample 148-504B-239R-1, 26–30 cm, has a distribution that can be described as normal. **B.** Sample 148-504B-242R-1, 12–16 cm, and (**C**) Sample 148-504B-244R-1, 3–8 cm, have distributions that are between normal and log-normal. **D.** The distribution in Sample 148-504B-247R-1, 79–83 cm, is log-normal.

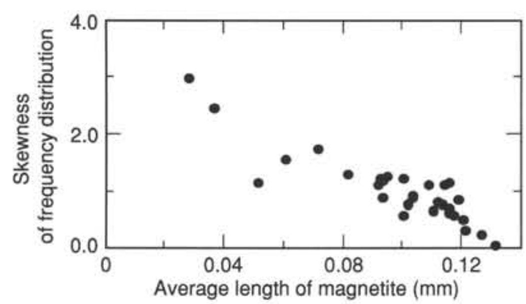

Figure 23. Skewness of frequency distribution of magnetite grain sizes against average length of magnetite grains. Note that there is a linear relationship between both parameters indicating normal distribution in coarser grained and skewed distributions in finer grained rock samples from Hole 504B.

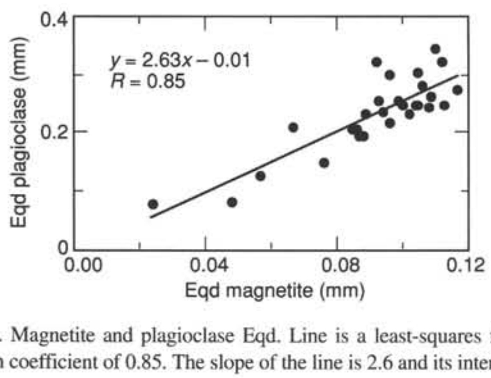

Figure 24. Magnetite and plagioclase Eqd. Line is a least-squares fit with a correlation coefficient of 0.85. The slope of the line is 2.6 and its intercept is 0.

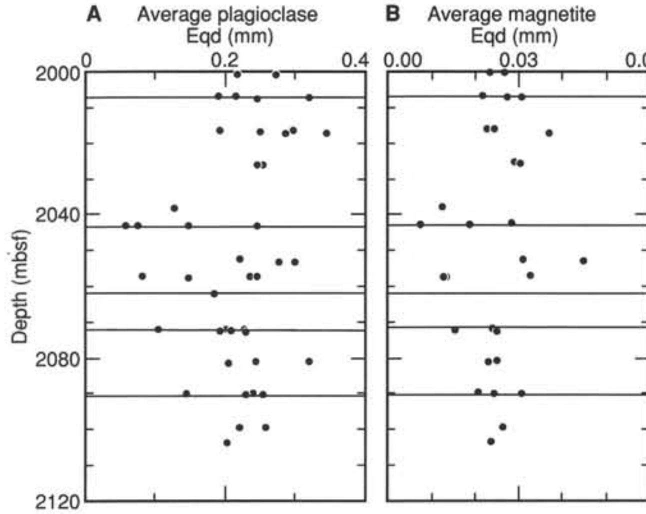

Figure 25. Variation of Eqd in the drilled section. Horizontal lines indicate the presence of chilled contacts. **A.** Plagioclase. **B.** Magnetite Eqd with depth. Additional contacts are suggested by low Eqd values at 2058 mbsf.

was suggested by a low average intergranular grain size (Fig. 25). These five boundaries divide this 50 m section into four units with an average width of about 2 m, assuming the dikes dip at 80°.

The average Eqd values of plagioclase and magnetite (Fig. 25) do not have the saw-tooth pattern seen in the Leg 140 grain sizes (Dick, Erzinger, Stokking, et al., 1992). The interruption of the saw-tooth pattern near the boundary between Legs 140 and 148 may be due to differences in the way grain-size measurements were made or to insufficient recovery.

The minima of the average Eqd values of magnetite and plagioclase appear to increase downward from 2042 mbsf (Fig. 25). One possible interpretation is that the dikes intruded sequentially and progressively heated the country rock so that the last dike in the group (lowest dike in section) intruded into the hottest rock and had the largest grain size. The largest Eqd values in this same section do not increase regularly, possibly due to the variable thickness of the dikes or to grain size that is controlled by factors other than cooling rate. Limited recovery makes this interpretation speculative.

Glomerocrysts

Glomerocrysts and megacrysts were reported from basalts and diabases recovered from Hole 504B during Legs 69, 83, 111, and 140. In particular, a great variety of crystal clots, including ultramafic (dunitic, wehrlitic, and pyroxenitic), troctolitic, gabbroic, and ferrogabbroic have been found during Leg 140, and these were divided into two major types described previously (i.e., syngenetic glomerocrysts that are derived from the host rocks and xenolithic glomerocrysts that are unrelated to the host rocks; Dick, Erzinger, Stokking, et al., 1992). In this study all mineral aggregates are referred to as glomerocrysts because the distinction of the two types is not always apparent.

Most of Leg 148 diabases contain a variety of glomerocrysts that are classified by mineral assemblage as follows: plagioclase, plagioclase-clinopyroxene, plagioclase-clinopyroxene-olivine, plagioclase-clinopyroxene-magnetite, and others. For each glomerocryst, the number of crystals, grain size, presence of spinel, and approximate modal composition were determined (Appendix F). The occurrence of plagioclase and clinopyroxene megacrysts are also included in Appendix F.

The dominant glomerocrysts are the plagioclase type; these consist of 3 to 25 grains with a wide variety of textures and grain sizes. Individual grains within the glomerocrysts range from euhedral to subhedral (Fig. 26) but anhedral grains are also found. The grains are usually randomly oriented mats and laths, but some aligned plagioclase mats are present. These mats usually have little or no interstitial minerals, suggesting that interstitial liquids were expelled by adcumulus growth.

Plagioclases in the center of glomerocrysts have no conspicuous zoning, but crystals at the margin have normally zoned mantles and

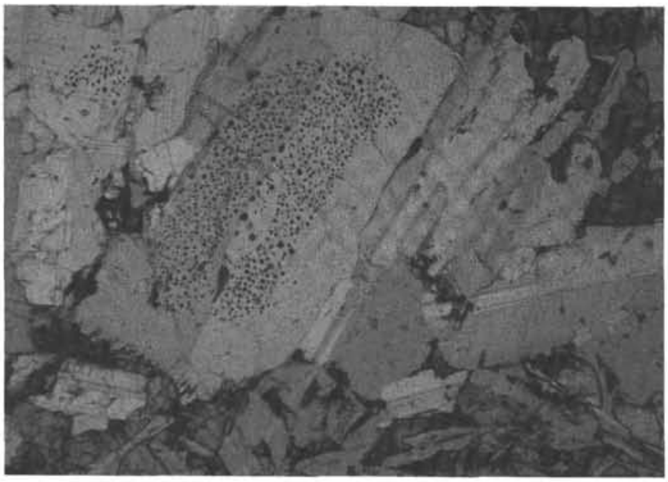

Figure 26. Plagioclase glomerocryst in Sample 148-504B-253R-1, 0–4 cm, Piece 1. Aggregate of 16 grains without intergranular material. Largest grain is 1.8 mm. Glass inclusions in core of large grain are frequently observed in other glomerocrysts. Photographed in plane-polarized light.

rims, which are probably overgrown on the glomerocrysts in situ. Some glomerocrysts are composed of plagioclases with oscillatory-zoned cores and resorbed cores with irregular, low-An patches (Fig. 11). Such resorbed plagioclases frequently contain numerous glass inclusions (Fig. 26). The mixture of textures and weak zoning of the cores suggest that individual grains in some glomerocrysts have had different origins.

Plagioclase-olivine glomerocrysts are the next most abundant type, consisting of about 10 to 20 grains each (Appendix F). The grain size ranges from about 0.3 to 3 mm. The plagioclases are euhedral to subhedral, are interlocking without interstitial minerals, and lack zoning. These facts suggest that they are adcumulates (troctolitic) that form where crystallization rate is slow (Wager et al., 1960).

The plagioclase-clinopyroxene type of glomerocrysts consists mainly of euhedral to subhedral plagioclases with interstitial clinopyroxene. The plagioclases are medium-grained, ranging from 2.0 to 0.3 mm. These plagioclases commonly show normal zoning accompanied by fine oscillatory zoning in the core. These textural features suggest that the glomerocrysts are orthocumulates.

Plagioclase-clinopyroxene-olivine glomerocrysts are composed of euhedral to subhedral plagioclase and olivine with interstitial clinopyroxene. Some clinopyroxenes are granular, and plagioclase exhibits generally weak normal zoning. Grain size generally ranges from 1.8 to 0.3 mm, but coarse olivines attain 4 mm in one specimen. Textures of these glomerocrysts correspond to mesocumulates.

Plagioclase-clinopyroxene-magnetite glomerocrysts are found rarely. Plagioclase grains are subhedral laths and clinopyroxene grains are ophitic clinopyroxenes. Small (0.8 to 0.1 mm) rounded magnetites appear in the interstices of the plagioclase. The cores of plagioclase grains may show fine oscillatory zoning. Olivine glomerocrysts are rare (one example; see Appendix F) and the textural relationships cannot be determined because the olivine is completely altered.

Megacrysts of plagioclase commonly occur in many specimens and they may show complex zoning patterns and irregular shapes due to resorption and these grains may be xenocrysts. The largest plagioclase megacryst attains a size of 5 mm in diameter. Megacrysts of other minerals are rare but some of these appear to be reacting with the host rock (Fig. 15); they exhibit irregular zoning and may also be xenocrysts.

Several sources for the glomerocrysts at Hole 504B are possible and all glomerocrysts need not be derived from the same source. The high frequency of occurrence of the plagioclase glomerocrysts (relative to the cotectic crystallization proportions of 2 plagioclase to 1 olivine at high temperature, or 3 plagioclase to 3 clinopyroxene to 1 olivine at lower temperature) suggests that either they are derived from a plagiogranite (possibly at the top of the magma chamber) or that plagioclase has been separated from olivine and clinopyroxene due to differences in density. On the basis of textural features some of the plagioclase glomerocrysts may be regarded as cumulates interlayered where adcumulus growth advanced intensively because of very slow crystallization rate.

The plagioclase-olivine glomerocrysts may be fragmented troctolites that are commonly found from ocean basins (e.g., ODP Hole 735: Robinson and Von Herzen, 1989). Similarly, plagioclase-clinopyroxene, plagioclase-clinopyroxene-olivine, and plagioclase-clinopyroxene-magnetite glomerocrysts may be derived from gabbro, olivine gabbro, and ferrogabbro, respectively.

Conclusion

The rocks recovered on Leg 148 are a continuation of the dikes found on previous legs. Twenty-five units were described in the 110.6 m that were drilled, and these are fine-grained diabase with plagioclase as the dominant phenocryst, followed in abundance by olivine. Clinopyroxene and spinel are sometimes present. Plagioclase megacrysts and glomerocrysts were as common as in rocks recovered previously at this site.

ALTERATION AND METAMORPHISM

Introduction

Alteration of basement recovered from Hole 504B on previous legs has been documented in detail (Alt et al., 1985; Alt et al., 1986; Alt, Muehlenbachs, Honnorez, 1986; Alt et al., 1989; Alt, Anderson, Bonnell, 1989; Alt et al., in press; Honnorez et al., 1983; Ishizuka, 1989; Laverne et al., 1989, in press; Shipboard Scientific Party, 1983, 1985, 1988, 1992a and b). The sampled section can be divided into 3 main zones: the upper 310 m of the volcanic section (274 to 584 mbsf) affected by an oxidative, low-temperature (0°–110°C) alteration; the lower portion of the volcanic section (from 584 to 898 mbsf) affected by an anoxic to reducing, low-temperature (<150°C) alteration; and below 898 mbsf in the transition zone and dikes (2000 mbsf, before Leg 148), which were hydrothermally altered under conditions similar to the greenschist facies, with superimposed zeolite facies-like conditions.

Summary of Previous Results

Before describing the alteration observed in Leg 148 core, a short summary of diabase alteration observed previously is given below.

Heterogeneity

The most striking feature of the alteration in the dikes of Hole 504B is its heterogeneity at various scales. At the thin-section scale this is mainly reflected by olivine alteration. Six main mineral associations after olivine are common:

1. Talc ± talc/chlorite + magnetite ± pyrite ± chalcopyrite.
2. Chlorite ± magnetite ± pyrite ± chalcopyrite.
3. Mixed-layered chlorite-smectite ± chlorite ± magnetite ± pyrite ± chalcopyrite.
4. Chlorite + actinolite ± pyrite ± chalcopyrite.
5. Smectite ± hematite or magnetite.
6. Chlorite + hematite.

Quartz may be present in all of these assemblages.

Several of these associations commonly occur in the same thin section, particularly below 1600 mbsf. No systematic spatial or temporal distribution of the different alteration assemblages is apparent. Nevertheless, in some samples the type of olivine replacement is controlled by the proximity to veins: in the least altered diabases, olivine is totally replaced by talc and talc/chlorite mixtures + magnetite close to an actinolite-chlorite vein (even if no alteration halo is observed), whereas relict olivine exists farther away from the vein. In the most altered diabases, olivine is replaced by actinolite ± chlorite in the alteration halo adjacent to actinolite veins, and by chlorite in the host rock. The heterogeneity of alteration products after olivine suggests that the physical and chemical conditions were variable at a submillimeter scale.

The composition of the amphibole is also highly variable within a single thin section. It ranges from actinolite to magnesio-hornblende, ferroactinolite, and edenite (Alt et al., in press; Laverne et al., in press).

Background Alteration in the Dike Complex

A background alteration, characterized by the partial (5%–40%) replacement of primary minerals by secondary phases, affects all the diabase samples. Clinopyroxene is fresh or partly replaced by actinolite. Plagioclase may be replaced by one or more generations of secondary plagioclase, chlorite, Ca-zeolites, anhydrite, epidote, or some combination of these minerals. Olivine is variably replaced by chlorite, mixed-layer chlorite-smectite, talc, talc-chlorite, actinolite, quartz, sulfides, magnetite, and hematite. Titanomagnetite is partly replaced by titanite.

Alteration Patches

Many diabase samples contain irregularly shaped alteration patches up to several centimeters wide of highly altered (up to 100%) diabase where actinolite prevails.

Veins and Alteration Halos

Detailed descriptions of veins are presented in Shipboard Scientific Party (1985, 1988, 1992a and b) and in Tartarotti et al. (in press). Hydrothermal veins, less than 1 to several millimeters thick, generally contain actinolite, chlorite, or actinolite + chlorite. Apatite and titanite are common accessory phases. Less abundant vein minerals include quartz, epidote, prehnite, laumontite, and anhydrite. Epidote, quartz, and various sulfide veins are abundant in the stockwork-like section of the transition zone (910–928 mbsf; Honnorez et al., 1983).

Alteration halos around chlorite ± actinolite veins in the transition zone and upper dike section (900–1600 mbsf) are characterized by 20%–80% replacement of primary minerals, with mineralogy similar to the background alteration. In the adjacent host rock, replacement of primary igneous minerals is less intensive (about 10%–20%), with particularly less abundant albite and laumontite.

Alteration halos (<1 to 15 mm wide) adjacent to actinolite veins in the lower dike section are usually characterized by extensive replacement of the original igneous mineral assemblage (typically 40%–90% in the lowest 400 m of the dike section). The halos can be either simple or compound, the latter commonly consisting of a dark interior layer and a lighter outer layer. Primary clinopyroxene is commonly completely replaced by amphibole, which is the dominant secondary phase. Igneous plagioclase is partially replaced by one or more generations of secondary plagioclase. Halos also contain accessory titanite, apatite, and chlorite.

Heterogeneity of the Alteration at the Entire Dike Section Scale: Variations with Depth

There are some general trends of the alteration features with depth, although exceptions occur. The variations of the alteration effects are reflected in the amount and composition of the olivine, plagioclase, and clinopyroxene replacement products, and the abundance of veins, alteration patches and halos.

The least altered diabases are characterized by the presence of relict olivine, talc replacing olivine, less abundant actinolite and chlorite, and the lack of alteration patches. These diabases occur between 1704 and 1733 mbsf, and at 1778, 1914, 1920, and 1992 mbsf, whereas only one fresh olivine-bearing sample was found above 1704 mbsf. The 1704–1778 mbsf and 1914–1920 mbsf intervals correspond to high resistivity (Laverne et al., in press), or poorly fractured zones, and are interpreted as having been altered at low water-rock conditions. This was also the interpretation for relatively fresh unfractured diabases from 1189 to 1319 mbsf (Alt et al., 1985). The more altered samples, in which actinolite prevails and which commonly contain patches of alteration, are located in the higher permeability and porosity—or lower resistivity—zones (Laverne et al., in press).

Plagioclase is more extensively altered to albite in the upper section of the dikes, whereas only small amounts of albite replace plagioclase below 1700 mbsf. Secondary Ca-plagioclase replaces magmatic plagioclase rims in the deepest dikes (i.e., below 1500 mbsf). Epidote, laumontite, heulandite, and prehnite are progressively less abundant with depth.

Clinopyroxene is relatively unaltered in the upper dikes, but it is progressively more altered as depth increases. It is generally completely altered in the alteration halos below 1550 mbsf. There is a general trend with depth towards greater proportions of amphibole, more abundant actinolite veins, and more extensive replacement of clinopyroxene in alteration halos, possibly reflecting increasing temperatures downward in the dike section. Amphibole becomes the dominant secondary mineral in the most altered diabases below 1500 mbsf.

Sequence of Alteration

A sequence of four hydrothermal alteration stages in the transition zone and dikes was established on the basis of crosscutting vein relationships. During Stage 1 actinolite and chlorite ± titanite formed in veins while albite, titanite, chlorite, and actinolite developed in the host rocks. This initial assemblage is cut by epidote, quartz, and sulfide veins that formed during Stage 2. These two stages took place at the ridge axis at temperatures ranging from 250°C to 380°C. The movement of the newly formed crust away from the ridge axis into a recharge zone allowed the penetration of seawater into still-warm rocks, resulting in the precipitation of anhydrite both in cracks and as localized replacements of plagioclase (Stage 3). The final stage of alteration is recorded by the presence of laumontite, scolecite, heulandite, carbonates, and prehnite formed in fractures and host rocks during later off-axis alteration at temperatures up to 250°C (Stage 4).

This alteration event sequence generally applies to the entire dike section. Nevertheless, there is evidence for an earlier stage of high-temperature (>400°C) fluid-rock interaction below 1500 mbsf. It is characterized by the partial replacement of plagioclase by Ca-rich plagioclase rims (An_{77-93}) and by the local crystallization of secondary diopside and hornblende within patches and veins (Laverne et al., in press; Alt et al., in press). In these deeper dikes, chlorite, actinolite-chlorite, and actinolite veins are mutually crosscutting, indicating several generations of fracturing and fluid penetration during the initial axial alteration stages.

Alteration Studies: Leg 148

We report here on the alteration and metamorphism observed in rocks cored during Leg 148, based on observations of hand specimen and 40 thin sections. Detailed documentation of alteration effects and vein abundances and types are given in the Alteration Log and Vein Log (Appendixes G and H), and thin section modal data on alteration phases are given in Appendix I.

Mineral Identification

Secondary mineral identifications in hand specimen were based on descriptions made during legs conducted prior to Leg 148; mineral identifications were based on the previous crossed checks between hand specimen and thin section observations. Optical property measurements yielded the mineral identifications in thin section. Secondary minerals that posed identification problems are discussed below, in order of decreasing abundance.

Actinolite

In hand specimen, actinolite was recognized by the light and medium greenish-gray color it gave to veins and host rocks, respectively. In thin section, actinolite was identified by its acicular habit, very pale green to green to bluish-green pleochroism, moderately high relief, medium birefringence, and length slow elongation. The $\gamma \wedge c$ angle varied from 17° to 19°, indicating a transitional composition between actinolite and hornblende. No idioblastic diamond-shaped section was observed and basal sections exhibiting the characteristic 56°–124° cleavages are scarce.

Chlorite

Chlorite was recognized in hand specimen by its dark green to black color and its softness. In thin section chlorite was identified by its very light green to green pleochroism, relatively low relief, and very low birefringence often with abnormal "berlin blue" to "tobacco brown" interference tints, and subparallel extinction.

Talc

Talc was not recognized in hand specimen. In thin section it was readily identified through its occurrence as colorless occicular crystals with moderate relief, high to very high birefringence, and parallel extinction.

Albite

Albite (we use this term for sodic plagioclase $<An_{18}$) was not recognized in hand specimen. In thin section albite was identified by its lower relief and higher birefringence than that of the host plagioclase.

Anorthite

Anorthite (for simplicity, we use this term for secondary plagioclase that is more calcic than the primary igneous plagioclase; anorthite compositions from Leg 140 samples range from An_{75-93}) was not recognized in hand specimen. It was identified by its higher relief and by the presence of abundant tiny fluid inclusions. Sections perpendicular to 010 exhibit higher extinction angles than the host primary plagioclase.

Laumontite

Laumontite was tentatively identified in hand specimen, and its presence was confirmed by X-ray diffraction.

Pumpellyite

Pumpellyite was observed once in thin section and was identified on the basis of its high relief, colorless to pale bluish-green pleochroism, and medium birefringence with abnormal blue interference colors.

The identification of prehnite and pumpellyite must be confirmed by microprobe analysis because size and scarcity prevented measurement of optical properties.

Background Alteration

Except for patches, veins, and associated halos (see "Alteration Patches" and "Veins and Associated Alteration Halos," this section), the background alteration is moderate (about 10%–30% recrystallized), with igneous textures well preserved. The degree of background alteration is higher in the fine-grained crystalline rocks than in the microcrystalline chilled margins. The effect of background alteration is partial or total replacement of primary (igneous) phases, including interstitial materials. Heavily altered (up to 70% recrystallized) samples occur (e.g., Samples 148-504B-251R-1, 12–47 cm [2090 mbsf], and 148-504B-252R-1, 11–37 cm [2100 mbsf]), in which igneous textures are nearly non-existent. Because no lithologic contacts were sampled, it is uncertain whether heavily altered samples represent background alteration or simply large alteration patches.

Olivine

Pseudomorphic alteration of olivine is generally complete, although in some rocks there are relict olivine phenocrysts with secondary minerals along margins and irregular cracks. Pseudomorphs after olivine phenocrysts as well as groundmass olivine are recognized by a characteristic olivine crystal form; in hand specimen pseudomorphs after olivine phenocrysts are dark green to dark brown. Secondary minerals include actinolite, chlorite, talc, quartz, sulfide minerals (pyrite and chalcopyrite), and magnetite.

Successive mineral associations are recognized replacing olivine. Fresh olivine with incipient alteration is recrystallized to talc + magnetite ± quartz. Further recrystallization involves chlorite ± quartz. In the most highly altered samples, olivine pseudomorphs are chlorite with small blades of actinolite and the olivine pseudomorphs generally lack their crystal form. Sulfide minerals occur commonly in olivine pseudomorphs, and they tend to be more abundant associated with talc. Pyrite up to several tenths of a millimeter in size is euhedral to subhedral, and chalcopyrite is smaller and anhedral.

Clinopyroxene

Phenocryst and groundmass clinopyroxene are generally partly altered. Secondary minerals are restricted to margins or cracks in clinopyroxene phenocrysts, whereas some groundmass clinopyroxene is totally altered to secondary minerals. Actinolite is the most common secondary mineral replacing clinopyroxene as fibrous crystals. Chlorite (?) and <1- to 10-µm magnetite grains occur associated with fibrous actinolite. There is a tendency for clinopyroxene in contact with plagioclase to be less altered than that associated with interstitial material.

In much more altered rocks, primary crystal habits both of phenocrysts and groundmass clinopyroxenes are sometimes modified by alteration, and it is difficult to define primary igneous textures. Bladed actinolite with tiny secondary magnetite completely replaces these clinopyroxenes.

Plagioclase

Plagioclase phenocrysts and groundmass are the least altered primary phases. Alteration is restricted to fractures and small irregular areas. The secondary minerals are mainly chlorite and albite with minor actinolite, prehnite, and pumpellyite.

Several grains of pumpellyite are observed in one sample (148-504B-249R-1, 87–89 cm); they occur as a partial replacement of one plagioclase phenocryst that is associated with chalcopyrite and albite. Based on its bluish-green color in plane polarized light, this pumpellyite may be a ferric iron-rich variety. In the same sample, a trace of prehnite occurs as a small crystal aggregate replacing another plagioclase phenocryst.

In more highly altered rocks, plagioclase retains its crystal form, but irregular patches and fractures filled with secondary minerals develop within both phenocrysts and groundmass plagioclase. The secondary minerals include chlorite, albite, actinolite, anorthite, epidote, and laumontite.

Fe-Ti Oxide Minerals

Primary Fe-Ti oxides (titanomagnetite or magnetite) in the groundmass usually display exsolution lamellae of ilmenite. Tiny crystals of titanite, and rarely sulfide minerals, are interstitial to these exsolution lamellae. In more altered samples, alteration of Fe-Ti oxides to titanite is more intensive, but has no associated sulfide minerals.

Cr-Spinel

Euhedral to subhedral Cr-spinel with a translucent dark-brownish color is sometimes observed in olivine, plagioclase, and rarely clinopyroxene phenocrysts, or in the groundmass. Cr-spinel is partially altered to magnetite around the margins and along internal cracks. The degree of alteration of Cr-spinel included in olivine pseudomorphs seems to be higher than that in plagioclase, and groundmass Cr-spinel is more altered than that included in phenocrysts.

Sulfide Minerals

In addition to the sulfides observed in olivine pseudomorphs, sulfide minerals (pyrite, chalcopyrite, and rare pyrrhotite) are scattered in interstices. They are sometimes closely associated with Fe-Ti oxide minerals. Pyrite is commonly euhedral to subhedral whereas chalcopyrite is anhedral, and the pyrite is coarser than chalcopyrite. In chilled margins pyrite is very small, and it is uncertain whether these sulfide minerals are igneous or secondary. In more highly altered samples sulfide minerals are rare.

Glass Inclusions

In large plagioclase phenocrysts, glass inclusions with rounded or ellipsoidal shapes (rarely irregular) less than 0.1 mm in diameter are observed parallel to twin planes. They are completely altered to chlorite and/or finely fibrous actinolite.

Interstitial Materials

In localized areas actinolite forms extremely fine, felted, fibrous mats interstitial to plagioclase laths and clinopyroxene crystals, with accessory fine titanite and/or chlorite. This actinolite contrasts texturally with the fibrous to bladed actinolite that, along with dusty opaque minerals, replaces groundmass clinopyroxene. It is possible that primary interstitial material originally comprised glass or very fine-grained mesostasis. Alternatively, these interstices may have been original voids.

Alteration Patches

Zones of intensive mineral recrystallization are recorded by the presence of irregular, sub-rounded, dark-green patches. Within these patches the original igneous subophitic texture is no longer visible in hand specimen, and a finer-grained, fibrous appearance is observed. On dry sawn surfaces the patches are commonly less reflective than the background diabase, and they absorb water more rapidly when moistened. Concentric margins around the patches are not observed and the boundary between the background diabase and the more altered areas is generally narrow (≈1–5 mm). Within the alteration patches ≈50%–80% of the original igneous mineral assemblage is replaced by secondary phases whereas typically the host diabase is only 10%–40% recrystallized.

Alteration patches vary from centimeter to decimeter scale (e.g., Samples 148-504B-240R-1, Piece 9, 33–38 cm, and 148-504B-251R-1, Pieces 5A and 5B, 21–30 cm, respectively). Sample size is insufficient for any alignment or structurally-controlled elongation of the patches to be discerned. Examples of alteration patches are shown in Figures 27 and 28.

Figure 27. Photograph of medium-grained actinolite-rich alteration patch in Sample 148-504B-252R-1, Piece 5. Lighter gray areas are actinolite.

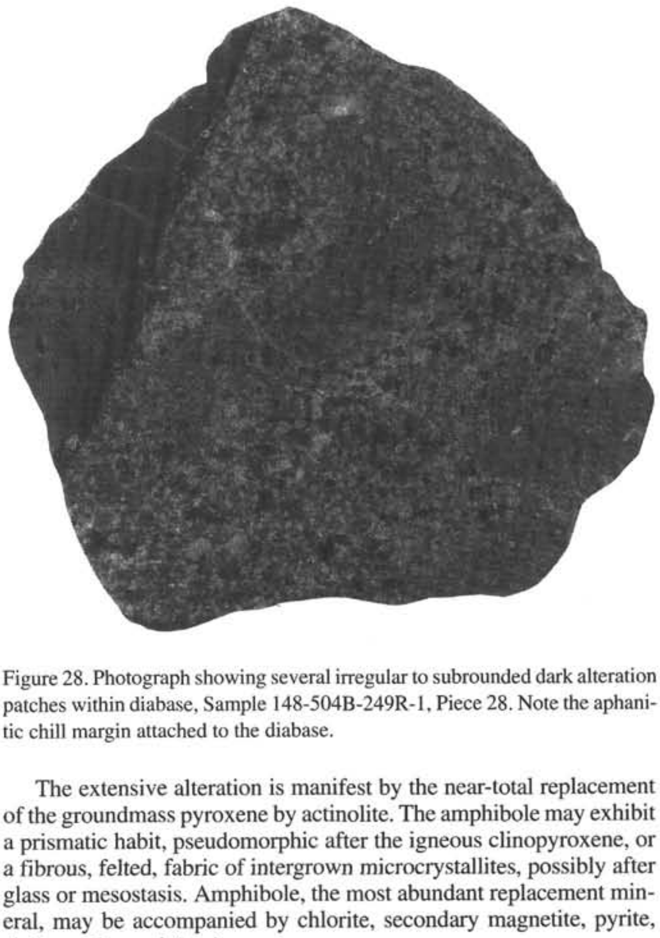

Figure 28. Photograph showing several irregular to subrounded dark alteration patches within diabase, Sample 148-504B-249R-1, Piece 28. Note the aphanitic chill margin attached to the diabase.

The extensive alteration is manifest by the near-total replacement of the groundmass pyroxene by actinolite. The amphibole may exhibit a prismatic habit, pseudomorphic after the igneous clinopyroxene, or a fibrous, felted, fabric of intergrown microcrystallites, possibly after glass or mesostasis. Amphibole, the most abundant replacement mineral, may be accompanied by chlorite, secondary magnetite, pyrite, chalcopyrite, and titanite.

Plagioclase is partly altered, similar to grains observed in the less altered diabase. Within the larger alteration patches (>5 cm), calcic plagioclase rims, riddled with fluid inclusions, may be developed around the plagioclase (e.g., Sample 148-504B-252R-1, Piece 5, 15–20 cm), and individual feldspar grains are commonly crosscut by narrow veinlets of albite and/or chlorite ± secondary magnetite. Epidote and prehnite are uncommonly developed within the cores of larger plagioclase grains.

Olivine is completely altered to a variety of assemblages, similar to those observed within the host diabase (e.g., including talc, chlorite, actinolite, quartz, secondary magnetite, pyrite, chalcopyrite, and titanite). The presence of concentric zones of chlorite with different optical orientations suggests that olivine alteration was a multistage process.

Primary igneous magnetite is nearly absent. These grains have been replaced by either a trellis of exsolved ilmenite lamellae with an associated microgranular silicate mineral (titanite) or by pyrite and/or chalcopyrite.

No unequivocal evidence for the relative timing of the development of alteration patches and halos associated with millimeter-wide actinolite veins has been observed. The same mineral assemblages are present in both these manifestations of more extensive fluid-rock interaction. Narrow (<1 mm) actinolite veinlets, commonly with cataclastic margins, that occupy brittle crosscutting fractures, are observed penetrating through alteration patches. Veinlets of similar style also post-date the coarser actinolite veins with well-developed alteration halos.

Figure 29 shows the variation of the volume proportion of sample altered to alteration patches and to veins and halos with depth in the Leg 148 section. The mean grain size of groundmass plagioclase for each lithologic unit is shown as an index of the variation in grain size. There are no strong correlations between the occurrence of alteration patches and of veins with halos, and no preference for the development of one style of alteration with grain size. Individual core pieces typically exhibit either veins with halos or alteration patches, but exceptionally both. Single lithologic units, on the other hand, commonly exhibit both these alteration types (e.g., Unit 276). Only one sample (Sample 148-504B-247R-1, Piece 10) exhibits both a vein with halos and a patch: Figure 30 illustrates an intersection between an alteration patch and a 1.5-mm-thick actinolite vein with a thin (2–3 mm) alteration halo. The patch illustrated in Figure 30 may have developed independently of, and before, the intersecting veins. Alteration halos that overprint veins have not been observed.

The mean grain size of the groundmass is generally constant downhole (≈0.20 ± 0.05 mm), but three lithologic units (279, 281, and 286) have significantly finer average grain size (≤0.15 mm). No alteration patches have developed in these finer grained rock types though the samples may be cut by actinolite veins with minor halos. There are no consistent trends in alteration with respect to the coarser grained rocks.

The development of hydrous mineral assemblages in the alteration patches indicates more intensive fluid-rock interaction than in the background diabase. This presumably reflects local variations in groundmass porosity and permeability. Poor core recovery and the unidimensional nature of the sampling do not constrain the relative juxtaposition of alteration patches with other patches or vein halos, or provide any indication of whether patches and/or halos form interconnected fluid pathways in 3 dimensions. Some of the observed patches may be halos of veins that do not crop out within the drill core. Neither open-space filling textures, the development of secondary porosity, nor an increase in recrystallization to more idioblastic crystal habits are observed within the alteration patches.

The alteration patches apparently represent independent, isolated zones of more intensive fluid-rock interaction than the host rock.

The alteration patches differ from those observed in the shallower dike section between 1054 and 2000 mbsf (e.g., Alt et al., 1985; Shipboard Scientific Party, 1992a and b). There, centimeter-scale alteration patches commonly contained millimeter-scale amygdular features within them. The amygdules, possibly representing primary vugs or pore space, were filled by actinolite, chlorite, laumontite, and epidote, etc. Similar amygdules were observed during Leg 148, filled by actinolite ± laumontite, only in Unit 293 (2090 mbsf).

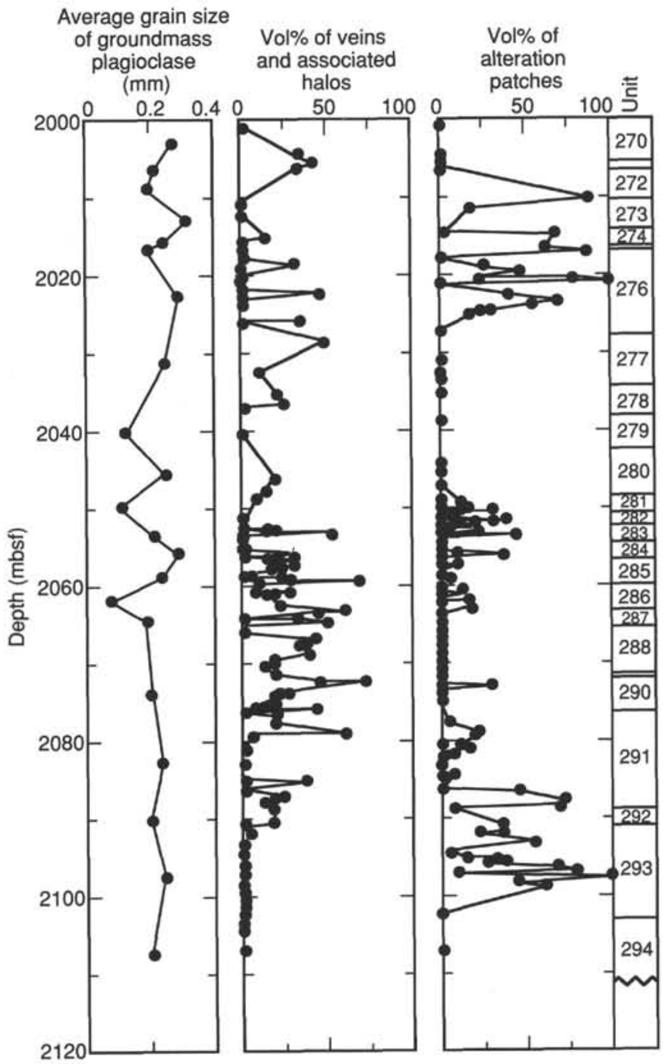

Figure 29. Diagram showing the variation with depth of the volumetric proportions of veins plus their associated halos, and of alteration patches. The average grain size of the groundmass plagioclase is shown for reference. There is no strong correlation between samples with well-developed halos and alteration patches.

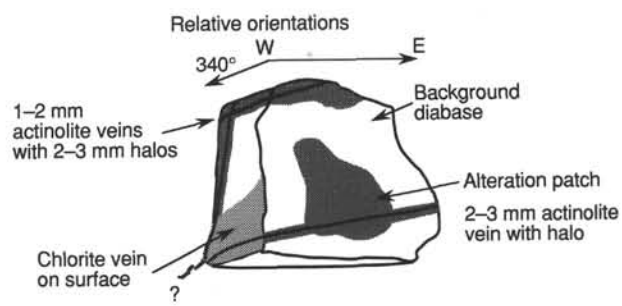

Figure 30. Perspective sketch of Sample 148-504B-247R-1, Piece 10. W shows the intersection between an irregular alteration patch and an actinolite vein. Halos are developed along the margins of the veins. The alteration halo of the sub-horizontal vein and the patch merge into a single amphibole-rich region with uniform mineral abundances: The relative timing of the development of veins and patches cannot be constrained but the alteration patch does appear to have formed independent of the vein halo.

Veins and Associated Alteration Halos

Veins were observed in the archive half of the core and were recorded on the Vein Log (see Appendix H). Veins are interpreted to result from brittle failure and subsequent filling by a variety of minerals. Thus, the texture, abundance (expressed as number of veins per meter of core), volume, mineralogy, and crosscutting relationships exhibited by veins provide important clues about the conditions and controls on rock alteration. Related observations on veins are included in the "Structure and Deformation" section of this chapter.

Veins were classified in hand specimen according to their color: dark green, light green, medium green, pistachio, and colorless. Thin section study shows that the medium- and light-green varieties are dominantly actinolite veins, the dark-green ones are chlorite-dominated veins, the pistachio vein is epidote, and the colorless vein contains quartz.

Vein Types

Five distinct vein types are documented according to thin section observations: actinolite ± chlorite ± titanite, chlorite ± quartz ± titanite, epidote, laumontite ± chlorite, and quartz + chlorite + pyrite. Apatite, which was identified in many veins by cathodoluminescence and electron microprobe studies of Leg 140 samples, may also be present in Leg 148 veins, but its grain size is generally too small to allow microscopic identification. Table 2 summarizes the vein types recorded in the vein log.

Actinolite Veins

The actinolite veins were logged variably as light green or medium green, and they are generally less than 1 mm thick. The largest ones reach nearly 3 mm in thickness. The majority contain actinolite alone in the form of fibrous to tabular crystals, typically of the order of 0.1 mm across, and exhibiting a variety of orientations. Actinolite crystals near vein edges may be crystallographically continuous with wallrock clinopyroxene, suggesting that the vein fill began as syntaxial overgrowths on the pyroxene. Commonly, actinolite extends across the vein with its *c*-axis normal to the vein walls, giving a cross-fiber texture (see "Structure and Deformation" section, this chapter). In other cases, actinolite near the vein wall is oriented parallel to the wall, and interior actinolite is oriented randomly.

Actinolite veins generally contain accessory titanite, and many also contain accessory chlorite. The latter probably accounts for some of the veins logged as dark green in hand specimen. A few actinolite veins probably contain accessory laumontite (identified based upon electron microprobe studies of similar Leg 137/140 occurrences) as a clear interstitial mineral in limited areas where the actinolite is relatively acicular and forms an open mat. Many actinolite veins are flanked by centimeter-scale alteration halos, which are described separately below.

Chlorite Veins

These veins were logged as dark green. Many chlorite veins were noted only as sub-planar faces on the core pieces that are coated with a thin, soft, dark-green material. X-ray diffraction of scrapings from one example (Sample 148-504B-241R-1, Piece 12), including an ethylene glycol treatment, confirm the presence of chlorite with perhaps a small admixture of expandable layers. Chlorite veins are thin, generally logged as <1 mm across. Veins may be pure chlorite or contain accessory sulfide. One vein, observed in thin section, consists of chlorite with accessory titanite and quartz (Sample 148-504B-249R-1, Piece 35, 119–123 cm). This vein occurs in a host rock which contains chlorite and quartz pseudomorphs of olivine phenocrysts, and the vein actually cuts through one such pseudomorph.

Chlorite veins, particularly those that form planar rock faces, chiefly have steep dips (see "Structure and Deformation" section, this chapter), though rarely the dips are near horizontal. Most chlorite veins have no alteration halos.

Table 2. Summary of number of veins logged in hand specimen.

Major mineral	Number	Average width (mm)	Average halo width (mm)
Actinolite	103	1	5
Chlorite	76	<1	0
Quartz	1	2	3
Epidote	1	?	none
Laumontite	1	?	none
Total	182		

Quartz Veins

In addition to the quartz-bearing vein just described, one vein about 2 mm thick is dominated by quartz and chlorite, with accessory pyrite and chalcopyrite (Sample 148-504B-251R-1, Piece 2). The vein cuts a single small piece of fine-grained diabase. Fine acicular actinolite extends into the vein where the wall-rock mineral is clinopyroxene, but not elsewhere. A thin (5 μm) selvage of secondary green diopside occurs between the wallrock pyroxene and the actinolite. This diopside was the first mineral to have formed within the vein.

Laumontite Veins

One sample has an incomplete coating on an exterior face of millimeter-scale flat fibrous crystals of laumontite (Sample 148-504B-246R-1, Piece 24). The crystals are soft and waxy, and vary from white to light green. X-ray diffraction indicates that the white grains are pure laumontite, and the light-green grains are laumontite plus chlorite.

Epidote Veins

One sample has a centimeter-scale section of fine, tan, chilled-margin material attached to one exterior surface (Sample 148-504B-251R-1, Piece 4). Associated with this chilled margin is an incomplete coating, probably a thin vein in cross section, of epidote (confirmed by X-ray diffraction).

Alteration Halos

Alteration halos are present on both sides of 55% of the actinolite veins, and only rarely do they flank chlorite veins. Halos can be simple light-, dark-, or medium-green discolorations of the wall rock wherein magmatic minerals are recrystallized more extensively than in the host rock (Fig. 31). Other halos are complex, consisting of darker inner zones bearing chlorite grading to lighter, chlorite-free outer zones (Fig. 32). Dimensions of halos, typically of centimeter scale, are given in Appendix H.

Halos are always more extensively altered than the corresponding host diabase. A good indication of degree of alteration is the modal percentage of actinolite, which varies from about 5% to 35% in the background alteration of the host diabase, and from about 35 to 70 modal% in vein halos and alteration patches. Generally all igneous clinopyroxene is recrystallized to actinolite in halos. In addition, olivine pseudomorphs comprising actinolite ± chlorite commonly occur in halos, whereas olivine pseudomorphs outside of the halo, such as those in the host diabase, are composed of chlorite instead (e.g., Sample 148-504B-247R-1, 79–83 cm).

Vein halos also contain a greater degree of plagioclase alteration. The earliest plagioclase alteration consists of incomplete rims of fluid-inclusion-filled secondary calcic plagioclase. Further plagioclase alteration in halos consists of a later, crosscutting generation of

Figure 31. Photograph of a diabase sample cut by an actinolite vein that has a simple light-colored halo (Sample 148-504B-249R-1, Piece 40).

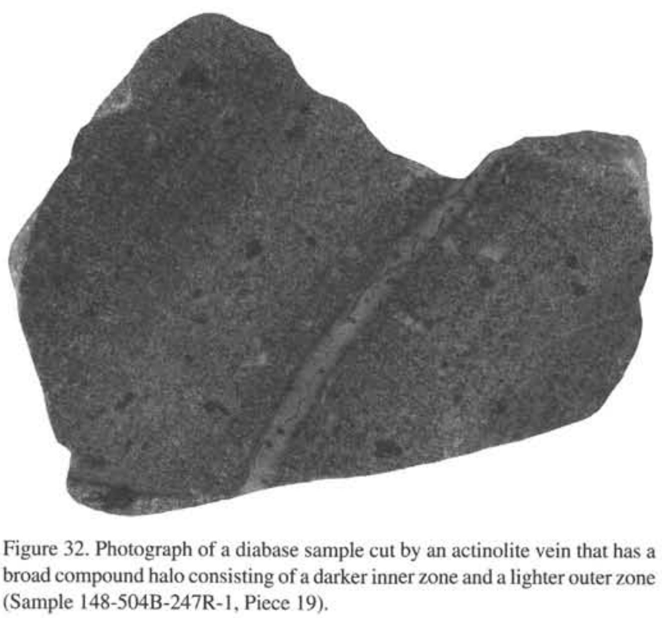

Figure 32. Photograph of a diabase sample cut by an actinolite vein that has a broad compound halo consisting of a darker inner zone and a lighter outer zone (Sample 148-504B-247R-1, Piece 19).

sodic plagioclase (albite), which may be accompanied by minor calc-silicates such as epidote and laumontite.

Vein Abundance

Approximately 180 veins were logged during hand specimen study (Table 2). There is no recognized systematic distribution of veins and vein types downhole in the Leg 148 section. There are, however, noted heterogeneities in vein distribution locally. For example, Unit 290 (with 27 pieces) has 17 chlorite veins and only two actinolite veins (ratio 9:1), whereas Units 291 and 293 combined (totalling 57 pieces) have 17 chlorite and 55 actinolite veins (a ratio of 1:3). The intervening Unit 292 is a single 2.5-cm piece with one vein.

The volume of veins was estimated by summing their thicknesses and comparing this number to the total length of recovery (veins logged as <1 mm wide were counted as 0.5-mm thick). By this estimate, veins account for about 1.2 vol% of the recovered material, or about twice the corresponding value for the Leg 137/140 material (0.6 vol%; Shipboard Scientific Party, 1992a and b).

The overall average number of veins recorded per meter of recovered rock is 21 (Fig. 33). This value exceeds the Leg 137/140 average of 15 veins/m. During Leg 137/140, it was noted that microcrystalline igneous units had an average 48 veins/m, and fine- to medium-grained units had 10–13 veins/m. The Leg 148 average of 21 veins/m comes from fine-grained lithologies, a few of which contain microcrystalline chill margins, and one 2.5-cm-long microcrystalline piece (Unit 289).

Temporal Relations

Crosscutting relationships between veins were observed in only a few cases. In one sample (148-504B-247R-1, Piece 12, 46–50 cm), crosscutting relationships indicate at least four generations of optically similar actinolite veins (Fig. 34). This, along with textural evidence for vein re-opening (such as variable actinolite textures, see the "Structure and Deformation" section of this chapter), demonstrates that actinolite veining occurred in an episodic fashion.

Where multiple actinolite veins occur, it is common for thin veins to be oriented either subparallel to thicker major veins, or orthogonal to them. The thin veins commonly cut the wider actinolite veins and their associated halos and alteration patches and are thus generally later (e.g., in Sample 148-504B-245R-1, Piece 8, 21–24 cm).

In chilled margins, fine actinolite veins are present in orientations both sub-parallel and sub-perpendicular to the margin. The perpendicular veins cut the parallel ones (e.g., Sample 148-504B-249R-1, Piece 28, 92–98 cm). Veins in the chill margin of Sample 148-504B-245R-1 (Piece 13, 36–39 cm) are oriented oblique (≈20°–30°) to the margin. These actinolite veins cut both the chill margin groundmass and phenocrysts, and are accompanied by small alteration halos. Phenocrysts in the chilled margins appear to be a preferential locus for vein intersections.

Variations with Depth in the Leg 148 Section

Alteration styles do not vary significantly with depth in the Leg 148 section. Figure 35 illustrates the lack of systematic changes in mineralogy with depth over this relatively short cored interval.

The greatest degree of alteration besides that in vein halos and centimeter-scale alteration patches occurs in portions of Unit 293 (Core 148-504B-251R-1, Pieces 4-6, and Core 148-504B-252R-1, Pieces 4-9), where several pieces in succession exhibit approximately 60 vol% groundmass alteration, and nearly complete obliteration of the original igneous texture.

Discussion

Comparison with Previously Cored Material at Hole 504B

Alteration minerals observed in Leg 148 rocks are similar to those observed on Leg 137/140, except that one Leg 148 sample (148-504B-249R-1, Piece 27, 87–89 cm) contains the first reported occurrence of pumpellyite in Hole 504B (Fig. 4). The abundance of alteration minerals continues trends at Site 504 noted during previous legs. An increase in actinolite and a decrease in albite with depth was noted during Leg 111. Subsequently, a further decrease in modal albite and a concomitant slight decrease in the modal percentage of chlorite, noted during Leg 140 at about 1950 mbsf, is upheld in the Leg 148 samples (Fig. 35). However the mean actinolite content in samples from below 2000 mbsf is higher than that for the section above this depth.

Styles of alteration generally remain consistent from Legs 83, 111, and 137/140 to the Leg 148 material: hydrothermal veins, with or without halos, alteration patches, and a ubiquitous background altera-

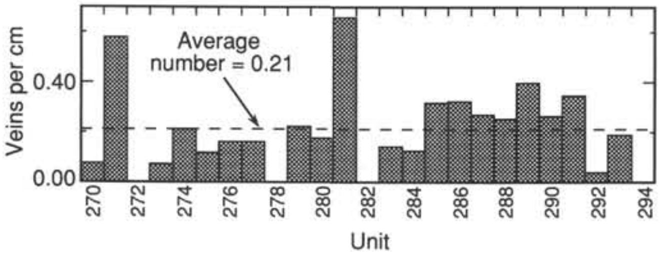

Figure 33. Plot of the number of veins logged per meter of core recovery, for each lithologic unit. The average vein density is 0.21 veins/cm (21 veins/m).

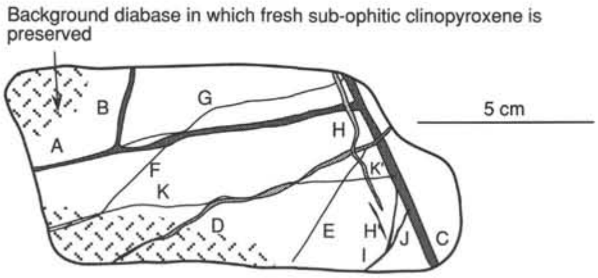

Figure 34. Sketch of the vein relations observed in the thin section from Sample 148-504B-247R-1, Piece 12, 46–50 cm. Fine-grained diabase is cut by several vein generations, predominantly composed of fibrous actinolite with minor accessory phases. The diabase originally comprised igneous plagioclase, pyroxene, olivine, and magnetite. Halos exhibiting extensive replacement of the igneous minerals have developed around the earliest vein generations (A, B, and C). No halos formed around later veins (D–K). Small regions bearing relict igneous phases with slight alteration are preserved in the periphery of the section. Crosscutting relationships constrain the following vein chronology: (1) A, B, C, and associated halos; (2) D, E, F, G; (3) H-H′, I, J; (4) K-K′. Bulk of thin section comprises veins with associated alteration halos in which clinopyroxene is replaced by fine-grained fibrous to prismatic amphibole. The alteration halos appear to be associated with the thicker, earliest generation veins (A, B, C). Smaller crosscutting veinlets do not show evidence for the development of over-printing vein halos (e.g., vein D–K′).

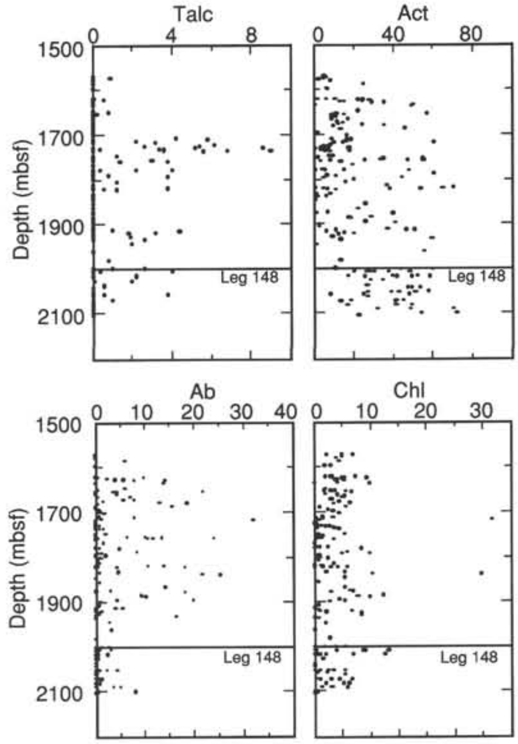

Figure 35. Plots of alteration mineral modes vs. depth (note that the section includes only the interval cored during Legs 137, 140, and 148). Data above the line at 2000 mbsf are from Dick, Erzinger, Stokking, et al., 1992. Data below 2000 mbsf are from Appendix I. Actinolite is generally more abundant in the Leg 148 section, reflecting more intensive alteration of these rocks. Chlorite modes are similar to those in the Leg 137/140 section. Albite is less than 10 modal%, continuing a characteristic that began around 1950 mbsf. Talc is absent below about 2075 mbsf: when present in the Leg 148 samples above 2075 mbsf, it has modal proportions similar to those in Leg 137/140 samples (i.e., ≤4%), excepting the higher talc samples near 1720 mbsf.

tion are present. However, the alteration patches in Leg 148 samples differ from those from previous legs, as noted above. The number of veins in Leg 148 samples, amounting to roughly 21 veins per meter of cored interval, exceeds the Leg 137/140 value of 15 veins per meter, but it is unclear whether this difference has any statistical significance. The types of veins and their relative abundance (mostly actinolite, lesser chlorite, and very few quartz, epidote, or laumontite veins) remain the same as the those from the Leg 137/140 section. Actinolite veins are more prevalent than in the shallower Leg 83 and Leg 111 sections (above 1562 mbsf).

Processes of Hydrothermal Alteration

The most striking feature of the rocks from the dike section cored during Leg 148 (as well as Legs 83, 111, 137, and 140) is the heterogeneity of their alteration, which is manifest in several different ways: as patchy alteration to highly recrystallized rock in zones up to 10 cm long; as <1-mm- to 2-mm-thick veins, half of which are accompanied by halos; and as secondary minerals dispersed throughout the rock (i.e., "background alteration"). In one thin section primary olivine may be replaced by as many as three different secondary mineral associations; in another thin-section, actinolite veins cut alteration patches, primary mineral replacements, and other veins, regardless of whether they are of the same mineralogy. Finally, relict igneous minerals co-exist with one or more secondary mineral assemblages (ranging from secondary anorthite or clinopyroxene to laumontite) formed under widely different conditions. Highly localized variations, on the scale of centimeters, in temperature and pressure are not physically valid, and hence the heterogeneity in the proportions of secondary phases must reflect spatial and temporal variations in the extent of fluid-rock interaction. Thus, water-rock interactions of very highly variable intensities occurred throughout the dikes and at various times after their emplacement and crystallization.

The intensity of hydrothermal exchange is a function of the local porosity and permeability structure, temperature, the fluid and rock compositions, the total fluid flux, and the kinetics of fluid-solid exchange. An abundance of veins filling brittle cracks indicates that fluids were predominantly channelled along fractures. In addition, the common development of vein halos and isolated alteration patches requires permeability of fluids or diffusion along grain boundaries for short distances (centimeters) into the bulk of the rock. The presence of less altered regions, in which there has been only a small amount of replacement of the igneous phases by hydrothermal minerals, indicates that the spacing of fluid channels (crack/veins) was too large and the total fluid flux insufficient to pervasively recrystallize the host diabase to the alteration assemblages observed in patches and vein halos.

The heterogeneity of hydrothermal alteration reflects a lack of pervasive fluid-mineral equilibrium during successive water-rock interactions. In contrast, metamorphic facies "represent the results of equilibrium crystallization of rocks under a restricted range of externally imposed physical (and chemical) conditions" (Bates and Jackson, 1980). Hence, the concept of metamorphic facies is not strictly applicable to the rocks studied because the mineral assemblages observed are not equilibrium parageneses connoting contemporaneous formation. Each one of the observed mineral assemblages that form a vein, a halo, a patch, or a primary phase replacement can represent a sequence of mineral formation in response to locally evolving conditions.

The successive changes in hydrothermal conditions must have taken place rather close to the ridge axis and over a relatively short time because the range of predominant physical (and chemical) factors appears to have been relatively narrow. Talc + magnetite replacement of olivine could have occurred at temperatures as high as 600°C. The presence in patches and halos of Ca-rich plagioclase and coexisting actinolitic hornblende suggest high temperatures (possibly greater than 400°C) and calcic plagioclase-actinolitic hornblende stability (Spear, 1980). This temperature is slightly higher than the formation temperature of actinolite in the veins or as a replacement product of clinopyroxene and interstitial material in the halos adjacent to the veins. Another alteration event at slightly lower temperature is represented by the formation of chlorite in veins or as olivine replacement. However, even in these two cases the frequent association of chlorite with minor actinolite fibers indicates that the formation of both secondary minerals was intimately related. Finally the presence of albite replacing the primary plagioclase and cutting across the secondary Ca-rich plagioclase, or of prehnite and laumontite in the primary plagioclase point to the lowest temperature alteration events.

The formation of amphibole-rich patches and halos, hypothesized to have occurred beneath a ridge axis, attests to a localized redistribution of chemical species. Regions of intense fluid-rock interaction and chemical leaching, such as the epidosites that are common in ophiolites (thought to represent hydrothermal reaction zones and the channelways of hydrothermal fluid upwelling; Schiffman et al., 1987) are not observed at this site. The heterogenous alteration stages preserved in the lower portions of Hole 504B most probably reflect the typical results of time-integrated fluid-rock interaction in extensive lower crustal regions that have never been zones of concentrated upwelling of hydrothermal fluids or black smoker vents.

BOREHOLE FLUID GEOCHEMISTRY

Samples of water from within the open borehole of Hole 504B were obtained prior to drilling during Leg 148. Samples were taken to analyze the chemical composition of the fluid and aid understanding of chemical and hydrological conditions within open oceanic boreholes. During Leg 148, six water samples were recovered, three of which contained large quantities of suspended particles presumably due to inadequate circulation at the end of Leg 140. Because the hole apparently contained drilling mud, the three samples that were relatively particle free must have lost any borehole water they recovered during their ascent through the ocean. Only one sample has chemistry significantly different than seawater, and interpretation of the source of reaction is complicated by the presence of the bentonite drilling mud.

Background

The original intent for sampling these fluids was to obtain formation fluids that potentially could have entered the borehole annulus by diffusive or advective means. Whereas large changes in chemistry relative to seawater have been observed, evidence for collection of formation fluids from oceanic boreholes is equivocal. Mottl and Gieskes (1990) define two possible modes of fluid sampling within oceanic boreholes: passive and active. In the active mode, a packer or other sealing device is used to seal the formation and actively withdraw fluids from the formation using a pressure gradient. The passive mode relies on allowing enough time between drilling and sampling to allow formation fluids to enter the borehole by diffusive or advective means. Active mode sampling has been attempted on Legs 70, 83, and 111, but has been unsuccessful to date for sampling fluids from basement formations. Passive mode sampling, while less desirable, uses much less complex tools but requires visiting a potential site years after drilling to allow enough time for formation fluids to exchange with borehole waters. Passive sampling is necessary as a control to the eventual success of active mode sampling, as the fluid within the borehole must be sampled to distinguish that active samples actually obtained fluid from the formation. The samples collected on Leg 148 were collected passively.

Borehole fluid has been sampled on DSDP Legs 70, 83, 92, and ODP Legs 111 and 137, after allowing the borehole to remain undisturbed for 39, 710, 470, 1233, and 1633 days, respectively. A compilation of data from Legs 70, 83, 92, and 111 can be found in Mottl and Gieskes (1990), and a discussion of results from Leg 137 (Shipboard Scientific Party, 1992a and b) can be found in Magenheim, Bayhurst, et al. (1992). Past studies of borehole fluids from Hole 504B have revealed large chemical gradients with depth. The fluids from past legs can be described as a mixture of surface seawater with a reacted fluid (Mottl and Gieskes, 1990; Magenheim, Bayhurst, et al., 1992). Increases in calcium (Ca^{2+}) and silica (H_4SiO_4) with depth have been balanced by uptake of magnesium (Mg^{2+}), sodium (Na^+), sulfate (SO_4^{2-}), and potassium (K^+).

Mottl and Gieskes (1990) proposed three possible processes affecting the chemistry of the borehole fluid: (1) downhole mixing of bottom seawater through the casing; (2) reaction with the wall rocks within the borehole; and (3) true water from the formation entering either by advection or molecular diffusion. The only clear evidence for the advection of formation fluids into an oceanic borehole is from Hole 534A sampled during the Dianaut Re-Entry Expedition (Gieskes and Magenheim, 1992). Hole 534A is a sedimented borehole on the Blake Bahama Plateau, and borehole fluids collected seven years after drilling contained a component of sediment pore fluid traceable to a suspected aquifer. Passive sampling in a basement borehole has not demonstrated recovery of formation waters. Evidence for diffusive exchange with formation waters has been equivocal and is inferred from tritium displacement models of Mottl et al. (1985) and Mottl and Gieskes (1990). Tritium, a product of atmospheric testing during the 1950s and 1960s, is present only in the surface waters of the Pacific Ocean. Fluids used during drilling and circulation at the end of a drilling leg are surface seawater, and thus, tritium is introduced to the borehole as an unambiguous tracer of the original fluid placed in the borehole. However, molecular diffusion cannot account for all the tritium removed (Mottl and Gieskes, 1990). In fact the removal of tritium can be entirely explained by convective mixing of bottom seawater into the borehole, as tritium concentrations increase with depth in Hole 504B (Magenheim, unpublished calculations). This explanation is also in agreement with the analysis of Fisher and Becker (1991), suggesting that thermal convection must occur in 504B.

Systematic inter-leg changes in the fluid chemistry have been related to the increase in bottom hole temperature as the borehole has been drilled deeper (Magenheim, Bayhurst et al., 1992). This, combined with recovery of anhydrite crusts and rubble coated by reaction products from the bottom of Hole 504B at the start of Leg 137, suggests a reaction zone at the bottom of the hole (Magenheim, Bayhurst et al., 1992).

During the interim between drilling legs Hole 504B apparently acts as a passive in-situ water-rock experiment. Evidence from past legs has given information of relatively long-term reaction of basalt and seawater at temperatures between 80°C (Leg 70) and 162°C (Leg 137). Thus the objective for borehole fluid sampling during Leg 148 was to extend these observations to maximum borehole temperatures of 200°C. While past sampling in Hole 504B suggests that borehole fluid is not formation water, it is important to understand reactions and hydrologic processes occurring in oceanic boreholes if we are to

Table 3. Summary of fluid sampling operations.

Run no.	Depth (mbrf)	Depth (mbsf)	Date (1993)	Time (GMT) Start	End	Comments
148-1M	3761	301	28 Jan.	0143	0425	No sample
148-2M	4020	560	28 Jan.	1729	1949	Overpressure, orange particulates
148-3M	4256	796	28 Jan.	1952	2214	Orange particulates
148-4M	4491	1031	28 Jan.	2217	0040	No particulates
148-5M	4726	1266	29 Jan.	0042	0317	Overpressure, rust colored precipitates
148-6M	4961	1501	29 Jan.	0319	0643	Green particulates
148-7M	5196	1736	29 Jan.	0648	0946	No sample
148-8M	5430	1970	29 Jan.	0949	1224	No particulates

develop a successful active-mode sampling program. Without a firm understanding of what is in the hole, it will be impossible to distinguish formation fluid from reacted borehole water.

Results

A total of eight sample runs were made, resulting in collection of six water samples. Complete details of the sampling operation are summarized in Table 3. The two runs that did not recover water apparently did not fire until the tools were removed from the drill string because of the trigger mechanisms' malfunction. Of the six water samples recovered, three samples contained substantial quantities of suspended material that was apparently drilling mud left in Hole 504B from Leg 140.

As discussed by the Shipboard Scientific Party (1992a and b) and by Lysne (1992), the Los Alamos tool and other fixed volume samplers suffer from the problem of sample contraction as the sampler is withdrawn from the hot borehole into the cold (2°C) oceanic bottom waters. This contraction creates an internal underpressure allowing the valves to open and the void to fill with cold seawater, thus diluting the samples. In the worst case scenario, opening of the valves could result in the loss of the entire sample. After equilibrating the pressure to compensate for this cooling effect, the sample then expands as it ascends to shallower depths. Internal hydrostatic overpressure was observed on all samples from Leg 137, causing difficulty in extracting the samples, but on Leg 148 overpressure was observed only in two samples: 148-2M and 148-5M. Many of the seals from the recovered samples were badly damaged, which may have compromised the integrity of these samples. The seals appear to have been crushed by the large internal hydrostatic pressure associated with moving water from the seafloor to the sea surface. This sampler design, although functional in some situations, is not suitable for oceanic conditions.

An indication of the sample integrity can be made by comparing the expected recovery based on the in-situ temperature and pressure to the actual mass of fluid recovered. Table 4 shows actual mass of recovered fluid versus the expected mass for the sampler volume at in-situ conditions based on the density algorithms of Pitzer et al. (1984) for 0.5 M NaCl. A calculation of the minimum percent dilution is also given in Table 4. This is a minimum due to the assumption that the internal underpressure is quenched solely by filling with cold seawater, without losing any fluid in the process. Any spillage during the sample extraction could make this calculation too low, as the actual mass recovered would be greater than recorded. In all cases, the samplers were recovered with greater mass of fluid than expected for the in-situ conditions.

The results of shipboard analyses of Hole 504B borehole fluid samples and surface seawater collected at the start of Leg 148 are given in Table 5. The composition of surface seawater from Legs 137 and surface and deep water composition reported from Leg 111 are provided for reference. Figure 36 shows profiles of magnesium and calcium concentration with depth. Of the six water samples collected only one (148-6M) appears to be significantly different from seawater composition. The composition of the other samples are very similar to either surface or deep ocean water.

Three of the fluid samples (148-3M, 148-5M, and 148-6M) contained relatively large amounts of particulates (Table 6). It is likely that these solids are remnants of drilling mud that was not flushed from Hole 504B at the end of Leg 140. Similar circumstance led to large quantities of particulates recovered during fluid sampling on Leg 92. A program of extensive circulation was adopted at the end of Leg 92, successfully clearing the hole of drilling mud for sampling programs on Leg 111 and subsequently on Leg 137. No record of

Table 4. Comparison between expected and recovered sample masses.

Sample	Depth (mbsf)	T (°C)	Recovered mass (g)	In-situ density (g/mL)	Expected mass (g)	Minimum dilution (%)	Comments
148-2M	560	91	1001.58	1.0048	992.67	0.90	Overpressured, lost 5 mL
148-3M	796	115	1020.65	0.9901	990.13	3.08	Muddy orange
148-4M	1031	133	980.59	0.9783	966.42	1.47	Lost 10–20 mL
148-5M	1266	146	1006.30	0.9694	969.43	3.80	Overpressured, lost 5 mL, muddy
148-6M	1501	157	997.00	0.9618	950.18	4.93	Greenish mud, valve hard to open
148-8M	1970	180	977.60	0.9450	933.52	4.72	No particles

Table 5. Chemical compositions of borehole fluid samples.

Sample	Depth (mbsf)	Salinity	pH	Alkalinity (mM)	Cl^- (mM)	Mg^{2+} (mM)	Ca^{2+} (mM)	Na^+ (mM)	K^+ (mM)	SO_4^{2-} (mM)	CO_2 (mM)	H_4SiO_4 (µM)	Fe (µM)	H_2S (µM)	NO_3^- (µM)	NO_2^- (µM)	PO_4^{3+} (µM)	NH_4^+ (µM)	Solids (g/L)
148-2M	560	34.2	7.86	2.38	542	51.81	9.97	460	10.4	28.0	1.85	9	0	0	0	0.0	0	5	78
148-3M	796	34.2	7.06	2.04	542	51.56	10.11	459	10.2	27.4	1.97	165	434	11	0	0.0	0	20	316
148-4M	1031	34.0	7.69	2.10	545	52.06	10.42	458	9.9	27.6	1.81	76	0	0	0	0.0	0	7	26
148-5M	1266	34.0	7.25	2.40	535	50.69	10.15	459	10.1	27.3	2.07	323	318	16	0	0.0	0	19	399
148-6M	1501	32.1	6.32	1.03	547	35.21	18.49	441	9.8	8.1	1.53	2865	295	51	0	0.0	0	11	396
148-8M	1970	34.0	7.24	2.09	534	50.78	10.55	456	10.2	26.9	1.84	189	26	0	0	0.0	0	5	119
148-SSW1		34.1	7.78	2.22	535	52.68	10.09	460	10.1	27.7	1.94	0	0	0	0	0.2	0	<5	
137-SSW		33.5	8.03	2.36	549	53.75	10.33	473	10.4	27.7		2			8	0.4	1	0	
111-DEEP		34.8	7.62	2.50	554	53.41	10.45	475	10.4	28.6		165			39		2		
111-SSW		32.5	8.17	2.33	540	52.03	9.82	463	10.1	27.4					0				
2σ				0.10	10	1.00	0.10	8	0.5	0.3	0.05	7	10	10	2	0.1	1	5	

Note: SSW = Surface Seawater, Deep = Deep seawater from near 504B, 137-SSW from Shipboard Scientific Party (1992a), 111-SSW, 111-DEEP from Shipboard Scientific Party (1988). Solids were estimated by taking the total solids recovered in the first aliquot plus two times the solids recovered on the filter(s).

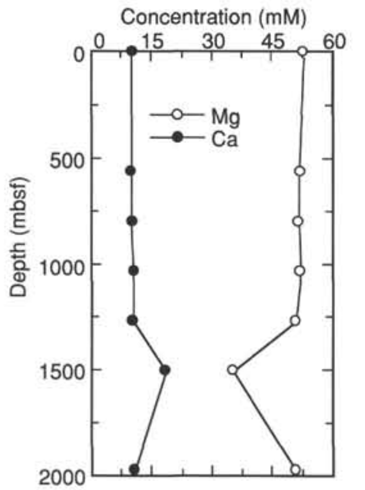

Figure 36. Downhole profiles of magnesium and calcium from Leg 148 borehole fluid samples from Hole 504B.

Table 6. Partial chemical composition of surface seawater (148-9M), NaBr-spiked surface seawater (148-10M), and a borehole fluid sample obtained from 475 mbsf on 5 March 1993 (148-11M).

Sample	Salinity	pH	Alkalinity (mM)	Cl^- (mM)	Mg^{2+} (mM)	Ca^{2+} (mM)	SO_4^{2-} (mM)	Br- (mM)	H_4SiO_4 (µM)
148-9M	33.8	7.99	2.16	522	51.78	10.14	27.2	0.76	9
148-10M	33.8	8.02	2.17	524	51.92	10.06	27.4	4.35	14
148-11M	33.8	7.90	2.09	525	50.07	10.33	27.4	1.12	147

rigorous circulation was noted in the operations during Leg 140; apparently the circulation was inadequate, thus leaving the borehole containing significant amounts of mud.

Because Samples 148-4M and 148-8M contained less particulates than samples from shallower depths, it is unlikely that these samples recovered fluid from within the borehole. Also, the chloride concentration in both samples is close to that of surface seawater, and it is likely that these samples lost any borehole fluid which may have been sampled. Major element compositions of these samples are also very close to surface seawater. Trace element and isotopic studies (e.g., $^{87}Sr/^{86}Sr$) should be able to discern whether or not a component of borehole fluid is present in these samples.

Only Sample 148-6M shows a large deviation from seawater composition. Relative to seawater values, salinity, alkalinity, pH, magnesium, sodium, potassium, sulfate, and dissolved carbon dioxide were depleted in this sample (Table 5). Calcium was enriched along with silica. In all samples that contained large particulate loads (148-3M, 148-5M, and 148-6M), trace quantities of H_2S were observed suggesting anoxic conditions in the borehole. These samples also contained high concentrations of dissolved Fe, which decreases with depth. Elevated concentrations of silica were also observed in samples with high particulate concentration.

The solids had distinct color variations with depth, from rusty orange color at 796 mbsf to dark green at 1501 mbsf. Shipboard X-ray diffraction (XRD) was performed on the solids recovered in Samples 148-3M, 148-5M, and 148-6M. Anhydrite was observed in the diffractograms of Samples 148-5M and 148-6M. Formation of anhydrite is expected upon heating of seawater to 200°C and at temperatures as low as 150°C in the presence of reacting basalt (Seyfried and Bischoff, 1979; Bischoff and Seyfried, 1978). X-ray diffraction of air-dried and glycolated samples indicated the presence of smectite in Samples 148-3M and 148-5M, and smectite plus chlorite in 148-6M. The smectite is most likely left-over bentonite drilling mud from Leg 140 that has reacted in the borehole. Gieskes et al. (1986) observed similar downhole trends in the clay mineralogy during sampling of the mud-filled Hole 504B fluids on Leg 92. The absence of orange iron hydroxides from the deeper samples is consistent with the lower iron concentration of these samples. A decrease in iron concentration with depth was also observed on Legs 92 and 137. Apparently iron concentration decreases further away from the oxic bottom waters that are capable of rusting the steel sediment casing.

Discussion

In the past, borehole samples collected from various depths show mixing trends between seawater and a reacted fluid endmember when plotted in element versus element space. Since the data from this leg indicate that only one sample is significantly different than seawater, we have plotted the data on the mixing trends for Ca and Si vs. Mg observed on Leg 137 in Figure 37. Ca is plotted both as measured and corrected for the anhydrite removal (Ca*). Corrected Ca is calculated by adding the Ca removed in anhydrite (the change in SO_4 concentration from the seawater value of 28 mM) to the measured value. In both cases the Ca and Ca* plot below the lines for the Leg 137 samples. Decreased concentration of dissolved CO_2 in this sample may indicate precipitation of $CaCO_3$, reducing the observed Ca concentration even further than by anhydrite precipitation alone.

Carbonate precipitation is supported by observation of aragonite and smectite coatings (confirmed by XRD) on fractured surfaces of a breakout (Section 148-504B-254M-1, #1) recovered in the drill collars removed from the borehole on 21 January, 1992 (Fig. 38). This breakout had apparently fallen into the hole in the 10 days during which drilling was conducted at Site 896. Because no record of aragonite has been made in the core logs of the deep sections of Hole 504B we believe that this mineral formed in the borehole environment. Similar evidence for reaction within Hole 504B was observed during Leg 137 when anhydrite crusts and smectite/chlorite-coated rubble were recovered from the bottom of the hole (Magenheim, Bayhurst, et al., 1992). Oxygen isotopic analysis should be able to confirm the temperature of formation of this aragonite, and therefore the borehole depth at which it formed. However, the small decrease

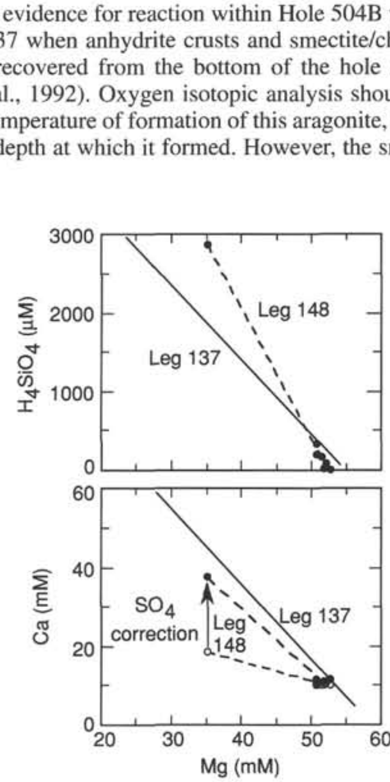

Figure 37. Calcium vs. magnesium and silica (H_4SiO_4) vs. magnesium for Leg 148 borehole fluid samples from Hole 504B. Mixing lines from Leg 137 (Shipboard Scientific Party, 1992a) are provided for reference. Ca is expressed as measured (open circles) and corrected for anhydrite precipitation (solid circles) (Magenheim, Bayhurst, et al., 1992), from the sulfate depletion as described in the text.

in CO_2 (and alkalinity) is not sufficient to account for the decrease in Ca added relative to Mg removed from the fluids.

A plot of silica versus Mg (Fig. 37) provides a reasonable mixing line for the Leg 148 samples, indicating that a small component of borehole fluid may have been retained in some of the samples. In this figure it appears that greater quantities of Si are released relative to Mg taken up when compared with Leg 137.

The differences observed between the two legs are difficult to interpret because of the presence of drilling mud in the samples from Leg 148. Magenheim, Bayhurst, et al. (1992) demonstrate that there has been a monotonic increase in Ca* released versus Mg consumed as the hole has been drilled deeper and bottom-hole temperatures have increased from 80°C on Leg 70, through 160°C on Leg 137. Considerable scatter in mixing trends observed during Leg 92 caused by the presence of drilling mud in the borehole obscures this relationship. This may also explain the discrepancy observed during Leg 148.

The observed differences might also be attributed to the fact that only 418 days passed between Leg 140 and Leg 148. This interval could have two effects: (1) reacted fluids from the rubble zone at the hole bottom may not have had sufficient time to mix more than the observed 500 m from the hole bottom; and (2) slow reactions may not have progressed due to kinetic limitations. The borehole is 500 m deeper than on the last sampling attempt on Leg 137, and the time between drilling legs reduced from 1633 days to 418 days. Mixing of a reacted fluid from the bottom of the hole may not move the fluid efficiently through the whole borehole. Magenheim, Gieskes, et al. (1992) suggest that formation of smectite (and/or chlorite) and transformation of calcic plagioclase to albite can account for the observed chemical changes in the Leg 137 samples. Albitization is a slow process that has not successfully been demonstrated on laboratory time scales, while formation of clays is relatively rapid (Rosenbauer et al., 1983). A kinetic argument would account for the lesser extent of Ca release, as well as the greater dissolved Si concentration that is consumed during formation of albite from anorthite.

Oceanic Borehole Spike Experiment

A tracer experiment was initiated in Hole 504B at the end of Leg 148. The borehole was filled with surface seawater containing a spike of sodium bromide (NaBr). When Site 504 is next revisited, either on a future ODP leg or by wireline re-entry, the downhole Br^- concentrations and Br^-/Cl^- ratio should constrain the volume of bottom water mixed downhole, below the underpressured inflow zone. The Br concentration will serve as a conjugate to tritium measurements, yielding much more timely information about the quantity of surface seawater remaining in the borehole, as tritium measurements take over a year to produce. Any discontinuity between tritium and Br results should provide useful information regarding the efficiency of flushing the borehole.

Bromide is an unreactive constituent of seawater, showing a constant ratio to Cl^- with an implied residence time in the ocean of over a million years. Seawater contains approximately 0.86 mM of Br^-, compared to a total halide concentration of 559 mM (or 0.15% of total halides). Since Br^- is a minor anion in the oceans, a spike resulting in a fivefold increase in Br^- concentration will affect the total halide concentration by less than 1.0%. The introduction of NaBr will also increase the Na^+ concentration by less than 1.0%, well below the common precision of analysis for this constituent. The precision of Br^- measurements is greater than 5% (2σ); thus it should be possible to determine the effects of downhole mixing, and/or exchange with basement fluids. With the exception of Br^-, the effects of the introduction of NaBr should not be detectable. The change in density and composition will be indistinguishable with the exception of Br^- itself, permitting the collection of high-quality borehole samples during future investigations.

Prior to the second phase of logging operations at Hole 504B the borehole was cooled by circulation. This opportunity was taken to flush the hole of drilling mud and suspended debris and to place in the hole surface seawater spiked with sodium bromide as a passive tracer experiment. Both operations will benefit borehole water-sampling programs on future expeditions to Site 504.

Figure 38. Photograph of breakout recovered from core barrel during fishing operations on 26 January 1992. Rosette-like growths of alteration minerals are aragonite, which presumably precipitated after regional and thermal stresses formed this breakout. Sample 148-504B-254M-1.

Tritium has been used to trace the surface seawater originally placed in the borehole (e.g., Mottl and Gieskes, 1990); however, its usefulness as a tracer will soon expire as its concentration is continuously decaying in surface seawater. Also, it is unclear whether the entire hole is replaced with surface seawater or some fraction of the drilling fluid is retained. The presence of drilling mud in borehole water samples from this leg seems to suggest inefficient removal of drilling fluids. The addition of NaBr to the fluid placed in the borehole adds a second tracer for monitoring the borehole fluids. The tracers were introduced in different parts of the operation: tritium was introduced during the entire time surface water was flushed into the borehole, while the NaBr-spiked surface water (with present-day surface water tritium content) was added at the end of the operation.

On 26 February the borehole was flushed with surface seawater for 3 hr at a rate of 1893 L/min. Then the NaBr-spiked surface seawater was placed in the hole to the level of the casing (~275 mbsf). A total of 340,661 L of surface seawater were flushed through the hole, greater than triple the volume of the open borehole (assuming a 25.4 cm diameter). This volume should have been adequate to flush the borehole of all drilling mud used during Leg 148 and to effectively fill the hole with surface seawater containing present-day tritium concentration and the NaBr-spiked surface water. The NaBr-spiked surface seawater was mixed while the borehole was being cooled by circulating surface seawater. The mixing tank was first filled with seawater and emptied twice to remove any mud remaining in the tank. This process removed all but about 10 mg/L of suspended solids, which unavoidably remained in the tank. Thirty-five kilograms of high purity NaBr (99+%, Lot 06304EX, Aldrich Chemical Company) were added to approximately 94,000 L of fresh surface seawater in the mud tank. The tank was mixed for 1 hr and then allowed to settle for approximately 0.5 hr prior to placing the NaBr-spike in the borehole. The fluid was visibly particle free after settling, and because the pumps were located a foot above the bottom of the tank, it is unlikely that significant amounts of bentonite were in the solution put into the borehole. Samples were taken of the fluid both before and after adding the NaBr directly from the mixing tank, and some solid NaBr was retained for later reference. Archived samples were stored without any preservation in sealed 20 mL ampoules for future reference: 504B-148-9M (unspiked seawater); and 504B-148-10M (NaBr-spiked seawater).

On 5 March a borehole fluid sample was obtained from 475 mbsf (504B-148-11M) using the WSTP tool. Sampling was conducted seven days after placing the NaBr spiked seawater in the borehole and after 48 hrs of logging operations conducted in Hole 504B. The fluid sample arrived on deck still warm (39.7°C), indicating that fluid from within the borehole was recovered. The fluid was visually particle free indicating that the 3 hrs of flushing was successful in removing drilling mud from Hole 504B. Initial analyses of the fluid before and after spiking, and of the borehole water from 475 mbsf, are given in Table 6.

The borehole fluid has surface seawater Cl^- concentration, indicating little or no deep ocean water ($Cl^- = 554$ mM) in the borehole. The Br^- concentration indicates that only 10% of the NaBr-spiked surface water was recovered in sample 148-11M. Two explanations are possible: (1) the borehole spike was diluted with surface seawater as logging operations proceeded, pushing surface seawater through the drillstring into the borehole; or, (2) the NaBr-spiked seawater resides below the sampled depth in the borehole. Dilution with bottom seawater seems unlikely, as a 90% dilution with bottom seawater would raise the Cl^- concentration to 551 mM, an easily detectable difference from the 525 mM of the borehole fluid. Dilution of the entire spiked volume (93,159 L) with all the surface seawater contained in the drillstring during the logging operations (3640 m of drillstring with 10.43-cm inner diameter = 30,280 L) would yield a Br^- concentration of 3.46 mM. Dilution of the NaBr-spike with the drillstring water is therefore impossible, as the measured concentration (1.12 mM) requires a much larger dilution. The second possibility is supported by measurements of the borehole diameter during logging operations of Leg 148 indicating average borehole diameters near 35.5 cm (see "Downhole Measurements," this chapter). This is substantially larger than the standard bit outer diameter of 25.4 cm initially used to calculate the borehole volume. With a diameter of 35.5 cm, the 93,159 L of NaBr-spiked fluid would have only been placed in the bottom 938 m of the borehole, or to a depth of 1162 mbsf. Part of the NaBr-spiked fluid could have been mixed upward during logging operations, or while removing the drillstring to logging depth. Substantial mixing of the spiked fluid is not evident, as little deep ocean water was mixed into the borehole during the third phase of logging at Hole 504B that was conducted immediately prior to the fluid sampling.

Evaluation of the success or failure of this experiment, of course, awaits future expeditions. Information gained during this first attempt at an oceanic well-spiking experiment will allow future use of DSDP/ODP boreholes for tracer studies that will elucidate hydrodynamic properties of the basement and within the boreholes themselves.

IGNEOUS AND METAMORPHIC GEOCHEMISTRY

Introduction

A vast number of analyses from the pillowed and massive basalt flows and dike complex of the 2000.4-m-deep hole are available from the six previous DSDP and ODP legs (Legs 69, 70, 83, 111, 137, and 140) and are reported in several papers (Autio et al., 1983; Etoubleau et al., 1983; Marsh et al., 1983; Emmermann, 1985; Kempton et al., 1985; Tual et al., 1985; Autio et al., 1989; Kusakabe et al., 1989; Shimizu et al., 1989; Dick et al., 1992). The most relevant material for comparison to Leg 148, however, comes from Leg 140, which drilled 379 m of diabase dikes above the 111 m of diabase drilled on Leg 148.

We will summarize the major and trace element data from selected diabase samples, which visually were considered representative of the material recovered from Hole 504B during Leg 148. Although the percent alteration of the analyzed samples is as high as 61%, the samples do not include the more intensively altered patches and halos (described in "Alteration and Metamorphism"). Twenty-one samples from the 25 igneous units that were defined by the Shipboard Scientific Party were analyzed for major and trace elements, as well as for structural water (H_2O^+) and carbon dioxide (CO_2). The sample preparation and analytical procedures, with precision and accuracy values, are given in the "Explanatory Notes" chapter under "Igneous and Metamorphic Geochemistry."

The diabase samples range from sparsely to highly phyric, but the majority (approximately 75%) are moderately plagioclase-olivine phyric (2%–10% phenocrysts; see the "Igneous Petrology" section).

Results

The chemical composition of the diabases are shown along with other relevant information (lithologic unit, lithology, grain size, percent alteration, and depth) in Table 7. The diabases are strongly depleted, moderately evolved MORB (MgO: 8.48–9.61 wt%, Fe_2O_3*: 8.68–10.83 wt%, Mg-number value: 0.637–0.693, Ni: 95–151 ppm, Cr: 205–336 ppm), and as previously stated (e.g., Dick et al., 1992), highly depleted in incompatible elements (e.g., Zr: 39–53 ppm, Nb: commonly <1 ppm). With increasing degree of fractionation (expressed as decreasing Mg-number value), the major oxides show increase with respect to SiO_2, TiO_2, Fe_2O_3, MnO, Na_2O, and P_2O_5, and decrease in Al_2O_3, MgO, and CaO (Fig. 39). As regards the trace elements, V, Zn, Sr, Y, and Zr increase, and Cr and Ni decrease (Fig. 40). Sc and Rb do not show any well-defined trends, the latter probably due to mobility during alteration.

Variation with Depth

The variations in major and trace element concentrations with increasing depth are shown in Figures 41 and 42, respectively. The SiO_2 content, with the exception of Sample 148-504B-251R-1, 9–51 cm (2090.39 mbsf), shows a slight tendency to increase with depth. Al_2O_3 shows a rather well-defined trend: an increase defined by the first five samples (2000.6–2007.72 mbsf; Samples 148-504B-239R-1, 26–30 cm, and 148-504B-240R-1, 82–90 cm), a decrease between Samples 148-504B-240R-1, 82–90 cm, and 148-504B-245R-1, 21–24 cm, renewed increase between 2043–2072 mbsf (Samples 148-504B-245R-1, 21–24 cm, and 148-504B-249R-1, 92–98 cm), and then a decrease downhole. This trend is antipathetic to that defined by TiO_2, Fe_2O_3*, and MnO. CaO shows a trend defined by several increases (2000–2017.55 mbsf, 2026.02–2052.21 mbsf, 2053.31–2072.12 mbsf), interrupted by rapid decreases. The concentrations of the trace elements V, Y, and Zr (Fig. 42) and the major elements TiO_2 and Na_2O (Fig. 41) show similar patterns (i.e., a general increase downhole to 2043.1 mbsf, Sample 148-504B-245R-1, 21–24 cm), then decrease to 2090.39 mbsf (Sample 148-504B-251R-1, 49–51 cm), followed by a pronounced increase at 2103.5 mbsf (Sample 148-504B-253R-1, 0–4 cm). Samples 148-504B-240R-1, 52–63 cm, 148-504B-241R-1, 105–108 cm, 148-504B-246R-1, 111–115 cm, and 148-504B-247R-1, 64–68 cm (at 2007.42, 2017.55, 2053.31, and 2057.34 mbsf), however, diverge from this trend (particularly with respect to Zr) by being extremely depleted. The elements Ni, Cr, Sr, and Zn may show large variations, but no clearly defined trends (Fig. 42). Cu and S contents are bimodal, presumably controlled by the abundance of Cu-Fe sulfide minerals.

In Figures 43 and 44 the major and minor/trace element data of the samples from Leg 148 have been added to the total database archived from previous legs for Hole 504B. The new data are a continuation of the existing trends.

Alteration

An important issue that always arises when dealing with the geochemistry of altered and metamorphic magmatic rocks concerns to what extent elements have been mobilized, and in which direction.

Table 7. Geochemical analyses of Hole 504B diabases, Leg 148.

Core	239R-1	239R-1	240R-1	240R-1	240R-1	241R-1	241R-1	242R-1	244R-1	245R-1	245R-1	246R-1	246R-1	247R-1	247R-1	248R-1	249R-1	249R-1	250R-1	251R-1	253R-1
Interval (cm)	26–30	45–51	33–38	52–63	82–90	0–4	105–108	12–16	3–8	21–24	39–46	21–25	111–115	64–68	72–76	43–48	92–98	19–24	112–117	49–51	0–4
Piece #	9	14	9	14	21	1	19	4	2	8	14	8	32	15	17	13	28	6	32	7	1
Unit	270	271	272	273	274	275	276	277	279	280	281	283	284	285	286	288	290	291	292	293	294
Lithology	M-PO	M-PO	M-P	M-OP	M-PO	H-PO	M-P	M-PO	M-PO	S-P	H-PO	S-PO	M-PO	S-PO	M-POC	H-PO	H-POC	M-PO	M-POC	M-PO	M-POC
Grain size	F	F	F	F	F	F	F	F	F	F	F	F	F	F	F	F	F	F	F	F	F
Depth (mbsf)	2000.66	2000.85	2007.23	2007.42	2007.72	2016.5	2017.55	2026.02	2038.23	2043.01	2043.19	2052.41	2053.31	2057.34	2057.42	2062.23	2072.12	2072.87	2081.52	2090.39	2103.5
% alteration	22	45	31	26	49	23	48	34	29	43	61	56	44	31	12	34	44	20	23	44	26
Major elements (wt%)																					
SiO_2	50.02	49.08	49.82	48.73	48.51	49.89	48.88	49.57	49.69	49.79	50.34	49.55	49.61	49.17	50.06	49.68	49.22	49.84	50.19	48.28	50.27
Al_2O_3	14.77	15.19	15.05	16.00	16.64	15.39	16.14	14.89	14.66	13.78	14.85	14.74	14.88	15.20	14.59	15.66	15.70	14.93	14.88	15.01	14.33
TiO_2	0.86	0.82	0.82	0.75	0.77	0.79	0.72	0.82	0.84	0.96	0.87	0.87	0.70	0.74	0.92	0.81	0.74	0.89	0.83	0.81	0.95
Fe_2O_3*	9.73	9.28	9.55	8.93	8.66	9.35	8.68	10.00	10.20	10.83	9.31	9.68	9.49	9.37	10.09	9.26	8.77	9.86	9.73	9.87	10.40
MgO	8.94	8.81	9.04	9.09	8.75	8.96	9.08	9.24	9.10	8.63	8.48	9.04	9.60	9.61	8.90	8.80	9.15	8.57	8.60	9.88	8.89
CaO	12.88	13.03	12.85	13.11	13.23	13.14	13.35	12.80	12.81	13.03	13.16	13.24	12.56	13.02	12.85	12.91	13.21	12.88	13.02	12.77	12.48
Na_2O	1.87	1.80	1.75	1.73	1.79	1.80	1.73	1.80	1.83	2.03	1.95	1.84	1.84	1.65	1.85	1.81	1.70	1.87	1.71	1.57	1.93
K_2O	<0.01	<0.01	<0.01	<0.01	<0.01	<0.01	<0.01	<0.01	<0.01	<0.01	<0.01	<0.01	<0.01	<0.01	<0.01	<0.01	<0.01	<0.01	<0.01	<0.01	<0.01
MnO	0.17	0.16	0.15	0.14	0.14	0.16	0.14	0.17	0.17	0.18	0.12	0.14	0.14	0.14	0.18	0.16	0.14	0.17	0.17	0.16	0.18
P_2O_5	0.05	0.05	0.05	0.03	0.04	0.04	0.04	0.04	0.04	0.05	0.04	0.04	0.03	0.04	0.05	0.05	0.04	0.04	0.04	0.04	0.05
LOI	0.55	1.48	1.04	1.14	1.13	0.48	1.00	0.50	0.30	0.48	0.68	0.60	0.98	0.73	0.48	0.83	1.05	0.65	0.48	1.61	0.53
Total	99.84	99.70	100.12	99.65	99.66	100.00	99.76	99.83	99.64	99.76	99.80	99.74	99.83	99.67	99.97	99.97	99.72	99.70	99.65	100.00	100.01
H_2O+	1.17	2.13	1.63	2.07	2.21	1.19	1.77	1.40	1.17	1.58	1.59	1.59	1.89	1.59	1.22	1.77	1.95	1.52	1.66	2.69	1.41
CO_2	0.07	1.99	1.39	0.37	0.08	0.15	0.07	0.31	0.23	0.15	0.10	0.08	0.03	0.09	0.04	0.09	0.05	0.06	0.17	0.08	0.06
Trace elements (ppm)																					
S	1360	901	1455	319	175	1334	156	1311	1468	166	71	234	93	333	1361	891	170	872	1538	1262	1450
Sc	41	38	39	39	41	39	39	44	47	48	48	45	45	40	41	39	34	36	38	41	39
V	229	218	212	210	194	222	204	224	242	290	255	249	207	209	249	230	217	237	227	219	246
Cr	312	308	302	316	276	320	286	316	308	205	247	330	309	329	277	336	265	261	229	259	221
Ni	110	119	113	138	134	121	138	129	112	99	101	118	139	149	105	123	144	109	105	151	95
Cu	81	89	82	64	23	84	26	89	84	38	21	39	13	92	82	81	23	89	82	104	79
Zn	50	40	52	31	30	48	30	43	62	36	27	29	33	37	60	48	29	51	69	42	61
Ga	16	15	16	14	16	15	16	15	16	16	15	16	14	14	13	16	15	14	15	16	16
Rb	1	<1	<1	1	1	<1	1	<1	<1	<1	<1	1	1	<1	2	<1	3	2	2	<1	1
Sr	58	58	55	58	55	59	52	52	55	50	56	53	49	53	63	61	55	60	55	48	61
Y	22	21	23	19	22	22	19	24	27	29	26	23	20	20	25	22	20	24	21	23	24
Zr	48	46	46	40	45	48	41	47	50	52	48	46	38	39	47	45	46	47	44	43	53
Nb	<1	<1	1	<1	2	<1	<1	<1	1	<1	<1	1	<1	<1	<1	<1	<1	<1	2	<1	<1
Ba	19	20	16	12	13	29	<8	15	<8	29	21	20	<8	<8	20	24	15	12	<8	12	15
Mg*-value	0.669	0.676	0.676	0.691	0.69	0.678	0.697	0.67	0.663	0.637	0.667	0.673	0.69	0.693	0.66	0.677	0.697	0.657	0.66	0.688	0.653

Note: Unit rock names and grain size data are from the thin section description. Abbreviations for rock names: S = sparsely phyric; M = moderately phyric; H = highly phyric; P = plagioclase; O = olivine; C = clinopyroxene. Abbreviations for grain- size data: F = fine grained. Fe_2O_3* is the total amount of iron expressed as Fe_2O_3. The Mg-numbers value is the molar ratio MgO(MgO + FeO), where FeO is calculated to be 90% of the total iron as FeO.

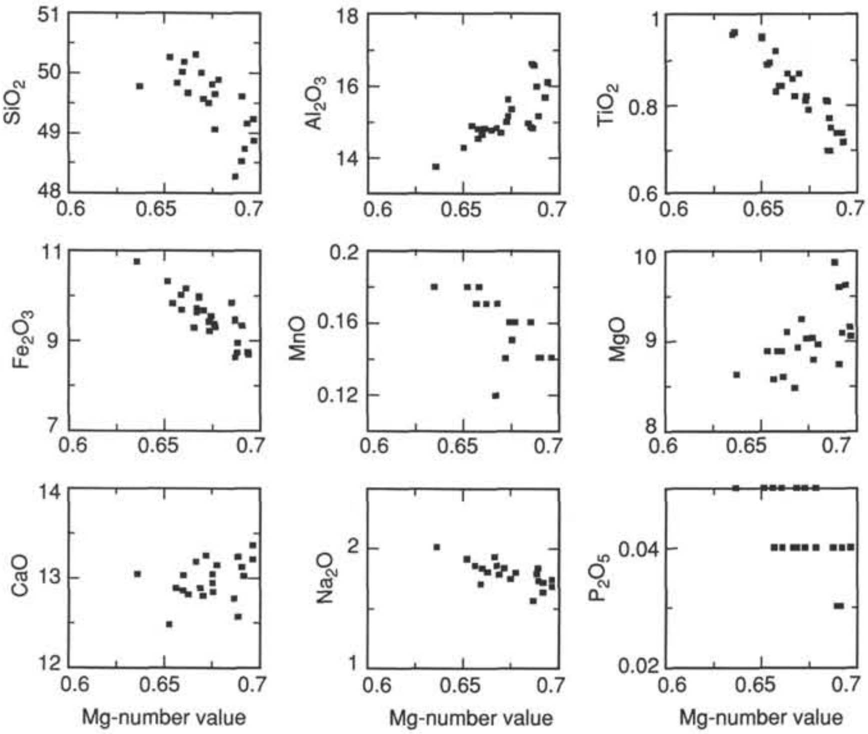

Figure 39. Major element geochemistry plotted against Mg-number value fractionation index of the diabases from Hole 504B recovered during Leg 148. Mg-number value is the molar ratio of O(O + FeO), where FeO is 90% of total iron as FeO.

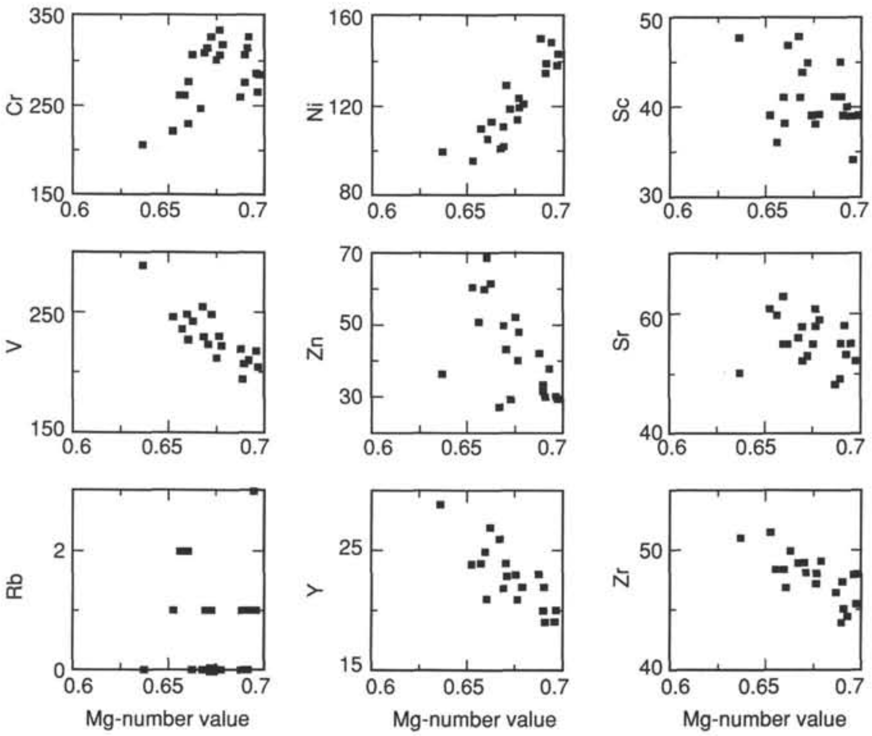

Figure 40. Trace element geochemistry plotted against Mg-number value fractionation index of the diabases from Hole 504B recovered during Leg 148.

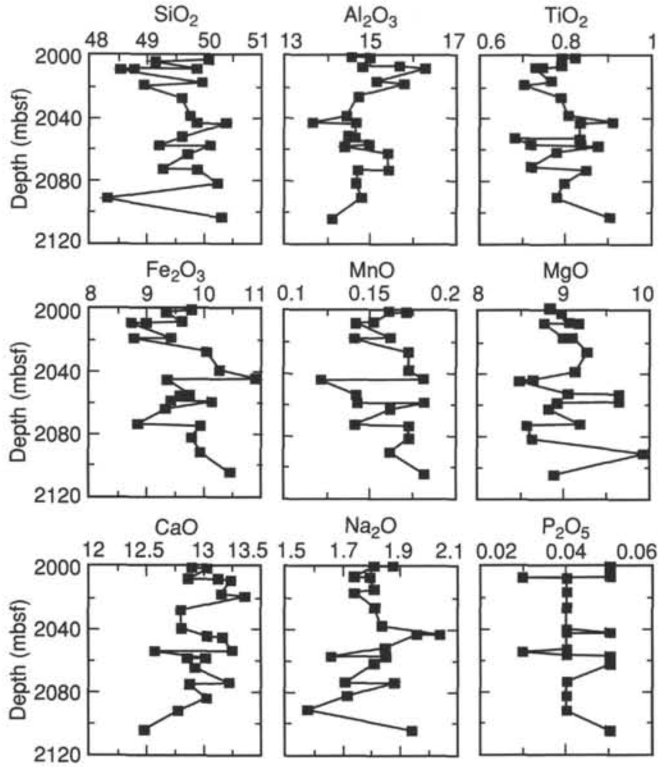

Figure 41. Downhole variation of the major element chemistry of the diabases from Hole 504B recovered during Leg 148.

This is difficult, and in many cases, impossible to resolve with confidence, because the fresh rock with which the altered rock should be compared, is usually no longer preserved. Secondly, if the altered rocks show "trends" when plotted against an "alteration index," these trends may be caused by the combined effect of both primary igneous and secondary processes for which there is generally no resolution. Ideally, fresh and altered parts from the same specimen should be investigated. In the absence of such data for the samples from Leg 148, Hole 504B, only tentative conclusions can be drawn.

In discussing the effects of alteration on the bulk-rock geochemistry for the diabases recovered during Leg 140 (Dick et al., 1992), the bulk structural water (H_2O^+) content was chosen to represent an indicator of the extent of alteration. A limit was set at a H_2O^+ content of 1.53 wt%, above which the concentrations of elements such as Zr and Ti were considered to decrease. Figure 45 shows H_2O^+ versus TiO_2, Zr, Y, Sr, V, Zn, Ni, and Cr, for the rocks recovered from Leg 148, as well as from earlier legs. We see no change in the data at 1.5 wt% H_2O^+. Above approximately 3 wt% H_2O^+, however, there is an increased spread in the TiO_2, Zr, and Y, and a slight tendency for increased Zn and Ni contents. We assume that Nb would have shown a similar behavior, but because of the extremely low concentrations for this element, we regard the uncertainty of the analyses as very large and hence have not considered this element. For Sr and Cr no change can be seen. We are therefore hesitant to use H_2O^+ to index the rocks as "altered" or "fresh" and to use this as a basis to reject samples as not representative of the original fresh rock. This would be in agreement with the general observations concerning elements like Ti, Zr, Y, Nb, Cr, and Ni, which indicate that they are usually stable during alteration and low-grade metamorphism (e.g., Cann, 1970; Hart, 1970; Frey et al., 1973; Thompson, 1973; Coish, 1977; Seyfried and Mottl, 1982; Staudigel and Hart, 1983; Valsami and Cann, 1992).

The alteration minerals of the recovered diabase samples are principally actinolite, chlorite, and talc, of which the former is the dominant. As the actinolite, which commonly replaces the groundmass clinopyroxene, does not contain H_2O^+ exceeding 2.5 wt% (Alt et al., 1985), this places an upper limit on the H_2O^+ content of the most severely altered samples. In Figure 46 we have plotted the percentage alteration, as indicated by the replacement of primary minerals by secondary minerals versus Zr, TiO_2, Y, Sr, V, Cr, and Ni. If we make an assumption that the spread in the element concentrations at the lowest degree of alteration (i.e., <1%) represents the primary chemical variation of the magma, the relationships shown in Figure 46 do not indicate any obvious trends with increasing degree of alteration. Sr, which usually is found to be a mobile element during alteration and metamorphism, does not show any evidence for mobilization. This may be so partly because the plagioclase, which accommodates Sr, generally is only slightly altered. The lack of correlation between the major and trace elements and indices of alteration (i.e., H_2O^+) suggests limited element mobility in this part of the dike complex, and that the analyzed compositions are representative of the original magmatic compositions. The samples analyzed do not include the more intensively altered patches and halos. The latter have been shown to exhibit various chemical changes due to alteration (Alt et al., 1986; Alt, Muehlenbachs, Honnorez, 1986; Alt et al., in press).

Discussion

Provided that alteration has not disturbed the element concentration to any significant extent, the major and trace element trends shown in Figures 39 and 40 reflect magmatic processes. The trends shown by SiO_2, Al_2O_3, TiO_2, Fe_2O_3*, MgO, and Ni (Figs. 39 and 40) can be explained in terms of fractional crystallization of plagioclase and olivine, in agreement with the petrographic observations (see "Igneous Petrology" section). Fractionation of plagioclase would account for the decrease in Al_2O_3, olivine for the decrease in MgO, and Ni with decreasing Mg-number value. Further, since these minerals will have lower SiO_2–, TiO_2–, and Fe_2O_3– contents than that of the melt from which they crystallize, the concentration of these elements will increase. Cr does not show any clear trend, although the lowest Cr values occur at the lowest Mg-number values. This would be in agreement with late fractionation of clinopyroxene, to account for the depletion in Cr following plagioclase and olivine fractionation, again in agreement with the observed petrography. The trends of increasing V, Y, and Zr with decreasing Mg-number would also be explained by fractional crystallization of the above mentioned minerals.

STRUCTURE AND DEFORMATION

Introduction

This report is based on observations from hand specimens and thin sections of core recovered during Leg 148, in conjunction with information derived from paleomagnetic and logging studies. The methods and nomenclature are described in the "Explanatory Notes" chapter, this volume. The structure log is included as Appendix J, and the hand-specimen and thin-section descriptions are available from the ODP database.

Gross Structure

Seismic reflection data over Hole 504B (Langseth et al., 1988) suggest the presence of a series of north-dipping half-graben structures with blocks tilted <5° away from the Cocos Ridge. This interpretation is supported by an approximately east-west strike and steep northward dips determined for two dikes from Leg 140 (Dick, Erzinger, Stokking, et al., 1992). This sense of tilting, however, contradicts the evidence of negative paleomagnetic inclinations assuming the site is reversely magnetized, as indicated by magnetic anomalies (Smith and Banerjee, 1986). The degree of tilting is also somewhat ambiguous: pillow lavas have paleomagnetic inclinations suggesting 20° to 30°, whereas inclinations from the sheeted dike complex suggest <10° of tilt (Smith and Banerjee, 1986; Becker et al., 1988; Dick et al.,

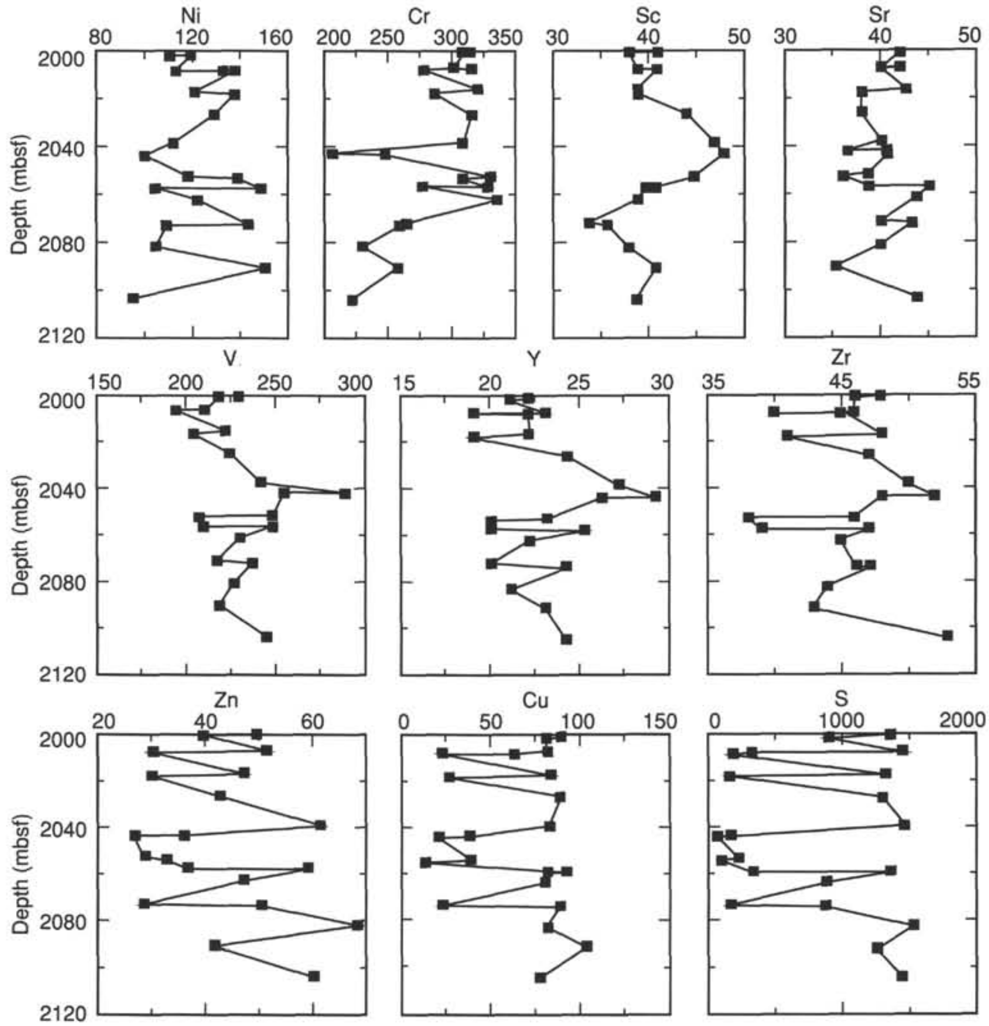

Figure 42. Downhole variation of the trace element chemistry of the diabases from Hole 504B recovered during Leg 148.

1991). This latter value is based on dips of three chilled dike margins in Leg 148 (76° to 88°), in addition to those from Leg 140 (79°–84°), Leg 111 (70°–90°), and Leg 83 (~55°–90°).

Numerous microfaults were recovered in core and junk baskets from Hole 504B during Leg 148, and it is likely that drilling difficulties encountered at the bottom of the hole were related to penetration of a fault zone. With the exception of microfaults, very little strain is evident in the Leg 148 core. Observed structures include dike margins, veins, open fractures, and microfaults. No mylonites and only a few millimeter-scale cataclastic zones were recovered during Leg 148.

Recovery of fault rocks generally has been rare in Hole 504B. Small-scale faulting associated with hydrothermal alteration (including a stockwork-like zone), however, has been documented by Agar (1990, 1991) in the lowermost pillow lavas and upper transition zone (840-959 mbsf). Becker et al. (1989) and Becker, Sakai, Adamson, et al., (1989) suggested that a fault is present approximately 50 m above this zone at approximately 800 mbsf, based on an abrupt change in magnetic inclinations and resistivity. Whether or not significant fault displacement has occurred in this interval (800 and 960 mbsf), however, is unknown.

Igneous Contacts

Structures associated with chilled dike margins and a micro-dike are described in this section; the petrographic characteristics of these contacts are described in the "Igneous Petrology" section of this chapter. On a macroscopic scale the oriented margins and the micro-dike are steeply dipping (76°–88°), whereas the one paleomagnetically reoriented margin, Sample 148-504B-251R-1, 13–15 cm (Piece 4), has a strike of 118° and dips 84° to the south. The strike has considerable uncertainty, however, because only a small area of chilled material was attached to the rounded face of the core, making azimuthal measurement difficult.

The margins are planar at hand-specimen scale, and no highly convolute or brecciated samples were obtained (in contrast to Legs 83, 111, and 140), although this may be a function of sampling rather than a change in intrusive mechanism. In thin section (Samples 148-504B-245R-1, 36–39 cm, Piece 13, and 148-504B-249R-1, 92–98 cm, Piece 28) the chilled margins are planar and generally cut across crystals, although in Sample 148-504B-249R-1, 92–98 cm, the margin appears to deviate at crystal boundaries and thin apophyses of the margin follow grain boundaries, fracture surfaces, and cleavage planes in the wall rock. Where these apophyses rejoin the margin they enclose elongate pods of host lithology or angular crystal fragments. Inclusions of host rock wholly within the main body of the margin suggest a continued process of stoping and perhaps partial-to-complete(?) assimilation of small amounts of the wall rock. The origin of the micro-dike in Sample 148-504B-241R-1, Piece 15, is problematic: it appears to terminate in both a cataclastic zone and a poorly defined vein, and it is described in more detail in the "Microstructural Characteristics" section, below.

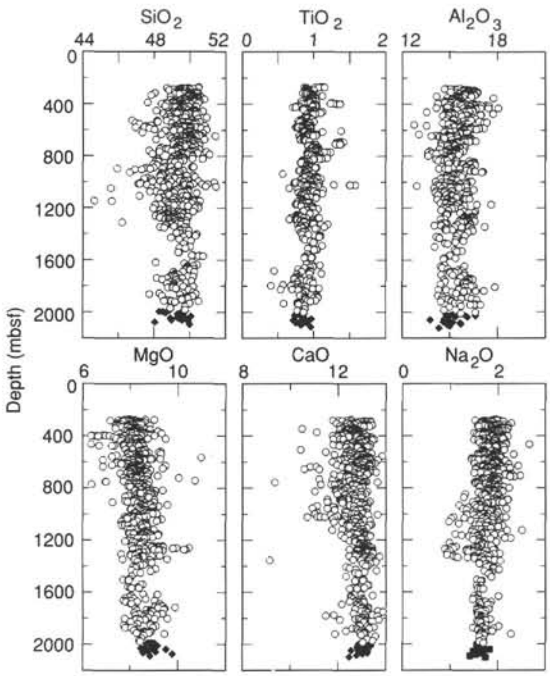

Figure 43. Downhole variation of the major element chemistry of the basalts and diabases of the entire database from Hole 504B (Autio, Rhodes, et al., 1983; Etoubleau et al., 1983; Marsh et al., 1983; Emmermann, 1985; Kempton et al., 1985; Tual et al., 1985; Autio et al., 1989; Kusakabe et al., 1989; Shimizu et al., 1989; Dick, Erzinger, Stokking, et al., 1992). Solid diamonds represent the Leg 148 data; open circles represent data from previous legs (Legs 69, 70, 83, 111, 137, and 140).

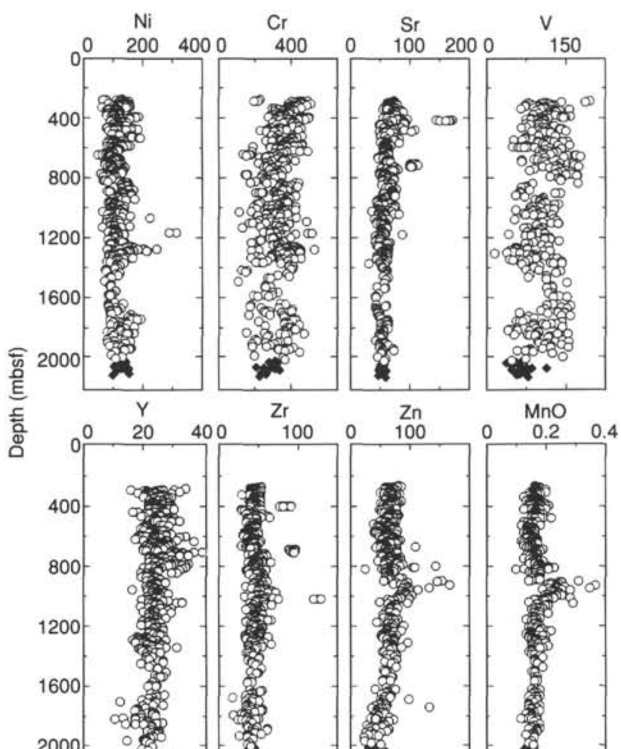

Figure 44. Downhole variation of some trace and minor element chemistry of the basalts and diabases of the entire database from Hole 504B (data sources as in Fig. 43). Solid diamonds represent the Leg 148 data; open circles represent data from previous legs (Legs 69, 70, 83, 111, 137, and 140).

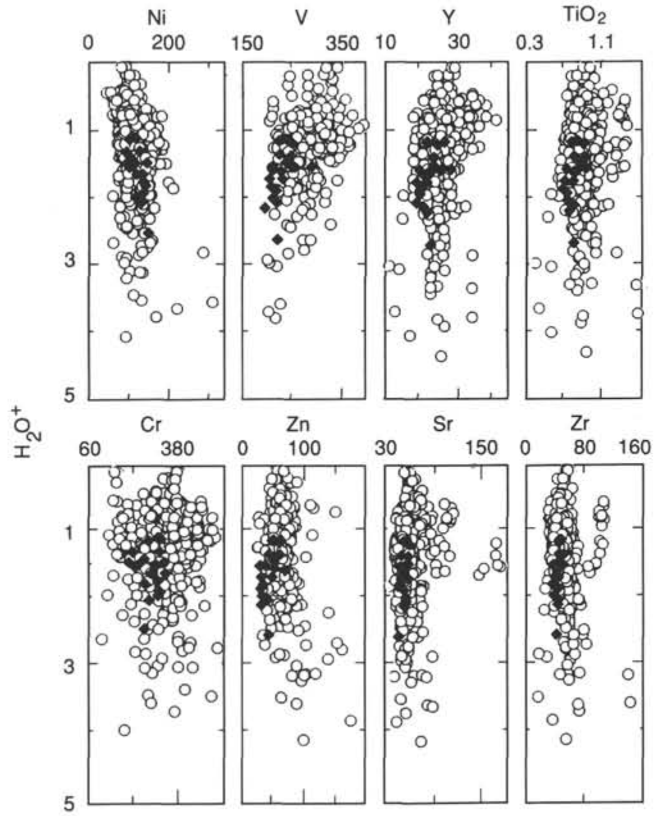

Figure 45. H_2O^+ vs. Ni, V, Y, TiO_2, Cr, Zn, Sr, and Zr for the diabases recovered during Leg 148 (solid diamonds), compared with data from previous legs.

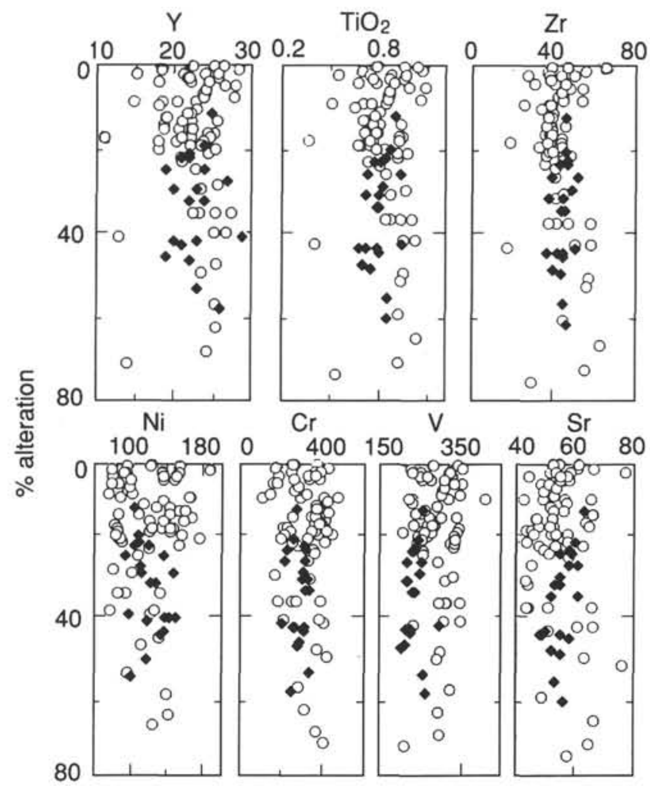

Figure 46. Percent alteration vs. Y, TiO_2, Zr, Ni, Cr, V, and Sr for the diabases recovered during Leg 148 (solid diamonds), compared with data from Leg 140 (Dick, Erzinger, Stokking, et al., 1992).

Parallel to, and adjoining the chilled margin in Sample 148-504B-245R-1, 36–39 cm, is a thin zone of fine-grained actinolite, possibly a shear zone (discussed below), similar to some samples from Leg 140. Two sets of actinolite veins, one subparallel to the chilled margin and the second at a high angle to the margin, are present. The high-angle veins are less common and are rarely continuous across the chilled margin into wall rock.

In Sample 148-251R-1, 13–15 cm, Piece 4, an epidote vein parallels the chilled margin. The chilled margin is extensively altered and bleached to a cream color, in contrast to the usual black to green-gray color, and it is cut by a network of fine quartz(?) veins.

Veins

Four vein types have been defined on the basis of mineralogy, although only chlorite and actinolite veins are widespread through the drilled section. The mineralogy and distribution of these vein types are discussed in more detail in the "Alteration and Metamorphism" section of this chapter; the mode of formation and crosscutting relationships are discussed later in this section. The majority of these veins could only be partially re-oriented (i.e., the vertical axis could be recognized from cylindrical cut marks, but the up direction could not be determined), and thus, as with the Leg 140 interval, interpretation rests largely on true-dip data. The problems of interpreting such a data set have been described by Dick, Erzinger, Stokking, et al. (1992), Newmark et al. (1985), and Newmark, Zoback, Anderson, et al. (1985).

Actinolite Veins

Actinolite is the most common vein type with 46 dip measurements recorded. Dips are variable (Fig. 47A), but maxima in dip directions occur at 20°–25° and 85°–90°. This bimodal distribution is similar to that obtained from Leg 140 (Fig. 47B).

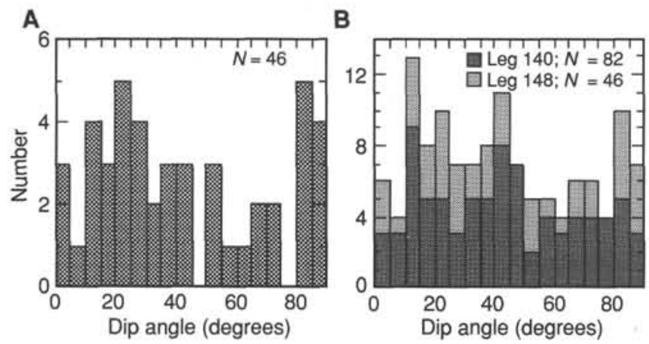

Figure 47. **A.** Dips of actinolite veins in Leg 148. **B.** Dips of actinolite veins from Leg 140 and Leg 148.

Chlorite Veins

The majority of chlorite veins are steeply dipping, (75°–90°; Fig. 48A). Most of these veins are "chlorite-coated fractures," probably formed by reopening of the veins during drilling-induced fracturing (discussed below). Only two unfractured chlorite veins were re-oriented using paleomagnetic data, and these have shallow (<25°) dips. This is in contrast to the interval drilled during Leg 140 where both moderately and shallowly dipping chlorite veins were dominantly unfractured. When plotted with the Leg 140 data (Fig. 48B), the predominance of steep dips in the Leg 148 core is evident, whereas the lower angle veins have a much more even distribution.

Minor Vein Types

Only one epidote and one quartz-chlorite-sulfide vein were observed. These have dips of 84° and 27,° respectively. These vein types are also poorly represented in the Leg 140 data set and no further comment on their orientation is possible.

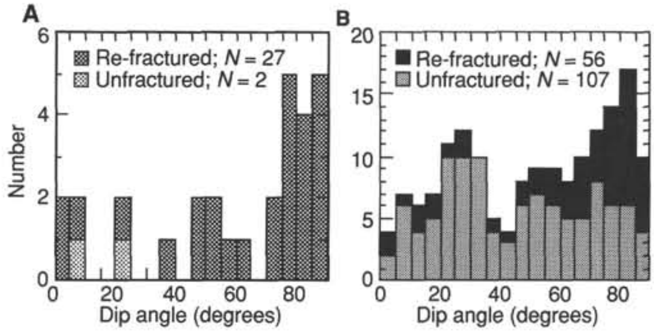

Figure 48. **A.** Dips of chlorite veins in Leg 148. **B.** Dips of chlorite veins from Leg 140 and Leg 148.

Vein Orientation

The true-dip direction has been determined using the stable paleomagnetic declination (see "Structure and Deformation" section in the "Explanatory Notes" chapter) for 13 of the veins described above. Poles to these veins have been superimposed on a Kamb contour plot of the Leg 140 data (Fig. 49). Note that this plot differs from that in Dick, Erzinger, Stokking, et al. (1992) in two ways: (1) 14 additional veins have been reoriented (Allerton et al., unpubl. data); and (2) an error in the correction for paleomagnetic inclination has been removed, producing a plot that is the mirror image of Figure 78B of Dick, Erzinger, Stokking, et al. (1992). These new vein data follow the pattern established on Leg 140 with two maxima: (1) steeply dipping, east-southeast striking (dike parallel?); and (2) generally north-northeast striking (dike normal?) and steeply-to-shallowly dipping. The former may represent dike-parallel fractures generated during dike intrusion, whereas the latter may represent shrinkage fractures formed as the dikes cooled (Dick, Erzinger, Stokking, et al., 1992).

Microstructural Characteristics

Microstructural features observed in samples from Leg 148 cores include veins, fractures and microfaults, dikelets and related chilled margins, and crosscutting relations between these structures (Table 8). In general, all the samples selected for thin-section studies have an isotropic texture with no shape fabric or preferred orientation of grains and crystals, and they display well-preserved primary (igneous) characteristics. Planar and linear anisotropy represented by crys-

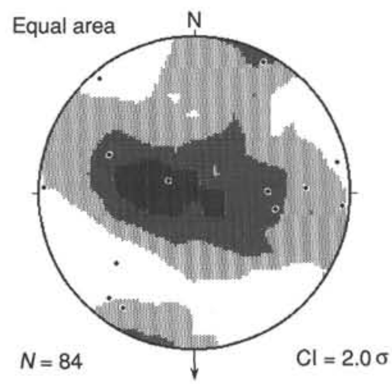

Figure 49. Poles to veins from Leg 148 (solid circles) superimposed on a Kamb contour plot of Leg 140 vein data. Arrow is the paleomagnetic reference direction used to correct the azimuths of the structural data. CI = contour interval.

Table 8. Summary of thin-section observations from representative rock samples.

Core, section, interval (cm)	Piece	Oriented	Igneous fabric	Fractures	Cataclastic fabric	Veins: Minerals	Veins: Density	Veins: Displacement
148-504B-								
239R-1, 45–51	14	No	Isotropic	Occasional fractures with no observable placement	Undeformed	Am, Ep, Zeo?	Moderate to intense	None
240R-1, 82–90	21	Yes	Isotropic	Unfractured	Undeformed	Am	Moderate	None
241R-1, 32–36	6	No	Isotropic	Moderate with no observable displacement	Hydrofracturing and incipient brecciation	Am	Occasional	None
242R-1, 28–33	9	Yes	Isotropic	Occasional fractures with no displacement	Undeformed	Am	Occasional	None
244R-1, 3–8	2	No	Isotropic	Moderate fractures with no observable displacement	Undeformed	—	None	None
245R-1, 21–24	8	No	Isotropic	Unfractured	Undeformed	Am, Ti	Moderate to intense	None
245R-1, 36–39	13	No	Isotropic	Occasional fractures with no displacement	Microbreccia along chilled margin	Am	Occasional	None
245R-1, 39–46	14	No	Isotropic	Occasional with no observable displacement	Undeformed	Am	Occasional	None
246R-1, 91–94	26	No	Isotropic	Moderate	Undeformed	Am	Moderate	None
246R-1, 111–115	32	No	Isotropic	Occasional fractures with no displacement	Undeformed	Am	Moderate	None
247R-1, 46–50	12	No	Isotropic	Occasional fractures with no displacement	Undeformed	Am	Intense	Very small (<1mm)
249R-1, 78–81	15	No	Isotropic	Occasional fractures with no displacement	Anastomozing fracturtures and incipient brecciation	Am	Occasional	No apparent displacement
249R-1, 134–138	40	No	Isotropic	Unfractured	Undeformed	Am	Moderate	None
251R-1, 28–30	5	Yes	Isotropic	Occasional fractures with no displacement	Anastomozing fractures and associated grain-size reduction	Am, Ch (?)	Occasional	None

tal orientations and preferred direction of fiber growth are confined to veins and vein margins.

Fracturing resulting from brittle deformation occurs both at macroscopic and microscopic scales and is locally pronounced in some intervals (see Deformation Log, Appendix K, and Table 8). Usually there is no observable displacement associated with fractures at either scale, and most fractures are open and unfilled. The orientation of microfractures is mostly random, although subparallel-to-parallel sets of fractures occur associated with incipient vein formation (Sample 148-504B-244R-1, 3–8 cm, Piece 2) and overlapping fractures and microfaults having step structures (Sample 148-504B-245R-1, 36–39 cm, Piece 13, and Sample 148-504B-245R-1, 39–46 cm, Piece 14). The most widespread mode of microfracturing is intracrystalline cracking in plagioclase grains, particularly near the veins and vein systems (Table 8). Fine cracks in plagioclase grains display nearly orthogonal to obliquely intersecting (50°–75°) fracture systems and are generally unfilled.

Cataclastic Zones

Three cataclastic zones have been observed in thin section. The first is associated with an amphibole-filled vein in Sample 148-504B-241R-1, 32–36 cm (Piece 6). This zone is about 1.5 mm wide and consists of fresh plagioclase and amphibole clasts, 0.1 to 0.2 mm in diameter (Fig. 50A). The clasts exhibit a sub-rectangular shape and show no evidence of dissolution. They are enveloped in a matrix composed of fine-grained plagioclase and amphibole. Based on textural relations, this cataclastic zone is interpreted to be a product of hydraulic fracturing resulting from high-pressure fluids introduced into the pre-existing vein.

The other two occurrences of cataclastic zones are associated with chilled margins. In one case (Sample 148-504B-241R-1, 78–81 cm, Piece 15) the cataclastic zone is a thin band (<1 mm) connecting an amphibole-filled vein and a thin (2 mm) portion of the chilled material. A thick (2 cm) alteration halo is developed around the chilled material and the vein. The breccia zone consists mainly of plagioclase clasts. The second occurrence of a cataclastic zone associated with a chilled margin is characterized by a 0.2-mm-thick band consisting of fine-grained and brecciated plagioclase, amphibole, and clasts of chilled material (Sample 148-504B-245R-1, 36–39 cm, Piece 13). Near the cataclastic zone, grains in the host rock appear slightly deformed, or bent. Other examples of incipient cataclasis are found in Sample 148-504B-251R-1, 28–30 cm, Piece 5, where veins converge into a braided network. Grain-size reduction of plagioclase and amphibole is significant in this sample.

Veins

The density of veins varies from "none" to "abundant", following the nomenclature defined in the "Explanatory Notes," this volume (Table 8 shows vein density in selected samples). There is no well-defined pattern to the orientation and distribution of veins and vein arrays. Most of the veins observed in the split surfaces of the recovered cores have been sampled for microscopic observations. In thin sections, veins range from 0.1 mm to about 2 mm in thickness with a maximum value of about 2.8 mm (Sample 148-504-249R-1, 87–89 cm, Piece 27). Veins are mostly planar to curvilinear; some appear sinuous (Sample 148-504B-251R-1, 28–30 cm, Piece 5; Sample 148-504B-246R-1, 91–94 cm, Piece 26) or stepped (Sample 148-504B-245R-1, 21–24 cm, Piece 80). Veins commonly abut against each other at high angles with no apparent displacements (Sample 148-504B-239R-1, 45–51 cm, Piece 14; Sample 148-504B-246R-1, 21–25 cm, Piece 8), reminiscent of the shape and morphology of T-type joints (Pollard and Aydin, 1988). Where several veins intersect, crosscutting relations are obscured by secondary fiber growth, probably formed by the crack-seal mechanism (Ramsay, 1980; Ramsay and Huber, 1983). Thinner veins generally appear to merge into larger veins in many rock samples having moderate to abundant vein density (e.g., Sample 148-504B-239R-1, 45–51 cm, Piece 14, and Sample 148-504B-245R-1, 21–24 cm, Piece 8). Some sinuous veins pinch and swell in width, and they commonly thicken along (extensional?) jogs (Sample 148-504-245R-1, 21–24 cm, Piece 8). A parallel set of very thin fractures was observed in Sample 148-504B-244R-1, 3–8 cm, Piece 2. These fractures are defined only by the linear distribution of alteration minerals replacing the igneous phases (mostly amphibole replacing clinopyroxene; Fig. 50B) and are inferred to represent incipient vein development.

Almost all the sampled veins are filled by amphibole fibers. Only a few examples of chlorite veins are present in thin sections, because most of the chlorite veins and chlorite-coated fractures occur in the exposed core surfaces (see "Alteration and Metamorphism" section, this chapter). A thin (<0.1 mm) vein filled by titanite (±amphibole) has also been observed. The titanite forms lens-shaped crystals that give the vein an irregular, sinuous shape.

The internal fabric of the veins is characterized by different orientations of the vein-filling crystals. The majority of veins are filled by

Table 8 (continued).

Core, section, interval (cm)	Cross-cutting Relations	Chilled Margins	Comments
148-504B-			
239R-1, 45–51	Merging veins; open fractures crosscutting the veins		None
240R-1, 82–90	None	None	Intracrystalline cracks in plagioclase grains; sinuous veins
241R-1, 32–36	None	None	Intracrystalline fractures in plagioclase grains near the cataclastic zone, which contains broken, fresh plagioclase and amphibole (after px) clasts
242R-1, 28–33	None	None	Planar, smooth vein; microfaulted surface with faint lineations and steps, and associated fracturing
244R-1, 3–8	None	None	* Incipient vein formation associated with a parallel set of fractures and related alteration (accompanied w/ Am growth)
245R-1, 21–24			
245R-1, 36–39	Between the Am veins and the chilled margin	Irregular, associated w/ a 0.2 mm wide cataclastic zone	Microfaulted surfaces w/ well-developed steps and slickenlines; the cataclastic zone includes lens(es) of host rock reduced in grain size
245R-1, 39–46	Two crosscutting Am veins.	None	Microfaulted surface w/ well-developed steps and slickenlines; overlapping open fractures
246R-1, 91–94	Am veins cuts across another Am vein.	None	Intracrystalline fractures in plagioclase; curvilinear to sinuous veins; pure extension
246R-1, 111–115	None	None	
247R-1, 46–50	Merging and crosscutting veins with minute displacement.	None	
249R-1, 78–81	None	Irregular, 0.8-2 mm	Complex relations of diking, fracturing, veining, and cataclasis; cataclastic zone contains mainly plagioclase clasts; chilled material includes plagioclase and px clasts
249R-1, 134–138	None	None	Intracrystalline cracks in plagioclase grains; planar and continuous veins
251R-1, 28–30	Merging veins	None	Localized foliation of vein fibers associated with vein thinning; Ch-coated fractures

Notes: The terminology is based on the nomenclature shown in Table 5 and "Explanatory Notes" chapter (this volume). Key to abbreviations: Am = amphibole, Ep = edpidote, Ch = chlorite, Ze = zeolites, Ti = titanite.

coarse-grained amphibole fibers connecting the opposite vein walls. Amphibole fibers are commonly oriented with cleavage oblique to the vein walls (Fig. 51A), and the orientation of fibers may change along the vein. This phenomenon seems to be controlled by the orientation of igneous minerals in the wall rock because the vein amphiboles are typically in optical continuity with amphiboles (replacing pyroxene) in the groundmass (Fig. 51A). Thus the shape and crystallographic fabric of the amphibole fibers reflects the orientation of the clinopyoxene in the wall rock (syntaxial overgrowth). The coarse-grained amphibole fibers in the center of the veins are generally cut and/or replaced by extremely fine-grained amphibole fibers (Figs. 51B and 51C). These fibers are generally randomly oriented, and their arrangement is not controlled by the orientation of amphiboles in the wall rock.

Vein actinolite crystals are commonly deformed, and this deformation is confined entirely to the veins. Deformation is marked by bending and kinking of the coarse-grained amphibole fibers (Sample 148-504B-239R-1, 45–51 cm, Piece 14; Sample 148-504B-250R-1, 57–60 cm, Piece 16; Sample 148-504B-251R-1, 28–30 cm, Piece 5; Sample 148-504-242R-1, 28–33 cm, Piece 9; Sample 148-504B-246R-1, 1–94 cm, Piece 26; Sample 148-504-246R-1, 111–115 cm, Piece 32; Sample 148-504B-251R-1, 28–30 cm, Piece 5). Bending has produced curved fibers that exhibit wavy extinction. Kinking is usually restricted to the coarser-sized fibers, and the sense of kinking is inconsistent along the vein (Figs. 52A and 52B). In a few samples, fine-grained fibers filling the center of the vein are sheared and foliated (Sample 148-504B-245R-1, 21–24 cm, Piece 8; Sample 148-504B-249R-1, 134–138 cm, Piece 40; Sample 148-504B-251R-1, 28–30 cm, Piece 5; Sample 148-504-249R-1, 87–89 cm, Piece 27; Sample 148-504B-247R-1, 46–50 cm, Piece 12). Shearing is inferred in a few samples, based on thin stepped veins consisting of very fine-grained, foliated fibrous amphibole associated with opaque seams (Fig. 52C). The depth and true dip of veins containing deformed amphibole fibers is summarized in Table 9. Although deformation appears to be concentrated in samples at deeper crustal levels (from 2057.2 to 2090.2 mbsf),

Table 9. Vein occurence vs. depth based on thin-section observations (compiled for oriented veins only).

Core, section, interval (cm)	Piece number	Depth (mbsf)	Top known?	Veins compostion	True dip angle (degrees)	True dip direction (degrees)	Internal fabric	Deformation
148-504B-								
239R-1, 45–51	14	2000.9	No	Amphibole	88		Fibers oblique to high angle to the walls; syntaxial fibers crosscut in the center by foliated, fine-grained amphibole fibers	Coarse-grained, syntaxial fibers curved into the foliation
					4		Random orientation of fibers	Underformed
					27			
241R-1, 82–90	21	2007.7	Yes	Amphibole	15	282	Stretched fibers oblique to parallel to the vein walls	Undeformed
241R-1, 32–36	6	2016.8	No	Amphibole	23		Syntaxial fibers nearly orthogonal to the vein walls	Undeformed
241R-1, 78–81	15	2017.3	No	Amphibole	88		Fibers oblique to high angle to the vein walls; random orientation	Undeformed
242R-1, 12–16	4	2026.0	No	Amphibole	41		Fibers nearly orthogonal to the vein walls	Undeformed
247R-1, 46–50	12	2057.2	No	Amphibole	3		Fibers oriented normal to the vein walls	Undeformed
					85		Coarse-grained fibers parallel to the vein walls; fine-grained fibers in the center	Locally deformed
					40		Fine-grained fibers	Locally deformed in the center of the vein
249R-1, 87–89	27	2072.1	Yes	Amphibole	13	306	Coarse-grained synthetic fibers along the vein walls; fine-grained fibers in the center	Deformed fibers in the center of the vein (shear?) associated with opaque seam
250R-1, 57–60	16	2081.0	No	Amphibole	31		Coarse-grained fibers parallel to the vein walls; fine grained amphibole in the center	Coarse-grained fibers, slightly bent
					32			
251R-1, 28–30	5	2090.2	Yes	Amphibole	17	98	Coarse-grained synthetic axial fibers parallel to the vein walls; fine-grained fibers in the center of the vein	Curved coarse-grained fibers; localized foliation related to vein thinning

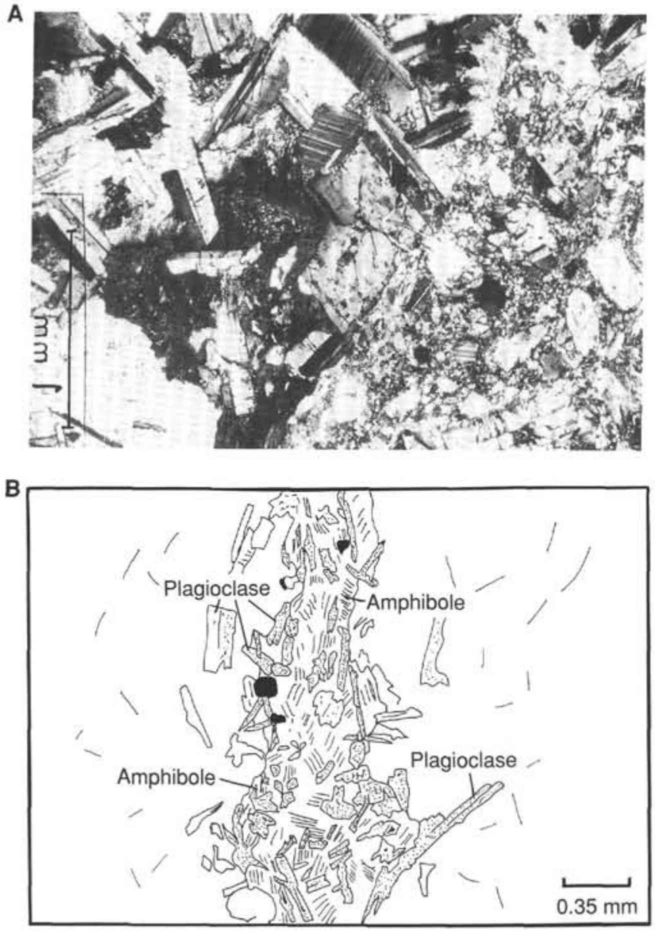

Figure 50. **A.** Vein-associated cataclastic zone containing clasts of fresh plagioclase and amphibole. Sample 148-504B-241R-1, 32–36 cm, Piece 6. **B.** Sketch illustrating the replacement of igneous phases by alteration minerals. Sample 148-504B-244R-1, 3–8 cm, Piece 2.

there is no apparent relation with vein orientation: both gently and steeply dipping veins exhibit deformed fibers. It is inferred, therefore, that deformation was probably controlled by the internal fabric of the veins: kinking and bending are strictly associated with coarse-grained fibers, whereas the fine-grained fibers were apparently weaker and thus locally underwent shearing.

Mechanism of Vein Formation

The morphology and internal fabric of the veins, and the lack of displacement across veins, suggest formation as extension fissures (MODE I fracture, Pollard and Aydin, 1988). Some of these extension veins, however, may have subsequently been affected by shear deformation as observed in several samples (Samples 148-504B-245R-1, 21–24 cm, Piece 8; 148-504-249R-1, 87–89 cm, Piece 27; 148-504B-249R-1, 134–138 cm, Piece 40; 148-504-251R-1, 28–30 cm, Piece 5). There is no clear evidence suggesting the existence of "shear veins" (Ramsay and Huber, 1983). The occurrence of intersecting T-type veins suggests that some fracture patterns may be related to thermal contraction during cooling of dikes.

The arrangement of coarse vein-filling amphibole fibers may indicate formation by a crack-seal process where veins grow by repeated hydraulic fracturing followed by precipitation of vein minerals (Ramsay, 1980; Ramsay and Huber, 1983). Typical features of crack-seal veins include fibers oriented normal to the vein wall and vein-parallel bands of wall-rock and/or fluid inclusions. The Leg 148 amphibole veins do not have the latter features, but the coarser-grained amphibole does form fibers extending across the vein. The orientation of the amphibole fibers is not uniform as in typical crack-seal veins, although they tend to be oriented at a high angle to the vein wall. This amphibole fiber orientation appears to be controlled largely by the orientation of amphibole in the wall rock (pyroxene pseudomorphs). Thus the coarse-grained fibers linking the opposite vein walls are inferred to have nucleated on wall rock amphiboles and subsequently grew away from the wall rock as the vein opened by successive crack-seal increments. In most cases the veins probably opened in a single increment. The occurrence of very fine-grained fibrous amphibole filling the center of some veins suggests re-opening of veins by rupturing of the fibers along the center of the vein rather than by cracking along the vein walls. The random arrangement of these very fine-grained fibers suggest they grew freely inside the veins with no control on their orientation by wall rock or vein amphiboles (i.e., no syntaxial growth; Cox and Etheridge, 1983).

Crosscutting Relationships

Crosscutting relationships observed in thin sections include those between veins, between open fractures and veins, and between fractures and chilled margins. Amphibole-veins cut each other in Samples 148-504B-246R-1, 91–94 cm, Piece 26, and 148-504B-247R-1, 46–50 cm, Piece 12 (Figs. 53A and 53B). In these two examples, veins filled mainly by very fine-grained fibers are younger (and generally thinner) than veins that are filled by relatively coarse-grained fibers.

In Sample 148-504B-245R-1, 21–24 cm, Piece 8, a thin vein (0.1 mm) filled by titanite (±amphibole) cuts a thicker vein (0.25 mm) filled by amphibole with no observable offset. As for the veins in the Leg 148 core in general, there are no significant shear displacements associated with the crossing veins, although a few veins show offsets of much less than 1 mm (Samples 148-504B-246R-1, 91–94 cm, Piece 26, and 148-504B-247R-1, 46–50 cm, Piece 12).

Open Fractures and Microfaults

Fractures are the dominant structures in the cores recovered in Leg 148. They consist of the following varieties: (1) open fractures; (2) chlorite-coated open fractures; and (3) striated and stepped fractures (microfaults). The first two were observed and described in detail in Leg 140, but microfaults were only recovered in Leg 148.

Structural data on fractures in Hole 504B have been studied using results of downhole logging experiments during Legs 83 (Newmark, Anderson, Moos, and Zoback, 1985; Newmark, Zoback, and Anderson, 1985) and 111 (Morin et al., 1990; Pezard, 1990). In addition, Agar (1990, 1991) studied the microstructural evolution of fault rocks and fractures in the lowermost pillow lavas, transition zone, and uppermost sheeted dikes.

Open Fractures

Most open fractures in the Leg 148 core, especially the shallow dipping ones, are logged as "thin white cracks" (TWC) as defined by Dick, Erzinger, Stokking, et al. (1992). TWC's have thicknesses <0.2 mm and are typically discontinuous, planar-to-sinuous, and commonly branching. The discontinuous nature and lack of any visible offset in thin section indicate they are incipient fractures. Well-developed fractures, with the exception of microfaults discussed below, are similar except that they are wider (up to approximately 0.5 mm), generally more continuous, and commonly form broken faces on the core.

The dips of 28 open fractures are plotted in Figure 54A, and are plotted along with those from Leg 140 in Figure 54B. Data from both sets are dominated by shallow and steep dips. Many of the shallow dips are associated with disk-shaped fractures. Core pieces are often broken along these fractures, resulting in the 2- to 6-cm-thick disks that characterize many of the pieces in the Leg 148 core. Some of the disk fractures are saddle shaped (e.g., 148-504B-246-R-1, Piece 13).

Both the disk-shaped shallowly dipping fractures and steeply dipping fractures probably formed during drilling. "Discing" fractures and

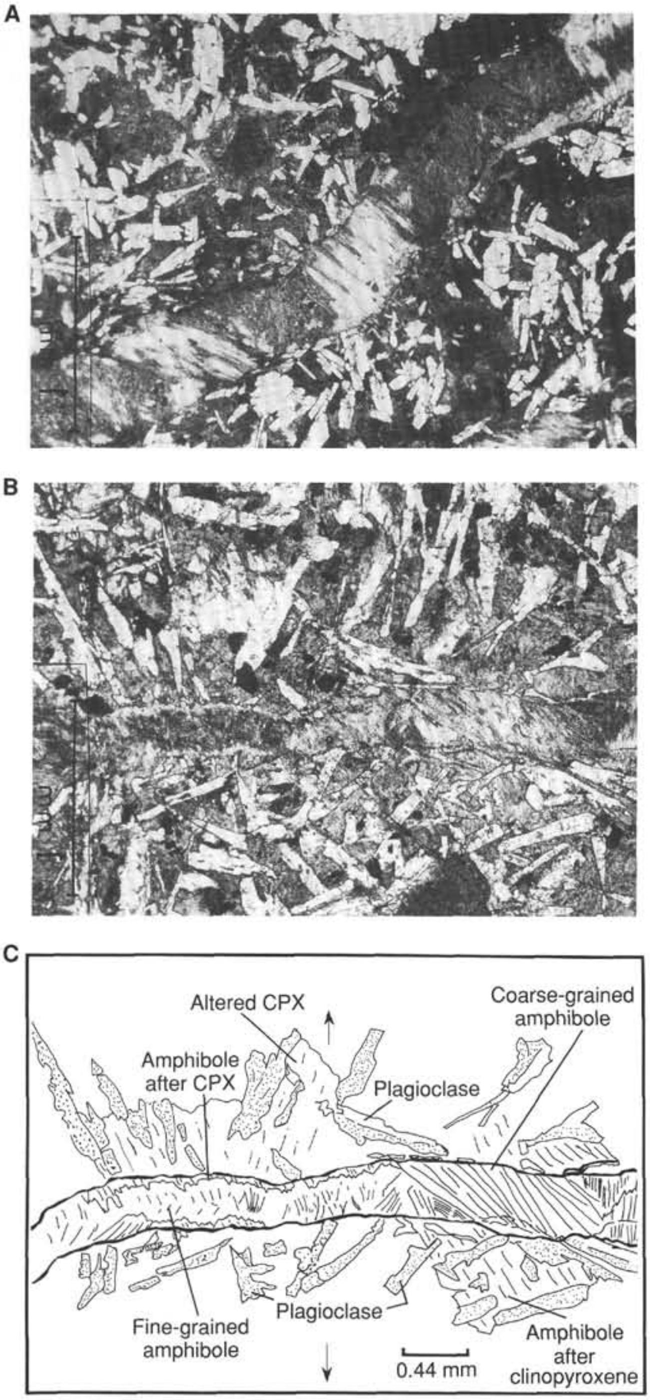

Figure 51. **A.** Coarse-grained amphibole fibers filling a vein. Fibers are oriented at high angle to the conjugate vein walls. Clinopyroxene in the wall rock is syntaxially replaced by amphibole. Sample 148-504B-240R-1, 82–90 cm, Piece 21. **B.** Coexistence of coarse- and fine-grained amphibole fibers filling a vein. Fine-grained fibers are inferred to have filled the vein after the re-opening stage. Arrows in the sketch show inferred extension direction. Sample 148-504B-245R-1, 21–24 cm, Piece 8. **C.** Sketch of B.

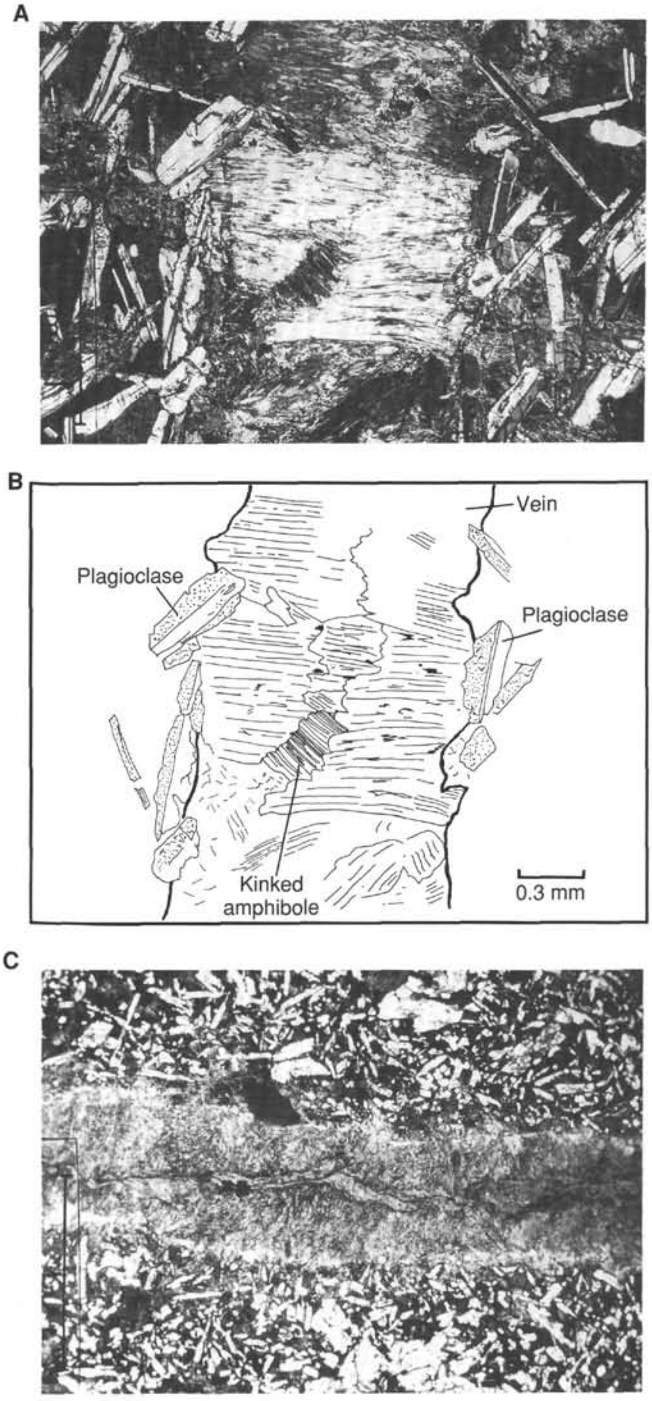

Figure 52. **A.** Kinking of coarse-grained amphibole fibers filling a vein. Arrows in the sketch point to the shortening direction. Sample 148-504B-246R-1, 111–115 cm, Piece 32. **B.** Sketch of A. **C.** Shear zone consisting of foliated amphibole fibers filling the center of a vein. Amphibole fibers are associated with an opaque seam. Sample 148-504B-249R-1, 134–138 cm, Piece 40.

associated steeply dipping "center-line" fractures are abundant below 3575 m depth in the Kontinentales Tiefbohrprogramm Bundesrepublik (KTB) holes in Germany (Wolter et al., 1990; Roeckel et al., 1992). The disks from the KTB holes show well-developed saddle-shaped morphology, and the trough axes of the disks are parallel to the maximum horizontal in-situ stress (Roeckel et al., 1992). Although disks are common in the Leg 140 and 148 core, only a few show well developed saddles, probably due to grinding as the core pieces rotate with respect to each other.

Only three open fractures have been oriented with respect to geographic coordinates using paleomagnetic techniques. They fall within the girdle defined by 55 oriented fractures from Leg 140 (Fig.

54C), which shows maxima corresponding to steep and subhorizontal fractures (note that steeply dipping fractures are under-represented because they are less likely to be encountered by vertical drilling). The girdle is symmetric to the present-day stress field (Morin et al., 1990), but the steep fractures strike at approximately 90° to the expected orientation for hydraulic fractures formed during drilling.

Thus the great majority of open fractures in the recovered core (except for microfaults) probably formed by unloading and hydraulic fracturing during drilling. Chlorite-coated fractures probably represent filled fractures in a favorable orientation to be reopened during drilling.

Microfaults

Lineated fractures (microfaults) are most abundant in Cores 148-504B-245R and -246R and are present in the two pieces comprising Core 148-504B-244R and in the single piece of Core 148-504B-253R. In addition, microfaults are abundant in angular platy pieces recovered in the junk basket following milling at 2038.2 mbsf. The abundance of microfaults in the Leg 148 core is shown in Figure 55B, where the percentage of pieces in each core having microfaults is plotted against depth. Only 3 of 14 cores contain no microfaults, which is especially significant in light of their absence during Leg 140. A zone of abundant fractures, possibly related to faulting, is suggested for 2026–2052 mbsf (Cores 148-504B-242R to -245R) by a high percentage of microfaults coinciding with low recovery (Fig. 55). A thick zone of fracturing (faulting?) is apparently present at the bottom of Hole 504B (2103–2111 mbsf), based on very low recovery (one piece containing microfaults, Core 148-504B-253R; Fig. 55), high rate of penetration during drilling, extreme borehole instability, and presence of platy pieces in the junk basket (~10%–15% of larger fragments).

Most core pieces containing microfaults are unoriented and bounded by parallel microfaults. Some of these pieces, and especially material from the junk basket at 2038 m, are platy ("foliated"). In addition to microfaults on the surfaces, the pieces commonly contain several microfaults within each piece. One fragment from the junk basket had anastomosing microfaults. Microfault spacing averages approximately 1 cm, but is on the order of a few millimeters in platy pieces. The microfault surfaces are planar and somewhat rough, and they have a faint lineation and steps (Fig. 56). The steps are smooth, and the trace of the steps on the microfaults is curvilinear but, on average, orthogonal to the lineation. The steps have a consistent sense of "offset" on an individual face, as well as on parallel faces of the same piece. In hand specimen, the microfaults consist of numerous individual lineated surfaces connected by smooth steps, similar to the "P-T" type of slickensides of Petit (1987). In thin section, the lineated surfaces can be seen to extend into the rock as cracks <0.2 mm wide; they then die out within a few millimeters. No resolvable offset is apparent along the cracks.

These lineated fractures could be interpreted as joints, in which case the lineations would represent hackle marks (Pollard and Aydin, 1988). The presence of steps oriented normal to the lineations, however, strongly suggest an origin by shearing. Thus these fractures are considered to be microfaults (or "shear joints"). They must represent incipient faulting based on the lack of polished surfaces and no resolvable displacement in thin section. They could be related to larger scale faulting, because core recovery was low in Leg 148 (Fig. 55A). More intensely faulted rocks having through-going open fractures are unlikely to survive drilling.

It was not possible to orient most of the core pieces containing microfaults because these pieces are generally small and bounded by microfaults (i.e., the cylindrical edge of the core is not preserved). The microfaults in those pieces that could be oriented are generally steeply dipping (72°–90°), but a few are subhorizontal. Slickenlines on the steeply dipping microfaults are subhorizontal in Section 148-504B-246R-1 (Pieces 12, 13, 19, and 20; 2052.6–2052.9 mbsf), whereas they are steeply plunging in Section 148-504B-241R-1 (Piece 6; 2007.1 mbsf). The latter sample was oriented with respect to geographic coordinates using paleomagnetic techniques, although it should be cautioned that there is a 10°–15° uncertainty in dip angle because paleo-vertical could only be roughly oriented: the sample is very elongate, but the cylindrical margin of the core is not present. Although little can be concluded from one sample, the strikes of these oriented microfaults are east-northeast (Fig. 57), distinct from the generally northwest strike of the steeply-dipping open fractures (Fig. 54C). Also the lineations are steep, indicating dominantly dip-slip motion.

The mode of formation of the lineated fractures is uncertain. An origin related to drilling cannot be ruled out, but the fractures are distinct from disk and center-line fractures discussed above, and they appear to have formed by shear failure rather than by hydraulic fracturing. Furthermore, the microfaults are only present in discrete horizons, whereas drilling-induced disk fractures occur throughout the core from both Legs 140 and 148. Because they are open fractures (i.e., no hydrothermal fill), they appear to be relatively young and possibly were formed by intra-plate stresses. Strike-slip earthquakes and borehole breakouts in Hole 504B indicate that the present-day minimum horizontal stress is oriented at approximately 123° (Morin et al., 1990). Some of the microfaults do show strike-slip lineations (e.g., those in Section 148-504B-246R-1), but little can be concluded from knowing their strike. More paleomagnetically oriented samples are needed, but the samples containing microfaults are rarely large enough to be oriented.

Summary

All the samples show well preserved primary (igneous) characteristics, and no shape fabric or preferred orientation of grains related to crystal-plastic deformation have been found. Observed structures include veins, microfaults, fractures, chilled margins, and rare cataclastic zones. Open fractures tend to have gentle or steep dips and probably formed during drilling. Veins are nearly all actinolite and chlorite with no clear crosscutting relations. Their orientations are very similar to those recovered in Leg 140 (Dick, Erzinger, Stokking, et al., 1992) and appear to be predominantly dike-parallel and dike-normal. The morphology and the internal fabric of the veins suggest they formed as extension fractures. Subsequent compression of some veins is indicated by kinked fibers. Shearing possibly associated with formation of very fine-grained amphibole appears to have affected some of the veins.

Microfaults are common in the core of Leg 148, though they were not observed in Leg 140 core. The microfaults are lineated and have steps, but they are discontinuous and show no resolvable displacement in thin section. The microfaults are steeply dipping, and slickenlines suggest both dip-slip and strike-slip senses of movement. Microfaults are most abundant from 2026–2052 mbsf, where recovery was relatively low. Large-scale faulting is likely from 2026–2052 mbsf and at the bottom of Hole 504B at 2103–2111 mbsf.

PALEOMAGNETISM

Paleomagnetic measurements were made of eight oriented minicores and 11 unoriented pieces sampled from core recovered during Leg 148 in order to examine the variation in magnetic properties with alteration, lithology, and depth in the crustal section. In general, the results of these measurements (shown in Tables 10 and 11) indicate that the magnetic properties of the newly drilled sheeted dikes are similar to those of the dikes sampled during DSDP Leg 83 and ODP Legs 111, 137, and 140 (Smith and Banerjee, 1986; Pariso and Johnson, 1991; Dick, Erzinger, Stokking, et al., 1992).

Natural Remanent Magnetism

The stability and direction of the natural remanent magnetism (NRM) have been studied using alternating field (AF) demagnetization techniques. Examples of orthogonal vector diagrams are included

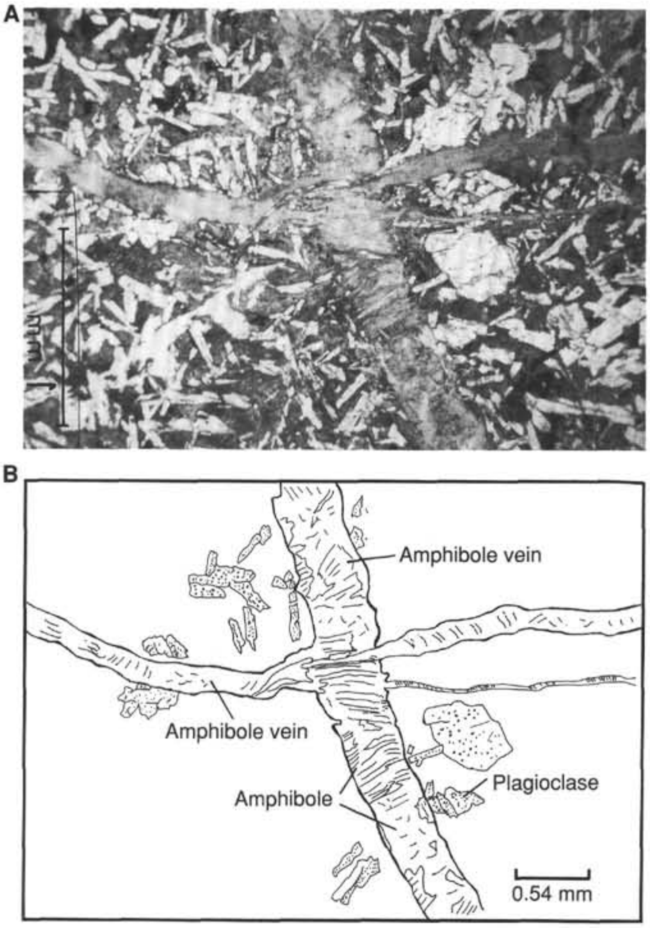

Figure 53. **A.** Crosscutting relations between amphibole veins. The fine-grained thin veins cut the wider coarse-grained vein. Sample 148-504B-246R-1, 91–94 cm, Piece 26. **B.** Sketch of A.

in Figure 58. The samples generally show a low-coercivity component below about 25 mT and a shallow-inclination stable component between 25 mT and 100 mT. The low-coercivity components have an intensity of magnetization similar to that of the stable component and are generally directed downwards, but with variable declinations. Given the low coercivity and the random direction it is likely that this component represents a viscous remanence. This behavior can be contrasted with that of the samples recovered on Leg 140 (Dick, Erzinger, Stokking, et al., 1992), which contain a component directed vertical and up with maximum coercivities of about 40 mT that was often 1 or 2 orders of magnitude stronger than the stable component. Such vertical components are often associated with rotary drilling (Ade-Hall and Johnson, 1976; Lowrie and Kent, 1978; Johnson, 1978) and are believed to be, at least in part, an isothermal remanent magnetism imparted by the drilling process (Audunsson and Levi, 1989; Pinto and McWilliams, 1990). One significant difference in the bottom-hole assembly used during Leg 148 was the use of new drill collars that had never been checked for imperfections by Magnafluxing, a process that subjects the drill collar to a large magnetic field.

The nature of the low-coercivity component is of great significance to the intensity of NRM (J_0), the Koenigsberger ratio (Q), and the median destructive field (MDF). The mean value of J_0 is 0.48 ± 0.39 A/m, compared to 3.0 A/m for the shipboard samples from Legs 137 and 140, and the mean MDF is 25 ± 15 mT, substantially higher than the value of 9.6 mT obtained from the Leg 137 and Leg 140 cores. These differences can be explained entirely by the effect of a strong drilling-induced remanence in the Leg 140 samples, without any fundamental change in the magnetic properties of the rock before it was drilled. The absence of a strong drilling-induced remanence in the Leg 148 core represents more the true in-situ NRM than does the core from Leg 137 and Leg 140. A better comparison between the cores from this and previous legs may be made by considering the intensity of the NRM at a coercivity higher than the stability of the drilling-induced remanence.

The stable magnetic inclination (I_s) values determined for Leg 148 are plotted vs. depth in Figure 59A. The mean I_s value of –1° ± 7° is similar to that observed in the upper part of the hole (Fig. 59B), although the observed range in I_s values (–9° to 15°) is considerably less, which perhaps reflects the smaller data set and the lack of a strong drilling-induced overprint. Assuming that the remanent magnetization was acquired in a geocentric axial dipole field, the predicted magnetic inclination for Site 504 is 0°. Models of secular variation (variations of the geomagnetic field with time) show that up to 17° of angular dispersion can be expected at this latitude (McFadden and Merrill, 1975). Therefore, the mean I_s value observed in Leg 148 samples falls within the range predicted by normal variations of the geomagnetic field for Site 504 and does not indicate significant tilting or rotation of the crustal section ("Structure and Deformation" section).

Induced Magnetization

Magnetic susceptibility (K) is a measure of the instantaneous magnetization induced in a sample in the presence of an external field; it is a function of composition, concentration, and grain size of the magnetic minerals within a rock. Values of K determined for Leg 148 samples are plotted vs. depth in Figure 60A and have a mean value of 0.018 ± 0.013 SI units. This is very close to the mean K value of the dikes obtained during previous legs (0.016–0.018 SI units), and, like

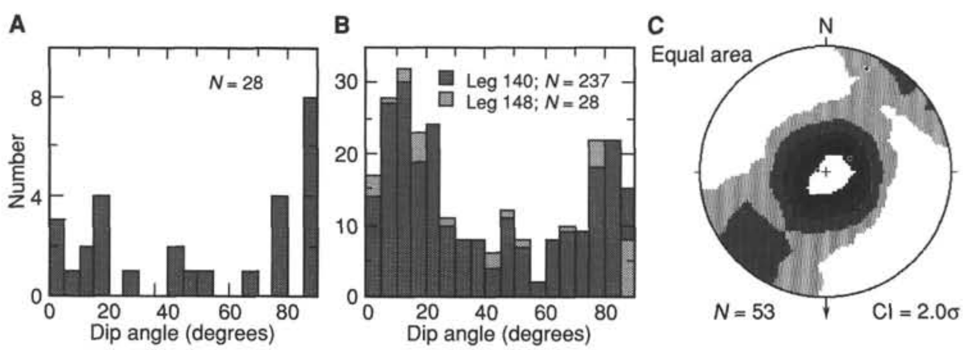

Figure 54. **A.** Histogram for true dips of fractures in Leg 148. **B.** Histogram for true dips of fractures for both Legs 140 and 148. **C.** Poles to open fractures from Leg 148 (solid circles) compared to those from Leg 140. Equal-area, lower hemisphere projection. The contoured plot of Leg 140 data is a mirror image of the same plot in Dick, Erzinger, Stokking, et al. (1992; their Fig. 78B) due to a plotting error in the latter (S. Allerton, pers. comm.).

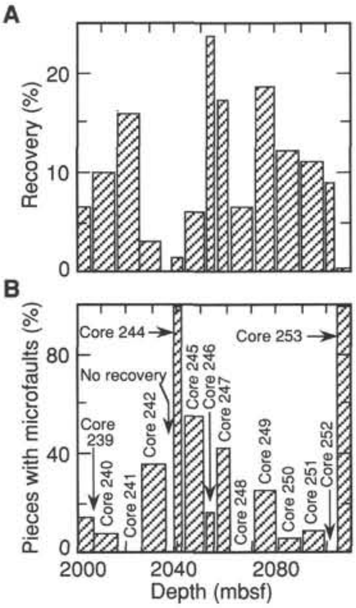

Figure 55. **A.** Histogram showing percent recovery as a function of depth. **B.** Histogram showing the proportion of pieces in each core that contain slickenlines.

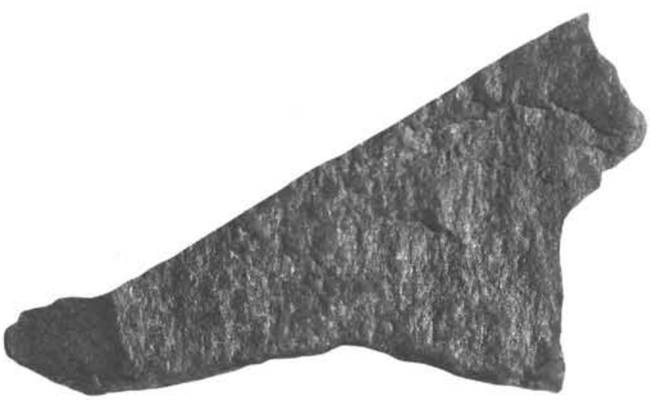

Figure 56. Microfault surface showing lineation (steep) and steps (subhorizontal). Note chilled margin parallel to the lineations on left side of sample. Sample 148-504B-245R-1, 36–39 cm, Piece 13.

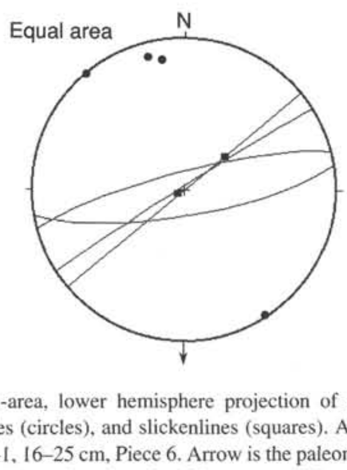

Figure 57. Equal-area, lower hemisphere projection of microfaults (great circles), their poles (circles), and slickenlines (squares). All data is for Core 148-504B-241-R-1, 16–25 cm, Piece 6. Arrow is the paleomagnetic reference direction used to correct the azimuths of the structural data.

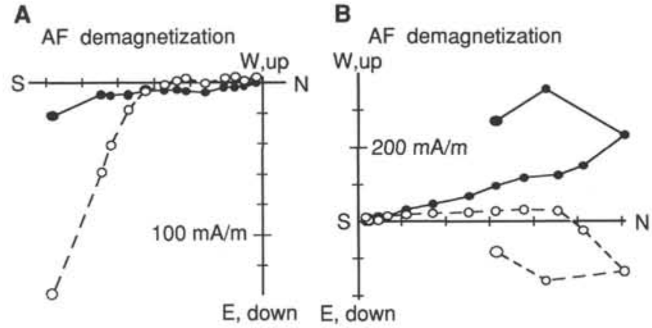

Figure 58. Orthogonal vector representations (Zijderveld, 1967) of AF demagnetization of NRM of Samples 148-504B-249R-1, 87–89 cm, and -251R-1, 49–51 cm.

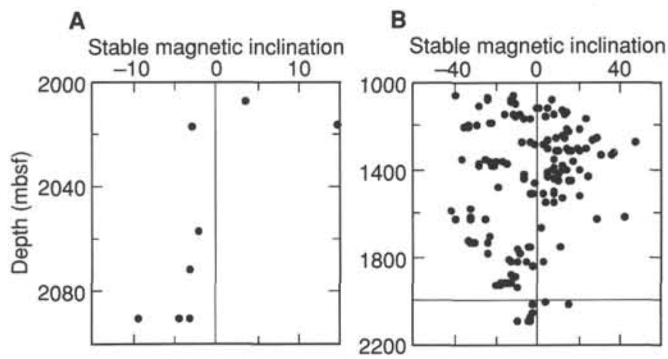

Figure 59. **A.** Stable magnetic inclination vs. depth for samples from Hole 504B cored during Leg 148. **B.** Stable magnetic inclination vs. depth (mbsf) for samples from the sheeted dike complex cored in Hole 504B.

the K values from the upper portion of the dike complex, the K values determined from Leg 148 samples are bimodally distributed (Fig. 60B). The variation in susceptibility of Hole 504B dikes was previously observed to correlate with the type of alteration experienced by opaque minerals (Pariso and Johnson, 1991). High K values are associated with primary titanomagnetite grains that experienced high-temperature, deuteric alteration, and low degrees of hydrothermal alteration. Low K values are characteristic of samples in which primary titanomagnetite grains have experienced less deuteric alteration (i.e., a higher rate of subsolidus cooling) and high degrees of hydrothermal alteration. One interpretation of these results is that samples with low values of magnetic susceptibility are characteristic of dikes that had a high initial permeability to water and thus cooled quickly and experienced extensive alteration by hydrothermal fluids.

The Koenigsberger ratio (Q) uses the ratio of J_0 and $K \times H$ to compare the strength of the remanent magnetization to that induced in the rock by the Earth's magnetic field (0.032 mT at Site 504). The mean Q value of the Leg 148 samples is 2.2, although this value is biased by a single sample with a Q of 19 because of a particularly low K. Excluding this sample gives a mean Q of 1.2. These values can be compared to a Leg 137 and Leg 140 mean Q of 6.9, which is artificially high because of the effect the drilling-induced remanence.

Rock Magnetic Measurements

The relatively low rate of core recovery on this leg made it possible to undertake a series of rock magnetic measurements of all minicores sampled for shipboard analysis. Acquisition of isothermal remanent magnetism (IRM) is a relatively rapid technique, useful in discriminating between high- and low-coercivity magnetic phases. The samples exhibited a steep gradient of IRM acquisition up to the saturation level (defined as 95% of maximum IRM intensity), after which no

Table 10. Magnetic data for samples from Hole 504B cored during Leg 148.

Core, section, top (cm)	Piece	Depth (mbsf)	NRM Dec	NRM Inc	J_o (A/m)	Dec	Inc	Delta	Low-coercivity component Dec	Low-coercivity component Inc	Low-coercivity component Delta	MDF (mT)	Bulk susceptibility (SI)	Q (at 100mT)	ARM (mA/m)	MDF of ARM (mT)	ARM/NRM (ARM at 100 mT)	Saturation IRM (A/m)	Hsat (mT)
148-504B-																			
239R-1, 26	9	2000.7			0.625								0.0229	1.07					
240R-1, 71	18	2007.6			0.105								0.0035	1.18					
240R-1, 82	21	2007.7	347.9	55.80	0.338	347.9	3.5	0.3	253.5	83.0	2.1	9	0.0205	0.65	412	12	2.45	446	130
241R-1, 16	5	2016.7	85.0	27.70	0.071	58.4	14.7	0.2	166.8	28.8	0.6	40	0.0035	0.79	208	4	3.19	150	190
241R-1, 71	13	2017.2			0.666								0.0357	0.73					
241R-1, 105	19	2017.6	177.4	–6.50	0.225	63.6	–2.9	0.3	207.3	–13.0	0.0	38	0.0237	0.37	864	11	3.93	941	90
241R-1, 139	25	2017.9			0.159								0.0023	2.77					
242R-1, 10	3	2026.0			1.147								0.0023	19.33					
244R-1, 4	2	2038.2			0.794								0.0202	1.54					
245R-1, 13	5	2042.9			1.144								0.0474	0.95					
246R-1, 12	5	2052.9			1.318								0.0260	1.99					
247R-1, 30	8	2057.0			0.168								0.0115	0.57					
247R-1, 54	13	2057.2	176.8	38.60	0.669	180.0	–2.1	0.4	174.5	52.5	0.4	8	0.0303	0.86	927	13	3.55	91	200
247R-1, 86	21	2057.6			0.304								0.0227	0.52					
248R-1, 33	10	2062.1			0.181								0.0335	0.21					
249R-1, 87	27	2072.1	169.3	49.40	0.188	170.4	–3.3	0.4	161.6	68.8	0.1	8	0.0096	0.77	308	20	1.66	26	135
251R-1, 18	4	2090.1	334.3	1.10	0.112	334.3	–3.1	0.1				40	0.0015	2.95	287	54	2.84	105	210
251R-1, 49	7	2090.4	319.2	11.20	0.432	343.7	–4.6	0.1				37	0.0207	0.82	1321	20	3.15	159	130
251R-1, 59	8	2090.5	164.8	6.30	0.567	170.1	–9.5	0.0				20	0.0080	2.76	770	34	1.37	78	175
Mean				22.95	0.485		–0.9					25	0.0182	2.15	637	21	2.77	249	158
SD				23.32	0.389		7.2					15	0.0132	4.24	394	16	0.89	307	42

Note: Declination (Dec) and inclination (Inc) are in degrees. MDF = median destructive field, Hsat = field required to produce a saturation IRM.

Table 11. Anisotropy of magnetic susceptibility (AMS) for samples from Hole 504B cored during Leg 148.

Sample (cm)	K_{mean} (SI)	K_{max} Magnitude (SI)	K_{max} Dec	K_{max} Inc	K_{int} Magnitude (SI)	K_{int} Dec	K_{int} Inc	K_{min} Magnitude (SI)	K_{min} Dec	K_{min} Inc	Lineation K_{max}/K_{min}	Foliation K_{int}/K_{min}	Anisotropy K_{max}/K_{min}	Standard error
148-504B-														
240R-1, 82–84	0.01118	0.01134	99.6	17.1	0.01115	255.5	71.4	0.01105	7.4	7.1	1.017	1.010	1.027	0.0004
241R-1, 16–18	0.00355	0.00363	99.1	5.7	0.00354	194.9	45.1	0.00349	3.5	44.4	1.025	1.014	1.039	0.0007
241R-1, 105–107	0.02549	0.02586	102.8	27.8	0.02551	266.8	61.3	0.02510	9.2	6.7	1.014	1.016	1.031	0.0005
247R-1, 54–56	0.03062	0.03124	119.6	35.6	0.03064	258.2	46.3	0.02998	13.0	21.8	1.020	1.022	1.042	0.0003
249R-1, 87–89	0.01036	0.01083	115.7	50.6	0.01036	281.3	38.5	0.00989	17.0	7.1	1.045	1.048	1.095	0.0005
251R-1, 18–20	0.00148	0.00149	288.7	5.1	0.00148	19.8	12.5	0.00146	177.0	76.5	1.007	1.012	1.019	0.0014
251R-1, 49–51	0.02206	0.02231	140.8	3.2	0.02215	50.4	5.8	0.02173	260.0	83.4	1.007	1.019	1.027	0.0008
251R-1, 59–61	0.00881	0.00890	338.5	5.7	0.00885	68.8	2.7	0.00868	184.2	83.7	1.005	1.020	1.025	0.0006

Note: K_{max}, K_{int} and K_{min} are the maximum, intermediate and minimum principal axes of AMS, respectively. Declination (Dec) and inclination (Inc) are in degrees.

significant increase in intensity was noted with increasing applied field (Fig. 61). Samples saturated in fields between 90 and 200 mT, indicating the predominance of magnetite and/or titanomagnetite, suggest the presence of additional, higher coercivity minerals.

Comparison of the acquisition and subsequent AF demagnetization of anhysteretic remanent magnetism (ARM) with the AF demagnetization of the NRM can provide valuable information on the origin of the NRM (Fig. 62). ARMs were acquired in direct fields of 0.032 mT, a field similar to the present Earth's field at Site 504, and alternating fields up to 100 mT. In all cases the shape of the ARM demagnetization curve was similar to that of the NRM, but the ARM intensity after 100 mT of AF demagnetization was always greater than the initial NRM intensity.

Anisotropy of Magnetic Susceptibility

Measurements of the anisotropy of magnetic susceptibility (AMS) have been made of the minicored samples from the Leg 148 Hole 504B core. Although the recorded anisotropies (K_{max}/K_{min}) are low, ≤ 4%, except for Sample 148-504B-249R-1, 87–89 cm, which had an anisotropy of 9%, the recorded errors are much smaller (Fig. 63), and the measurements are highly repeatable. The orientations of the AMS ellipses have been reoriented using the stable component of magnetization, assuming that this direction was approximately south-directed, as rocks at Site 504 are believed to have formed during a reversed magnetic epoch. The orientations of the fabrics fall into two groups (Fig. 64). In the samples from the first group, the minimum axes of magnetic susceptibility (K_{min}) are approximately horizontal and north directed, and the maximum axes (K_{max}) are oriented between horizontal and dipping about 50° to the east. The samples from the second group, all from Unit 293, are more dominantly oblate and have K_{min} axes which are nearly vertical, and dispersed K_{max} directions. Numerous studies have established that the AMS ellipsoid is an image of the preferred orientation of magnetic minerals in the rock (Hrouda, 1982). Two dike margins preserved in the Leg 140 core reoriented using the stable magnetic declination strike 94° and 74°, and dip 79° and 84° to the north, respectively. Thus for the first group, the foliation approximately parallels the dike margin, and the lineation is in the plane of the dike. This group can be interpreted to be the result of flow during the intrusion of the dike (e.g., Ellwood, 1978; Knight and Walker, 1988; Rochette et al., 1991). This would suggest that the dike emplacement was dominantly lateral rather than vertical in this limited data set. The second group has a horizontal foliation and no dominant lineation direction, which may result from settling of minerals after flow had been completed. Another possibility is that the magnetic fabric is controlled by external stress, as has been argued for the core recovered from Hole 896A (see below).

PHYSICAL PROPERTIES

Physical properties, including wet-bulk density, compressional wave velocity (V_p), thermal conductivity, and electrical resistivity were

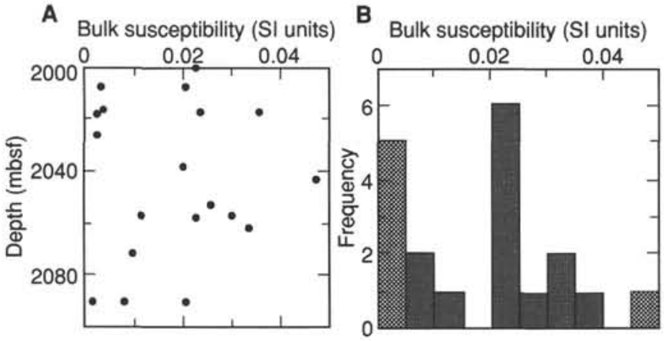

Figure 60. **A.** Bulk magnetic susceptibility (SI units) versus depth for samples from Hole 504B cored during Leg 148. **B.** Histogram of bulk magnetic susceptibility (SI units) for samples from Hole 504B cored during Leg 148.

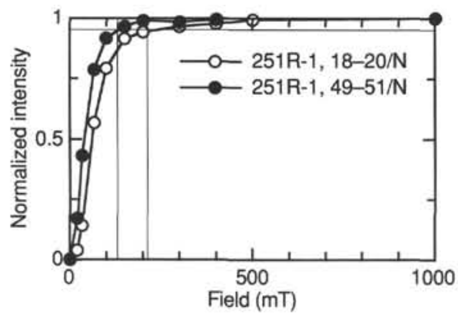

Figure 61. Intensity of IRM (normalized by the maximum intensity at saturation) against applied field (mT). Sample 148-504-251R-1, 18–20 cm, is highly altered, and includes a small, high-coercivity component. Sample 148-504-251R-1, 49–51 cm, from the same unit but much less altered, saturates at a lower field.

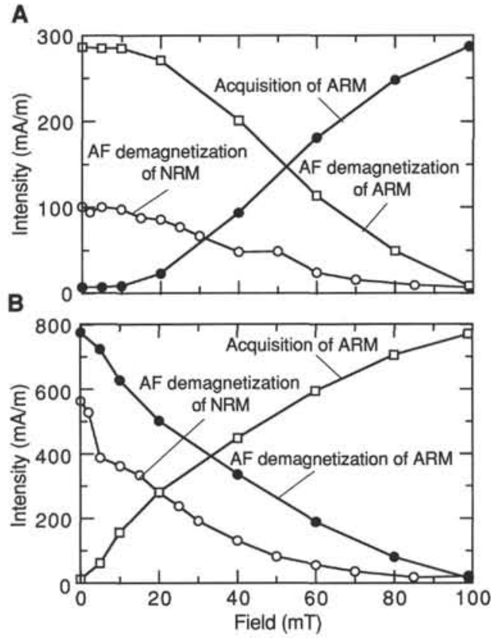

Figure 62. Plot of intensity of magnetization vs. applied AF field (mT), for NRM demagnetization, ARM acquisition, and ARM demagnetization. **A.** Sample 148-504-251R-1, 18–20 cm. This sample is highly altered, and acquisition of ARM indicates a predominance of high-coercivity material. **B.** Sample 148-504-251R-1, 59–61 cm. This sample is from the same unit as the sample shown in A., but exhibits a much lower degree of alteration. Acquisition of ARM indicates a component of low-coercivity material, probably multidomain magnetites, apparently absent from the more altered sample.

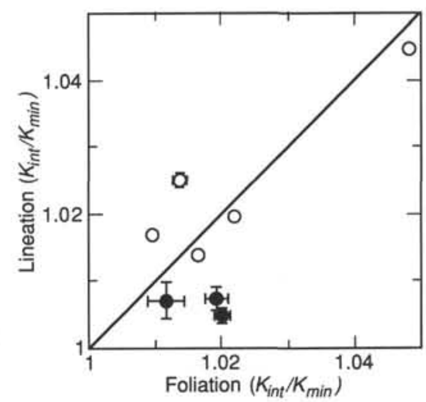

Figure 63. Anisotropy of magnetic susceptibility; Lineation (K_{max}/K_{int}) vs. foliation (K_{int}/K_{min}) for samples from Hole 504B cored on Leg 148. Data are separated into the two groups described in the text. First group are open circles; second group are filled circles. Error bars are 2 × standard error.

measured on selected water-saturated samples to establish a database for calibrating logging results and to assess changes in the physical properties of the crust as a function of depth. Porosities and grain densities were calculated for the same samples from the differences between wet and dry weights, and formation factors were calculated from measured resistivities, assuming a pore fluid (seawater) resistivity of 0.20 Ωm at room temperature (Table 12). Although poor recovery prevented more detailed studies of most properties, additional density measurements were made on irregular dike samples to investigate changes in density with grain size, mineralogy, and alteration.

Bulk densities were determined for eight minicores and 18 irregular dike pieces. The minicores were weighed both wet and dry to determine porosity. The irregular samples were not oven-dried and were only used for bulk density. Although there may have been some partial dehydration of the diabase samples while they were exposed to room temperature on the sampling table, these samples do not exhibit markedly different bulk densities than saturated minicores kept stored in water (Fig. 65).

The bulk density and porosity data compiled from previous Hole 504B studies are plotted with Leg 148 data in Figure 66 (Karato, 1983; Wilkens et al., 1983; Christensen and Salisbury, 1985; Christensen et al., 1989; Shipboard Scientific Party, 1983, 1985, 1988, 1992a, b; Iturrino et al., in press). Densities measured on Leg 148 are between 2.88 and 3.05 g/cm^3, with most greater than 2.90 g/cm^3. Porosities vary from near 0% to 5%. Both densities and porosities of the samples are generally concordant with trends of increasing density and decreasing porosity with depth seen in the earlier data, although porosity shows considerable scatter. The lowest density (highest porosity) sample (148-504B-251R-1, 19–22 cm) is a minicore with a prominent actinolite-filled vein. Fluctuations in bulk density between 2.95 and 3.05 g/cm^3 may reflect relative abundances of primary olivine or the amount of sample alteration.

Due to size requirements, velocity measurements were limited to the eight minicores for which other properties were determined. All measurements were made at room temperature and pressure using the Hamilton Frame velocimeter. As can be seen in Figures 65 and 67, the compressional wave velocities of the diabase samples recovered on Leg 148 range from 5.4–6.0 km/s. The measured velocities show no trend with increasing density for the Leg 148 samples and decrease with increasing density in the sheeted dikes from about 1300 mbsf to the

Table 12. Physical properties of samples collected from Hole 504B

Core, section, interval (cm)	Depth (mbsf)	Bulk density (g/cm^3)	Grain density (g/cm^3)	Porosity (%)	Vp (km/s)	Thermal conductivity (W/[m · K])	Resistivity (Ωm)	Formation factor
148-504B-								
239R-1, 27–30	2000.67	3.00						
240R-1, 72–75	2007.62	2.90						
240R-1, 82–85	2007.72	2.94	2.94	0.2	5.55		112.2	561
241R-1, 16–19	2016.66	2.90	2.95	2.9	5.96	2.03	126.7	633
241R-1, 71–74	2017.21	2.96						
241R-1, 105–108	2017.55	2.95	2.97	0.8	5.42	1.95	148.7	743
241R-1, 139–142	2017.89	2.93						
242R-1, 10–13	2026.00	2.99						
244R-1, 4–7	2038.24	3.02						
245R-1, 13–16	2042.93	3.04						
245R-1, 33–36	2043.13	3.00						
245R-1, 54–57	2043.34	3.00						
246R-1, 11–14	2052.31	2.98						
246R-1, 45–48	2052.65	2.98						
246R-1, 82–85	2053.02	2.96						
246R-1, 110–113	2053.30	2.92						
247R-1, 30–33	2057.00	2.96						
247R-1, 54–57	2057.24	2.98	3.00	1.0	5.83	2.15	145.4	727
247R-1, 86–89	2057.56	2.98						
248R-1, 33–36	2062.13	2.95						
249R-1, 9–12	2071.29	2.98						
249R-1, 87–90	2072.07	2.88	2.98	5.0	5.38	2.04	87.6	438
249R-1, 102–105	2072.22	3.01						
251R-1, 18–21	2090.08	2.91	2.96	2.3	5.82	2.19	263.3	1181
251R-1, 49–52	2090.39	2.98	3.00	0.6	5.69	2.21	197.3	986
251R-1, 59–62	2090.49	2.97	2.98	0.7	5.70	2.24	151.9	759

base of the hole, in violation of Birch's Law (Birch, 1961). We attribute the former discrepancy to the inherent scatter of velocity measurements made at room pressure, the latter to the opening of microcracks during decompression as the rocks were brought to the surface.

Thermal conductivity measurements were made on the archive halves of seven of the eight samples selected for other physical property studies (Table 12). The samples were stored in seawater and polished prior to measurement. All measurements were made using the half-space needle probe technique after careful calibration against rubber, macor, and basalt standards. As shown in Figure 67, the thermal conductivities of the Leg 148 samples range narrowly between 2.0–2.2 W/(m · K), in excellent agreement with the values obtained on similar material higher in the sheeted dikes between 950–1550 mbsf on Legs 83 and 111 (Shipboard Scientific Party, 1985, 1988).

The electrical resistivities of the eight minicores sampled from the 2003 to 2104 mbsf interval were measured at room temperature (20°C) and atmospheric pressure. The samples were kept saturated with seawater and measured using a 1 V current with a frequency of 50 Hz, similar to that used for downhole measurements.

With values between 80 and 250 Ωm (Table 12 and Figure 65), the present measurements appear similar to those recorded higher up in the dikes and in massive units of the volcanic section (e.g., Units

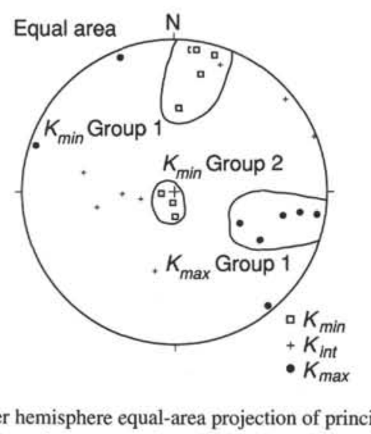

Figure 64. Lower hemisphere equal-area projection of principal axes of magnetic susceptibility anisotropy, reoriented using the stable remanence direction.

27 and 34; Pezard, 1990). The mean formation factor is on the order of 750. No particular trend between formation factor and depth, magnetic susceptibility, or V_p may be noticed from the dataset.

For most samples, a positive correlation appears to hold between formation factor and actinolite content. The sample with the most altered groundmass (148-504B-251R-1, 18–21 cm, with up to 70% actinolite measured in a nearby thin section) and the lowest magnetic susceptibility, has the highest electrical resistivity (236.3 Ωm). On the other hand, Sample 148-504B-249R-1, 87–90 cm, which contains a 1-mm-wide and minicore-parallel (hence sub-horizontal) actinolite vein, shows the lowest electrical resistivity. The presence of actinolite, either distributed in the groundmass or in veins, appears to lead to different electrical conductivity behavior.

DOWNHOLE MEASUREMENTS

Introduction

Leg 148 downhole measurements in Hole 504B were conducted in two phases. The first phase occurred immediately after the initial reentry of the hole and was aimed at recording a temperature log and sampling borehole fluids before any disturbance caused by subsequent coring operations. The second phase was a full logging program planned for the end of the leg, including Schlumberger geophysical and Formation MicroScanner (FMS) logs, a three-component magnetometer log, a borehole televiewer log, a vertical seismic profile (VSP), and packer experiments. The tools and methods for these downhole measurements are described in the "Explanatory Notes" chapter of this volume.

Coring was terminated in Hole 504B before the end of the leg, and the planned post-drilling logging was conducted after fishing operations with the hole at a total depth of 2111 mbsf. The geophysical, FMS, and magnetometer logs were run over the entire basement section. Because of instrumental problems no BHTV images were recorded and four attempts were made to record the VSP before success was achieved. Time allocated for packer measurements at Hole 504B was transferred to Hole 896A ("Site 896" chapter, this volume). This chapter includes summaries of the downhole measurements operations and preliminary results, and is divided into four sections that correspond to the measurements successfully conducted in Hole 504B: temperature log, Schlumberger logs, magnetometer log, and VSP.

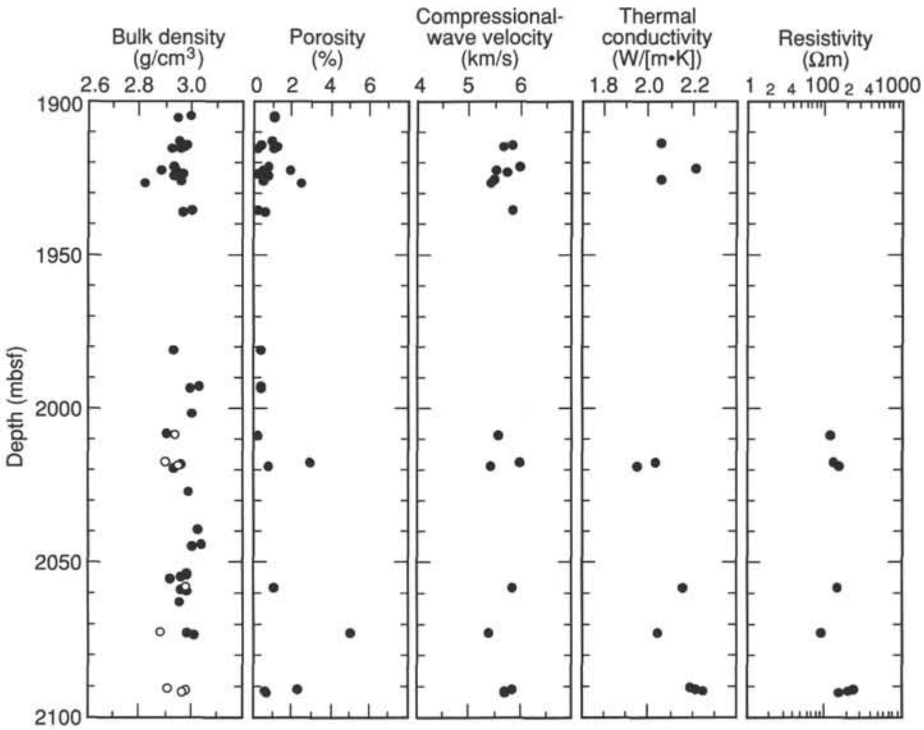

Figure 65. Wet-bulk density, porosity, compressional wave velocity (V_p), thermal conductivity, and resistivity of Leg 148 samples vs. depth in Hole 504B. Densities of minicore samples shown as open circles. Leg 140 data from 1900–2000 mbsf shown for comparison.

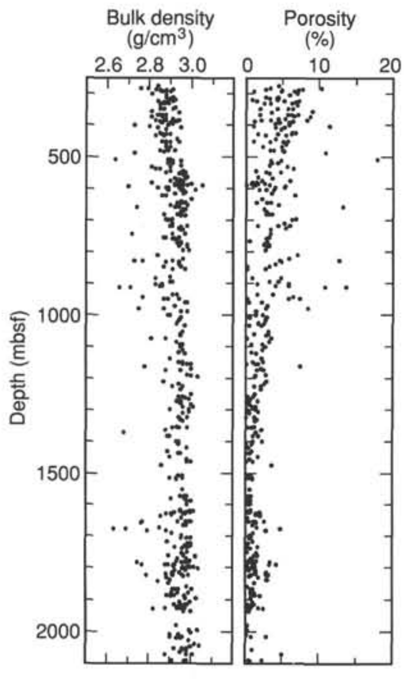

Figure 66. Wet-bulk density and porosity vs. depth in Hole 504B.

Initial Temperature Logging

Leg 148 provided a new opportunity to log equilibrium temperatures in Hole 504B, because 14 months had passed since the last thermal disturbance to the hole during Leg 140. Similar undisturbed temperature profiles had been obtained after the previous reentries of Legs 70, 83, 92, 111, 137, and 140 (Becker, Langseth, Von Herzen, 1983; Becker, Langseth, Von Herzen, Anderson, 1983; Becker et al., 1985, 1989, 1992; Becker, Sakai, Adamson, et al., 1989; Gable et al., 1989; Dick, Erzinger, Stokking, et al., 1992); thus, the Leg 148 temperature log represented the latest in a series of studies extending to greater and greater depths over a period of 14 yr. Major objectives of the Leg 148 measurements included resolving the previously observed reduction of heat flow with depth in the hole and the puzzling temperature variations in the upper part of the hole.

Temperature-logging Equipment

The equipment used for temperature logging was essentially the same as that used during Legs 111, 137, and 140 (Gable et al., 1989; Becker et al., 1992), except for the use of different sensors. The French BRGM downhole probe is a cylinder made of stainless steel, 60 mm in diameter, and 3-m long, weighing 50 kg. The temperature sensors are accurately calibrated thermistors housed in a 5-mm-diameter tube at the lower end of the tool. Temperatures are determined from the resistance of two thermistors that can be monitored separately or in combination for maximum sensitivity across the entire logged interval. Unfortunately, the failure of one of the thermistors at mid-run did not provide this sensitivity in the lower part of the hole. The control unit, monitored with a personal computer with an interface panel and a programmable precision voltmeter, records through the wireline the measured resistances across each thermistor. During logging the depth, the two resistances (individually and in series), and the calculated temperature are displayed and recorded every 10 cm.

The sensors were calibrated at the Laboratoire National de Mesures in Paris. The temperature-resistance calibration data were fit to the standard function for thermistor resistance:

$$1/T\ (K) = A + B\ln(R) + C\,[\ln(R)]^3. \quad (1)$$

The coefficients A, B, and C used for the different ranges of temperatures to convert resistance values (R) into temperatures are given in Table 13.

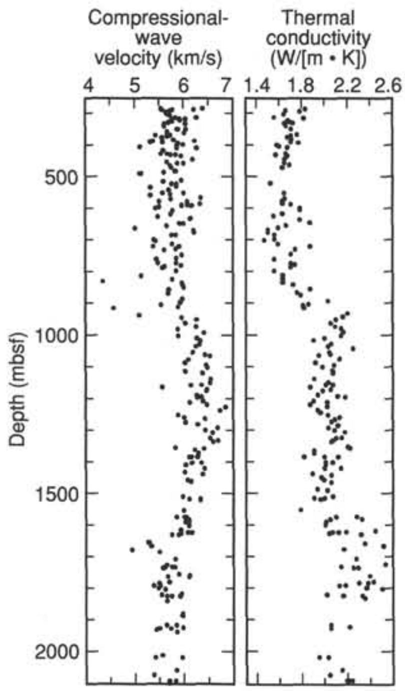

Figure 67. Compressional-wave velocity (V_p) and thermal conductivity vs. depth in Hole 504B.

As the resistance of each thermistor decreases substantially with increasing temperature, the two thermistors have to be used in series for high-temperature measurements. This increases the measured resistance, which is then much higher than the resistance of the wireline. After the log was run, the failure of one of the thermistors required correction of the measured resistance values for the resistance of the wireline and the variation of this resistance with temperature, which were no longer negligible compared to the measured values. This was accomplished knowing the resistivity of the copper conductors at 300°K (3.41×10^{-2} Ω/m), and the temperature coefficient of resistivity (3.9×10^{-3} K^{-1}). To check the behavior of the surviving thermistor, it was retested after the log (in ice-water at 0°C or 273°K), and it indicated a satisfactory value of 325.0 kΩ.

Logging Procedure

The probe was run with a sinker bar attached around the wireline. The tool signal shorted out at 300 m below rig floor (mbrf); the tool was flooded with seawater when it resurfaced. During replacement of the wet sensor and the O-rings, the water sampler was run to a depth of 310 mbsf. About 5 hr after the first attempt, the temperature log proceeded from the seafloor to 1975 mbsf.

The temperature tool was slowly run into the borehole at a logging speed of 2 m/min through the pipe, then at 4 m/min to 3900 mbrf where it was increased to 8 m/min. By mid-run, the signal recorded by one of the thermistors became erratic, and the last part of the logging was made with the remaining thermistor, without the accuracy of the two thermistors in series. At final depth, about 25 m above total depth, the measured temperature was 180°C.

The delay at the beginning and the necessity to come out slowly in order to minimize the mixing of the fluids in the hole for the following fluid sampling reduced the allocated logging time and eliminated the stationary measurement initially scheduled at the bottom of the hole and just above seafloor.

Temperature Profile and Geothermal Gradient

The temperature log measured during Leg 148 is illustrated in the composite log of Figure 68, which includes the previous temperature

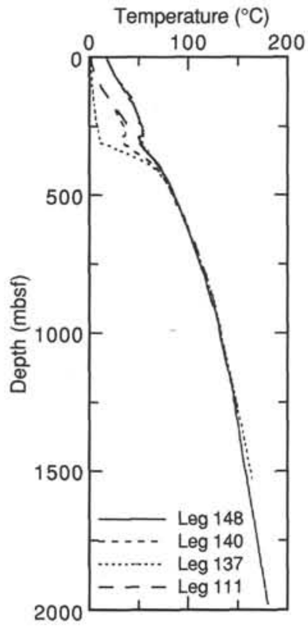

Figure 68. Temperature logs in Hole 504B measured during Legs 111, 137, 140, and 148.

logs measured during Legs 111, 137, and 140. Unexpectedly high temperatures were observed from the seafloor to approximately 250 m. These temperatures cannot be explained by the disturbance created by the single fluid sampler run and would suggest poor calibration of the sensor or acquisition system at these temperatures. Independent of this anomaly, the trend shown by the profile in this section is the same as that observed during Leg 140, which indicates some hydrothermal activity in the upper levels of the basement that seem to be recovering from the cooling observed during Leg 137.

Below 400 mbsf the measured temperatures closely resemble those measured during Legs 111 and 137. Linear portions of the profile have a gradient of 116°C/km above 800 mbsf and 61°C/km from 800 to 1200 mbsf. Below 1200 mbsf the gradient decreases again to 49°C/km, differing slightly from the Leg 137 trend. The profile is linear to the bottom of the hole, where the temperature reaches a recorded maximum of 180°C.

Schlumberger Logging

Run 1: Geophysical Combination (SDT/DLL)

Logging started with the geophysical combination consisting of the acoustic velocity array sonde (SDT) and the dual laterolog (DLL) resistivity sonde. The tool was lowered to the bottom of the hole and run successfully from 2078 to 275 mbsf. The logging speed was held to 400 m/hr in order to improve the sonic data quality. The log collected excellent resistivity and sonic data throughout the hole. The resistivity data proved to be extremely repeatable with respect to data recorded during Legs 111 and 140 in the upper part of the hole, and the quality of the acoustic waveforms is excellent.

Table 13. Calibration coefficients for the sensor used during the temperature log.

Temperature range (°C)	A	B	C
0–>60	0.0008296863580	0.00021116754438	7.519747444e^{-8}
60–>120	0.0008617088449	0.00020558313422	9.834128654e^{-8}
120–>200	0.0008642612881	0.00020609753964	1.007971614e^{-7}

Data Analysis

Resistivity data recorded with the DLL in the lower 500 m of the hole show a continuous increase of the electrical resistivity of Layer 2C basalts to 6000 Ωm near the bottom of the hole (Fig. 69). While the increase is somewhat gradual to 1400 m, it tends to proceed in a step-like fashion at greater depths, with abrupt decreases of the electrical resistivity between the steps, such as near 1450, 1700, and 1900 m. In the lower 300 m of the hole, the large difference between the shallow (LLs) and the deep (LLd) measurements can be attributed to hole conditions affecting the shallow value. This effect will be corrected post-cruise.

Compressional-wave velocity log data have been plotted against depth below seafloor in Figure 70. Added to the figure are sample velocities measured in the laboratory at 100 MPa confining pressure (Wilkens et al., 1983; Christensen and Salisbury, 1985; Christensen et al., 1989; Iturrino et al., in press). With the exception of several local excursions, velocities in basement generally fall between 4.5 and 5.5 km/s above 1100 mbsf. Between 1200 and 1700 mbsf, behavior of the velocity log is fairly regular with velocities varying within a narrow range of 6.0 to 6.5 km/s. A uniformly fast unit (V_p = 6.5 km/s) approximately 100-m thick extends from 1700 mbsf to 1800 mbsf. Beneath this unit velocities drop abruptly and then increase gradually. At the lowermost depths (2060 mbsf) the compressional wave velocity reaches 6.8 km/s.

At the top of basement, differences between laboratory values and in-situ measurements (Fig. 70) result from the scale of measurements. Laboratory samples may be representative of material making up the framework of the formation, but macroscale structure (i.e., fractures, pores) reduce the in-situ velocity. In-situ and laboratory velocities converge as depth of recovery of the samples increases. Agreement between laboratory and well-log velocity is particularly good within the coherent interval between 1700 and 1800 mbsf. High resistivity in this interval (Fig. 69) supports the assumption that few fractures exist between these depths.

The velocity of 6.8 km/s in the bottom of the hole is intriguing. Clearly most of the lower part of Hole 504B falls within the upper velocity range of seismic Layer 2B (6.5 km/s; Houtz and Ewing, 1976). However, 6.8 km/s is a Layer 3 velocity. This velocity was recorded in what appears to be relatively fresh, fine-grained diabase dikes, suggesting, though not proving, that the transition between seismic Layers 2 and 3 in the ocean crust need not coincide with a basalt-gabbro transition.

Run 2: FMS Electrical Images—Natural Gamma

The Formation MicroScanner (FMS) produces high-resolution borehole images, and thus allows for visual characterization of the structures located in the near vicinity of the borehole wall (Ekstrom et al., 1986). The natural gamma sonde was also included in this run for depth correlation purposes.

The FMS was lowered to the bottom of the hole, and recording started at 2080 mbsf at a logging speed of 600 m/hr. After 20 m of recording, the downhole sensor became stuck, perhaps on a ledge, and the sonde had to be closed in order to pass through the smaller hole diameter interval. The recording resumed at 2056 mbsf and continued to 1885 mbsf where a second ledge was encountered. One of the electronic channel multiplexers in the sonde failed near 2056 mbsf, probably because of high temperatures, and good data from only three pads were recorded above that. The tool encountered two more ledges during recording at 1098 mbsf and 995 mbsf. The data above 1856 mbsf were broken into three segments covering the following intervals: 1856 to 1098 mbsf, 1090 to 995 mbsf, and 977 to 293 mbsf. Attempts at recording data across ledges were avoided in order to minimize the risk of damage to the downhole sonde. The faulty multiplexer later revived within the upper basement and above seafloor, inside the drill pipe (with a surrounding temperature of 2°C), indicating that high temperatures encountered in the lower part of the hole caused the tool failure.

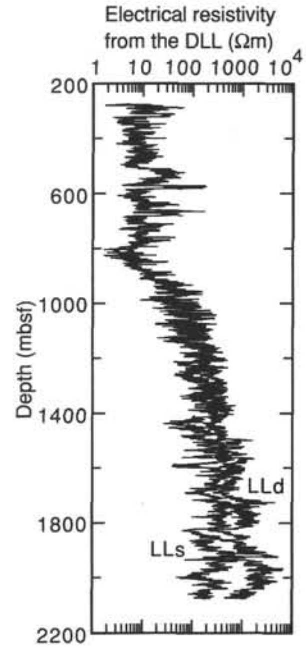

Figure 69. Electrical resistivity measurements in Hole 504B. Both deep (LLd) and shallow (LLs) logs are shown. The large differences between the logs at the bottom of the hole (where LLd > LLs) are borehole effects.

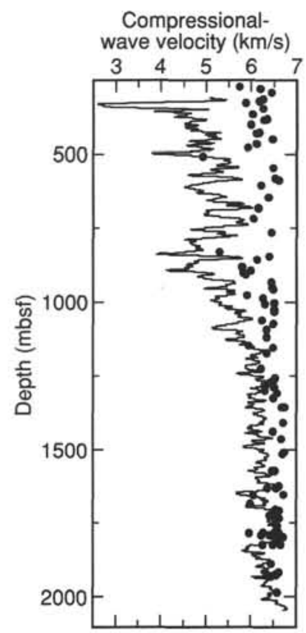

Figure 70. Compressional-wave velocity log from Hole 504B. Individual dots are velocities measured in laboratory samples at 100 MPa confining pressure.

FMS Analysis

The initial processing of the raw FMS data into electrical images was carried out aboard ship during Leg 148 using proprietary Schlumberger software on the L-DGO VAX 3100 workstation. The electrical images were transformed into resistivity maps of the borehole wall using the calibrated shallow-laterolog (LLs) measurements obtained during the preceding run.

The size, shape, and borehole deviation with respect to north can be described from data recorded by the calipers and within the inclinometry section of the FMS. From the top of the basement to the present total depth, Hole 504B tends to deviate to the north-east, with some sections trending more to the east (Fig. 71). The hole deviation from vertical is generally under 6°, with values under 2° from 600 to 1400 mbsf. Below 1880 mbsf, deviation increases steadily down to about 1930 m where it abruptly starts to decrease (Fig. 72). The hole diameter measured by the FMS is large in the upper part of the hole (from the casing shoe down to 1000 mbsf) and generally less than 30 cm below 1500 mbsf. In the latter interval, a few narrow intervals and a 70-m-long section near 2000 mbsf are characterized by the presence of breakouts, with values of the long axis of the borehole more than 35 cm. This long ovalized interval near the bottom of the hole might be the source of the large number of angular, planar pieces of fragmented diabase recovered in the core.

The presence of an elliptical borehole shape generally indicates the existence of breakouts (Bell and Gough, 1979), with the long axis of the borehole pointing toward the minimum horizontal stress direction. From the analysis of BHTV acoustic data and images of the borehole wall in the upper part of the hole, Morin et al. (1990) derived a main mode of ellipticity pointing 122° from north, which was proposed to be the minimum horizontal stress direction. A second less important, but exactly orthogonal, mode of enlargement was also found. It was attributed to thermal fracturing related to the cooling of the hole due to circulating cold seawater during drilling.

The two caliper measurements obtained with the FMS show a similar bimodal distribution of enlargements, with similar azimuthal orientations at about 015°N and 115°N (Fig. 73). Elongation azimuths (ELAZ) with caliper differences larger than 0.7 in., 1.5 in., and 2.5 in. are plotted against depth in Figure 73. While the depth-azimuth plot does not define these directions very well, histograms of these distributions provide much clearer descriptions of these directions (Fig. 74). The ELAZ filtered at 1.5 in., an intermediate value for the cut-off in the difference between the two caliper sizes, best defines the changes in the occurrence and orientation of breakouts in the hole (Fig. 73).

In the upper part of the basement, the ellipticity rotates from a 160°N direction near 300 mbsf, to 020°N at 500 mbsf at the top of a resistive zeolite-rich alteration zone in the volcanic section (Fig. 64). Throughout this zone and the underlying massive flow corresponding to lithologic Unit 27 (at 575 mbsf), the ellipticity direction remains stable at 020°N. Below this massive unit breakouts disappear until 820 mbsf where a fault occurs (Becker, Sakai, et al., 1988). Through the fault zone and the transition zone (846–1055 mbsf) to the sheeted dikes, down to about 1130 mbsf, a relatively stable elongation direction is obtained at about 110°N. This interval is somewhat different from the underlying section where a similar mean orientation direction with far more scattering is found.

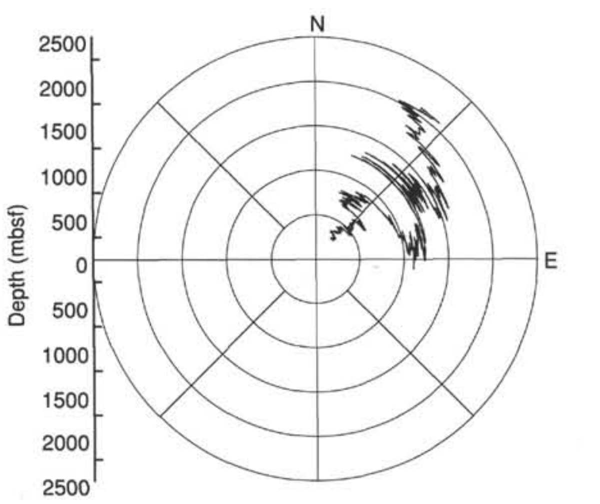

Figure 71. Hole 504B deviation with depth. Line represents direction of hole deviation from vertical at depths defined by rings. Hole 504B deviates to the northeast.

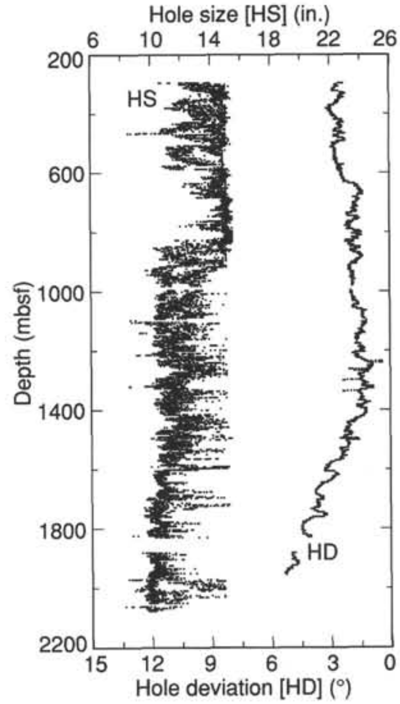

Figure 72. Hole 504B size (inches) and deviation in degrees from vertical. Hole size trace consists of two FMS calipers. Divergence of data are interpreted as borehole breakouts. Maximum deviation of the hole approaches 6° near 1930 m.

Below 1500 mbsf the record alternates between sections with no breakouts and those pointing 015°N. The latter generally coincide with sections characterized by high resistivity values (Fig. 69). These are probably due to a smaller fracture density, hence a lower degree of alteration leading to a smaller breaking strength of the material.

When the resistivities are transformed into a porosity (ϕ) profile by the relationship FF = 10/ϕ (where FF is formation factor; Pezard, 1990), values on the order of 0.03% are derived (using seawater conductivities) over the interval where large breakouts are observed (Fig. 75). The breakouts disappear where the porosity increases slightly, as found in the lower 40 m of the logged interval. The step-like transition outlined at 2042 mbsf is possibly related to the presence of a small fault, as shown by the large number of microfaults found in the core at this depth ("Structure and Deformation" section, this volume).

Above the interval cored during Leg 148 (i.e., at depths <2000 mbsf), the main structural features appear to be a pair of sudden increases in the porosity at 1925 and 1935 mbsf (Fig. 75). These zones show large increases in the fracture density of the diabase as interpreted from the DLL resistivities and may suggest the presence of two fracture traces. The abruptness of these events, as well as the reversal in resistivity profiles with LLs > LLd locally (Fig. 69), indicate the presence of a sub-horizontal structure. This proposed sub-horizontal fracture zone is also the site of an abrupt *P*-wave velocity decrease (Fig. 76) and the site of the reversal in hole deviation with respect to the vertical. Such structures contrast with others encountered in the overlying 500 m of the diabase (Fig. 77), generally appearing as sub-vertical from the analysis of DLL deep and shallow data. Examples of these are found at 1690 and 1830 mbsf.

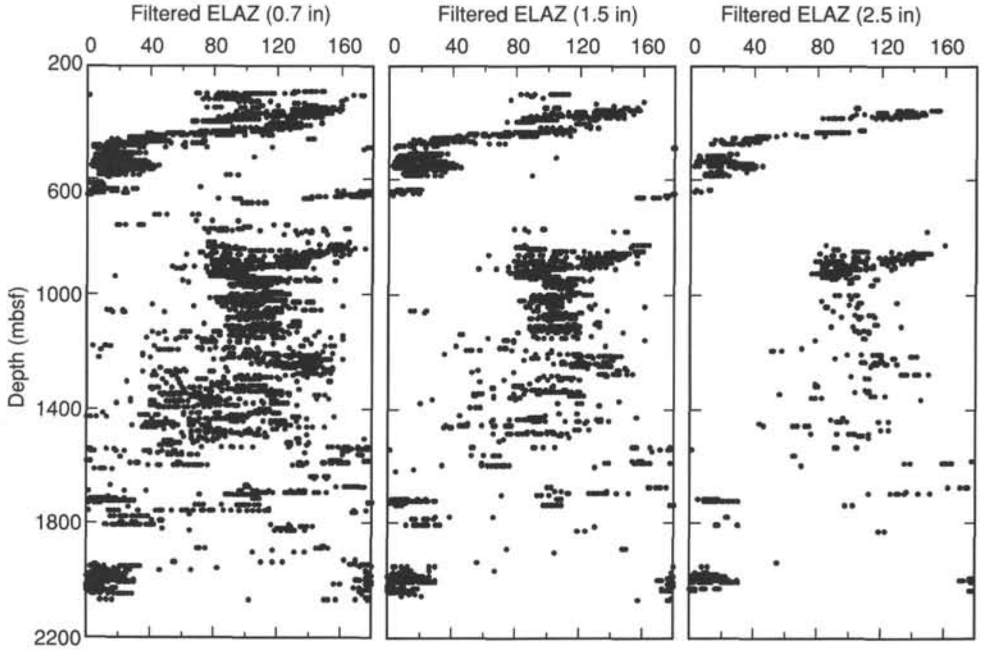

Figure 73. Azimuth of borehole breakouts in Hole 504B. Data have been filtered to show only elongations of greater than 0.7, 1.5, and 2.5 in. from left to right.

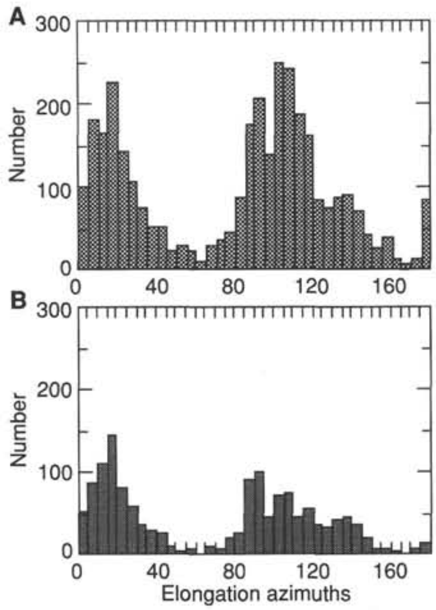

Figure 74. Histograms of elongation azimuths from FMS calipers, difference filtered at (**A**) 1.5 in., and (**B**) 2.5 in. data of Figure 73. Distribution is strongly bimodal.

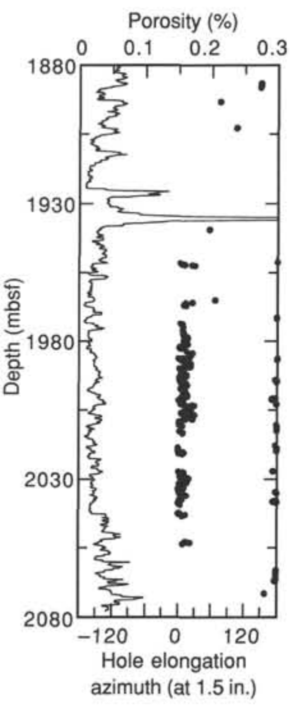

Figure 75. Porosity (derived from electrical resistivity) and breakout azimuth over the lowermost 200 m of Hole 504B. Note that breakouts tend to disappear when porosity increases.

Magnetic Field Log

The magnetic field measured in the borehole is the result of the superposition of the Earth's main field, defined by the International Geomagnetic Reference Field (IGRF), and the local anomaly field caused by the magnetization of the surrounding rocks. The IGRF for the surface of Site 504 is given in Table 14. The total field increases with increasing depth at a rate of 15 nT/km. By determining the magnetic field vector, constraints on the intensity, directions and geometry of the rocks' magnetization can be deduced. The analysis is, however, neither straightforward nor unique, in that a given magnetic anomaly can be caused by differently shaped and magnetized bodies. This must be kept in mind when interpreting the results.

Previous downhole magnetic measurements in Hole 504B were performed during Legs 69 and 111 and have been described by Ponomarev and Nekharoshkov (1983) and Kinoshita et al. (1989),

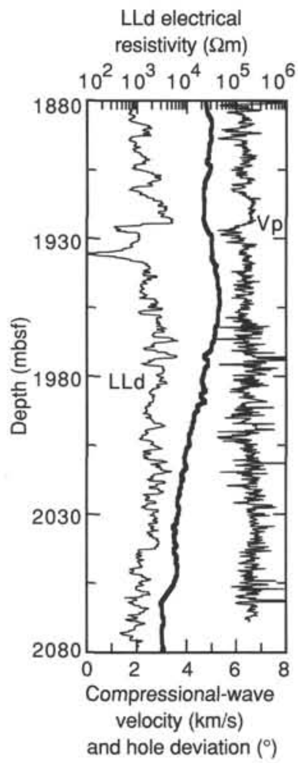

Figure 76. Electrical resistivity, compressional-wave velocity, and hole deviation over the lower 200 m of Hole 504B. Low resistivity, low-velocity zone between 1925 and 1935 mbsf corresponds to a dramatic shift in borehole deviation. (Compare with Fig. 77.)

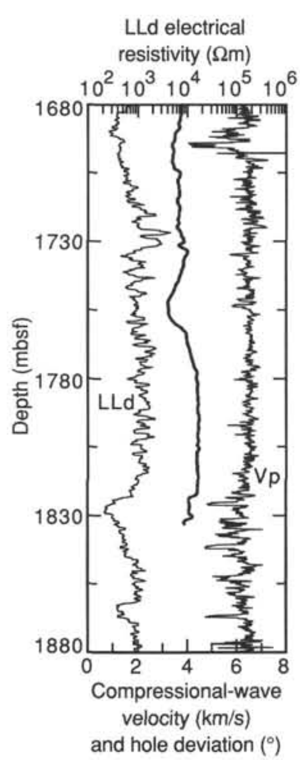

Figure 77. Electrical resistivity, compressional-wave velocity, and hole deviation of a 200-m-thick section of dikes from 1680 to 1880 mbsf.

respectively. During Leg 69 the vertical field component for the upper 200 m of basement rocks was measured. During Leg 111 a Japanese magnetometer failed to register data and instead the magnetic field data recorded by a Schlumberger inclinometer in 1100 m of basement rocks were presented for analysis. However, these data were not well calibrated, because the steel mass of the tool resulted in an average recorded field of >40 μT with an inclination of 40° in the weakly magnetic transition zone around 1000 mbsf, whereas the field should be close to the main field of 32 μT and have an inclination of 24°.

Logging Procedure

The high-temperature magnetometer of the Bundesanstalt für Geowissenschaften und Rohstoffe (BGR), Germany, described in the "Explanatory Notes" (this volume), recorded the horizontal and vertical magnetic field components in Hole 504B from the shoe of the casing at 274.5 mbsf to near bottom at 2078.8 mbsf. The downhole logging speed was 20 m/min; the uphole rate was 10 m/min. A sampling rate of 0.5 s results in sampling intervals of 16 cm and 8 cm. The centralizers attached to the instrument kept the tool away from the borehole wall and reduced rotations during logging. Besides magnetic field, the internal temperature and the dip of the probe in two perpendicular axes were also transmitted. Owing to thermal insulation and heat sinks within the tool, the internal temperature increased from 28°C at the beginning of logging to 60°C at the end of operation. The inclinometers worked correctly for most part of the logging, but they occasionally malfunctioned because of a bad connection within the probe.

Results

The horizontal, vertical, and total magnetic fields as a function of depth in Hole 504B are displayed in Figure 78. These data are presented as they were received during downhole operation and are uncorrected for possible time and temperature drifts as well as daily variations of the Earth's field, which can be on the order of 200 nT at this site. This will be accounted for after obtaining readings from the nearest magnetic observatory (in Colombia) on the variation of the Earth's field during the time of measurement. Moreover, apparent field changes can occur when the orientation of the instrument deviates from the vertical so that the vertical field sensor picks up horizontal field components and vice versa. In addition, distortions of the signals also occur when the probe rotates because the three sensors are not perfectly orthogonal, and the recorded field depends on the azimuthal orientation of the instrument. These errors will be corrected by applying results of a laboratory calibration.

Interpretation

On the basis of the amplitudes of magnetic anomalies the profile can roughly be divided into three zones: the upper part from 275 to 850 mbsf with amplitudes of up to 4000 nT, the middle part from 850 to 1050 mbsf with anomalies smaller than 100 nT, and the lower part from 1050 mbsf to bottom with anomalies of up to 1000 nT. These anomaly zones can be correlated with the well-established lithological units: the extrusive basalts, the transition zone, and the sheeted dike complex.

Table 14. IGRF (1990) field components at sea level of Site 504.

Component	Value
Vertical field	13.21 μT
Horizontal field	29.15 μT
Total field	32.00 μT
Inclination	24.4°
Declination	2.8°

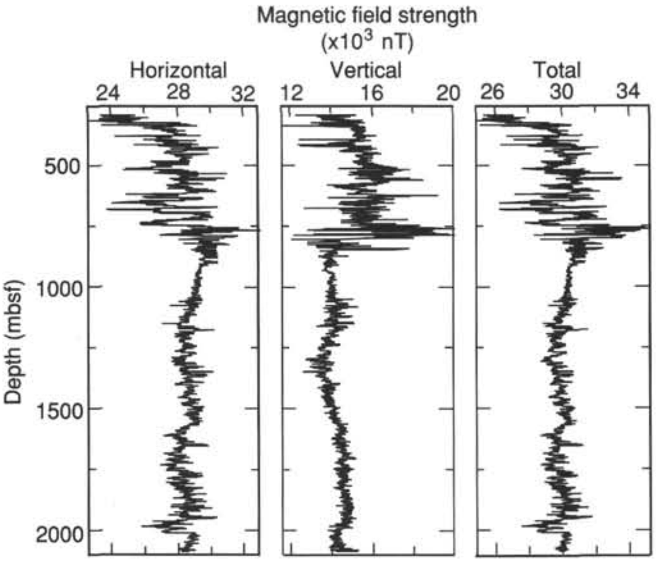

Figure 78. Logs of horizontal, vertical, and total magnetic fields in Hole 504B.

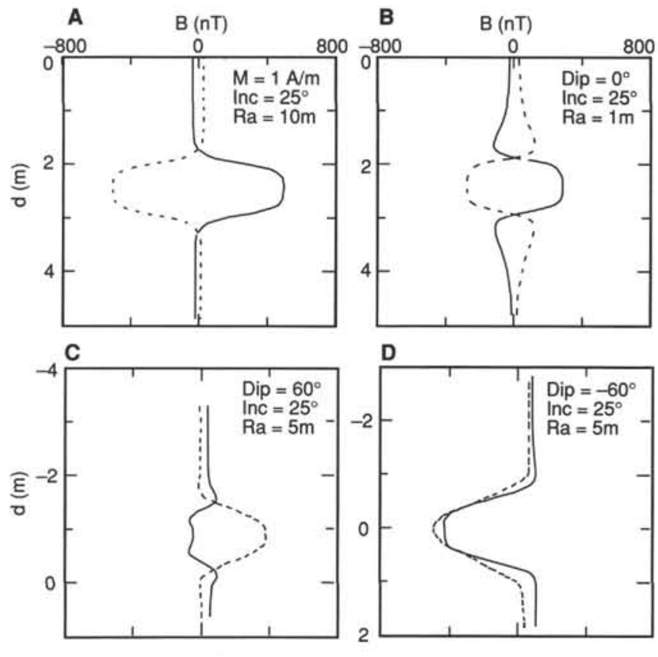

Figure 79. Models of magnetic borehole anomalies caused by cylinder-shaped bodies with inner (borehole) radius of 0.15 m, outer radius Ra, magnetization M = 1 A/m, inclination Inc, and dip of the layer (lateral surface of cylinder). Solid line = horizontal component of the magnetic field, Bh; dashed line = vertical component of the magnetic field, Bz. Dip for (**A**) and (**B**) is 0°.

Previous magnetic studies on drill cores from Hole 504B have been summarized by Smith and Banerjee (1986) and Pariso and Johnson (1991). Natural remanent magnetizations (NRM) average 5.2 A/m in the basalts, 0.35 A/m in the transition zone, and 1.6 A/m in the sheeted dikes. Induced magnetizations are only about 10% of the NRM intensities in the basalts and become larger with depth (relative to the NRM). At depths greater than 2000 mbsf, induced magnetizations are approximately equal to the remanence (see "Paleomagnetism" section, this chapter).

Based on the location within the negative magnetic Anomaly 3, the volcanic rocks at this site are expected to carry a reverse stable remanence. However, because the cores lack azimuthal orientation, this has never been proved directly. For sheeted dikes with high degrees of hydrothermal alteration, where the primary magnetite has been replaced by non-magnetic phases and the remanence is carried by secondary magnetite, the question of magnetic polarity is critical. Magnetite crystallization may have taken place after emplacement during a normal polarity chron. Downhole magnetic field measurements can answer the question of magnetic polarity of the surrounding rocks.

In a first order approximation, borehole magnetic anomalies can be modeled by cylindrical source bodies of large lateral extent (Eberle, 1985). The effects of normally and reversely magnetized rocks can clearly be distinguished because they produce horizontal anomalies of the same polarity. The vertical anomaly is of opposite polarity as the vertical magnetization component (Fig. 79A). When the outer diameters of the cylindrical source bodies become smaller, the anomalies decrease in amplitude and develop shoulders of opposite polarity (Fig. 79B). The maximum theoretical horizontal and vertical anomaly fields generated by this model are 628 nT per A/m and 1256 nT per A/m of rock magnetization, respectively. Steeply dipping source layers can give more complex anomalies depending on the relative orientations of field inclination and dip (Figs. 79C and D) (Worm and Bosum, unpubl. data).

The upper extrusive zone produces predominantly negative horizontal and positive vertical field anomalies that we interpret to indicate reverse remanent magnetizations of the basalts. The few positive horizontal anomalies could be caused by normally magnetized rocks, but they could equally be the result of steeply dipping and non-cylinder-shaped source bodies. The largest anomalies with amplitudes of 4000 nT require rock magnetizations of at least 5 A/m, and indeed maximum NRM intensities exceed 10 A/m (Smith and Banerjee, 1986).

The anomalies in the sheeted dikes appear also to be mostly negative in the horizontal component, but a detailed analysis must await final corrections of the raw data.

The wavelength of the anomalies may correspond to the thickness of the different lithological units with varying magnetizations, but other factors including the dip of the layers, borehole breakouts, and deviations of the tool orientation from the vertical and center of the hole must also affect the recorded data.

Vertical Seismic Profile

Experimental Set-up

The seismic source was a 300 in.^{3} Bolt model PAR1500 air gun, operating at 1500 psi. Shots were hand-fired with a maximum repetition rate of 12 s. Shot-instants were determined from a blast phone about a meter from the air gun.

The receiver was a Schlumberger model WSTA vertical-component seismic tool containing 10 geophones. Each phone has a sensitivity of 0.4 V/[cm per second] and 800 ohms impedance; the phones are arranged in two stacks of five. The recording was made on the Cyber Service Unit (CSU) computer at a 1-ms digitizing rate. The CSU amplifier gain was 8; downhole amplifier gain was 8 with no filtering.

The bottom-hole assembly (BHA) was used for the VSP in Hole 504B. It consisted of a clean-out bit, packer, three stands of drill collars, and the casing landing tool (CLT). The CLT sits in the reentry cone and immobilizes the drill string vertically in the hole. The BHA extended 74 m into casing at Hole 504B, leaving 200 m of casing accessible. The drill string was hung on the ship's heave compensator, with the upper guide horn (piccolo and insert) removed to minimize the noise conducted by the drill string into the hole.

The two-arm caliper on the FMS log indicated hole diameters of 10–15 in. for the interval in which the VSP was conducted, 1516–2076 mbsf.

Ship's heading was approximately 043° for the duration of the experiment. Current from the north-northeast varied from 0.2 to 0.7 knot. Weather was calm and clear; sea state was between 0 and 1. There was a slight 10–11 s roll and negligible pitch. Four fishing boats were in the area, but at ranges of more than a mile from the drill ship.

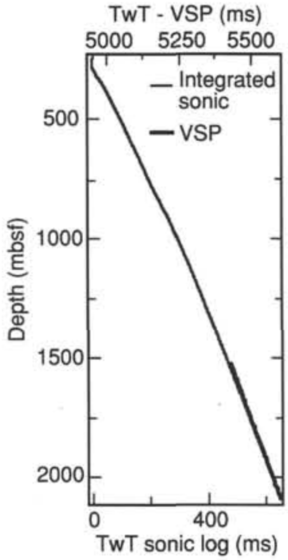

Figure 80. Comparison of integrated traveltime from acoustic well logs to traveltime from the VSP conducted in Hole 504B during Leg 148. The agreement suggests that the integrated sonic curve can be reliably used to translate seismic times to sub-bottom depths.

Table 15. Summary of results of Leg 148 VSP experiment in Hole 504B.

Depth (mbsf)	Travel-time (ms)	Interval velocity* (km/s)	Depth (mbsf)	Travel-time (ms)	Interval velocity (km/s)
1516	2701.8		1796	2743.4	6.41
1526	2703.2		1806	2746.0	7.14
1536	2705.2		1816	2746.7	5.95
1546	2706.3	6.85	1826	2748.6	5.81
1556	2707.8	6.17	1836	2750.9	6.49
1566	2709.1	6.58	1846	2752.0	6.02
1576	2711.3	7.35	1856	2753.7	6.33
1586	2712.8	7.46	1866	2755.0	6.58
1596	2713.1	6.76	1876	2756.5	6.94
1606	2714.5	7.04	1886	2758.5	6.67
1616	2716.5	7.25	1896	2759.2	5.95
1626	2718.4	6.10	1906	2761.2	6.85
1636	2719.7	6.67	1916	2763.4	6.94
1646	2721.3	6.33	1926	2763.8	6.33
1656	2722.0	6.94	1936	2765.7	5.95
1666	2724.4	6.41	1946	2767.1	6.67
1676	2725.6	6.67	1956	2769.6	5.62
1686	2727.5	6.33	1966	2770.9	6.02
1696	2728.8	7.69	1976	2772.7	6.10
1706	2729.9	6.49	1986	2774.0	7.04
1716	2730.9	6.67	1996	2775.3	7.35
1726	2733.3	6.94	2006	2776.7	7.58
1736	2735.0	6.58	2016	2777.7	6.76
1746	2736.0	6.25	2026	2779.3	7.14
1756	2737.5	6.02	2036	2781.4	6.41
1766	2738.9	6.67	2046	2782.3	6.41
1776	2741.6	6.76	2056	2784.5	6.58
1786	2742.5	5.88	2066	2785.5	
			2076	2786.9	
Average for whole section:					6.58

Note: Traveltimes are averages of 5 to 7 shots at each clamping depth.
*(running 50-m smoothing)

The minimal ship motion made for favorable recording conditions, although the current was probably a noise source.

Experimental Narrative

Hole 504B was reentered at 06:45 UTC on 5 March. The landing of the CLT in the cone and heave compensator spacing were verified at 3475 mbrf. The WSTA tool was run into the hole at 22:15 UTC and lowered at 23:30 UTC to 317 mbsf, where its operation was checked. The tool was then lowered to 1536 mbsf, the deepest clamping depth achieved during the Leg 111 VSP, for a second clamping at 00:00 UTC. Because the bottom hole temperature was comparable to the 175°C temperature rating of the tool (seven days having passed since the hole was last flushed and cooled), it was decided to run the clampings in two segments of 260–270 m each. The first started at 1816 mbsf and worked up the hole to 1546 mbsf; the second started near the bottom of the hole at 2076 mbsf and worked up to 1816 mbsf. Both sequences were conducted in 10-m increments. The seismometer noise was erratic but greatly reduced when the wireline heave compensator was activated, which also resulted in speeding up data acquisition to as little as 4 min per clamping. The estimated precision in clamping positions is 1 m. The tool had to be maneuvered to properly clamp at about 1/6 of the stations. Typically the logging cable was slacked 4–5 m at each clamping. The two spring-loaded arms (10-3/4 in. and 19 in., extended lengths) were left extended while the tool was drawn up 10 m from one station to the next. During the deepest clampings, there was passing indication of possible thermal noise, but nothing significant. Five to seven "good" shots were taken at each station. Selected shots were used to make the stacks. All of the shots were recorded in one file and the stacks from each clamping were stored in separate files. Three of the deepest Leg 111 clampings (also taken with the Schlumberger WSTA tool) were re-occupied to provide data overlap. The experiment was completed at 06:45 UTC on 6 March, and the tool was brought up on deck at 08:45 UTC.

Data Summary

Clampings were made at 57 depths, 10 m apart, from 1516 to 2076 mbsf. Together with the 124 clampings made during Leg 111, these clampings cover the entire basement section of the hole from 286 to 2076 mbsf in a consistent recording format. The traveltime difference between the top and bottom Leg 148 clampings is 85.1 ms. Three repeated clamping stacks agree within 1.9 ms. Using stacks of five to seven shots, preliminary interval velocities ranged between 5.5 and 7 km/s, with an average for the section of 6.58 km/s. This agrees well with velocities measured on recovered samples and with acoustic log velocities. Figure 80 compares the integrated traveltimes from the sonic log and the VSP measurements. Table 15 lists the unedited picks and Figure 81 is a plot of interval velocities based on five running picks at each depth.

The data were processed using the Schlumberger Seismic Quick Look (SQL) package. A composite of the stacked traces is shown in Figure 82. The separation of the upgoing and downgoing wave fields is shown in Figures 83 and 84.

There does not appear to be an extensive reflector that could be associated with Layer 3.

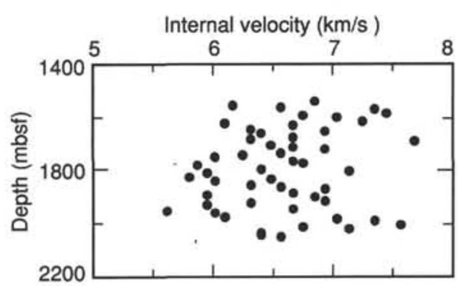

Figure 81. Hole 504B vertical seismic profile, interval velocities (50 m running average). Plot of interval velocities and depths from Table 15. Interval velocities are sensitive to errors in clamping positions; running averages reduce this effect, but limit resolving differences over small intervals.

REFERENCES[*]

Ade-Hall, J.M., and Johnson, H.P., 1976. Paleomagnetism of basalts, Leg 34. *In* Yeats, R.S., Hart, S.R., et al., *Init. Repts. DSDP,* 34: Washington (U.S. Govt. Printing Office), 513–532.

Agar, S.M., 1990. Fracture evolution in the upper ocean crust: evidence from DSDP Hole 504B. *In* Knipe, R.J., and Rutter, E.H. (Eds.), *Deformation Mechanisms, Rheology and Tectonics.* Geol. Soc. Spec. Publ. London, 54:41–50.

————, 1991. Microstructural evolution of a deformation zone in the upper ocean crust: evidence from DSDP Hole 504B. *J. Geodyn.,* 13:119–140.

Alt, J.C., Anderson, T.F., Bonnell, L., 1989. Geochemistry of sulfur in a 1.3 km section of hydrothermally altered oceanic crust, DSDP Hole 504B. *Geochim. Cosmochim. Acta,* 53:1011–1023.

Alt, J.C., Anderson, T.F., Bonnell, L., and Muehlenbachs, K., 1989. Mineralogy, chemistry, and stable isotopic compositions of hydrothermally altered sheeted dikes: ODP Hole 504B, Leg 111. *In* Becker, K., Sakai, H., et al., *Proc. ODP, Sci. Results,* 111: College Station, TX (Ocean Drilling Program), 27–40.

Alt, J.C., Honnorez, J., Laverne, C., and Emmermann, R., 1986. Hydrothermal alteration of a 1 km section through the upper oceanic crust, Deep Sea Drilling Project Hole 504B: mineralogy, chemistry, and evolution of seawater-basalt interactions. *J. Geophys. Res.,* 91:10309–10335.

Alt, J.C., Laverne, C., and Muehlenbachs, K., 1985. Alteration of the upper oceanic crust: mineralogy and processes in DSDP Hole 504B, Leg 83. *In* Anderson, R.N., Honnorez, J., Becker, K., et al., *Init. Repts. DSDP,* 83: Washington (U.S. Govt. Printing Office), 217–241.

Alt, J.C., Muehlenbachs, K., and Honnorez, J., 1986. An oxygen isotopic profile through the upper kilometer of the oceanic crust, DSDP Hole 504B. *Earth Planet. Sci. Lett.,* 80:217–229.

Alt, J.C., Zuleger, E., and Erzinger, J., in press. Mineralogy and stable isotopic compositions of the hydrothermally altered lower sheeted dike complex, ODP Hole 504B, Leg 140. *In* Erzinger, J., Becker, K., Dick, H.B.J., Stokking, L. (Eds.), *Proc. ODP, Sci. Results,* 140: College Station, TX (Ocean Drilling Program).

Anderson, R.N., Honnorez, J., Becker, K., et al., 1985. *Init. Repts. DSDP,* 83: Washington (U.S. Govt. Printing Office).

Anderson, R.N., Honnorez, J., Becker, K., Adamson, A.C., Alt, J.C., Emmermann, R., Kempton, P.D., Kinoshita, H., Laverne, C., Mottl, M.J., and Newmark, R.L., 1982. DSDP Hole 504B, the first reference section over 1 km through Layer 2 of the oceanic crust. *Nature,* 300:589–594.

Anderson, R.N., and Skilbeck, J.N., 1981. Oceanic heat flow. *In* Emiliani, C. (Ed.), *The Sea* (Vol. 7): *The Oceanic Lithosphere:* New York (Wiley), 489–524.

Audunsson, H., and Levi, S., 1989. Drilling-induced remanent magnetization in basalt drill cores. *Geophys. J.,* 98:613–622.

Autio, L.K., and Rhodes, J.M., 1983. Costa Rica Rift Zone basalts: geochemical and experimental data from a possible example of multistage melting. *In* Cann, J.R., Langseth, M.G., Honnorez, J., Von Herzen, R.P., White, S.M., et al., *Init. Repts. DSDP,* 69: Washington (U.S. Govt. Printing Office), 729–745.

Autio, L.K., Sparks, J.W., and Rhodes, J.M., 1989. Geochemistry of Leg 111 basalts: intrusive feeders for highly depleted pillows and flows. *In* Becker, K., Sakai, H., et al., *Proc. ODP, Sci. Results,* 111: College Station, TX (Ocean Drilling Program), 3–16.

Auzende, J.-M., Bideau, D., Bonatti, E., Cannat, M., Honnorez, J., Lagabrielle, Y., Malavielle, J., Mamaloukas-Frangoulis, V., and Mevel, C., 1989. Direct observation of a section through slow-spreading oceanic crust. *Nature,* 337:726–729.

————, 1990. The MAR-Vema Fracture Zone intersection surveyed by deep submersible, *Nautile. Terra Nova,* 2:68–73.

Bates, R.L., and Jackson, J.A. (Eds.), 1980. *Glossary of Geology:* Alexandria, VA (American Geological Institute).

Becker, K., Foss, G., et al., 1992. *Proc. ODP, Init. Repts.,* 137: College Station, TX (Ocean Drilling Program).

Becker, K., Langseth, M.G., and Von Herzen, R.P., 1983. Deep crustal geothermal measurements, Hole 504B, Deep Sea Drilling Project Legs 69 and 70. *In* Cann, J.R., Langseth, M.G., Honnorez, J., Von Herzen, R.P., White, S.M., et al., *Init. Repts. DSDP,* 69: Washington (U.S. Govt. Printing Office), 223–236.

Becker, K., Langseth, M.G., Von Herzen, R.P., and Anderson, R.N., 1983. Deep crustal geothermal measurements, Hole 504B, Costa Rica Rift. *J. Geophys. Res.,* 88:3447–3457.

Becker, K., Langseth, M.G., Von Herzen, R.P., Anderson, R.N., and Hobart, M.A., 1985. Deep crustal geothermal measurements, Hole 504B, Deep Sea Drilling Project Legs 69, 70, 83, and 92. *In* Anderson, R.N., Honnorez, J., Becker, K., et al., *Init. Repts. DSDP,* 83: Washington (U.S. Govt. Printing Office), 405–418.

Becker, K., Sakai, H., Adamson, A.C., Alexandrovich, J., Alt, J.C., Anderson, R.N., Bideau, D., Gable, R., Herzig, P.M., Houghton, S., Ishizuka, H., Kawahata, H., Kinoshita, H., Langseth, M.G., Lovell, M.A., Malpas, J., Masuda, H., Merrill, R.B., Morin, R.H., Mottl, M.J., Pariso, J.E., Pezard, P., Phillips, J., Sparks, J., and Uhlig, P., 1989. Drilling deep into the oceanic crust at Hole 504B, Costa Rica Rift. *Rev. Geophys.,* 27:79–102.

Becker, K., Sakai, H., et al., 1988. *Proc. ODP, Init. Repts.,* 111: College Station, TX (Ocean Drilling Program).

————, 1989. *Proc. ODP, Sci. Results,* 111: College Station, TX (Ocean Drilling Program).

Bell, J.S., and Gough, D.I., 1979. Northeast-southwest compressive stress in Alberta: evidence from oil wells. *Earth Planet. Sci. Lett.,* 45:475–482.

Bergman, E.A., 1986. Intraplate earthquakes and the state of stress in oceanic lithosphere. *Tectonophysics,* 132:1–35.

Birch, F., 1961. The velocity of compressional waves in rocks to 10 kilobars, 2. *J. Geophys. Res.,* 66:2199–2224.

Bischoff, J.L., and Seyfried, W.E., 1978. Hydrothermal chemistry of seawater from 25°C to 350°C. *Am. J. Sci.,* 278:838–860.

Bryan, W.B., Thompson, G., Frey, F.A., and Dickey, J.S., 1976. Inferred settings and differentiation in basalts from the Deep Sea Drilling Project. *J. Geophys. Res.,* 81:4285–4304.

Cann, J.R., 1970. Rb, Sr, Y, Zr and Nb in some ocean floor basaltic rocks. *Earth Planet. Sci. Lett.,* 10:7–11.

Cann, J.R., Langseth, M.G., Honnorez, J., Von Herzen, R.P., White, S.M., et al., 1983. *Init. Repts. DSDP,* 69: Washington (U.S. Govt. Printing Office).

Christensen, N.I., and Salisbury, M.H., 1975. Structure and constitution of the lower oceanic crust. *Rev. Geophys. Space Phys.,* 13:57–86.

————, 1985. Seismic velocities, densities and porosities of Layer 2B and Layer 2C basalts from Hole 504B. *In* Anderson, R.N., Honnorez, J., Becker, K., et al., *Init. Repts. DSDP,* 83: Washington (U.S. Govt. Printing Office), 367–370.

Christensen, N.I., Wepfer, W.W., and Baud, R.D., 1989. Seismic properties of sheeted dikes from Hole 504B, ODP Leg 111. *In* Becker, K., Sakai, H., et al., *Proc. ODP, Sci. Results,* 111: College Station, TX (Ocean Drilling Program), 171–174.

Coish, R.A., 1977. Ocean floor metamorphism in the Betts Cove ophiolite, Newfoundland. *Contrib. Mineral. Petrol.,* 60:277–302.

Collins, J.A., Brocher, T.M., and Purdy, G.M., 1989. Seismic-reflection structure of the upper oceanic crust: implications from DSDP/ODP Hole 504B, Panama Basin. *In* Becker, K., Sakai, H., et al., *Proc. ODP, Sci. Results,* 111: College Station, TX (Ocean Drilling Program), 177–191.

Cox, S.F., and Etheridge, M.A., 1983. Crack-seal fibre growth mechanisms and their significance in the development of oriented layer silicate microstructures. *Tectonophysics,* 92:147–170.

CRRUST (Costa Rica Rift United Scientific Team), 1982. Geothermal regimes of the Costa Rica Rift, east Pacific, investigated by drilling, DSDP-IPOD Legs 68, 69, and 70. *Geol. Soc. Am. Bull.,* 93:862–875.

Dick, H.J.B., Erzinger, J., Stokking, L.B., et al., 1992. *Proc. ODP, Init. Repts.,* 140: College Station, TX (Ocean Drilling Program).

Dick, H.J.B., Meyer, P.S., Bloomer, S., Kirby, S., Stakes, D., and Mawer, C., 1991. Lithostratigraphic evolution of an *in-situ* section of oceanic Layer 3. *In* Von Herzen, R.P., Robinson, P.T., et al., *Proc. ODP, Sci. Results,* 118: College Station, TX (Ocean Drilling Program), 439–538.

Eberle, D., 1985. Interpretation von bohrlochmagnetometrischen Messungen in drei Komponenten. *Geol. Jahrb.,* E28:191–217.

Ekstrom, M.P., Dahan, C.A., Chen, M.-Y., Lloyd, P.M., and Rossi, D.J., 1986. Formation imaging with microelectrical scanning arrays. *Trans. SPWLA 27th Ann. Logging Symp.,* Pap. BB.

Ellwood, B.B., 1978. Flow and emplacement direction determined for selected basaltic bodies using magnetic susceptibility anisotropy measurements. *Earth Planet. Sci. Lett.,* 41:254–264.

Emmermann, R., 1985. Basement geochemistry, Hole 504B. *In* Anderson, R.N., Honnorez, J., et al., *Init. Repts. DSDP,* 83: Washington (U.S. Govt. Printing Office), 183–199.

Etoubleau, J., Corre, O., Joron, J.L., Bougault, H., and Treuil, M., 1983. Costa Rica Rift: variably depleted basalts in the same hole. *In* Cann, J.R.,

[*] Abbreviations for names of organizations and publication titles in ODP reference lists follow the style given in *Chemical Abstracts Service Source Index* (published by American Chemical Society).

Langseth, M.G., Honnorez, J., Von Herzen, R.P., White, S.M., et al., *Init. Repts. DSDP,* 69: Washington (U.S. Govt. Printing Office), 765–773.

Fisher, A.T., and Becker, K., 1991. The reduction of measured heat flow with depth in DSDP Hole 504B. *Sci. Drill.,* 2:34–40.

Fisher, A.T., Becker, K., Narasimhan, T.N., Langseth, M.G., and Mottl, M.J., 1990. Passive, off-axis convection through the southern flank of the Costa Rica rift. *J. Geophys. Res.,* 95:9343–9370.

Fisk, M.R., and Bence, A.E., 1980. Experimental crystallization of chrome spinel in FAMOUS basalt 527-1-1. *Earth Planet. Sci. Lett.,* 48:111–123.

Fox, P.J., Schreiber, E., and Peterson, J.J., 1973. The geology of the oceanic crust: compressional wave velocities of oceanic rocks. *J. Geophys. Res.,* 78:5155–5172.

Francheteau, J., Armijo, R., Cheminee, J.L., Hekinian, R., Lonsdale, P., and Blum, N., 1990. 1 Ma East Pacific Rise oceanic crust and uppermost mantle exposed by rifting in Hess Deep (equatorial Pacific Ocean). *Earth Planet. Sci. Lett.,* 101:281–295.

————, 1992. Dike complex of the East Pacific Rise exposed in the walls of Hess Deep and the structure of the upper oceanic crust. *Earth Planet. Sci. Lett.,* 111:109–121.

Frey, F.A., Bryan, W.B., Thompson, G., and Roy, S., 1973. Petrological and geochemical results for basalts from DSDP Legs 2 and 3. *Eos,* 54:463.

Furuta, T., and Tokuyama, H., 1983. Chromian spinels in Costa Rica basalts, Deep Sea Drilling Project Site 505—a preliminary interpretation of electron microprobe analyses. *In* Cann, J.R., Langseth, M.G., Honnorez, J., Von Herzen, R.P., White, S.M., et al., *Init. Repts. DSDP,* 69: Washington (U.S. Govt. Printing Office), 805–810.

Gable, R., Morin, R.H., and Becker, K., 1989. Geothermal state of Hole 504B: ODP Leg 111 overview. *In* Becker, K., Sakai, H., et al., *Proc. ODP, Sci. Results,* 111: College Station, TX (Ocean Drilling Program), 87–96.

Gieskes, J.M., Kastner, M., Erzinger, J., and Boulegue, J., 1986. Geochemical studies in Hole 504B, Leg 92. *In* Leinen, M., Rea, D.K., et al. *Init. Repts. DSDP,* 92: Washington (U.S. Govt. Printing Office), 547–562.

Gieskes, J.M., and Magenheim, A.J., 1992. Borehole fluid chemistry of DSDP Hole 395A and 534A results from operation Dianaut. *Geophys. Res. Lett.,* 19:513–516.

Hart, R.A., 1970. Chemical exchange between seawater and deep ocean basalts. *Earth Planet. Sci. Lett.,* 9:269–279.

Hey, R., Johnson, L., and Lowrie, A., 1977. Recent plate motion in the Galapagos Area. *Geol. Soc. Am. Bull.,* 88:1385–1403.

Hobart, M.A., Langseth, M.G., and Anderson, R.N., 1985. A geothermal and geophysical survey on the south flank of the Costa Rica Rift: Sites 504 and 505. *In* Anderson, R.N., Honnorez, J., et al., *Init. Repts. DSDP,* 83: Washington (U.S. Govt. Printing Office), 379–404.

Honnorez, J., Laverne, C., Hubberten, H.-W., Emmermann, R., and Muehlenbachs, K., 1983. Alteration processes in layer 2 basalts from Deep Sea Drilling Project Hole 504B, Costa Rica Rift. *In* Cann, J.R., Langseth, M.G., Honnorez, J., Von Herzen, R.P., White, S.M., et al., *Init. Repts. DSDP,* 69: Washington (U.S. Govt. Printing Office), 509–546.

Houtz, R., and Ewing, J., 1976. Upper crustal structure as a function of plate age. *J. Geophys. Res.,* 81:2490–2498.

Hrouda, F., 1982. Magnetic anisotropy of rocks and its application in geology and geophysics. *Geophys. Surv.,* 5:37–82.

Ishizuka, H., 1989. Mineral paragenesis of altered basalts from Hole 504B, ODP Leg 111. *In* Becker, K., Sakai, H., et al., *Proc. ODP, Sci. Results,* 111: College Station, TX (Ocean Drilling Program), 61–76.

Iturrino, G.J., Christensen, N.I., Boldreel, N.I., and Harvey, P., in press. Physical properties and elastic constants of upper crustal rocks from laboratory and well log measurements from Hole 504B. *In* Dick, H.J.B., Erzinger, J., Stokking, L.B., et al., *Proc. ODP, Sci. Results,* 140: College Station, TX (Ocean Drilling Program).

Johnson, H.P., 1978. Paleomagnetism of igneous rock samples—DSDP Leg 45. *In* Melson, W.G., Rabinowitz, P.D., et al., *Init. Repts. DSDP,* 45: Washington (U.S. Govt. Printing Office), 387–396.

Karato, S., 1983. Physical properties of basalts from Deep Sea Drilling Project Hole 504B, Costa Rica Rift. *In* Cann, J.R., Langseth, M.G., Von Herzen, R.P., White, S.M., et al., *Init. Repts. DSDP,* 69: Washington (U.S. Govt. Printing Office), 687–695.

Kempton, P.D., 1985. An interpretation of contrasting nucleation and growth histories from the petrographic analysis of pillow and dike chilled margins, Hole 504B, Deep Sea Drilling Project, Leg 83. *In* Anderson, R.N., Honnorez, J., Becker, K., et al., *Init. Repts. DSDP,* 83: Washington (U.S. Govt. Printing Office), 165–181.

Kempton, P.D., Autio, L.K., Rhodes, J.M., Holdaway, M.J., Dungan, M.A., and Johnson, P., 1985. Petrology of basalts from Hole 504B, Deep Sea Drilling Project, Leg 83. *In* Anderson, R.N., Honnorez, J., Becker, K., et al., *Init. Repts. DSDP,* 83: Washington (U.S. Govt. Printing Office), 129–164.

Kinoshita, H., Furuta, T., and Pariso, J., 1989. Downhole magnetic field measurements and paleomagnetism, Hole 504B, Costa Rica Ridge. *In* Becker, K., Sakai, H., et al., *Proc. ODP, Sci. Results,* 111: College Station, TX (Ocean Drilling Program), 147–156.

Klitgord, K.D., Huestis, S.P., Mudie, J.D., and Parker, R.L., 1975. An analysis of near-bottom magnetic anomalies, seafloor spreading and the magnetized layer. *Geophys. J. R. Astron. Soc.,* 43:387–424.

Knight, M.D., and Walker, G.P., 1988. Magma flow directions in dikes of the Koolau complex, Oahu, determined from magnetic fabric studies. *J. Geophys. Res.,* 93:4301–4319.

Kusakabe, M., Shibata, T., Yamamoto, M., Mayeda, S., Kagami, H., Honma, H., Masuda, H., and Sakai, H., 1989. Petrology and isotope characteristics (H, O, S, Sr, and Nd) of basalts from Ocean Drilling Program Hole 504B, Leg 111, Costa Rica Rift. *In* Becker, K., Sakai, H., et al., *Proc. ODP, Sci. Results,* 111: College Station, TX (Ocean Drilling Program), 47–60.

Langseth, M.G., Cann, J.R., Natland, J.H., and Hobart, M., 1983. Geothermal phenomena at the Costa Rica Rift: background and objectives for drilling at Deep Sea Drilling Project Sites 501, 504, and 505. *In* Cann, J.R., Langseth, M.G., Honnorez, J., Von Herzen, R.P., White, S.M., et al., *Init. Repts. DSDP,* 69: Washington (U.S. Govt. Printing Office), 5–29.

Langseth, M.G., Mottl, M.J., Hobart, M.A., and Fisher, A., 1988. The distribution of geothermal and geochemical gradients near Site 501/504: implications for hydrothermal circulation in the oceanic crust. *In* Becker, K., Sakai, H., et al., *Proc. ODP, Init. Repts.,* 111: College Station, TX (Ocean Drilling Program), 23–32.

Laverne, C., Alt, J.C., and Honnorez, J., 1989. Transition entre l'altéation à basse température et le métamorphisme hydrothermale de la croûte océanique: étude pétrographique et géochimique du puits 504B, Est-Pacifique. *Bull. Soc. Geol. France,* 8:327–337.

Laverne, C., Vanko, D.A., Tartarotti, P., and Alt, J.C., in press. Chemistry and geothermometry of secondary minerals from the deep sheeted dike complex, DSDP/ODP Hole 504B. *In* Dick, H.J.B., Erzinger, J., Stokking, L.B., et al., *Proc. ODP, Sci. Results,* 140: College Station, TX (Ocean Drilling Program).

Leinen, M., Rea, D.K., et al., 1986. *Init. Repts. DSDP,* 92: Washington (U.S. Govt. Printing Office).

Lowrie, W., and Kent, D.V., 1978. Characteristics of VRM in ocean basalts. *J. Geophys.,* 44:297–315.

Lysne, P., 1992. Pressure, volume and temperature states within the VC-2B corehole, Valles Caldera, New Mexico, USA. *Appl. Geochem.,* 6:665–670.

Magenheim, A.J., Bayhurst, G., Alt, A.C., and Gieskes, J.M., 1992. ODP Leg 137, borehole fluid chemistry in Hole 504B. *Geophys. Res. Lett.,* 19:521–524.

Magenheim, A.J., Gieskes, J.M., Bayhurst, G., and Alt, J.C., 1992. Oceanic borehole fluid chemistry from Site 504B: seawater/rock reaction within the borehole environment. *In* Karaka, Y.K., and Maest, A.S. (Eds.), *Water-Rock Interaction, Proc. 7th Int. Symp. on Water Rock Interaction—WRI-7:* Rotterdam (A.A. Balkema), 1655–1658.

Marsh, N.G., Tarney, J., and Hendry, G.L., 1983. Trace element geochemistry of basalts from Hole 504B, Panama Basin, Deep Sea Drilling Project Legs 69 and 70. *In* Cann, J.R., Langseth, M.G., Honnorez, J., Von Herzen, R.P., White, S.M., et al., *Init. Repts. DSDP,* 69: Washington (U.S. Govt. Printing Office), 747–763.

McFadden, P.L., and Merrill, R.T., 1975. Geomagnetic secular variation over the past 5 m.y. *Rev. Geophys. Space Phys.,* 13:687–708.

Morin, R.H., Newmark, R.L., Barton, C.A., and Anderson, R.N., 1990. State of lithospheric stress and borehole stability at Deep Sea Drilling Project Site 504B, eastern equatorial Pacific. *J. Geophys. Res.,* 95:9293–9303.

Mottl, M.J., Druffel, E.R.M., Hart, S.R., Lawrence, J.R., and Saltzman, E.S., 1985. Chemistry of hot waters sampled from basaltic basement in Hole 504B, Deep Sea Drilling Project Leg 83, Costa Rica Rift. *In* Anderson, R.N., Honnorez, J., et al., *Init. Repts. DSDP,* 83: Washington (U.S. Govt. Printing Office), 315–328.

Mottl, M.J., and Gieskes, J.M., 1990. Chemistry of waters sampled from oceanic basement boreholes, 1979–1988. *J. Geophys. Res.,* 95:9327–9342.

Mutter, C.Z., 1992. DSDP Hole 504B: are gabbros in sight? *JOI/USSAC Newsl.,* 5:4–6.

Natland, J.H., Adamson, A.C., Laverne, C., Melson, W.G., and O'Hearn, T., 1983. A compositionally nearly steady-state magma chamber at the Costa Rica Rift: evidence from basalt glass and mineral data, Deep Sea Drilling

Project Sites 501, 504, and 505. *In* Cann, J.R., Langseth, M.G., Honnorez, J., Von Herzen, R.P., White, S.M., et al., *Init. Repts. DSDP,* 69: Washington (U.S. Govt. Printing Office), 811–858.

Newmark, R.L., Anderson, R.N., Moos, D., and Zoback, M.D., 1985. Sonic and ultrasonic logging of Hole 504B and its implications for the structure, porosity, and stress regime of the upper 1 km of the oceanic crust. *In* Anderson, R.N., Honnorez, J., Becker, K., et al., *Init. Repts. DSDP,* 83: Washington (U.S. Govt. Printing Office), 479–510.

Newmark, R.L., Zoback, M.D., and Anderson, R.N., 1985. Orientation of in situ stresses near the Costa Rica Rift and Peru-Chile Trench, Deep Sea Drilling Project Hole 504B. *In* Anderson, R.N., Honnorez, J., Becker, K., et al., *Init. Repts. DSDP,* 83: Washington (U.S. Govt. Printing Office), 511–514.

Pariso, J.E., and Johnson, H.P., 1991. Alteration processes at Deep Sea Drilling Project/Ocean Drilling Program Hole 504B at the Costa Rica Rift: implications for magnetization of oceanic crust. *J. Geophys. Res.,* 96:11703–11722.

Petit, J.P., 1987. Criteria for the sense of movement on fault surfaces in brittle rocks. *J. Struct. Geol.,* 9:597–608.

Pezard, P.A., 1990. Electrical properties of mid-ocean ridge basalt and implications for the structure of the upper oceanic crust in Hole 504B. *J. Geophys. Res.,* 95:9237–9264.

Pinto, M.J., and McWilliams, M., 1990. Drilling-induced isothermal remanent magnetization. *Geophysics,* 55:111–115.

Pitzer, K.S., Peiper, J.P., and Busey, R.H., 1984. Thermodynamic properties of aqueous sodium chloride solutions. *J. Phys. Chem. Ref.,* 13:1–52.

Pollard, D.D., and Aydin, A., 1988. Progress in understanding jointing over the past century. *Geol. Soc. Am. Bull.,* 100:1181–1204.

Ponomarev, V.N., and Nechoroshkov, V.L., 1983. First measurements of the magnetic field within the ocean crust: Deep Sea Drilling Project Legs 68 and 69. *In* Cann, J.R., Langseth, M.G., Honnorez, J., Von Herzen, R.P., White, S.M., et al., *Init. Repts. DSDP,* 69: Washington (U.S. Govt. Printing Office), 271–279.

Ramsay, J.G., 1980. The crack-seal mechanism of rock deformation. *Nature,* 284:135–139.

Ramsay, J.G., and Huber, M., 1983. *The Techniques of Modern Structural Geology* (Vol. 1): *Strain Analysis:* London (Academic Press).

Robinson, P.T., Von Herzen, R., et al., 1989. *Proc. ODP, Init. Repts.,* 118: College Station, TX (Ocean Drilling Program).

Rochette, P., Jenatton, L., Dupuy, C., Boudier, F., and Reuber, L., 1991. Diabase dikes emplacement in the Oman ophiolite: a magnetic fabric study with reference to geochemistry. *In* Peters, T. (Ed.), *Ophiolite Genesis and Evolution of the Oceanic Lithosphere.* Sultanate of Oman, Ministry of Petroleum and Minerals, 55–82.

Roeckel, T., Natau, O., and Dietrich, H.-G., 1992. Core reorientation by comparison of core instabilities and borehole instabilities. *In* Emmermann, R., Dietrich, H.-G., et al., *KTB Hauptbohrung, Results of Geoscientific Investigation in the KTB Field Laboratory, 0–6000 m.* KTB Rep. 92-2:F1–F17.

Rosenbauer, R.J., Bischoff, J.L., and Radke, A.S., 1983. Hydrothermal alteration of graywacke and basalt by 4 molal NaCl. *Econ. Geol.,* 78:1701–1710.

Salisbury, M.H., Christensen, N.I., Becker, K., and Moos, D., 1985. The velocity structure of Layer 2 at Deep Sea Drilling Project Site 504 from logging and laboratory experiments. *In* Anderson, R.N., Honnorez, J., Becker, K., et al., *Init. Repts. DSDP,* 83: Washington (U.S. Govt. Printing Office), 529–539.

Schiffman, P., Smith, B.M., Vargas, R.S., and Moores, E.M., 1987. Geometry, conditions, and timing of off-axis hydrothermal metamorphism and ore-deposition in the Solea Graben. *Nature,* 325:423–425.

Searle, R.C., 1983. Gloria survey over Costa Rica Rift Sites 501, 504, and 505. *In* Cann, J.R., Langseth, M.G., Honnorez, J., Von Herzen, R.P., White, S.M., et al., *Init. Repts. DSDP,* 69: Washington (U.S. Govt. Printing Office), 217–222.

Seyfried, W.E., Jr., and Bischoff, J.L., 1979. Low temperature basalt alteration by seawater: an experimental study at 70°C and 150°C. *Geochim. Cosmochim. Acta,* 43:1937–1947.

Seyfried, W.E., Jr., and Mottl, M.J., 1982. Hydrothermal alteration of basalt by seawater under seawater-dominated conditions. *Geochim. Cosmochim. Acta,* 46:985–1002.

Shimizu, H., Mori, K., and Masuda, A., 1989. REE, Ba, and Sr abundances and Sr, Nd, and Ce isotopic ratios in Hole 504B basalts, ODP Leg 111, Costa Rica Rift. *In* Becker, K., Sakai, H., et al., *Proc. ODP, Sci. Results,* 111: College Station, TX (Ocean Drilling Program), 77–83.

Shipboard Scientific Parties of Leg 68 (Site 501), Leg 69, and Leg 70, 1983. Sites 501 and 504: sediments and ocean crust in an area of high heat flow on the southern flank of the Costa Rica Rift. *In* Cann, J.R., Langseth, M.G., Honnorez, J., Von Herzen, R.P., White, S.M., et al., *Init. Repts. DSDP,* 69: Washington (U.S. Govt. Printing Office), 31–174.

Shipboard Scientific Party, 1985. Hole 504B, Leg 83. *In* Anderson, R.N., Honnorez, J., Becker, K., et al., *Init. Repts. DSDP,* 83: Washington (U.S. Govt. Printing Office), 13–120.

————, 1988. Site 504: Costa Rica Rift. *In* Becker, K., Sakai, H., et al., *Proc. ODP, Init. Repts.,* 111: College Station, TX (Ocean Drilling Program), 35–251.

————, 1992a. Site 504. *In* Becker, K., Foss, G., et al., *Proc. ODP, Init. Repts.,* 137: College Station, TX (Ocean Drilling Program), 15–55.

————, 1992b. Site 504. *In* Dick, H.J.B., Erzinger, J., Stokking, L.B., et al., *Proc. ODP, Init. Repts.,* 140: College Station, TX (Ocean Drilling Program), 37–200.

Smith, G.M., and Banerjee, S.K., 1986. The magnetic structure of the upper kilometer of the marine crust at Deep Sea Drilling Project Hole 504B, Eastern Pacific Ocean. *J. Geophys. Res.,* 91:10337–10354.

Spear, F.S., 1980. NaSi-CaAl exchange equilibrium between plagioclase and amphibole, an empirical model. *Contrib. Mineral. Petrol.,* 72:33–41.

Staudigel, H., and Hart, S.R., 1983. Alteration of basaltic glass: mechanisms and significance of the oceanic crust-seawater budget. *Geochim. Cosmochim. Acta,* 47:337–350.

Tartarotti, P., Allerton, S., and Laverne, C., in press. Vein formation mechanism in the sheeted dike complex from Hole 504B. *In* Dick, H.J.B., Erzinger, J., and Stokking, L.B., et al., *Proc. ODP, Sci. Results,* 140: College Station, TX (Ocean Drilling Program).

Thompson, G., 1973. A geochemical study of the low-temperature interaction of seawater and oceanic igneous rocks. *Eos,* 54:1015–1018.

Tual, E., Jahn, B.M., Bougault, H., and Joron, J.L., 1985. Geochemistry of basalts from Hole 504B, Leg 83, Costa Rica Rift. *In* Anderson, R.N., Honnorez, J., Becker, K., et al., *Init. Repts. DSDP,* 83: Washington (U.S. Govt. Printing Office), 201–214.

Valsami, E., and Cann, J.R., 1992. Mobility of rare earth elements in zones of intense hydrothermal alteration in the Pindos ophiolite, Greece. *In* Parson, L.M., Murton, B.J., and Browning, P. (Eds.), *Ophiolites and Their Modern Oceanic Analogues.* Geol. Soc. Spec. Publ. London, 60:219–232.

Wager, L.R., Brown, G.M., and Wadsworth, W.J., 1960. Types of igneous cumulates. *J. Petrol.,* 1:73–85.

Wilkens, R.H., Christensen, N.I., and Slater, L., 1983. High-pressure seismic studies of Leg 69 and 70 basalts. *In* Cann, J.R., Langseth, M.G., Honnorez, J., Von Herzen, R.P., White, S.M., et al., *Init. Repts. DSDP,* 69: Washington (U.S. Govt. Printing Office), 683–686.

Wolter, K.E., Roeckel, T., et al., 1990. Core disking in KTB drill cores and the determination of the in-situ stress orientation. *In* Emmermann, R., Dietrich, H.-G., et al. (Eds.), *Pilot Hole, Results of Geoscientific Investigation in the KTB Field Laboratory, 0–4000.1m.* KTB Rep. 90-8:G1–G13.

Zijderveld, J.D.A., 1967. AC demagnetization of rocks: analysis of results. *In* Collinson, D.W., Creer, K.M., and Runcorn, S.K. (Eds.), *Methods in Palaeomagnetism:* New York (Elsevier), 254–286.

Ms 148IR-102

NOTE: For all sites drilled, hard-rock core-description forms and core photographs can be found in Section 3, beginning on page 195. Thin-section data are given in Section 4, beginning on page 291. Conventional-log and FMS data can be found in the CD-ROM (back pocket). As a guide to the reader, only the first page of the 11 Appendixes to this chapter is printed, following the text. All 11 Appendixes are given in their entirety in the accompanying CD-ROM.

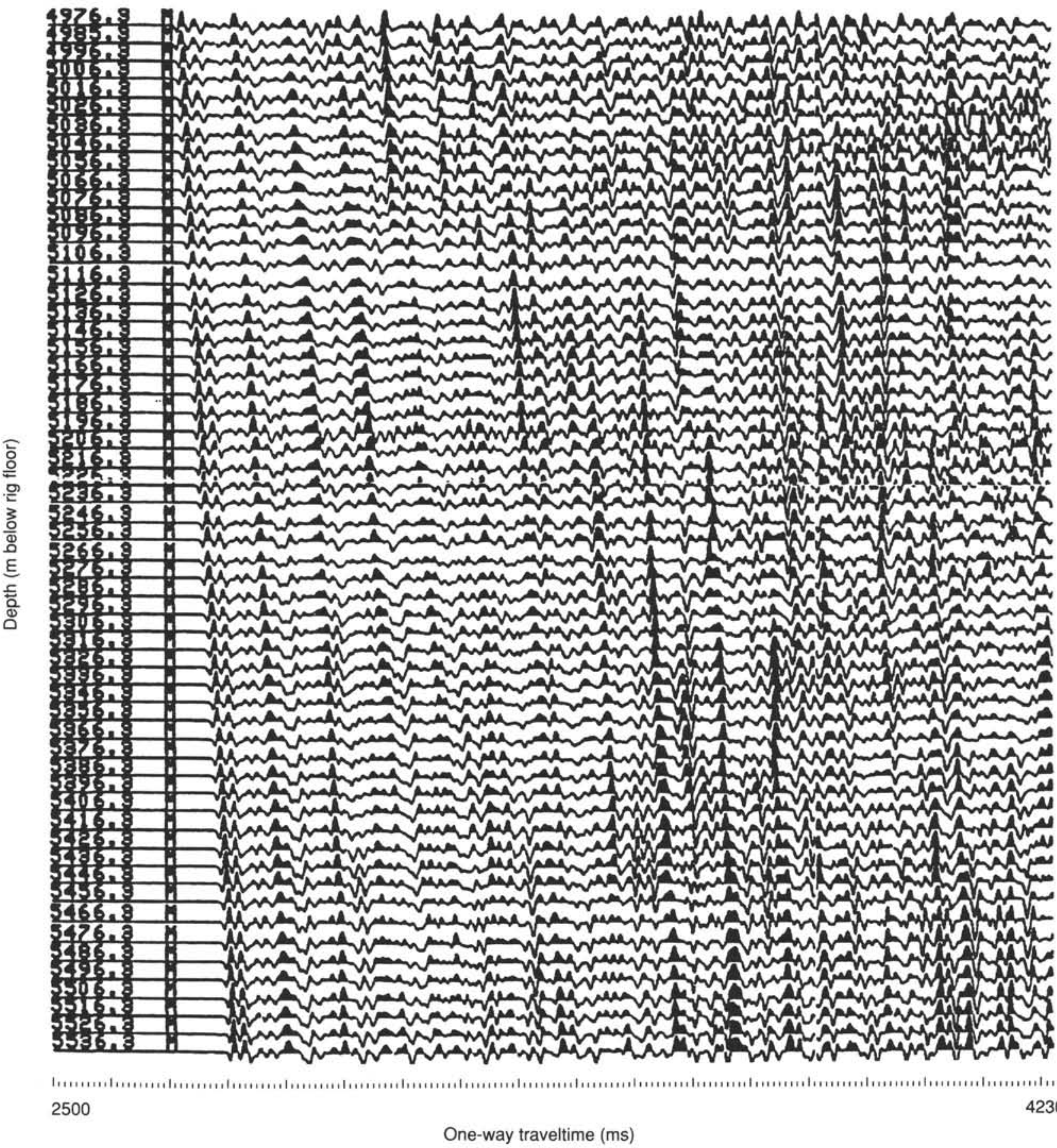

Figure 82. Composite of 57 stacked traces from depths of 1516 to 2076 mbsf in variable area presentation. Depths on left margin are meters below rig floor. Scale on bottom is one-way traveltime in milliseconds (ms). Traces are normalized to maximum value and time-varying gain is applied.

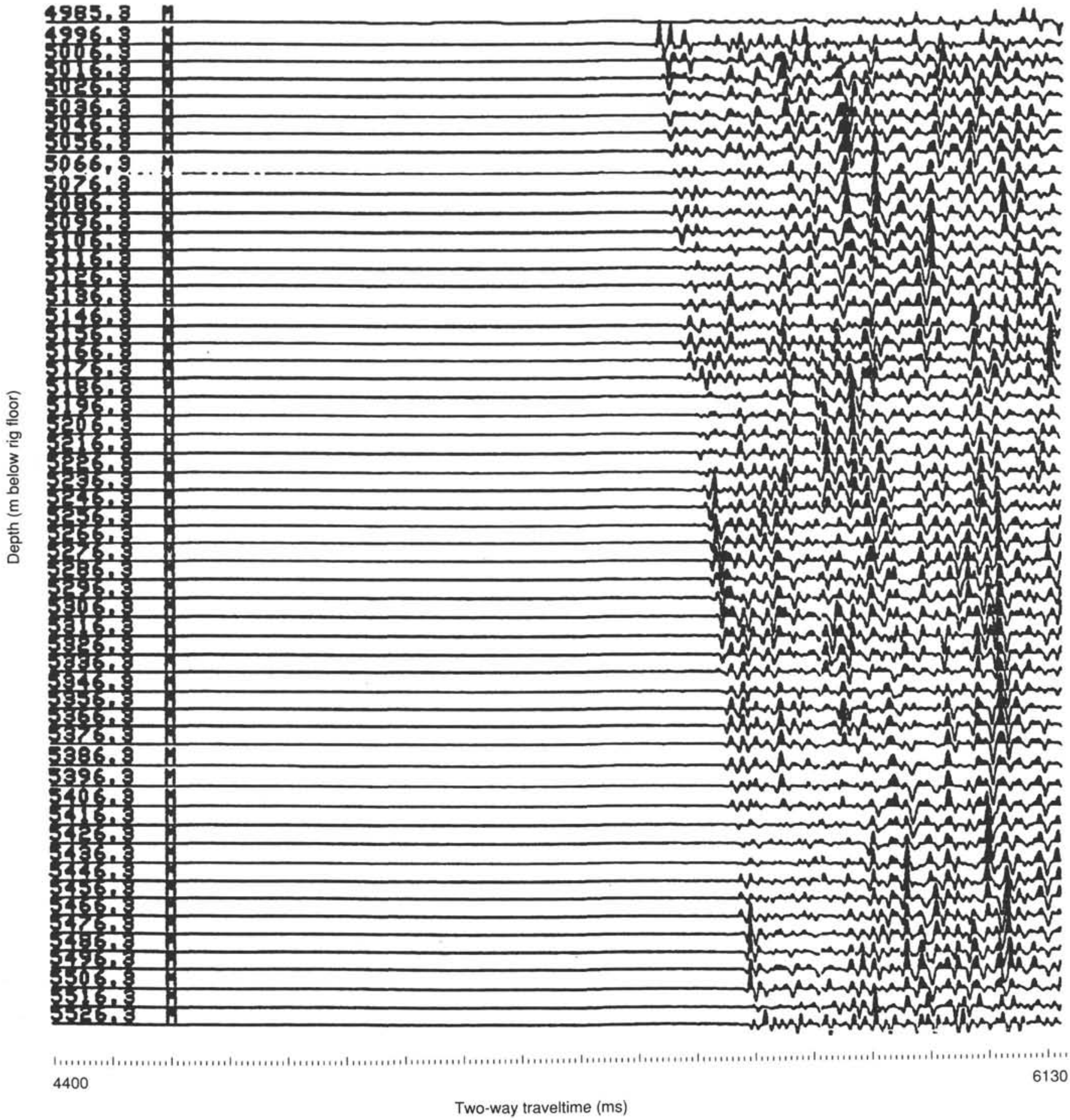

Figure 83. Upgoing reflections plotted in two-way traveltime (as would be seen at surface without effect of overlying material). Presentation and scales as in Figure 82.

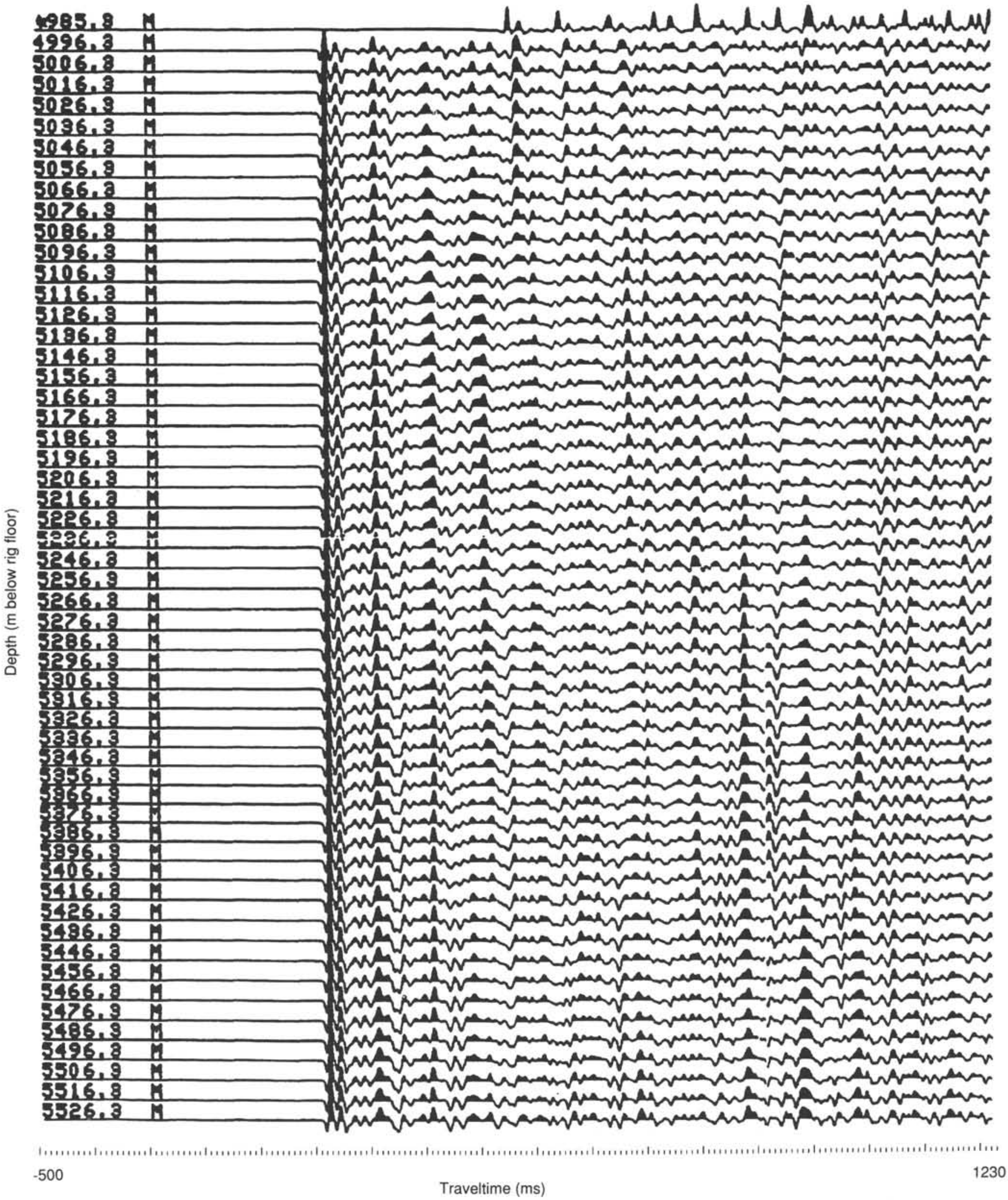

Figure 84. Down-going wave forms aligned on first motion. Bottom traveltime scale is in milliseconds (ms) with an arbitrary origin.

Hole 504B: Resistivity-Velocity Log Summary

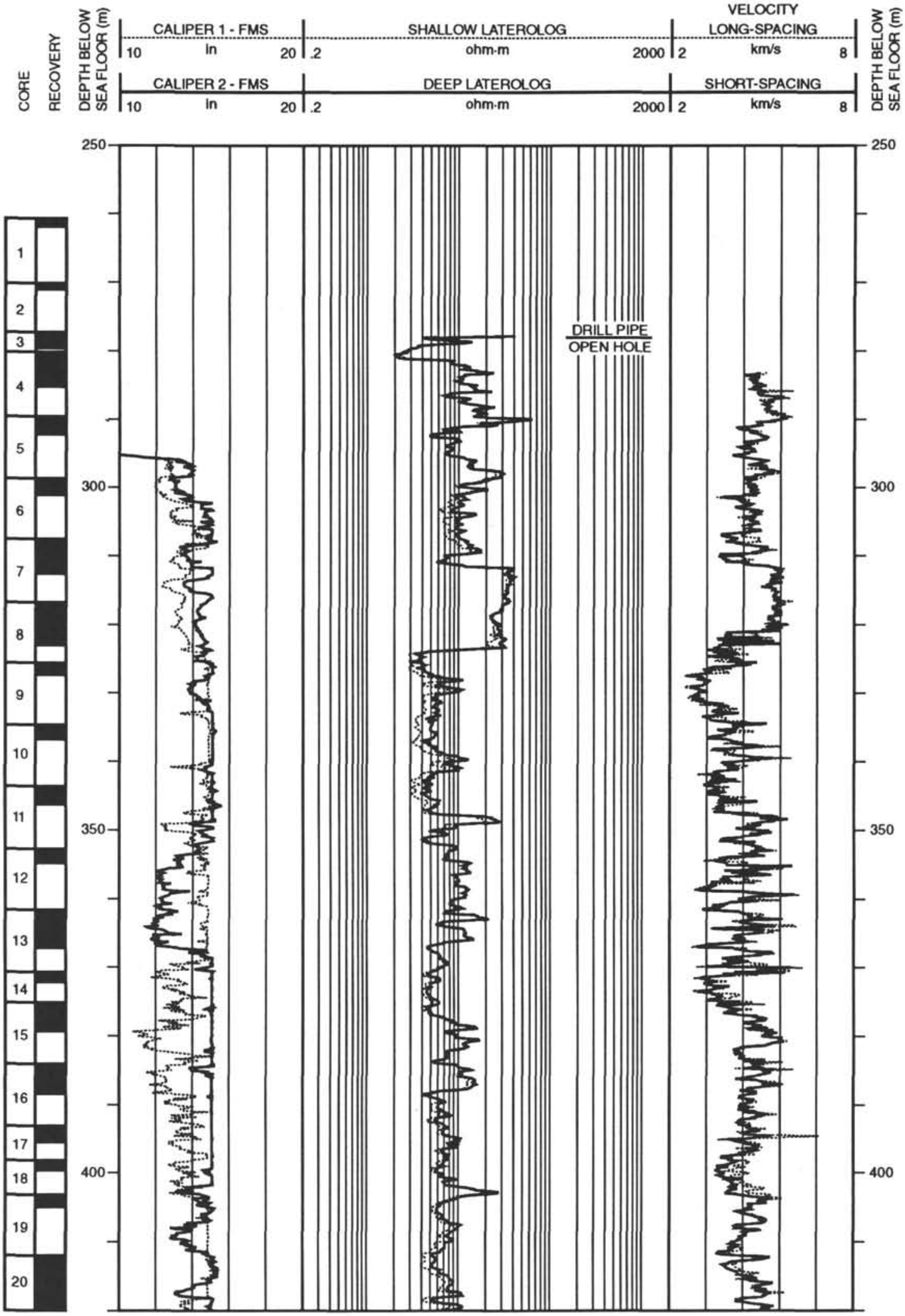

Hole 504B: Resistivity-Velocity Log Summary (continued)

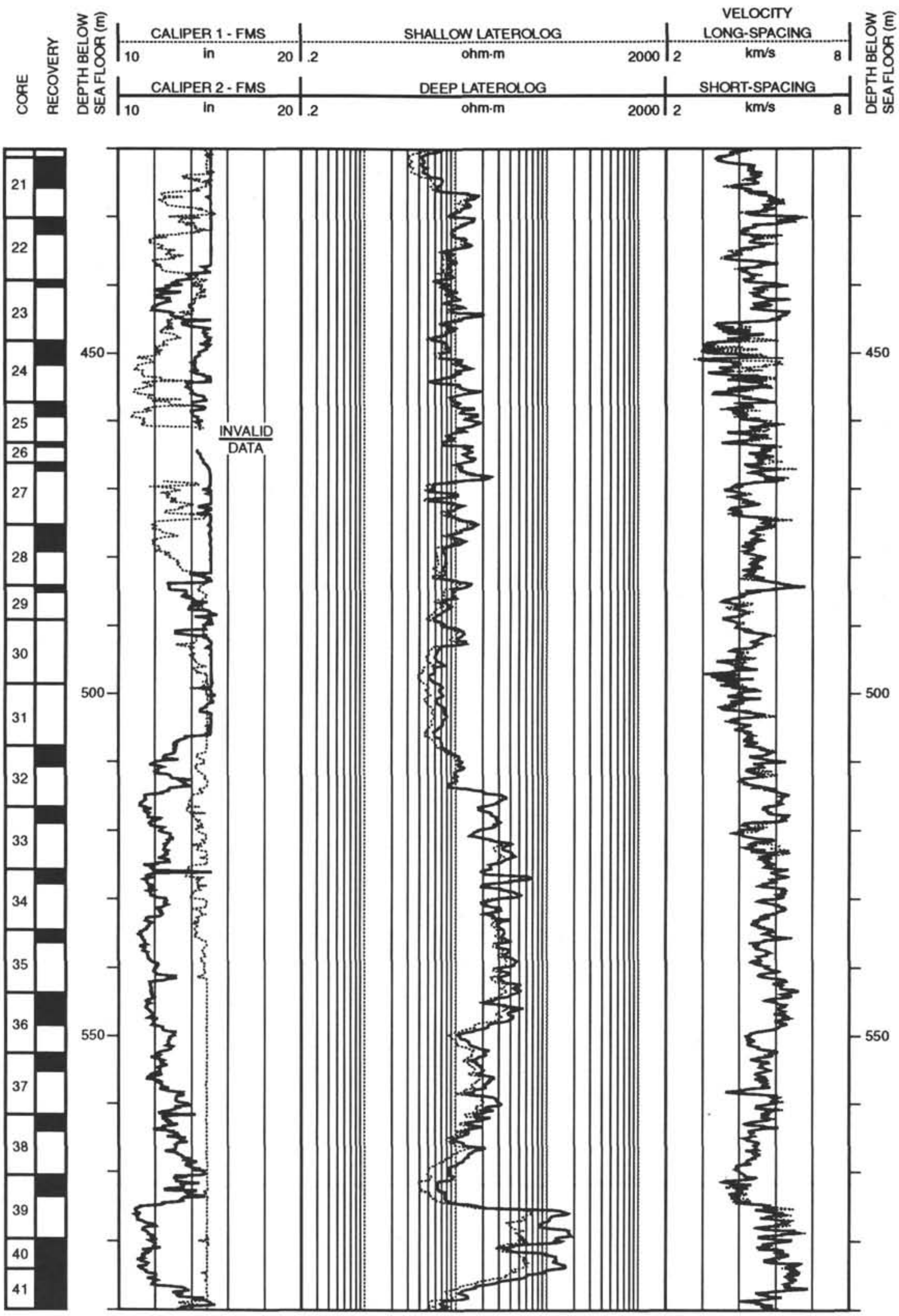

Hole 504B: Resistivity-Velocity Log Summary (continued)

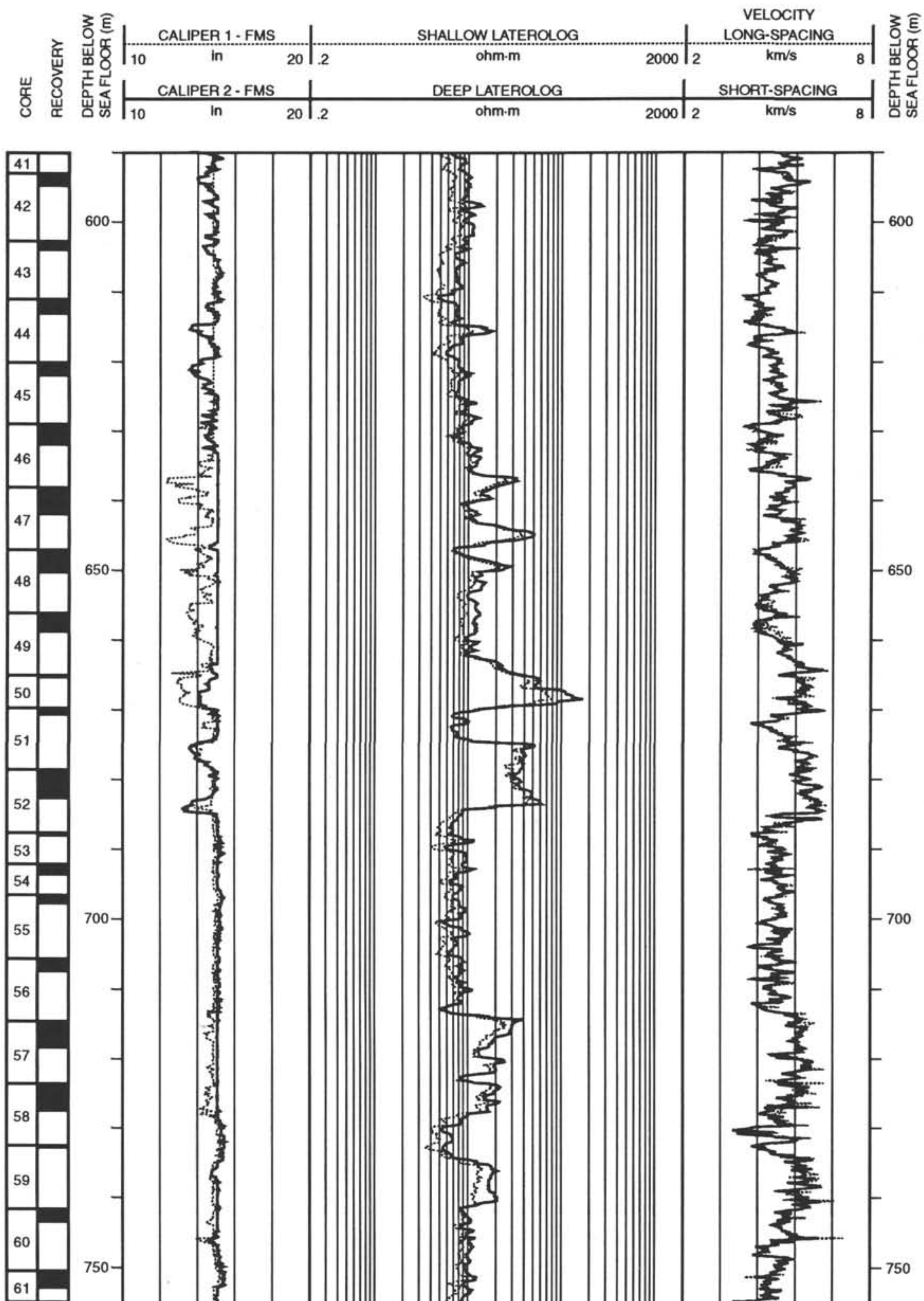

Hole 504B: Resistivity-Velocity Log Summary (continued)

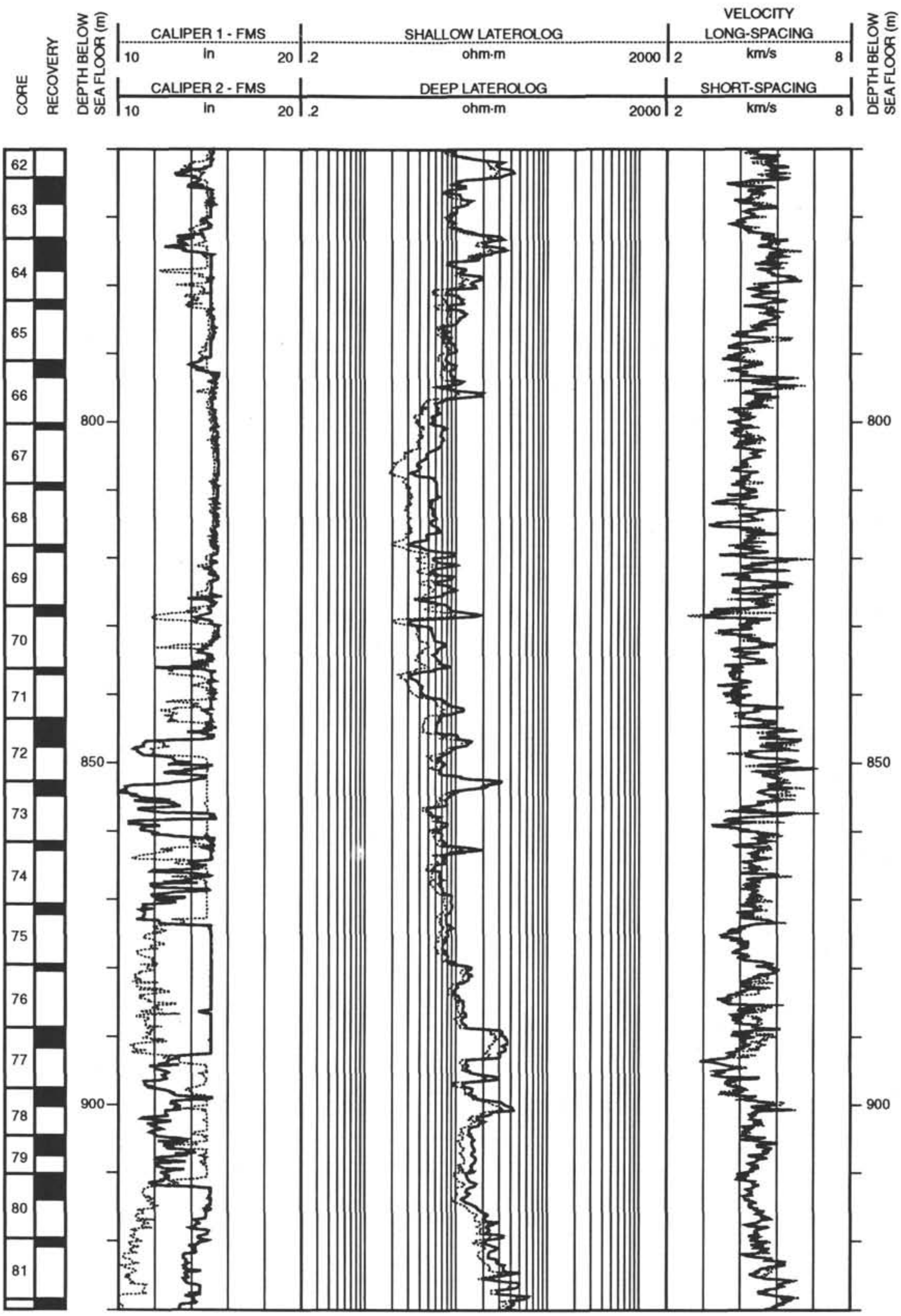

Hole 504B: Resistivity-Velocity Log Summary (continued)

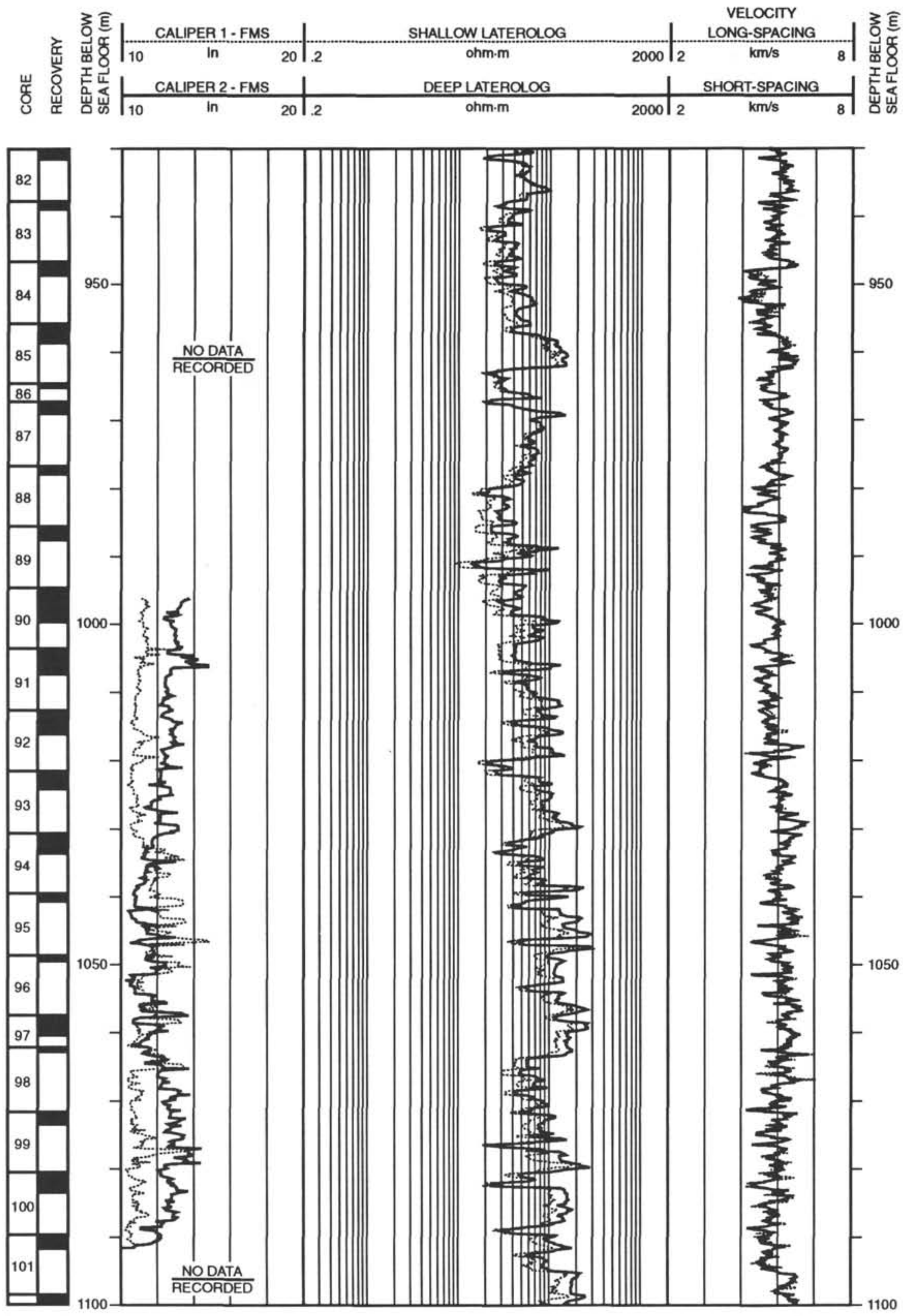

Hole 504B: Resistivity-Velocity Log Summary (continued)

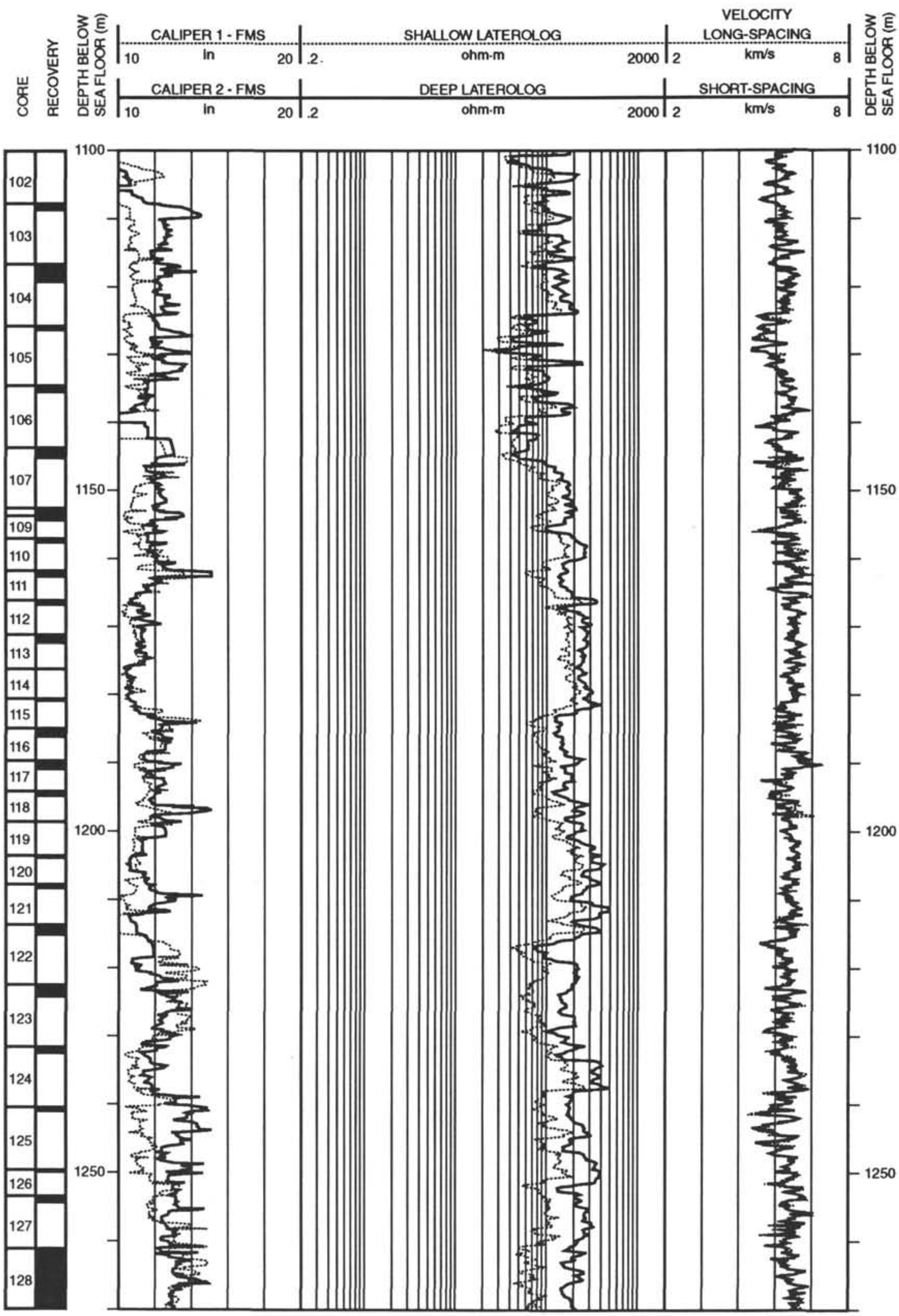

Hole 504B: Resistivity-Velocity Log Summary (continued)

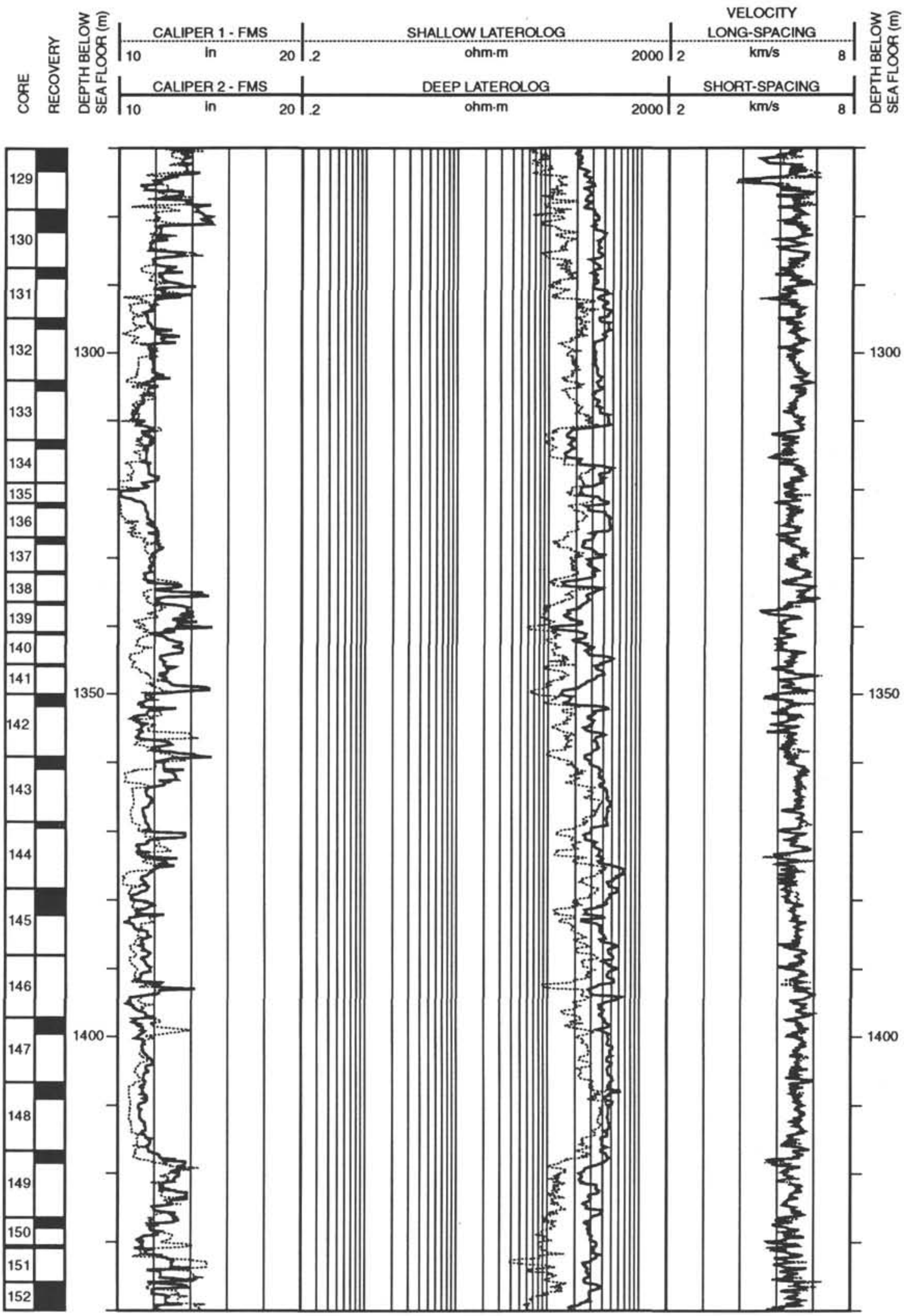

Hole 504B: Resistivity-Velocity Log Summary (continued)

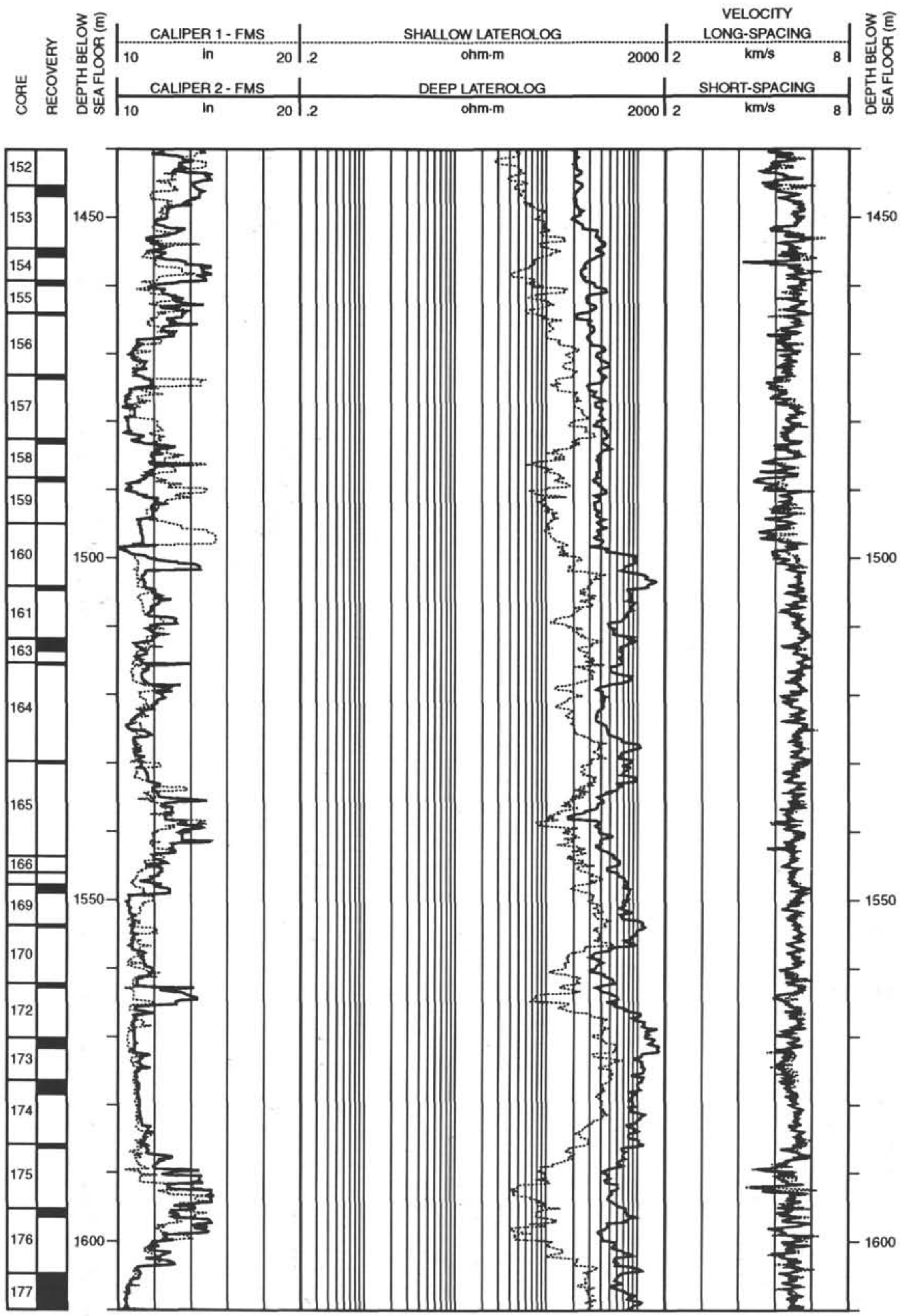

Hole 504B: Resistivity-Velocity Log Summary (continued)

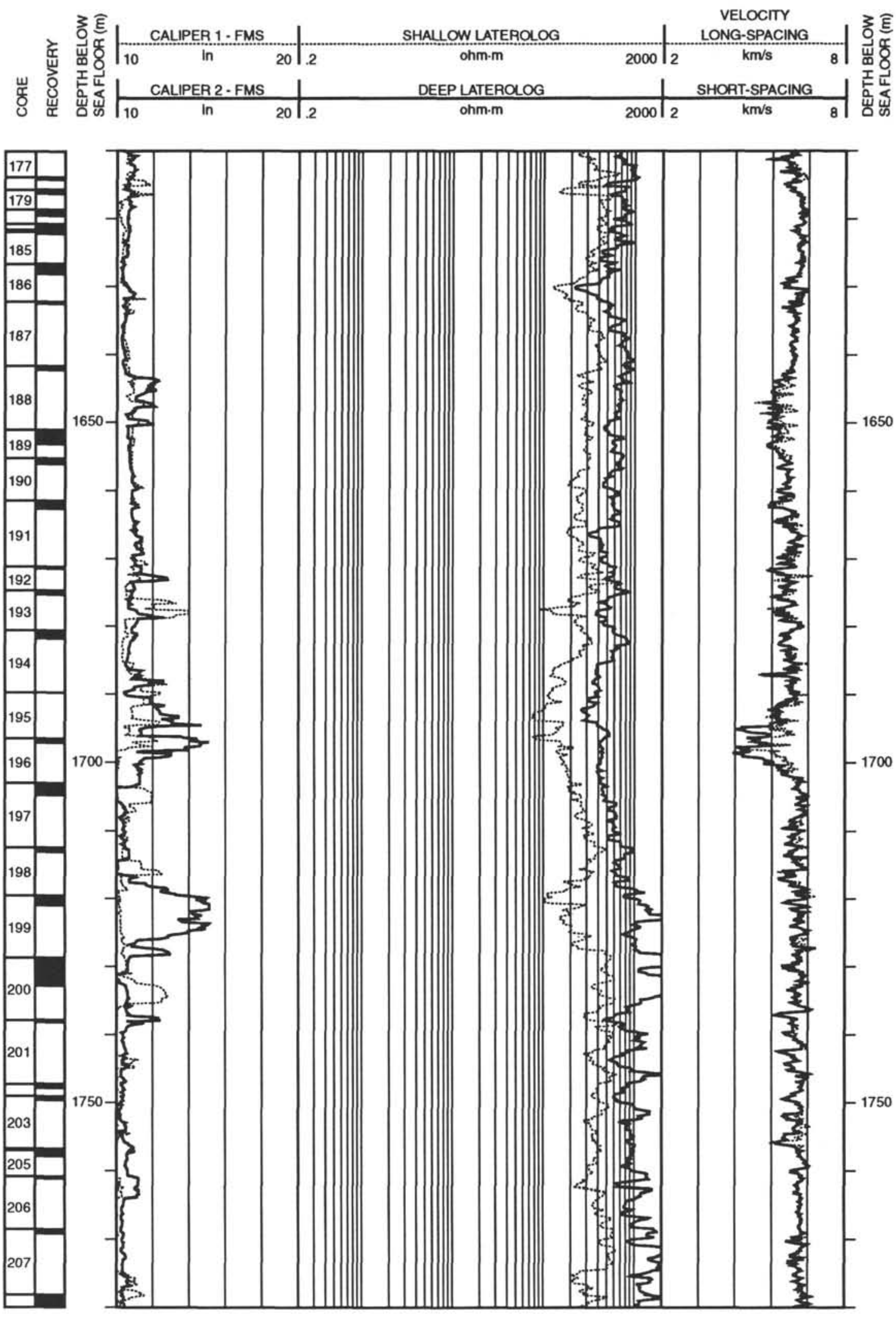

Hole 504B: Resistivity-Velocity Log Summary (continued)

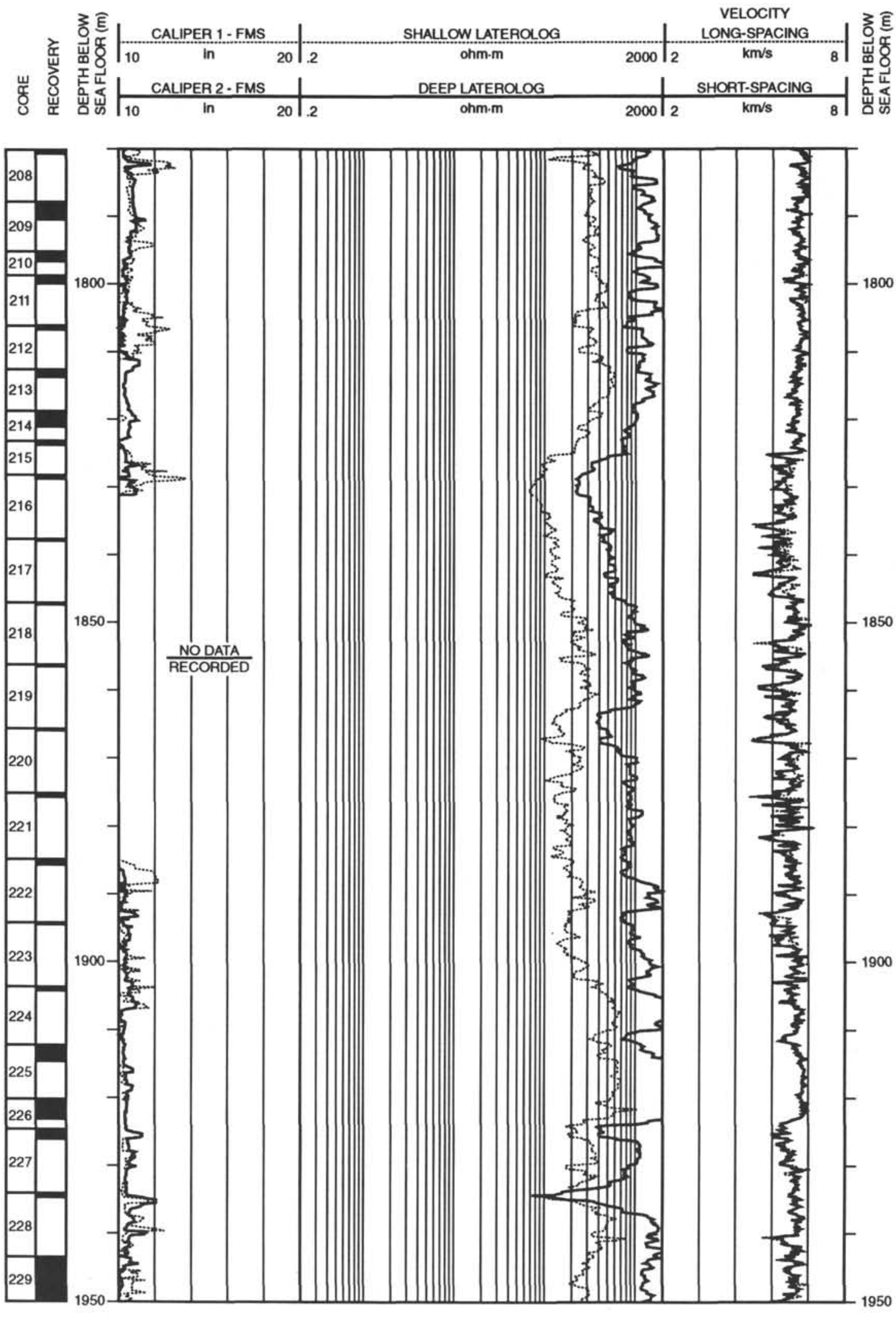

Hole 504B: Resistivity-Velocity Log Summary (continued)

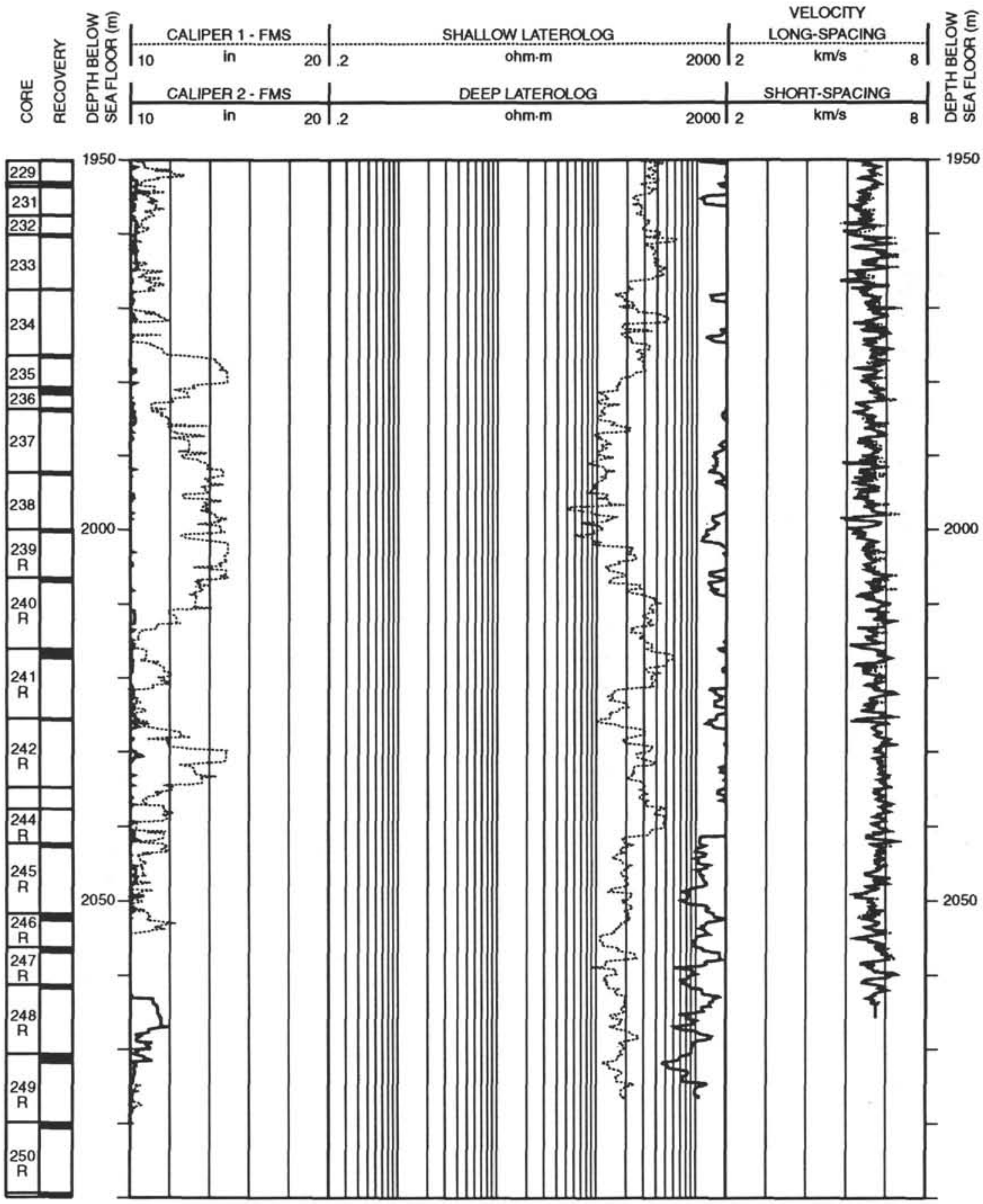

Hole 504B: Natural Gamma Ray Log Summary

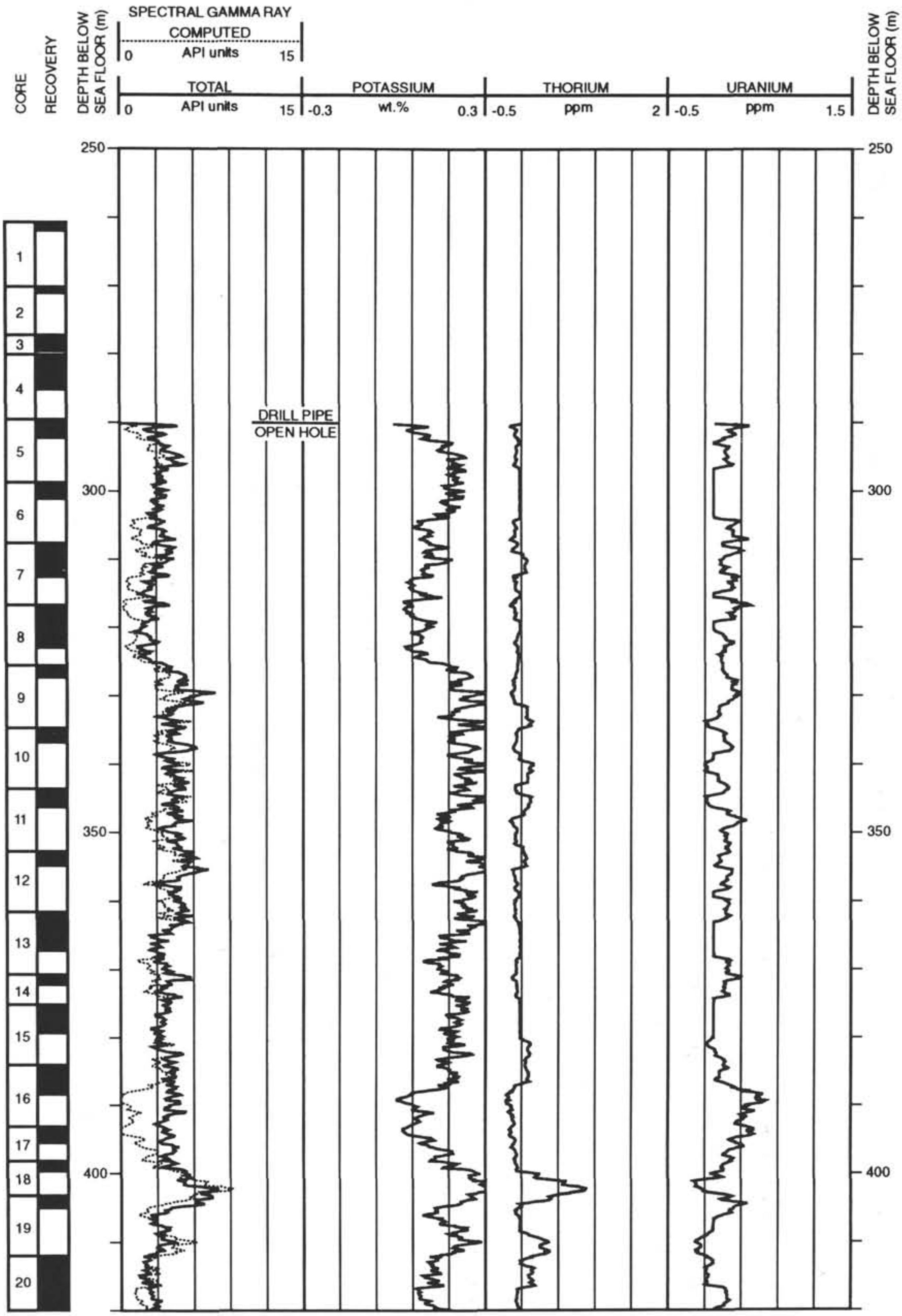

Hole 504B: Natural Gamma Ray Log Summary (continued)

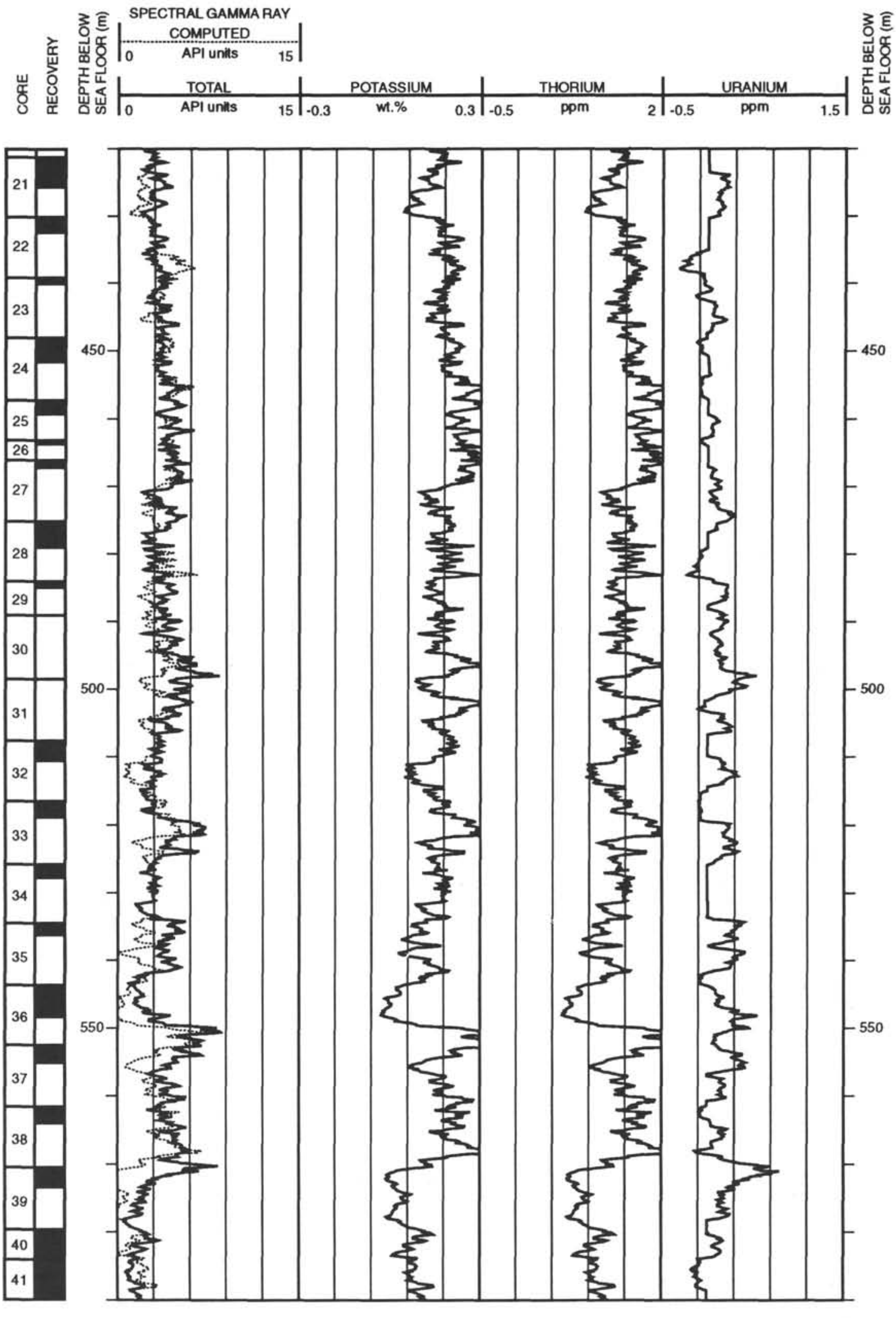

Hole 504B: Natural Gamma Ray Log Summary (continued)

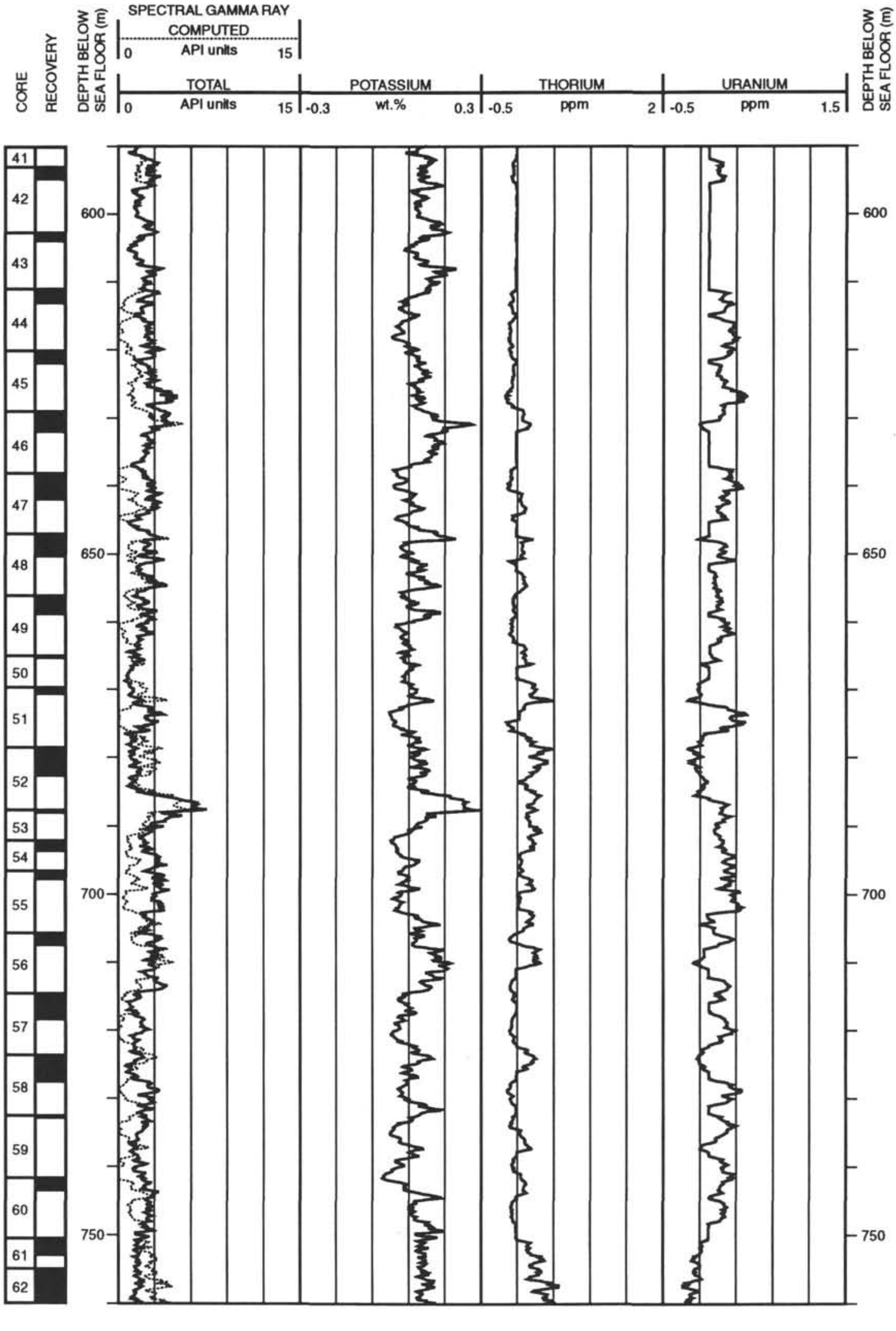

Hole 504B: Natural Gamma Ray Log Summary (continued)

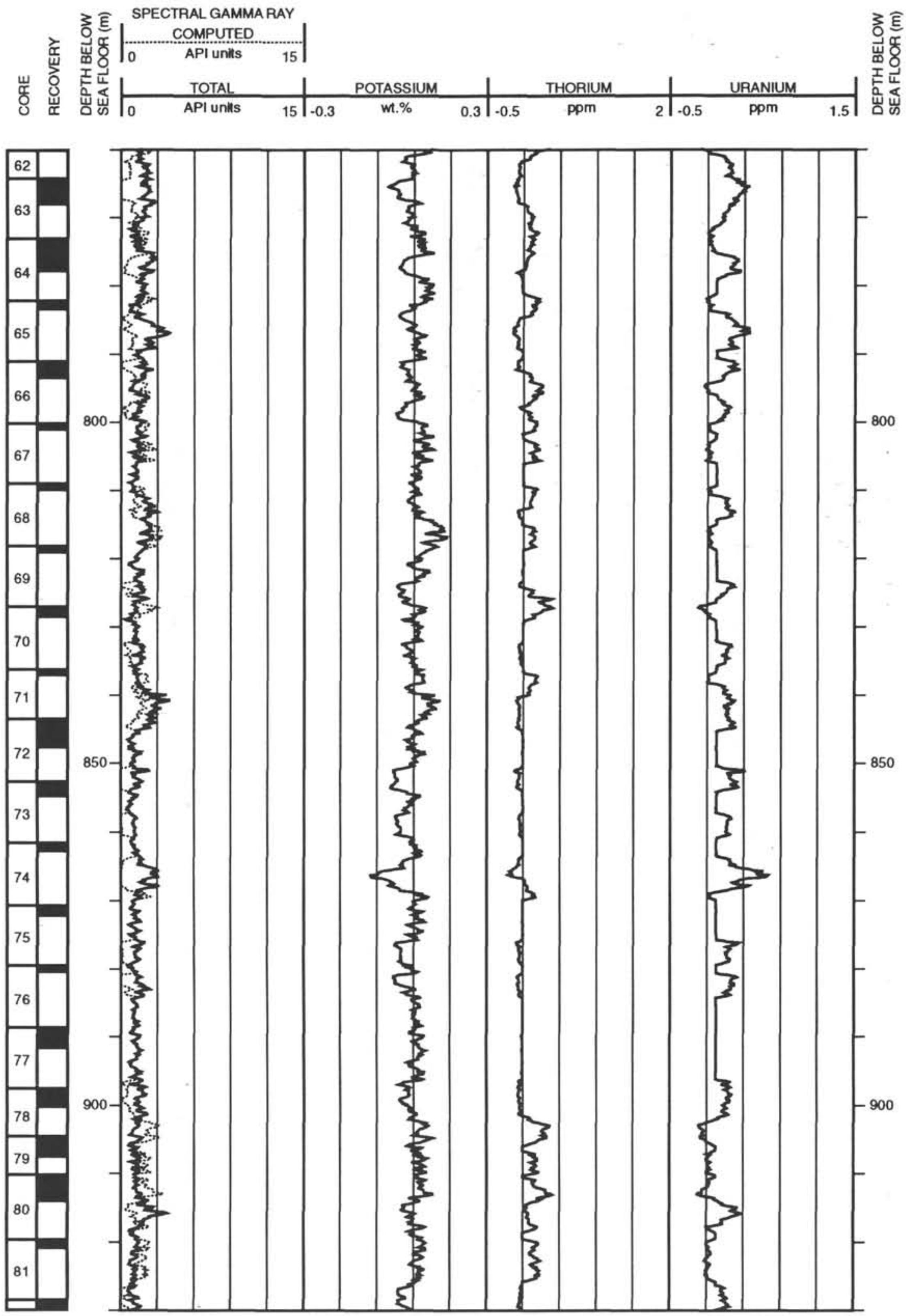

Hole 504B: Natural Gamma Ray Log Summary (continued)

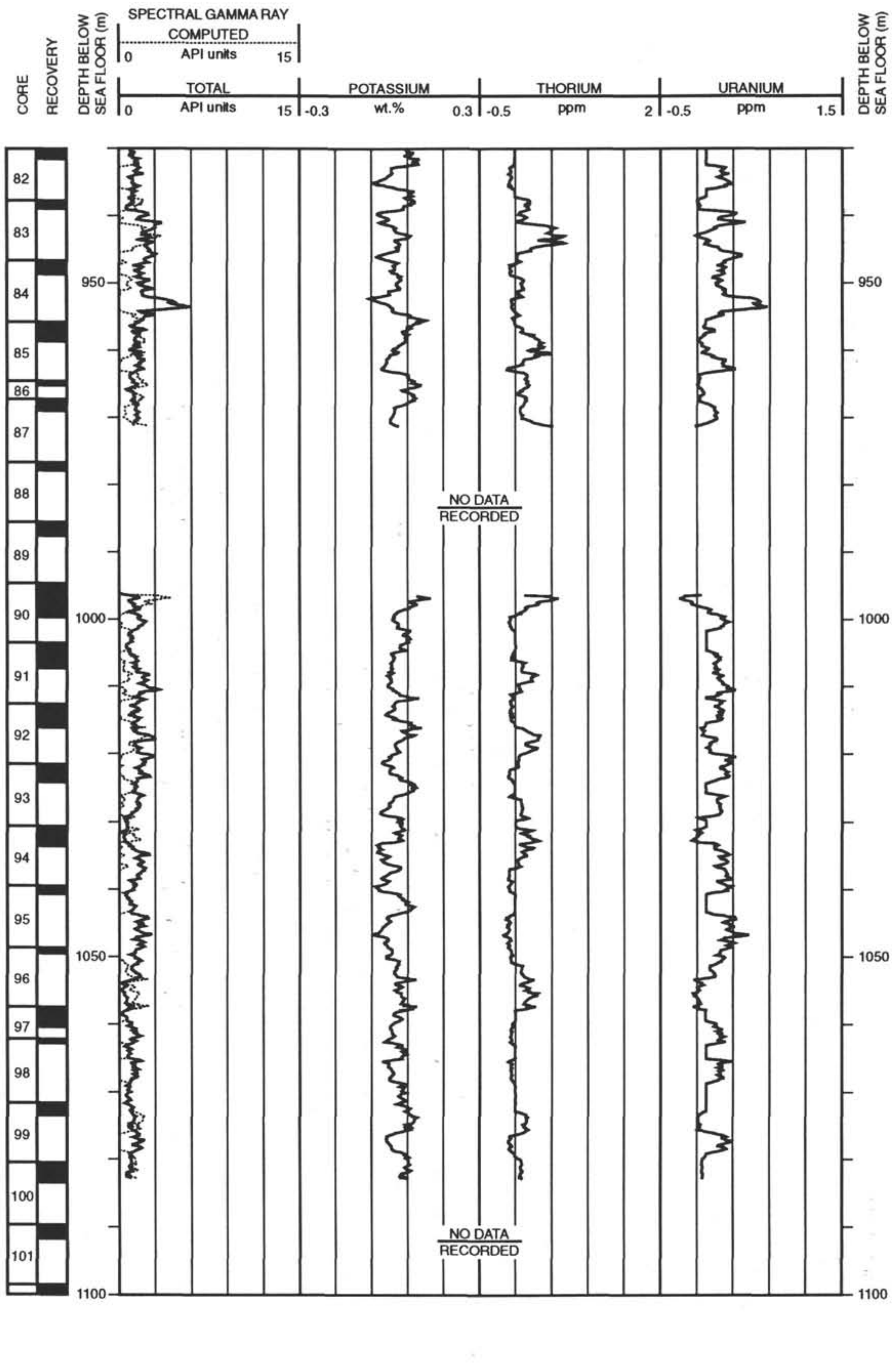

Hole 504B: Natural Gamma Ray Log Summary (continued)

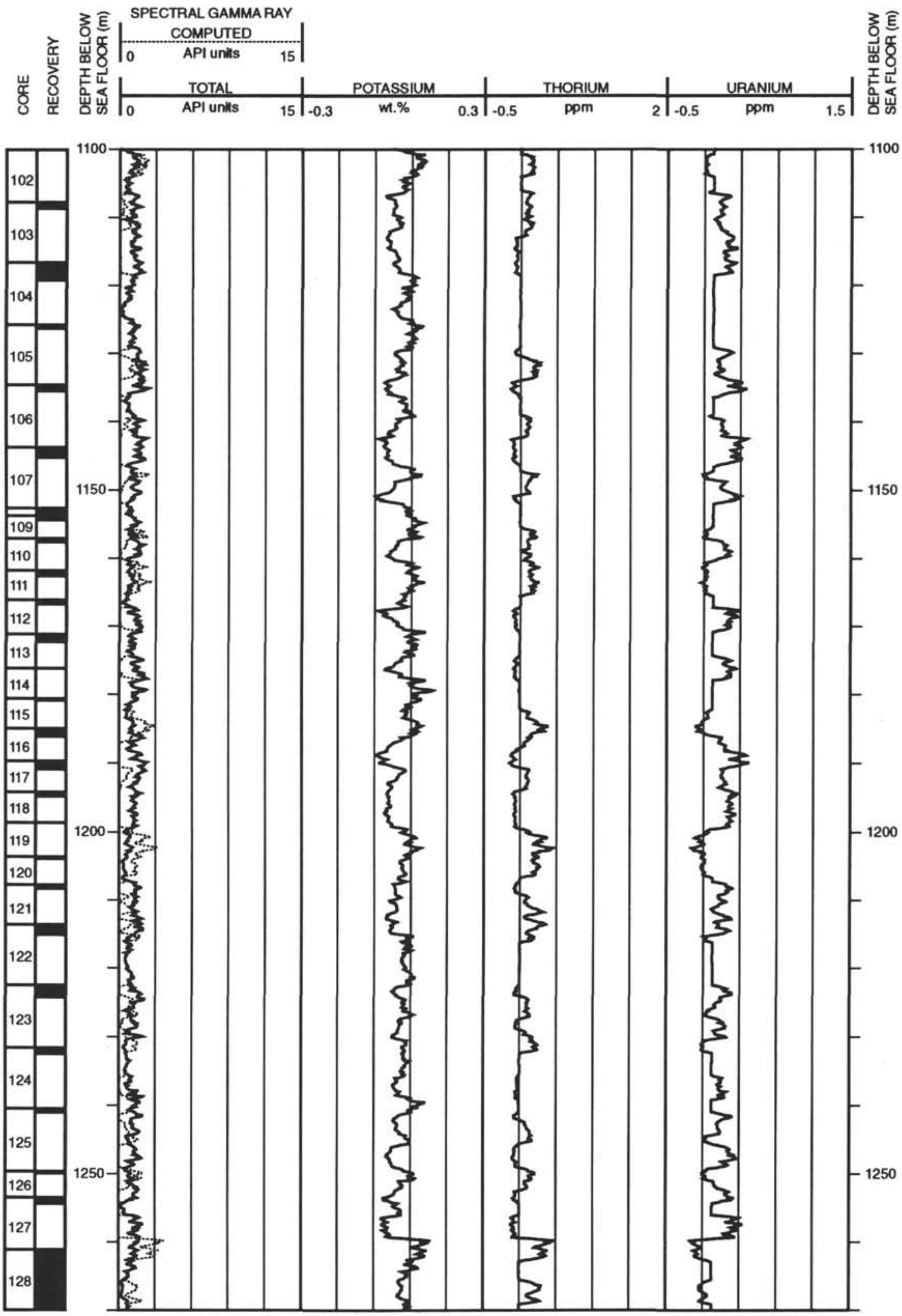

Hole 504B: Natural Gamma Ray Log Summary (continued)

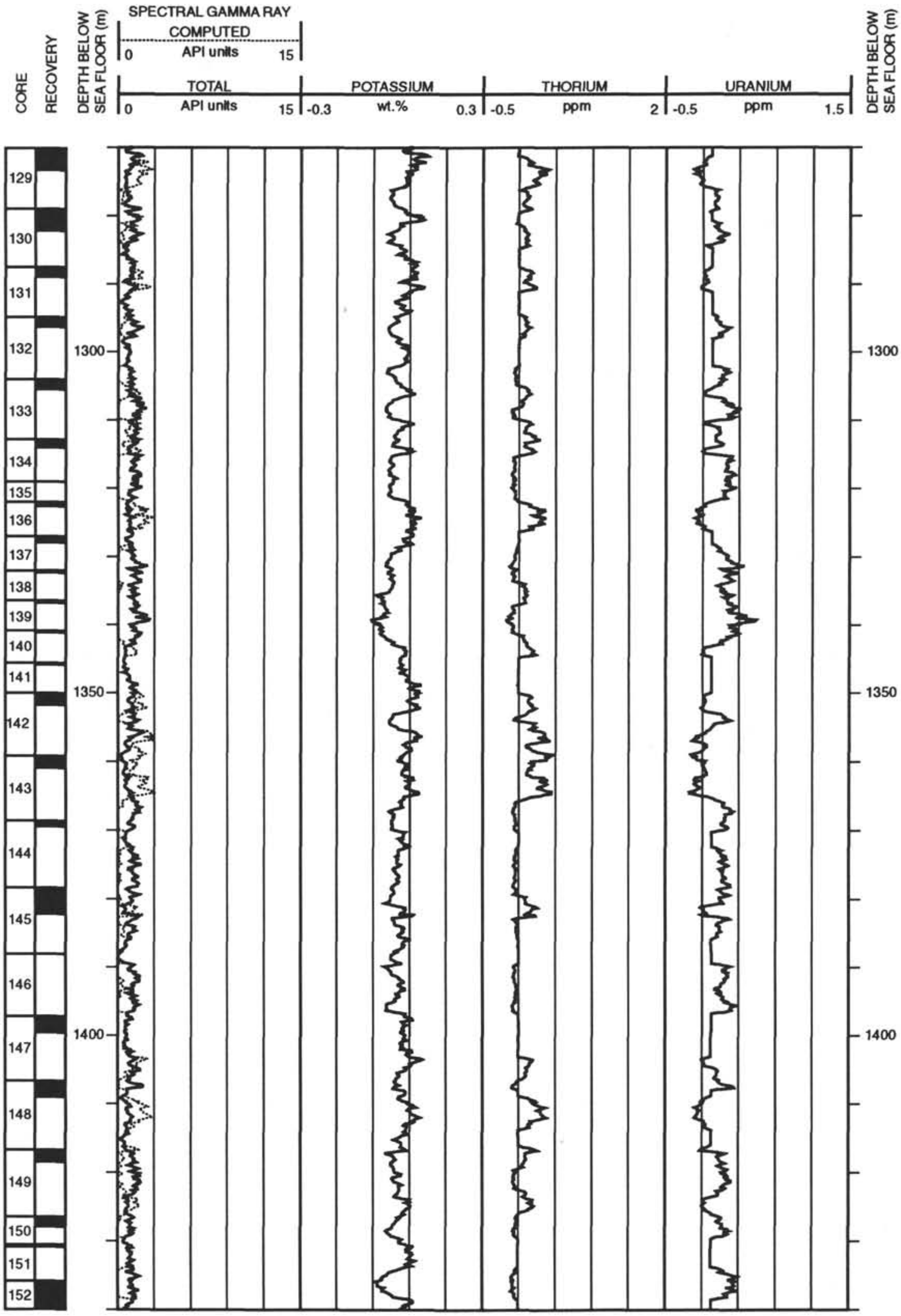

Hole 504B: Natural Gamma Ray Log Summary (continued)

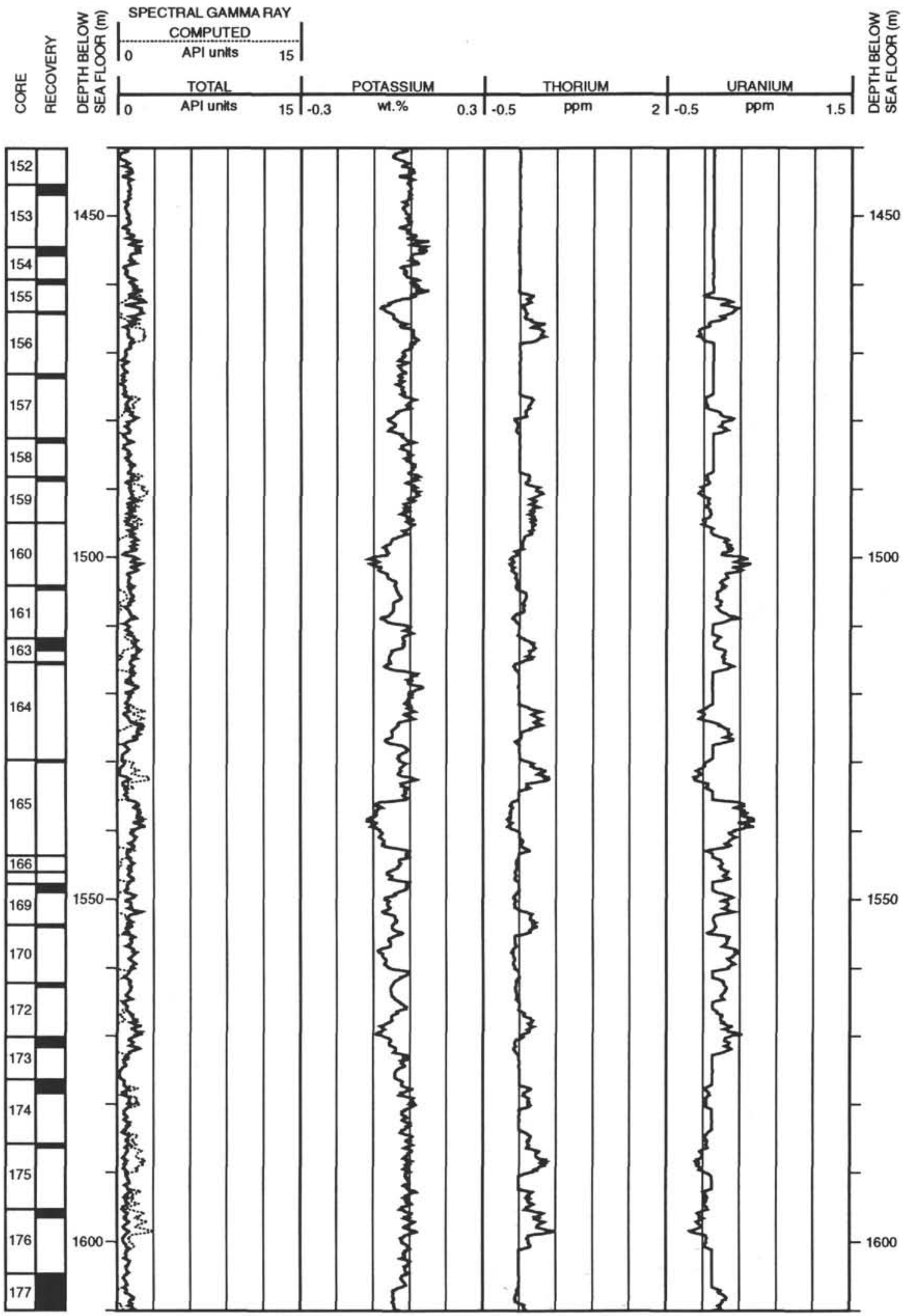

Hole 504B: Natural Gamma Ray Log Summary (continued)

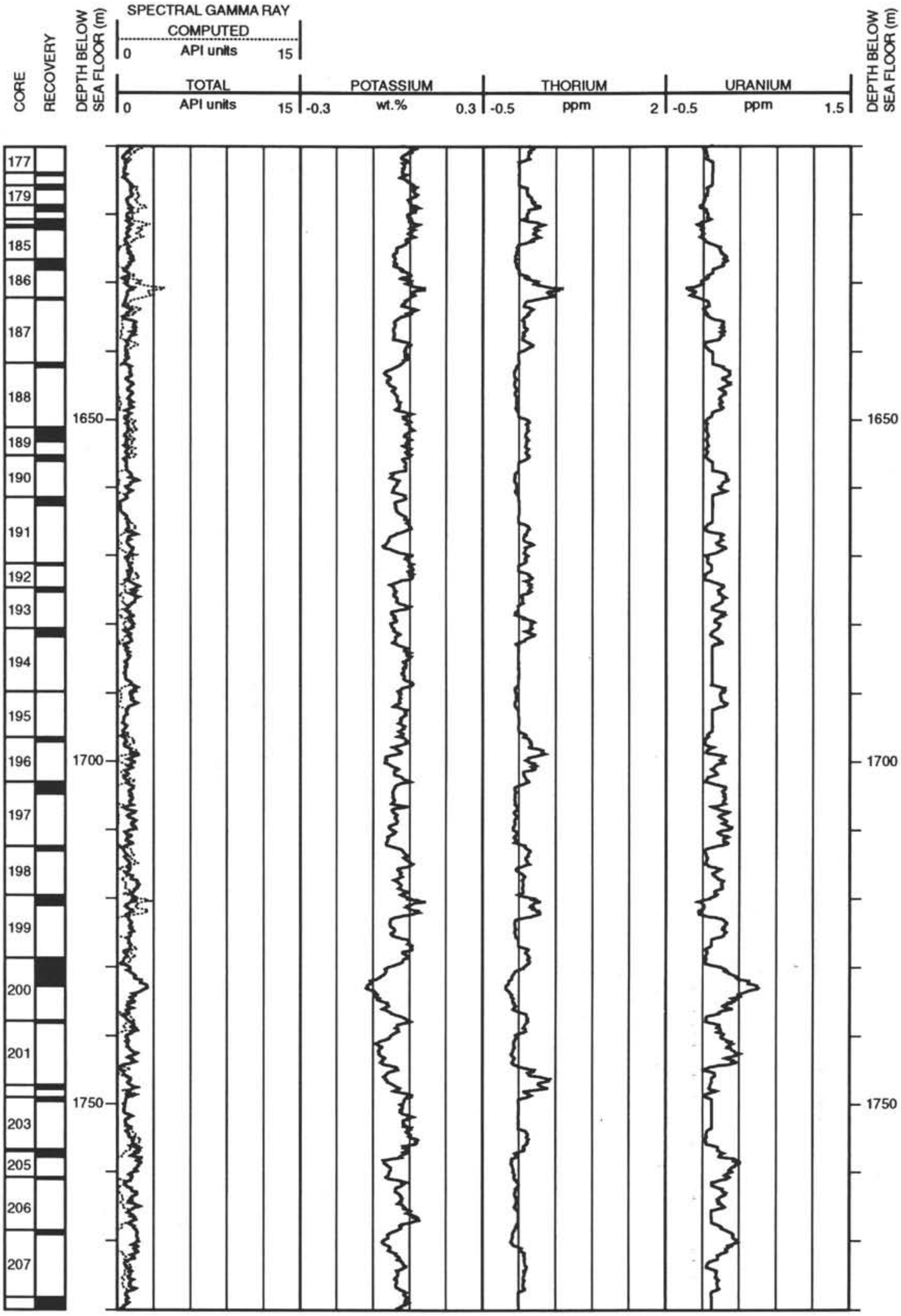

Hole 504B: Natural Gamma Ray Log Summary (continued)

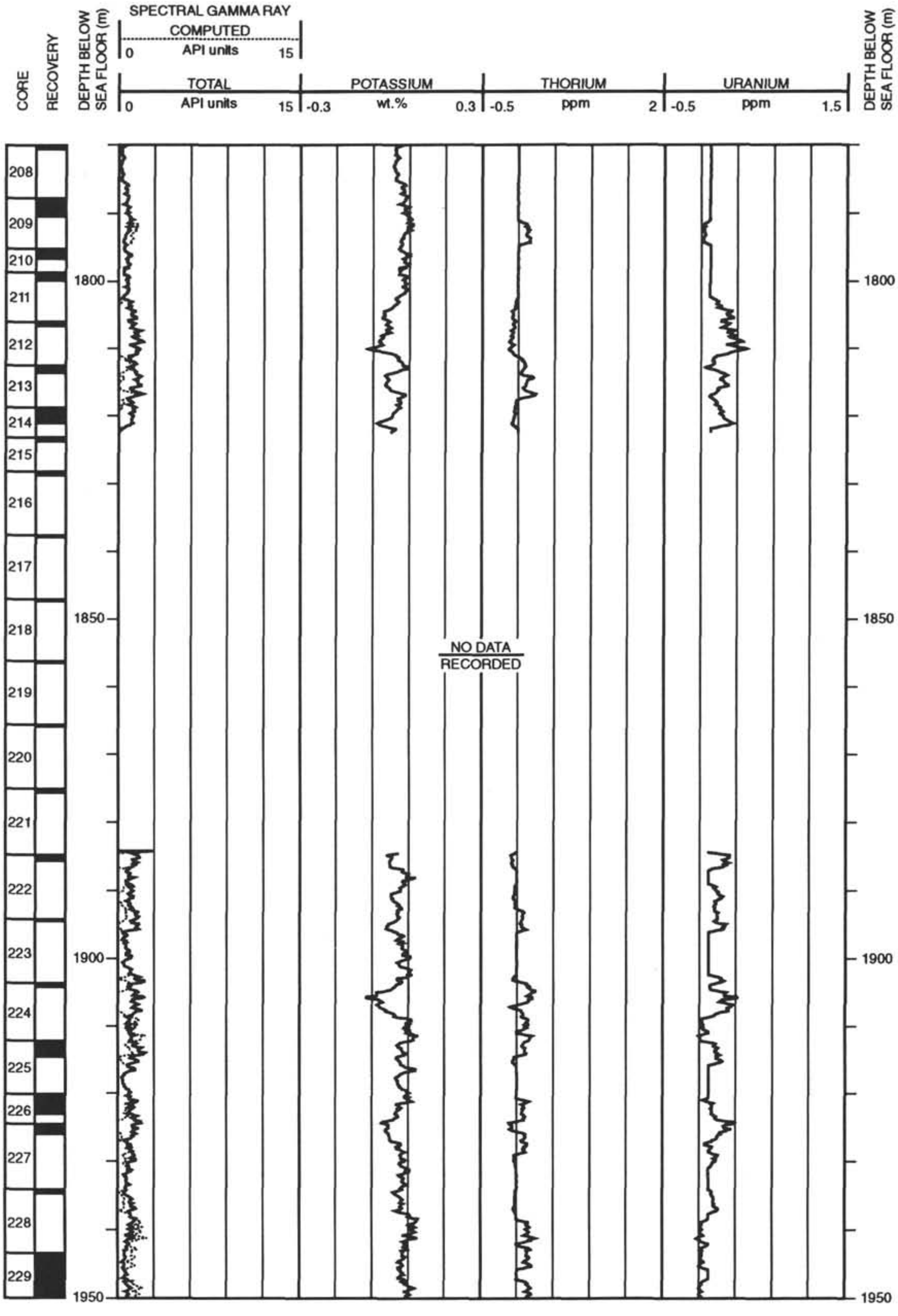

Hole 504B: Natural Gamma Ray Log Summary (continued)

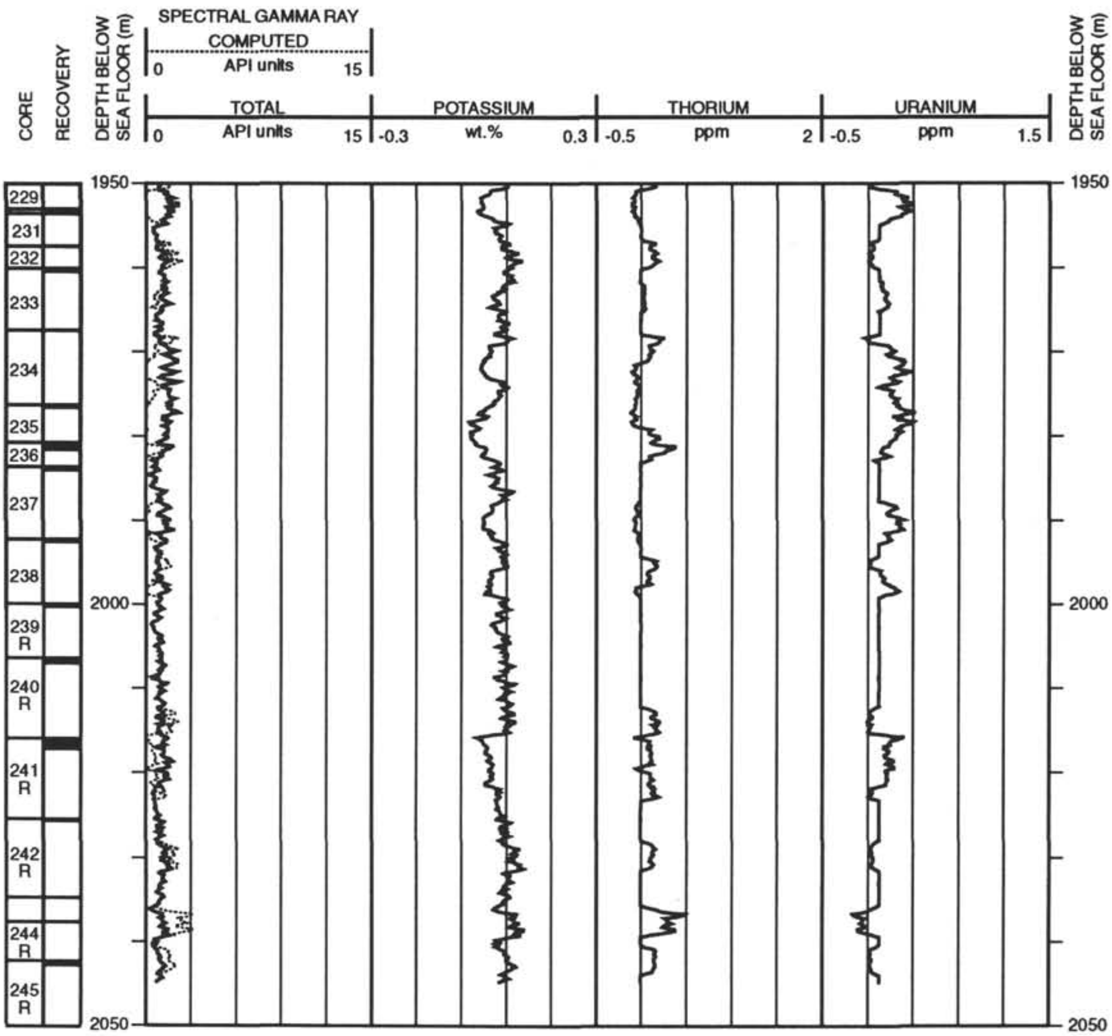

Appendix A. Leg 148, Hole 504B. Igneous contact log. Letters P, O, and C under lithology refer to the presence of plagioclase, olivine, and clinopyroxene phenocrysts, respectively. The types of contacts indicated in Character of lower contact are discussed in the "Explanatory Notes" and 504B site chapter.

Core	Section	Base of unit (cm)	Piece	Unit	Lithology	Character of lower contact	Dip	Notes
239R	1	41	12	270	Sparsely phyric PC diabase.	Not observed (case 3).	—	Upper unit has less olivine than lower unit.
239R	1	50	14	271	Moderately phyric POC diabase.	Not observed (case 3).	—	Upper unit has more olivine than lower unit.
240R	1	40	10	272	Sparsely phyric PC diabase.	Not observed (case 3).	—	Upper unit is finer grained and has less olivine.
240R	1	81	20	273	Moderately phyric POC diabase.	Chilled margin may be the bottom of this unit (case 1A). Contact is planar and sharp.	—	Units above and below the chilled margin are nearly identical in grain size and mineralogy.
240R	1	99	22	274	Moderately phyric POC diabase.	Not observed (case 3).	—	Upper unit coarser and has more olivine.
241R	1	11	3	275	Moderately phyric POC diabase.	Not observed (case 3).	—	Upper unit finer-grained less olivine phyric.
242R	1	10	2	276	Moderately phyric POC diabase.	Not observed (case 3).	—	Upper unit coarser.
242R	1	36	10	277	Aphyric diabase.	Not observed (case 3).	—	Upper unit aphyric, finer grained.
242R	1	39	12	278	Moderately phyric POC diabase.	Not observed (case 3).	—	Upper unit more coarse and more phyric.
244R	1	8	2	279	Aphyric diabase.	Not observed (case 3).	—	Upper unit finer grained and is gradational into aphanitic.
245R	1	36	12	280	Sparsely phyric PC diabase.	Case 1 A. Planar and sharp contact.	—	Glassy contact of Units 280 and 281 is in Piece 13.
245R	1	51	16	281	Sparsely phyric PO diabase.	Not observed (case 3).	—	Upper unit is a mixture of lithologies with different grain sizes and phenocrysts and phenocryst abundances.
246R	1	2	1	282	Sparsely phyric PC diabase.	Not observed (case 3).	—	Last piece in unit is extremely fine grained.
246R	1	73	20	283	Sparsely phyric PO diabase.	Not observed (case 3).	—	Upper unit is finer-grained.
247R	1	3	1	284	Sparsely phyric PO diabase.	Not observed (case 3).	—	Upper unit is coarser-grained.
247R	1	68.5	15	285	Moderately phyric PO diabase.	Not observed (case 3).	—	Upper unit is coarser-grained and less olivine phyric.
248R	1	11	3	286	Moderately phyric OP diabase.	Not observed (case 3).	—	Upper unit is finer grained and more olivine phyric.
248R	1	24	7a	287	Moderately phyric OP diabase.	Case 1B. Chilled margin is planar and sharp.	—	Fragment of chilled margin is on Piece 7A. Upper unit less olivine phyric.
249R	1	8	2	288	Moderately phyric POC diabase.	Not observed (case 3).	—	Upper unit coarser-grained and phenocrysts are more abundant.
249R	1	11	3	289	Aphyric basalt.	Not observed (case 3).	—	Upper unit finer-grained and less phenocryst rich.
249R	1	99	28	290	Moderately phyric PO diabase.	Case 1B. Chilled margin of Unit 291 is preserved.	76	Planar chilled margin in Piece 28. Also a small patch of chill in Piece 26 is probably part of this margin.
250R	1	103	28	291	Moderately phyric OPC diabase.	Not observed (case 3).	—	Upper unit is coarser-grained.
251R	1	12	3	292	Moderately phyric POC diabase.	Not observed (case 3) but chilled margin in Piece 4 is planar and sharp.	84	Thin rind of altered chilled margin on working half of Piece 4. Possible chilled margin to this unit but relationships unclear. Upper unit finer-grained.
252R	1	36	9	293	Moderately phyric POC diabase.	Not observed (case 3).	—	Upper unit glomerophyric and more phenocryst rich than lower unit.
				294	Sparsely phyric OPC diabase.	Base of unit not determined.	—	

Appendix B. Leg 148, Hole 504B. Igneous mineralogy log. Ph = phenocryst; Gm = intergranular material; GS = grain size; Mor = morphology; Ox = opaque minerals; and S = sulfides. Phenocryst and intergranular grain sizes are in millimeters (mm); — = not observed. Morphology 1 indicates phenocryst *a* is euhedral, *b* is subhedral, and *c* is anhedral. The estimates are based on observations made with the unaided eye and with binocular microscopes with magnification up to x50.

					Plagioclase					Augite					Olivine						
Core	Section	Piece	Interval (cm)	Unit	Ph (%)	Gm (%)	Ph GS	Gm GS	Mor	Ph (%)	Gm (%)	Ph GS	Gm GS	Morphology	Ph (%)	Gm (%)	Ph GS	Gm GS	Morphology	Ox (%)	S (%)
239R	1	1–12	0–41	270	1	57	1	0.5	1a,b	0.5	41	1.5	0.5	1a,b	0.1	—	1	—		—	0.1
239R	1	13–14	41–50	271	3	55	1	0.5	1a,b	1	40	2	0.5	1a,b	1	—	0.5	—	1a,b	—	0
240R	1	1–10, 12	0–40	272	1	55	1.5	0.5	1a,b	0.2	44	0.5	0.4	1b	0.1	—	0.5	—	1a,b	—	0.1
240R	1	11, 13–20	40–81	273	2	50	1	0.6	1a,b	1	45	0.8	0.5	1b	2	—	1.5	—	1a,b	—	0
240R	1	21,22	81–99	274	0.5	58.5	2	1	1a,b	0.5	39	2	1	1a	1.5	—	1.5	—	1b	—	—
241R	1	1–3	0–11	275	1	52.4	1.5	0.5	1a,b	0.5	44	2	0.4	1a,b	1	1	1.1	0.2	1b,a	—	0.1
241R	1	4–26	11–148	276	4	57	1.5	0.7	1a,b	1	37	1	0.5	1a,c	1	—	1	—	1a	0.1	0.1
241R	2	1	0–5	276	4	57	1.5	0.7	1a,b	1	37	1	0.5	1a,c	1	—	1	—	1a	0.1	0.1
242R	1	1,2	0–10	276	4	57	1.5	0.7	1a,b	1	37	1	0.5	1a,c	1	—	1	—	1a	0.1	0.1
242R	1	3–10	10–36	277	0.2	59.7	1.3	0.7	1a,b	0.2	40	1	0.5	1b,c	0.2	—	0.4	—	1a,b	—	0.1
242R	1	11–12	36–39	278	3	51	1	0.5	1a,b	1	44	1	0.5	1b	1	—	1	—	1a	0.1	0.1
244R	1	1–2	0–8	279	0.2	59	1.5	0.5	1a,b	—	40	—	0.4	1a,b,c	—	1	—	0.4	1a,b,c	—	—
245R	1	1–12	0–36	280	1	57.8	1.5	0.6	1a,b	1	40	1	0.5	1a,b	—	—	—	—	—	0.2	—
245R	1	13–16	36–51	281	1.5	58	1.5	0.4	1a	—	40	—	0.5	1b,c	0.2	1	1	0.1	1a,b	0.2	—
245R	1	17–18	51–58	282	0.5	54	1	0.5	1a, b, c	0.5	43	1.5	0.4	1b,c	—	1	—	0.2	1b	0.2	0.1
246R	1	1	0–2	282	0.5	54	1	0.5	1a, b, c	0.5	43	1.5	0.4	1b, c	—	1	—	0.2	1b	0.2	0.1
246R	1	2–20	2–73	283	1	53	1.2	0.8	1a,b,c laths	—	45	—	0.5	1a,b,c	0.5	—	1	0.5	1a	0.5	0.1
246R	1	21–32	73–115	284	1	54	1.5	0.8	1a,b,c	—	43	—	0.5	1b,c	1	—	0.8	—	1a	1	0.01
247R	1	1	0–3	284	1	54	1.5	0.8	1a,b,c	—	43	—	0.5	1b,c	1	—	0.8	—	1a	1	0.01
247R	1	2–15	3–68.5	285	2	50	1.5	0.6	1a,b	—	44	—	0.5	1b,c	2	0.5	1	0.3	1a,b	1.5	0.05
247R	1	16–21	68.5–89	286	1	50	0.8	0.3	1a,b	—	45	—	0.3	1c	2	0.5	1	0.2	1b	1	0.05
248R	1	1–3	0–11	286	1	50	0.8	0.3	1a,b	—	45	—	0.3	1c	2	0.5	1	0.2	1b	1	0.05
248R	1	4–7	11–24	287	1	50	1	0.5	1a,b	—	45	—	0.3	1b,c	2	1	1	0.5	1a,b	1	0.2
248R	1	8–17	24–62	288	0.5	50	1	0.5	1a	0.2	45	1	0.5	1b	1.5	—	1	—	1a	2.8	0.05
249R	1	1–2	0–8	288	0.5	50	1	0.5	1a	0.2	45	1	0.5	1b	1.5	—	1	—	1a	2.8	0.05
249R	1	3	8–11	289	0.2	—	0.25	—	1a,b	—	—	—	—	—	0.2	—	0.3	—	1b	—	—
249R	1	4–28	11–99	290	2	51	1	0.4	1a,b	—	44	—	0.4	1b,a	1	1	0.9	0.4	1a,b	1	—
249R	1	29–41	99–148	291	1	50	1.2	0.6	1a,b	0.5	44	1	0.6	1a,b	1.5	1	1	0.3	1a,b	2	0.05
249R	2	1–6	0–25	291	1	50	1.2	0.6	1a,b	0.5	44	1	0.6	1a,b	1.5	1	1	0.3	1a,b	2	0.05
250R	1	1–28	0–103	291	1	50	1.2	0.6	1a,b	0.5	44	1	0.6	1a,b	1.5	1	1	0.3	1a,b	2	0.05
250R	1	29–32	103–117	292	2	50	1	0.4	1a,b	1	45	0.8	0.4	1a,b	1.2	—	0.6	—	1a,b	0.7	0.1
251R	1	1–3	0–12	292	1	50	1	0.3	1a,b	1	45	0.8	0.4	1b,c laths + equant	0.5	—	0.5	—	1a,b equant	1	0.1
251R	1	4–20	12–109	293	2	50	1.5	0.5	1a,b	0.5	46	1	0.5	1a/1b,c	1.5	—	1	—	1b	1	0.2
252R	1	1–9	0–37				1.5	0.5	1a,b	0.5	46	1	0.5	1a/1b,c	1.5	—	1	—	1b	1	0.2
253R	1	1	0–5	294	0.5	51.3	1	0.3	1a,b	0.5	45	1.5	0.4	1b	1	—	1	—	1a,b	1.5	0.2

Appendix C. Leg 148, Hole 504B. Igneous lithology log. The lithology (rock name) is determined using the conventions given in the "Explanatory Notes."

Core	Section	Piece	Interval (cm)	Unit	Lithology	Texture	Structure	Munsell color
239R	1	1–12	0–42	270	Sparsely phyric PC diabase.	Fine-grained, porphyritic, subophitic.	Homogeneous.	5BG 6/1 greenish gray
239R	1	13,14	42–52	271	Moderately phyric POC diabase.	Fine-grained, porphyritic, subophitic.	Homogeneous.	5BG 6/1 greenish gray
240R	1	1–10, 12	1–40	272	Sparsely phyric PC diabase.	Fine-grained, intergranular.	Homogeneous.	5BG 6/1 greenish gray
240R	1	11, 13–20	40–81	273	Moderately phyric POC diabase.	Fine-grained porphyritic.	Homogeneous.	5B 5/1 bluish gray
240R	1	21,22	81–99	274	Moderately phyric POC diabase.	Ophitic/subophitic glomerophyritic.	Homogeneous.	5B 6/1 bluish gray
241R	1	1–3	0–11	275	Moderately phyric POC diabase.	Fine-grained, porphyritic, subophytic.	Homogeneous.	5B 5/1 bluish gray
241R	1	4–26	11–148	276	Moderately phyric POC diabase.	Fine-grained, porphyritic, subophytic.	Homogeneous.	5B 5/1-5B 6/1 bluish gray
241R	2	1	0–5	276	Moderately phyric POC diabase.	Fine-grained, porphyritic, subophytic.	Homogeneous.	5B 5/1-5B 6/1 bluish gray
242R	1	1–2	0–10	276	Moderately phyric POC diabase.	Fine-grained, porphyritic, subophytic.	Homogeneous.	5B 5/1-5B 6/1 bluish gray
242R	1	3–10	10–36	277	Aphyric diabase.	Fine-grained, intergranular.	Homogeneous.	5B 5/1 bluish gray
242R	1	11	36–39	278	Moderately phyric POC diabase.	Fine-grained, porphyritic, subophytic.	Homogeneous.	5BG 5/1-5B 5/1 greenish gray to bluish gray
244R	1	1–2	0–8	279	Aphyric diabase.	Fine-grained, grading into aphanitic.	Homogeneous, massive.	5B 5/1 bluish gray
245R	1	1–12	0–36	280	Sparsely phyric PC diabase.	Fine-grained hypidiomorphic granular diabase grading to smaller grains downward.	Homogeneous.	5B 5/1-5B 4/1 bluish gray to dark bluish gray
245R	1	13–16	36–51	281	Sparsely phyric PO diabase.	Fine-grained, porphyritic.	Homogeneous, massive.	5BG 5/1-5B 5/1-5B 4/1 greenish gray to dark bluish gray
245R	1	17–18	51–58	282	Sparsely phyric PC diabase.	Fine-grained, porphyritic.	Homogeneous, massive.	5BG 5/1-5B 5/1 greenish gray to bluish gray
246R	1	1	0–2	282	Sparsely phyric PC diabase.	Fine-grained, porphyritic.	Homogeneous, massive.	5BG 5/1-5B 5/1 greenish gray to bluish gray
246R	1	2–20	2–73	283	Sparsely phyric PO diabase.	Fine-grained intergranular, subophitic, seriate porphyritic, some pieces with varying grain size.	Homogeneous, massive.	5BG 5/1-5B 5/1 greenish gray to bluish gray
246R	1	21–32	73–115	284	Sparsely phyric PO diabase.	Fine-grained, porphyritic, subophitic.	Homogeneous, massive.	5B 4/1-5B 5/1 dark bluish gray to bluish gray
247R	1	1	0–3	284	Sparsely phyric PO diabase.	Fine-grained, porphyritic, subophitic.	Homogeneous, massive.	5B 4/1-5B 5/1 dark bluish gray to bluish gray
247R	1	2–15	3–68.5	285	Moderately phyric PO diabase.	Fine-grained, porphyritic, subophitic.	Homogeneous, massive.	5BG 5/1-5G 5/1 greenish gray
247R	1	16–21	68.5–90	286	Moderately phyric OP diabase.	Fine-grained, hypidiomorphic porphyritic, subophitic, Piece 1 is coarser than rest of unit.	Homogeneous, massive.	5G 5/1 greenish gray
248R	1	1–3	0–11	286	Moderately phyric OP diabase.	Fine-grained, hypidiomorphic porphyritic, subophitic, Piece 1 is coarser than rest of unit.	Homogeneous, massive.	5G 5/1 greenish gray
248R	1	4–7	11–24	287	Moderately phyric OP diabase.	Fine-grained, hypidiomorphic porphyritic, subophitic.	Homogeneous, massive.	5BG 6/1 greenish gray
248R	1	8–17	24–62	288	Moderately phyric POC diabase.	Fine-grained, hypidiomorphic, subophitic.	Homogenous, massive.	5BG 6/1 greenish gray
249R	1	1–2	0–8	288	Moderately phyric POC diabase.	Fine-grained, hypidiomorphic, subophitic.	Homogenous, massive.	5BG 6/1 greenish gray
249R	1	3	8–11	289	Aphyric basalt.	Aphanitic, microcrystalline.	Homogenous, massive.	5B 5/1 bluish gray
249R	1	4–28	11–99	290	Moderately phyric PO diabase.	Fine-grained, porphyritic, inequigranular, subophitic.	Homogenous, massive.	5G 5/1 greenish gray
249R	1	29–41	99–148	291	Moderately phyric OPC diabase.	Fine-grained, porphyritic, hypidiomorphic, subophitic.	Homogenous, massive.	5G 5/1 greenish gray
249R	2	1–6	0–25	291	Moderately phyric OPC diabase.	Fine-grained, porphyritic, hypidiomorphic, subophitic.	Homogenous, massive	5G 5/1 greenish gray
250R	1	1–28	0–103	291	Moderately phyric OPC diabase.	Fine-grained, porphyritic, hypidiomorphic, subophitic.	Homogenous, massive	5G 5/1 greenish gray
250R	1	29–32	103–117	292	Moderately phyric POC diabase.	Fine-grained, hypidiomorphic, granular.	Homogenous, massive.	5B 5/1–5B 4/1 bluish gray to dark bluish gray
251R	1	1–3	0–12	292	Moderately phyric POC diabase.	Fine-grained, hypidiomorphic, granular.	Homogenous, massive.	5B 5/1–5B 4/1 bluish gray to dark bluish gray
251R	1	4–20	12–109	293	Moderately phyric POC diabase.	Glomerophyric, fine-grained, intergranular, subophitic.	Homogenous, massive.	5BG 5/1 greenish gray
252R	1	1–9	0–37	293	Moderately phyric POC diabase.	Glomerophyric, fine-grained, intergranular, subophitic.	Homogenous, massive.	5BG 5/1 greenish gray
253R	1	1	0–5	294	Sparsely phyric POC diabase.	Fine-grained, intergranular.	Homogenous, massive.	5B 5/1 bluish gray

Appendix D. Occurrence of spinel. Thin sections are identified by core, section, and interval. The location of spinels within phenocrysts or intergranular material is indicated with the spinel size, shape, color, and other comments. E = euhedral; s = subhedral; a = anhedral. All grains are equant. Colors: r=red, y=yellow, b=brown, bl=black, g=green.

Thin section ID	Unit	Olivine	Plagioclase	Pyx	Ground-mass	Length (µm)	Width (µm)	Shape (e, s, a)	Color	Comments
148–504B–										
239R-1, 26–30 (9)	270									None.
239R-1, 45–51 (14)B	271		1			60	50	a	rb-bl	Fresh.
240R-1, 16–27 (6)	272		1			100	50	a	bl	Magnetite in plagioclase.
			2			100	100	a	rb	Plagioclase is part of large glomerocryst.
240R-1, 33–38 (9)	272									None.
240R-1, 52–63 (14)	273			1		35	35	e	rb	Fresh.
			2			70	70	e	bl,rb	Altered and in altered plagioclase.
			3			130	120	s	b bl	Touching cpx.
			4			50	50	s	rb,y	Adjacent to spinel 3.
			5			90	70	s	rb bl	Symplectic.
			6			70	30	a	bl	In same plagioclase as 5. Symplectic. Toughing augite.
			7			80	40	e	rb	Fresh, in plagioclase adjacent to spinels 5 and 6.
			8			30	20	a	rb	Fresh.
			9			30	30	e	yb	Fresh.
			10,11			70	70	e	rb-bl	Symplectic.
			12			80	80	a	bl	Symplectic in altered olivine.
			13			50	50	e	rb	Fresh.
			14–16			50	50	e	rb-bl	Three fresh grains in plagioclase glomerocyrst.
			17–18			50	50			Two grains at edge of large plagioclase.
240R-1, 82–90 (21)	274				1	120		e	yb-bl	In altered groundmass, grain partly altered and zoned.
			2					a	yb-yg	Fresh, not on surface.
			3			120		e	bl	Symplectic. At edge of plagioclase, round in groundmass.
241R-1, 0–4 (1)	275									None.
241R-1, 16–19 (5)	276		1			40	60	e	yb	Altered to magnetite on 3 sides.
					2, 3	70		e	yb	Altered to magnetite symplectite.
			4			60	80	s	bl	Altered to magnetite symplectite.
			5			50		s	bl	Altered to magnetite symplectite outside of plagioclase.
241R-1, 32–36 (6)	276				1	100		a	yb-bl	Symplectic, altered.
		2				100		e	bl	Altered.
					3	150	150	s	bl	Symplectic.
			4			20		a	y	Irregular, not on surface.
			5			100	30	a	yb-bl	Irregular, fresh.
			6			100	80	e	y-bl	Altered to filaments of magnetite.
			7			70	25	a	ry	
			8			150	150	e to a	ry-bl	Euhedral in plagioclase anhedral in groundmass.
241R-1, 78–81 (15)	276		1			70	70	a	rb	Fresh.
			2			150	100	e	bl	Magnetite in same plagioclase as spinel 1.
			3			90	70	e	bl	Rim and part of core altered.
			4, 5			130	100	e	bl	Core preserved, rim altered to magnetite.
			6			60	50	a	bl	Irregular, some core preserved.
241R-1, 105–108 (19)	276				1	20	10	e	b	In altered pyroxene.
			2			40	40	e	yb-bl	Color seen only on thin edges. Grain not on surface.
					3	130	110	s	yb	Color on edges, rest black, symplectic.
242R-1, 12–16 (4)B	277									None.
242R-1, 28–32 (9)B	277	1				70	70	a	b-bl	Symplectic in altered olivine.
			2			100	50	a	rb yb	Fresh.
					3	80	50	s	b-bl	In chlorite.
		4				100	100	s	b	Symplectic, hollow core in altered olivine.
244R-1, 3–8 (2)	279									None.
245R-1, 21–24 (8)	280									None.
245R-1, 36–39 (13)	281		1			20	10	e	bl	Several magnetite grains in plagioclase fresh.
246R-1, 21–25 (8)	283				1	50	50	a	rb	Fresh, altered to magnetite on rim. In altered olivine.
246R-1, 91–94 (26)	284		1			80	60	e,s	y yb	Fresh, below surface.
			2			100	90	e	yb	Symplectic with glass.
			3			65	60	e	y yb	Fresh.
246R-1, 111–115 (32)	284	1				50	50	a	rb bl	Three grains all altered. Fresh cores. Olivine is altered.
		2				100	80	s	bl	Altered at edges. In same olivine as spinel 1.
			3			120	60	a	y b	Fresh, altered to magnetite along edge.
			4			50	30	s	yb	Three fresh grains under surface in same plagioclase.
247R-1, 46–50 (12)	285		1			50	40	a	y b	Fresh. In plagioclase lath.
					2	60	60	s	bl	Altered to magnetite.

NOTE: As a guide to the reader, only the first page of this Appendix is reproduced here. The entire Appendix is given in the CD-ROM (back pocket).

Appendix E. Grain-size of phenocrysts and intergranular plagioclase and magnetite. A minimum of 100 grains were measured in each thin section. Grain size is reported as the diameter in millimeters (mm) of a circle with an area equal to the average area of the grains in the section (Eqd). Percent abundance are from point counts; "n.d." = not determined; chm = chilled margin.

			Plagioclase phenocrysts				Interstitial plagiolcase				Magnetite		
Sample	Piece	Depth (mbsf)	%	Mean size (mm)	Maximum (mm)	Minimum (mm)	%	Mean size (mm)	Maximum (mm)	Minimum (mm)	Mean size (mm)	Maximum (mm)	Minimum (mm)
148-504B-													
239R-1, 26–30	9	2000.66	7	0.95	1.48	0.63	42	0.27	0.5	0.08	0.117	0.026	0.003
239R-1, 45–51	14	2000.85	3	0.82	1.75	0.53	42	0.22	0.4	0.09	0.094	0.023	0.003
240R-1, 33–38	9	2007.06	7	0.53	0.84	0.41	44	0.19	0.39	0.06	0.088	0.021	0.003
240R-1, 16–27	6	2007.06	6	0.81	1.2	0.58	41	0.22	0.5	0.06	0.096	0.021	0.003
240R-1, 52–63	14	2007.42	2	1.06	3.26	0.51	43	0.32	0.6	0.08	0.112	0.03	0.003
240R-1, 82–90	21	2007.72	4	0.73	1.43	0.51	47	0.25	0.42	0.08	0.1	0.027	0.003
241R-1, 0–4	1	2016.5	9	0.78	0.9	0.65	43	0.19	0.4	0.09	0.087	0.023	0.003
241R-1, 16–19	5	2016.66	5	1.19	4.51	0.51	50	0.3	0.59	0.06	0.096	0.024	0.003
241R-1, 32–36	6	2016.82	5	0.93	1.81	0.52	42	0.25	0.49	0.08	n.d.	n.d.	n.d.
241R-1, 78–81	15	2017.28	4	0.63	1.03	0.51	45	0.29	0.7	0.06	n.d.	n.d.	n.d.
241R-1, 105–108	19	2017.55	8	0.79	1.17	0.61	41	0.34	0.69	0.08	0.11	0.037	0.003
242R-1, 12–16	4	2026.02	2	0.8	1.6	0.54	43	0.25	0.58	0.07	0.099	0.029	0.003
242R-1, 28–33	9	2026.18	1	0.45	0.48	0.41	48	0.25	0.46	0.09	0.104	0.03	0.003
244R-1, 3–8	2	2038.23	2	0.61	0.68	0.52	43	0.13	0.2	0.05	0.057	0.012	0.002
245R-1, 21–24	8	2043.01	1	0.61	0.68	0.52	40	0.25	0.46	0.09	0.113	0.028	0.004
245R-1, 36–39	13	2043.16	1	0.47	0.5	0.4	41	0.15	0.25	0.05	0.076	0.018	0.003
245R-1, 39 chm	13	2043.17	2	0.16	0.53	0.02	n.d.	0.06	0.53	0	0.024	0.007	0.002
245R-1, 39–46	14	2043.19	6	0.61	0.72	0.45	31	0.08	0.25	0.02	n.d.	n.d.	n.d.
246R-1, 21–25	8	2052.41	2	0.53	0.62	0.45	45	0.22	0.46	0.08	n.d.	n.d.	n.d.
246R-1, 91–94	26	2053.11	1	0.58	0.63	0.54	49	0.3	0.59	0.08	0.105	0.031	0.003
246R-1, 111–115	32	2053.31	2	1.17	1.71	0.8	49	0.28	0.58	0.09	0.106	0.045	0.003
247R-1, 46–50	12	2057.16	1	1.02	2.08	0.62	50	0.24	0.49	0.06	n.d.	n.d.	n.d.
247R-1, 64–68	15	2057.34	1	1.38	2.8	0.68	45	0.25	0.49	0.09	0.105	0.032	0.003
247R-1, 72–76	17	2057.42	6	0.48	0.52	0.44	38	0.08	0.28	0.02	0.048	0.014	0.002
247R-1, 78–83	19	2057.48	7	0.91	2.2	0.54	38	0.15	0.45	0.05	0.033	0.013	0.002
248R-1, 43–48	13	2062.23	8	0.76	1.54	0.58	45	0.18	0.46	0.06	n.d.	n.d.	n.d.
249R-1, 87–89	27	2072.07	2	0.83	1.66	0.51	51	0.2	0.45	0.06	n.d.	n.d.	n.d.
249R-1, 92–98	28	2072.12	8	0.87	1.47	0.54	42	0.23	0.5	0.07	0.089	0.024	0.002
249R-1, 92 chm	28	2072.13	7	0.25	0.9	0.06	n.d.	0.1	0.05	0	n.d.	n.d.	n.d.
249R-1, 119–123	35	2072.39	5	0.74	1.45	0.43	42	0.21	0.58	0.06	0.069	0.016	0.003
249R-1, 134–138	40	2072.54	6	0.73	1.05	0.57	45	0.19	0.47	0.06	n.d.	n.d.	n.d.
249R-2, 19–24	6	2072.87	4	0.65	1.34	0.51	45	0.23	0.46	0.07	0.102	0.025	0.003
250R-1, 57–60	16	2080.97	4	0.78	1.68	0.53	45	0.24	0.5	0.07	n.d.	n.d.	n.d.
250R-1, 77–81	22	2081.17	4	0.87	3.77	0.51	41	0.32	0.55	0.12	0.092	0.025	0.003
250R-1, 112–117	32	2081.52	3	0.84	1.48	0.52	48	0.2	0.47	0.07	0.085	0.023	0.003
251R-1, 6–7	2	2089.96	7	0.66	1.29	0.4	47	0.14	0.34	0.05	0.086	0.021	0.003
251R-1, 12–20	4	2090.02	3	0.9	2.56	0.51	37	0.24	0.48	0.09	n.d.	n.d.	n.d.
251R-1, 28–30	5	2090.18	2	0.83	2.15	0.51	46	0.23	0.49	0.06	0.108	0.031	0.003
251R-1, 49–51	7	2090.39	5	0.85	1.87	0.54	42	0.25	0.5	0.07	0.093	0.025	0.003
252R-1, 12–15	4	2099.52	4	0.9	1.37	0.51	43	0.26	0.48	0.06	0.109	0.027	0.004
252R-1, 15–20	5	2099.55	3	0.79	1.44	0.51	32	0.22	0.5	0.07	n.d.	n.d.	n.d.
253R-1, 0–04	1	2103.5	3	1.22	1.22	1.21	43	0.2	0.49	0.07	0.086	0.024	0.002

Appendix F. Glomerocrysts, classified by mineralogical type. The number of grains in each glomerocryst are indicated along with the modal proportions and the maximum and minimum dimensions of the glomerocryst. Mineral abbreviations: pl = plagioclase; cpx = clinopyroxene; ol = olivine; mt = magnetite. The symbol (+) indicates megacryst.

		Glomerocryst type						Number	Size	Relative abundance				
Sample	Piece	Pl	Pl-cpx	Pl-ol	Pl-cpx-ol	Pl-cpx-mt	Other	of grains	(mm)	Pl	Cpx	Ol	Mt	Comments
148-504B-														
239R-1, 26–30	9				+			7	1.6–0.4	85	5	10		Cpx interst.
			+					8	2–0.4	90	10			
						+		8	0.8–0.2	76	22		2	Cpx subophitic-poikilitic.
		+						4	1.2–0.6	95	5			
		+						3	3–0.3	98	2			Pl shows preferred orientation.
240R-1, 33–38	21				+			10	1–0.3	60	10	30		Gabbroic clot.
					+			7	1.2–0.3	70	10	15		Cpx interstitial.
						+		20	0.7–0.2	95	4		1	
				+				15	1.5–0.2	60	5	35		
			+					11	1–0.3	80	20			
240R-1, 52–63	14		+					5	2–0.4	80	20			Pl include Cr-spinel.
					+			40	1.5–0.2	45	10	35		+ Cr-spinel.
				+				13	1.3–0.2	85	4	10	1	+ Cr-spinel.
		+						10	0.7	95	5			Cpx interstisial, Pl complexed zoning.
240R-1, 82–90	21	+						3	1.5	100				Some Pl include glass inclusion.
		+						7	1	100				
				+				16	2–0.3	85		15		
		+						8	0.8	100				
241R-1, 0–4	1			+				10	1–0.4	80	2	18		Pl complexed zone. (n-r-n).
		+						4	2.2–0.6	100				Ab-Carlsbad-Pericline twin.
		+						10	1–0.2	100				Some Pl contain glass inclusion.
							Cpx	6	1.2–0.2	10	89		1	Oikocrsytal of Cpx.
		+						10	0.4	100				Subhedral-anhedral.
241R-1, 16–19	5	(+)						1	1	100				Anhedral xenocryst.
		+						7	1–0.2	100				
		+						6	0.8	100				
241R-1, 32–36	6	+						10	2–0.3	95	5			Most Pl show similar orientation.
		+						8	2–0.2	98	2			Pl margin is irregular.
		+						4	2–0.6	100				
		+						12	2–0.4	100				Glass incusions.
241R-1, 105–108	6		+					14	0.8–0.3	90	10			
					+			18	1.8–0.2	65	10	25		
		+						12	0.8–0.15	100				
244R-1, 3–8	2	+						3	1–0.5	100				
		+						3	0.8–0.3	95	5			
			+					3	1–0.4	85	15			
245R-1, 21–24	8					+		5	1–0.5	92	6		2	
245R-1, 36–39	13	+						3	0.5–0.2	100				
246R-1, 24–25	8	+						3	1.5–.04	100				
		(+)						1	1.8	100				Anhedral xenocryst.
246R-1, 91–94	26	+						5	1.5–0.5	100				
		(+)												
246R-1, 111–115	32	+						3	1.5–0.5	100				
		+						5	1.5–0.5	98	2			
247R-1, 46–50	12	+						8	0.8–0.3	100				
		+						5	1.3–0.5	100				
		(+)						1	2.2					Xenocryst with glass inclusion.
247R-1, 64–68				+				12	3–0.3	95		5		Glass inclusion, euhedral.
				+				16	1.5–0.3	65	2	33		Ol completely altered.
		+						10	2.5–0.5	100				
		+						10	1.4–0.2	100				
247R-1, 72-76				+				13	1–0.3	70	3	27		
				+				6	1.2–0.4	55	45			
		+						7	0.6–0.2	98	2			
		(+)					Cpx	1	1.3		100			Xenocryst.
							Cpx	4	1.2–0.4		100			
248R-1, 43–48	13		+					10	1–0.3	50	50			
		+						4	1.3–0.5	100				
				+				6	2–0.5	80	5	15		
249R-1, 87–89	27	+						7	2–0.4	100				
		(+)						1	1.8	100				Xenocryst.
249R-1, 92–98	28						Ol	4	0.8–0.3	100				Basalt.
			+					4	0.6–0.3	20		80		Basalt.
249R-1, 119–123	35			+				23	0.8–0.15	70	5	25		Adcumulus texture.
		+						10	1.5–0.2	100				
							Cpx	1	3	5	95			Oikocryst of Cpx including Pl.
			+				Cpx	3	1.8	10	90			Oikocryst of Cpx including Pl.
249R-1, 134–138	40	+						20	1–0.2	96	4			
		+						7	2–0.5	95	5			
		+						25	0.6–0.15	95	5			
249R-2, 19–24	6	+						8	2–0.4	100				
		+						20	1.5–0.3	97	3			
			+					14	2–0.4	95	4			
250R-1, 57–60	16	+						5	2–0.5	100				
		+						3	2–0.6	100				
250R-1, 77–81	22	+						13	1.2–0.4	96	4			

NOTE: As a guide to the reader, only the first page of this Appendix is reproduced here. The entire Appendix is given in the CD-ROM (back pocket).

Appendix G. Alteration log. Abbreviations are defined in Table 3, "Explanatory Notes" chapter.

Unit	Core	Section	Piece	Length	Interval (cm) Top	Bottom	Lithology	After olivine	%	After plagioclase	%	After augite	%	After others	%
270	239R	1	1												
270			2–12	27	4	41	db	chl	100						
271			13, 14	8.5	41	50	db	chl, pyr	100						
272	240R	1	1 -10, 12	30	0	41	db	chl	100						
273	240R	1	11, 13–20	27	41	82	db	chl ± Fe(OH) ± pyr	100						
274	240R	1	21–22	14	82	99	db	chl	100	Rims	<5				
275	241R	1	1–3	8	0	11	db								
276	241R	1	4–26	127	11	149	db	chl	100					White fibrous	
	241R	2	1		0	5									
	242R	3	1–2		0	9									
277	242R	1	3–10	18	9	36	db	chl	100						
278	242R	1	11	1	36	39	db	chl	100						
279	244R	1	1–2	4.5	0	7.5	db								
280	245R	1	1–12	23	0	36	db								
281	245R	1	13–16	6	36	52	db								
282	245R	1	17, 18	3	52	58	db								
282	246R	1	1	1	0	2	db								
283	246R	1	2–20	55	2	73	db								
284	246R	1	21–32	32	73	115	db								
285	247R	1	2–15	53	1.5	68	db								
286	247R	1	16–21	16	68	89	db								
286	248R	1	1–3	8.5	0	10	db								
287	248R	1	4–7	11	10	24	db								
288	248R	1	7–17	31	24	60	db	?+ FeOOH	100						
288	249R	1	1–2	8	0	8	db								
289	249R	1	3	2.5	8	11	db								
290	249R	1	4–28	60	11	99	db								
291	249R	1	29–41	39	99	148	db								
291	249R	2	1–6	20	0	25	db								
291	250R	1	1–28	82	0	103	db	chl, py	100						
292	250R	1	29–32	13	103	117	db								
292	251R	1	1–3	10	0	12	db	chl	100						
293	251R	1	4–6	30	12	47	db	chl,py	100						
293	251R	1	7–20	55	47	110	db	chl	100						
293	252R	1	1–3	9.5	0	11	db	chl	100						
293	252R	1	4–9	20	11	37	db								
294	253R	1	1	4	0	4	DB								

Appendix G. (continued).

After g'mass	%	Halos	AW Cm	AW %	Vugs	AD Cm	AD %	Comments
								Rubble fallen into hole.
amph	20			0				Halos all related to veining.
amph	20			0				More porphyritic.
amph	20			0				
amph	30	Green in piece 14	2	50				Patch in Piece 14 crosscuts core at moderate angle; light green core and dark green margins; 4 cm wide and > 6 cm long; extends past end of core.
amph	30	Green	2	50				Piece 22 – halo/patch comprises 80% of piece.
amph	20			0				Small pieces of rubble; small vein in Piece 2.
amph, plag, disseminated pyr	20	>80% alt in green halos (e.g., piece) 4,20,26	2	40				20–30% of rock is altered patches (>80% alteration); balance of rock is moderately altered db (20% alteration).
amph	20	Green	1	5				No patches; crossed by a few veins with 2–3 mm halos.
amph	35			0				Single Piece.; more altered; coarser grain size.
amph	20			0				Fine grained, slightly to moderately altered (20%).
		Green	<1	<5				Ditto. Piece 12 very fine grained.
				0				With chilled margins. Variable alteration up to moderate.
				0				Ditto.
				0				Ditto.
		Green	1	10				Variable alteation; moderate background alteration in host diabase; highly altered patches, more abundant at base.
		Green	1	10				Similar alteration style; unit coarser grained.
amph	30	Green	1	<5				Med to fine db, only a few patches.
				0				Chilled facies; 248R–1, Piece 1 seems out of place, has 25% patches of alteration; chilled facies has veins and halos, but no patches; black spots after olivine in both halos and groundmass.
				0				Ditto.
?	10			0				Fine grained, appears relatively unaltered.
amph	20	Green		<5				Coarsens from fine to medium down Unit; numerous veins with complex halos; little alteration outside of vein halos.
amph	20	Green		<5				Ditto.
								Very fine grained; no visible alteration.
amph	20	Green		<5				Coarsens from fine to medium down Unit; little alteration outside of vein halos.
amph	20	Green		<5				Highly variable grain size, similar to Unit 290.
amph	20	Green		<5				Ditto.
amph	20	Green	1	<5				Patches are not as strongly altered; can still see igneous texture in them.
amph	20			0				Finer-grained unit. No patches.
?	<5			0				Fresh cpx phenocrysts; only slight alteration. Quartz vein.
amph	60				epid.	0.5	<5	
amph	20	Green	1	10				
amph	20	Green	1	20				
amph	60			0	md gn	1	<1	Heavily altered, no igneous minerals left (except a few in Piece 8). Lt green amygdules may be laumontite (e.g., Piece 5); medium green may be epidote (e.g., Piece 6).
	<5			0				Slight alteration; fresh phenocrysts.

Appendix H. Vein log. Abbreviations are defined in Table 3, "Explanatory Notes" chapter.

Unit	Core	Section	Piece	Length	Interval Top	Interval Bottom	Type	Minerals	%	AW	Halo	%Alt	W	%H	Comments
270	239R	1	1	2	3	4	med grn(1)	act	3	2	dk grn	80	3	8	This piece has fallen in (rubble).
270	239R	1	9	3	28		frac (1)	None	<1	<1	None	0	0	0	Ditto.
270	239R	1	11	3	34		med grn (1)	act	3	1	None	0	0	0	Ditto.
270	239R	1		34	36		frac (1)	None	<1	<1	None	0	0	0	Ditto.
271	239R	1	13	4	41	45	med grn (1)	act	3	1.5	med grn	80	2		very diffuse boundary with the fresh rock.
271	239R	1	14	5	46	49	med grn (4)	act	1	1	dk grn	90	4	12	Dark halo contacts the vein. Smaller veins are offshoots.
271	239R	1			48		med grn (4)								
271	239R	1			46	47	med grn (4)								
271	239R	1			46		med grn (4)								
271	239R	1			47		frac (1)	None	<1	<1	None	0	0	0	Fracture locally enters the vein.
272	240R	1	4	2	11		frac (1)	None	<1	<1	None	0	0	0	
272	240R	1	6	11	18	25	frac (1)	None	<1	<1	None	0	0	0	Only one of these two intersects the open surface.
272	240R	1		11	16	24	frac (1)	None	<1	<1	None	0	0	0	Only one of these two intersects the open surface.
272	240R	1	9	5	33	34	frac (1)	None	<1	<1	None	0	0	0	
273	240R	1	14	10	52	59	dk grn (1)	chl	1	<1	None	0	0	0	Planar rock surface coated with chlorite.
273	240R	1			52	56	dk grn (1)	chl	1	<1	None	0	0	0	Planar rock surface coated with chlorite.
273	240R	1			57		frac (1)	None	<1	<1	None	0	0	0	
273	240R	1			59		frac (1)	None	<1	<1	None	0	0	0	
273	240R	1	19	2	76		frac (1)	None	<1	<1	None	0	0	0	
273	240R	1			77		frac (1)	None	<1	<1	None	0	0	0	
273	240R	1	20	2	80		frac (1)	None	<1	<1	None	0	0	0	
274	240R	1	21	7	83	85	md grn (1)	act	2	1	None	0	0	0	
274	240R	1			82	83	frac (1)	None	<1	<1	None	0	0	0	
274	240R	1	22	8	90	97	dk grn (1)	chl	<1	<1	None	0	0	0	Planar rock surface coated with chlorite.
274	240R	1			90		frac (1)	None	<1	<1	None	0	0	0	
274	240R	1			92		frac (1)	None	<1	<1	None	0	0	0	
274	240R	1			94		frac (1)	None	<1	<1	None	0	0	0	
274	240R	1			92	96	med grn (1)	act	1	<1	None	0	0	0	
275	241R	1	2	2	5	7	med grn (1)	act	4	1	med grn	80	5	20	
276	241R	1	4	4	15		med grn (1)	act	<1	<1	None	0	0	0	Mainly seen on the exposed surface.
276	241R	1	5	15	16	27	frac (1)	None	<1	<1	None	0	0	0	
276	241R	1			27		frac (1)	None	<1	<1	None	0	0	0	
276	241R	1			30	31	frac (1)	None	<1	<1	None	0	0	0	
276	241R	1			25	29	dk grn (4)	chl(?)	1	<1	None	0	0	0	One is on a planar rock surface.
276	241R	1			25	28	dk grn (4)								
276	241R	1			27	28	dk grn (4)								
276	241R	1			25	31	dk grn (4)								
276	241R	1	6	4	32	36	med grn (1)	act	8	<1	dk grn	90	<1	2	
276	241R	1			32	36	dk grn (1)	act/chl(?)	8	<1	lt grn	60	3	8	Light halo hardly distinguishable.
276	241R	1			32	34	colorless	???	<1	<1	None	0	0	0	Discontinuous; may be just alignment of colorless minerals; may not be a vein.
276	241R	1	10	6	47		frac (1)	None	<1	<1	None	0	0	0	
276	241R	1			49	50	frac (1)	None	<1	<1	None	0	0	0	
276	241R	1			51		frac (1)	None	<1	<1	None	0	0	0	
276	241R	1			47	52	dk grn (1)	chl	1	<1	None	0	0	0	Opened.
276	241R	1	11	6	56		frac (1)	None	<1	<1	None	0	0	0	
276	241R	1			59		frac (1)	None	<1	<1	None	0	0	0	
276	241R	1			54	58	frac (1)	None	<1	<1	None	0	0	0	
276	241R	1			57	59	frac (1)	None	<1	<1	None	0	0	0	
276	241R	1	12	8	64		frac (1)	None	<1	<1	None	0	0	0	
276	241R	1			66		frac (1)	None	<1	<1	None	0	0	0	
276	241R	1			68	69	frac (1)	None	<1	<1	None	0	0	0	
276	241R	1			63	70	dk grn (1)	chl	1	<1	None	0	0	0	Planar rock surface coated with chlorite.
276	241R	1	13	3	71	74	frac (1)	None	<1	<1	None	0	0	0	
276	241R	1	14	3	78		dk grn (1)	chl	1	<1	None	0	0	0	
276	241R	1	15	3	81		med grn (2)	act	6	1	med grn	80	6	60	Original sketch on shipboard log sheet. (Might be a chilled dikelet)

NOTE: As a guide to the reader, only the first page of this Appendix is reproduced here. The entire Appendix is given in the CD-ROM (back pocket).

Appendix I. Modal proportions of alteration minerals. Alteration modal data (point counts). Abbreviations are defined in Table 3, "Explanatory Notes" chapter.

Core	Section	Top	Bottom	Piece	Depth (mbsf)	Talc	Chl	Ab	Ep	Act	Tt	Qtz	An	Oxide	Pyr	
239	1	26	30	9	2000.66	2.6	0.2	0	0	20.8	0	0	0	0	0	
239	1	45	51	14	2000.85	0	1.8	2.6	0	59.6	0	0	0	1	0	Vein halo
239	1	45	51	14	2000.85	0	5.6	0	0	27.8	0	0	0	0	0	Background
240	1	16	27	6	2007.06	4	0	0	0	20	0	0	0	0	0	
240	1	33	38	9	2007.23	0.4	0.4	0.6	0	30	0	0	0	0	0	
240	1	52	63	14	2007.42	0	9.2	3	0	27.4	0	0	0	0	0.4	
240	1	82	90	21	2007.72	0	4	0	0	48.2	1	0	0	0	0	Vein halo
240	1	82	90	21	2007.72	0	13.2	0.4	0	26.6	0	0	0	0	0.2	Background
241	1	0	4	1	2016.5	2.2	0.6	0	0	17.2	0	0	0	0.8	2.4	
241	1	16	19	5	2016.66	0	0	0.4	0	39.6	0	0	0	0	0	
241	1	32	36	6	2016.82	0	1.2	2.4	0	52	0	0	0	0	0	
241	1	78	89	15	2017.28	0	1.2	0	0	58.2	0	0	2	1	0	Patch
241	1	78	89	15	2017.28	0	12.6	0	0	25.4	0	0.2	0	0	0	Background
241	1	105	108	19	2017.55	0	2	0	0	49	0.8	0	0	0	0	
242	1	12	16	4	2026.02	0.1	1.6	0	0	34.6	0	0	0.2	0.1	0	
242	1	28	33	9	2026.18	2	1.5	0.3	0	28.5	0	0	0.4	0.7	0	
244	1	3	8	2	2038.23	0.6	0	0	0	26.4	0	0	0	0	0	
245	1	21	24	8	2043.01	0	0	0	0	47	1	0	0	0	0	
245	1	36	39	13	2043.16	0	0	0	0	49	0	0	0	0	0	
245	1	39	46	14	2043.19	0	0	0	0	53.2	0	0	0	8.8	0	
246	1	21	25	8	2052.41	0	0	0	0	57.5	1.5	0	0	0	0	
246	1	91	94	26	2053.11	0	2.6	0.6	0	42.6	0	0	0	0	0	
246	1	111	115	32	2053.31	0	1.2	4.4	0	51	0	0	0	0	0	Vein halo
246	1	111	115	32	2053.31	0	5.6	0	0	26.8	0	0	0	0	0	Background
247	1	46	50	12	2057.16	0	0.4	0	0	47.8	0	0	0	1	0	
247	1	64	68	15	2057.34	3.8	2.4	0.2	0	24.8	0	0	0	0	0	
247	1	72	76	17	2057.42	0.6	0.6	0	0	8	0.4	0	0	0.6	0	
248	1	43	48	13	2062.23	0	5.6	0	0	26.8	0.1	0	0	0	0	
249	1	87	49	27	2072.07	0	1	0.4	0	41.8	0.6	0	0	0	0	
249	1	92	98	28	2072.12	0	3	0	0	45	0	0	0	0	0	
249	1	119	123	35	2072.39	0	4.6	0.8	0	13.4	0	0	0	0	0	
249	1	134	138	40	2072.54	0	6.8	1.3	0	41.1	0	0.8	0	0	0.1	
249	2	19	24	6	2071.39	1	0.4	0	0	18.6	0	0	0	0	0	
250	1	57	60	16	2080.97	0	2	0	0	49.3	0	0	0	0	0	
250	1	77	81	22	2081.17	0	6.2	0.8	0	41.2	0	0.4	0	0	0	
250	1	112	117	32	2081.52	0	5.2	0	0	16.8	0.4	0	0	0	0	
251	1	18	20	4	2090.08	0	1.4	5	0	70.2	0	0	4.6	0	0	
251	1	28	30	5	2090.18	0	3.2	3.6	0	48.6	0	0	5.2	0	0	
251	1	49	51	7	2090.39	0	6	0	0	32	1	0	3.7	0	0	
252	1	12	15	4	2099.52	0	0.6	0.4	0	54.2	0.6	0	13.4	0	0	
252	1	15	20	5	2099.55	0	0	8	0	72	0	0	0	0	0	
253	1	0	4	1	2103.5	0	0	0	0	22.4	0	0	0	0	3	

Appendix J. Structure log.

Core	Type	Section	Piece	Oriented?	Interval (cm) Top	Interval (cm) Bottom	Depth (mbsf)	Feature	Composition	Apparent dip 1 Dir.	Apparent dip 1 Angle	Apparent dip 2 Dir.	Apparent dip 2 Angle	True dip Angle	True dip Dir.	Mag. dec	Mag. inc	Corrected displacement Angle	Corrected displacement Dir.	Corrected displacement Sense	SBA	Comment
239	R	1	13	N	41	45	2000.9	vein	Ac	297	0	270	47	67								Continuous, smooth, planar, HSD.
239	R	1	14	N	46	49	2000.9	vein	Ac	090	27	177	5	27							T	Continuous, smooth, planar, HSD.
239	R	1	14	N	46	47	2000.9	vein	Ac	000	10	270	88	88							T	Discontinuous, smooth, planar, HSD.
239	R	1	14	N	48		2000.9	vein	Ac	270	4	352	1	4							T	Discontinuous, smooth, planar, HSD.
239	R	1	14	N	48		2000.9	fracture		090	1	345	0	1							T	Discontinuous, smooth-rough, planar-curved, HSD.
240	R	1	6	Y	16	25	2007.1	microfault						90	078	298	027	090	320	Normal/PTsteps	MT	Continuous, smooth, planar, forms face of core.
240	R	1	6	Y	16	25	2007.1	slickenline						62	168	298	027	062	050		MT	
240	R	1	6	Y	18	24	2007.1	microfault						76	288	298	027	076	170		MT	Continuous, smooth, planar, forms face of core.
240	R	1	6	Y	19	23	2007.1	microfault						88	085	298	027	088	327	Normal/PTsteps	MT	Continuous, smooth, planar, forms face of core.
240	R	1	6	Y	19	23	2007.1	slickenline						86	358	298	027	086	240		MT	N.B. poorly oriented with respect to vertical.
240	R	1	6	Y	22	23	2007.1	microfault						80	103	298	027	080	345		MT	Continuous, smooth, planar, forms face of core.
240	R	1	14	Y	52	59	2007.4	vein	Chl	096	0	090	79	89	006							Continuous, smooth, planar, chl coated fract. forms face of core.
240	R	1	14	Y	52	56	2007.4	vein	Chl					88	174							As above but discontinuous and on archive half only.
240	R	1	14	Y	58		2007.5	fracture		270	6	180	16	17	200							Continuous, curviplanar, smooth-weakly branching,TWC.
240	R	1	14	Y	59		2007.5	fracture		090	3	000	1	3	072							Continuous, curviplanar, smooth-weakly branching,TWC.
240	R	1	21	Y	82	83	2007.7	fracture		090	9	000	16	18	049	348	004	018	241		MT	Discontinuous, planar, smooth-rough, TWC.
240	R	1	21	Y	83	85	2007.7	vein	Ac	270	15	349	6	15	282	348	004	015	114		MT	Continuous, planar-weakly sinuous, smooth.
240	R	1	22	Y	90		2007.8	fracture		090	14	342	7	18	050							Discontinuous, planar, smooth-rough, TWC.
240	R	1	22	Y	90	97	2007.8	vein	Chl					83	263							Continuous, smooth, planar, chl coated fract. forms face of core.
240	R	1	22	Y	92	96	2007.8	vein	Ac	090	46	009	41	52	055							Continuous, smooth, sinuous.
241	R	1	4	N	15		2016.7	vein	Ac	090	72	358	0	75								Discontinuouos, planar, smooth.
241	R	1	5	Y	16	23	2016.7	fracture		090	77	170	0	77	080	058	015	077	202		MT	Discontinuous, planar, smooth-rough, TWC.
241	R	1	5	Y	17	26	2016.7	vein	Chl	150	0	090	85	86	330	058	015	086	092		MT	Continuous, smooth, planar, chl coated fract. forms face of core.
241	R	1	5	Y	25	31	2016.8	vein	Chl	187	0	270	76	76	277	058	015	076	039		MT	Discontinuous, smooth, planar, chl coated fract. forms face of core.
241	R	1	6	N	32	34	2016.8	vein	Chl	332	0	090	71	73							T	Discontinuous, smooth, planar, chl coated fract. forms face of core.
241	R	1	6	N	32	34	2016.8	fracture		180	27	090	35	41							T	Discontinuous, planar to weakly sinouous, TWC.
241	R	1	6	N	32	36	2016.8	vein	Ac	090	16	000	17	23							T	Continuous, smooth, planar.
241	R	1	6	N	32	36	2016.8	vein	Ac/Chl	090	13	000	26	28							T	Continuous, smooth, planar.
241	R	1	9	N	43	45	2016.9	vein	Chl	270	86	359	0	86								Continuous, smooth, planar, forms face of core. Only on working half.
241	R	1	10	Y	47	52	2017.0	vein	Chl	090	82	003	0	82	093							Continuous, forms face of core, seperates pieces 10a, 10b.
241	R	1	11	Y	54	58	2017.0	fracture		270	80	188	0	80	278							Discontinuous, planar, TWC.
241	R	1	11	Y	59		2017.1	fracture		270	16	000	23	27	326							Discontinuous, planar, TWC.
241	R	1	12	Y	63	70	2017.1	vein	Chl	167	0	270	75	75	257							Continuous, smooth, planar, forms fractured face of core.
241	R	1	14	N	78		2017.3	vein	Chl	178	0	090	78	78								Continuous, smooth, planar, forms fractured face of core.
241	R	1	15	N	81		2017.3	dikelet		270	88	164	0	88							T	Planar, complex branching, HSD.
241	R	1	15	N	81		2017.3	fracture		296	0	180	86	86							T	Continuous, Chl coated, forms face of core. Only on working half.
241	R	1	18	N	90	95	2017.4	fracture		270	88	274	88	88								Continuous, planar.
241	R	1	19	Y	95	108	2017.5	vein	Ac	052	0	090	78	83	142	064	–003	083	258		MT	Continuous, planar, somewhat irregular.
241	R	1	19	Y	96		2017.5	vein	Chl/Ac	090	20	180	36	39	153	064	–003	039	269		MT	Planar, continuous, smooth.
241	R	1	19	Y	96	105	2017.5	vein	Chl/Ac	249	0	090	77	85	159	064	–003	085	275		MT	Discontinuous, planar, smooth.
241	R	1	19	Y	97	98	2017.5	vein	Chl/Ac	090	14	180	43	44	165	064	–003	044	281		MT	Discontinuous, curvilinear, smooth.
241	R	1	19	Y	100	101	2017.5	vein	Chl/Ac	090	40	180	58	61	152	064	–003	061	268		MT	Discontinuous, planar, smooth.
241	R	1	19	Y	105	109	2017.6	vein	Chl/Ac	270	55	202	0	57	292	064	–003	057	048		MT	Discontinuous, planar, smooth.
241	R	1	19	Y	107	109	2017.6	vein	Chl/Ac	090	79	000	85	85	024	064	–003	085	140		MT	Discontinuous, planar, smooth.
241	R	1	20	Y	113	122	2017.6	fracture		270	86	348	0	86	258							Continuous, curved and branching.
241	R	1	20	Y	113	122	2017.6	fracture		270	8	348	0	8	258							Continuous, curved and branching.
241	R	1	22	N	125	131	2017.8	vein	Chl					90								Continuous, smooth, planar, forms fractured face of core.
241	R	2	1	N	0	5	2018.0	vein	Ac	270	19	006	12	23								
242	R	1	4	N	13	16	2026.0	vein	Ac	090	40	352	4	41							T	Planar, continuous, smooth.
246	R	1	9	N	27	29	2052.5	fracture		090	67	162	15	67								TWC.
246	R	1	12	N	37		2052.6	fracture		090	52	196	12	55								TWC.
246	R	1	12	N	37		2052.6	microfault						75	355					PT-steps		Somewhat irregular surface, incipient.
246	R	1	12	N	37		2052.6	slickenline				270	13	13	268							
246	R	1	13	N#	42		2052.6	fracture		090	72	349	0	72	079							Discontinuous, irregular, TWC.
246	R	1	13	N#	42		2052.6	microfault						86	187					Sinistral/PT steps		Irregular surface.
246	R	1	13	N#	42		2052.6	slickenline				270	9	9	276							
246	R	1	13	N#	42		2052.6	disk axis						3	207							
246	R	1	19	N	66	69	2052.9	microfault						88	182					Sinistral/PT steps		
246	R	1	19	N	66	69	2052.9	slickenline				090	8	8	092							

NOTE: As a guide to the reader, only the first page of this Appendix is reproduced here. The entire Appendix is given in the CD-ROM (back pocket).

Appendix K. Deformation log.

Core	Section	Piece	Interval (cm)	Unit	Depth (mbsf)T	Lithology	Magmatic	Crystal–plastic	Cataclastic	Fractures	Veins	Comments
239R	1	1–13	0–45	270/271	2000.4	Diabase	0	0	0	1/1	1/0	Most pieces are rollers. Pieces 2, 4, 7, 8, 9 have multiple parallel fractures, and Pieces 2 and 9 have faint slickenlines(?) and steps(?).
240R	1	1–5	0–15	272	2006.9	Diabase	0	0	0	1/1	0/0	Piece 1 has slickensides, other pieces are rollers.
240R	1	6	16–27	272	2007.0	Diabase	0	0	0	2/1	0/0	Well developed slickenlines on four subparallel fractures.
240R	1	7–10	27–40	272	2007.2	Diabase	0	0	0	0/0	0/0	
240R	1	11–13	40–51	273	2007.3	Diabase	0	0	0	0/0	0/0	
240R	1	14–22	51–99	273/274	2007.4	Diabase	0	0	0	1/1	1/0	Sinuous veins in Piece 21.
241R	1	1	0–5	275	2016.5	Diabase	0	0	0	0/0	0/0	
241R	1	2	5–8	275	2016.6	Diabase	0	0	0	0/0	1/0	
241R	1	3–5	8–31	275/276	2016.6	Diabase	0	0	0	1/1	1/0	
241R	1	6–9	31–47	276	2016.8	Diabase	0	0	0	0/0	1/0	
241R	1	10–18	46–95	276	2017.0	Diabase	0	0	0	1/1	1/0	
241R	1	19	95–109	276	2017.5	Diabase	0	0	0	0/0	2/0	Actinolite veins.
241R	1	20–26	109–147	276	2017.6	Diabase	0	0	0	1/1	1/0	
241R	2	1	0–5	276	2018.0	Diabase	0	0	0	1/1	1/0	
242R	1	1–8	0–28	277	2025.9	Diabase	0	0	0	1/1	1/0	Pieces 3 and 6 are platy and have parallel fractures with faint slickenlines.
242R		9–11	28–39	278	2026.2	Diabase	0	0	0	2/1	0/0	Platy pieces bounded by fractures. Well-developed slickenlines on Piece 9, faint slickenlines on Piece 10.
244R	1	1–2	0–8	279	2038.2	Diabase	0	0	0	1/1	0/0	Both pieces unoriented, but slickenlines on vertical planes. Continuous fracture surfaces.
(Junk basket)												Abundant platy pieces containing microfaults.
245R	1	1–4	0–12	280	2042.8	Diabase	0	0	0	1/1	0/0	Pieces 1, 2, and 3 have well developed slickenlines.
245R	1	5–7	12–21	280	2042.9	Diabase	0	0	0	1/1	0/0	Pieces 5 and 6 have well developed slickenlines.
245R	1	8–14	21–45	280/281	2043.0	Diabase	0	0	0	2/1	1/0	Pieces 8, 10, 13, and 14 have well developed slickenlines, associated with well-developed steps in 13 and 14.
245R	1	15–17	45–54	281/282	2043.2	Diabase	0	0	0	2/1	0/0	Small fracture-bound pieces 1 cm thick.
245R	1	18	54–57	282	2043.3	Diabase	0	0	0	2/1	0/0	Good slickenlines.
246R	1	1	0–2	282	2052.2	Diabase	0	0	0	1/1	0/0	Faint slickenlines.
246R	1	4, 6	2–17	283	2052.2	Diabase	0	0	0	0/0	1/0	
246R	1	7	18–21	283	2052.4	Diabase	0	0	0	1/1	1/0	
246R	1	8	21–24	283	2052.4	Diabase	0	0	0	0/0	0/0	
246R	1	9	27–29	283	2052.5	Diabase	0	0	0	1/1	0/0	Disking fracture + TWC.
246R	1	11	34–36	283	2052.5	Diabase	0	0	0	0/0	1/0	Plagioclase phenocryst offset by vein, suggesting pure extension.
246R	1	12	36–37	283	2052.6	Diabase	0	0	0	1/1	0/0	
246R	1	13	37–42	283	2052.6	Diabase	0	0	0	1/1	0/0	Disking fractures.
246R	1	14	42–47	283	2052.6	Diabase	0	0	0	1/1	0/0	
246R	1	15	51–52	283	2052.7	Diabase	0	0	0	1/1	0/0	Fracture forms face of core, no slickenlines.
246R	1	16	54–58	283	2052.7	Diabase	0	0	0	1/1	0/0	Slickenlines with steps.
246R	1	19	66–69	283	2052.9	Diabase	0	0	0	2/1	0/0	Slickenlines. Majority TWC.
246R	1	20	70–72	283	2052.9	Diabase	0	0	0	2/1	0/0	TWC
246R	1	24	83–86	284	2053.0	Diabase	0	0	0	0/0	1/0	
246R	1	25	87–89	284	2053.1	Diabase	0	0	0	1/1	0/0	
246R	1	26	91–93	284	2053.1	Diabase	0	0	0	0/0	1/0	
246R	1	29–30	100–107	284	2053.2	Diabase	0	0	0	1/1	0/0	Faint slickenlines in both pieces.
247R	1	1–2	0–5	284/285	2056.7	Diabase	0	0	0	2/2	0/0	Platy with fault slickensides, surfaces somewhat irregular.
247R	1	3–4	5–13	285	2056.8	Diabase	0	0	0	1/1	1/0	
247R	1	5–7	13–29	285	2056.8	Diabase	0	0	0	1/1	1/0	Flat surface with slickensides; no step structures.
247R	1	8–9	29–36	285	2057.0	Diabase	0	0	0	0/0	0/0	
247R	1	10–11	36–46	285	2057.1	Diabase	0	0	0	1/1	1/0	Continuous, planar and smooth veins; one chlorite covered face.
247R	1	12–13	46–58	285	2057.2	Diabase	0	0	0	1/1	3/0	Planar, smooth to irregular.
247R	1	14–15	59–68	285	2057.3	Diabase	0	0	0	0/0	1/0	Thin, planar, smooth.
247R	1	16–18	69–78	286	2057.4	Diabase	0	0	0	2/2	0/0	Slickensides
247R	1	19	79–82	286	2057.5	Diabase	0	0	0	1/1	1/0	Planar vein; sinous internal structure within the vein.
247R	1	20	83–85	286	2057.5	Diabase	0	0	0	2/2	0/0	Same as Pieces 16 through 18.
247R	1	21	86–89	286	2057.6	Diabase	0	0	0	1/1	2/0	Banded halo.
248R	1	1	0–4	286	2061.8	Diabase	0	0	0	1/1	0/0	One TWC.
248R	1	2–4	4–14	286/287	2061.9	Diabase	0	0	0	1/1	2/1	Branching veins; continuous, planar, smooth.
248R	1	5–8	14–27	287/288	2062.0	Diabase	0	0	0	1/1	1/0	Diffuse and planar veins.
248R	1	9–11	27–39	288	2062.2	Diabase	0	0	0	1/1	1/0	Smooth and sinuous veins; occasional TWC.
248R	1	12	39–42	288	2062.2	Diabase	0	0	0	1/1	0/0	TWC
248R	1	13–17	43–62	288	2062.4	Diabase	0	0	0	1/1	1/1	Discontinuous TWCs; some diffuse veins.

NOTE: As a guide to the reader, only the first page of this Appendix is reproduced here. The entire Appendix is given in the CD-ROM (back pocket).